FACULTY OF SCIENCE
UNIVERSITY OF COPENHAGEN

PhD Thesis in Physics

Exploration of the Challenges of Neutron Optics and Instrumentation at Long Pulsed Spallation Sources

Kaspar Hewitt Klenø

This thesis has been submitted to the PhD School of
The Faculty of Science, University of Copenhagen

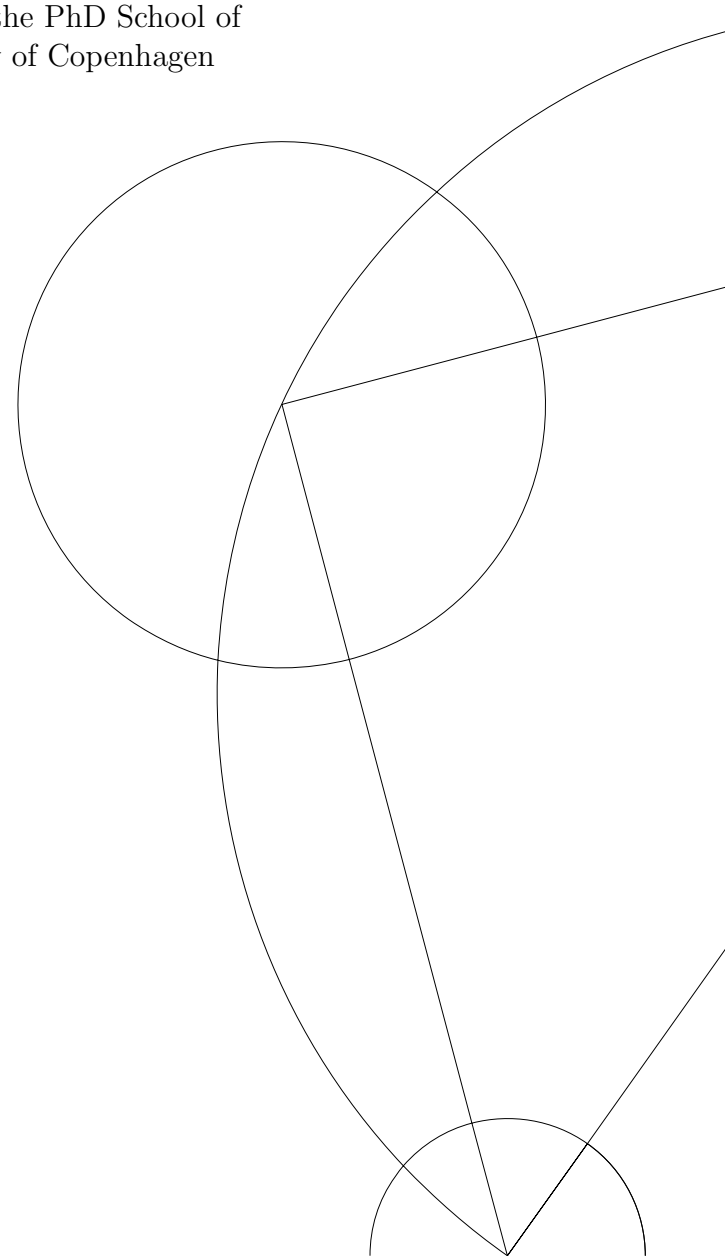

Academic Advisors:

Kim Lefmann
Niels Bohr Institute
University of Copenhagen

Ken Andersen
European Spallation Source

Submitted: September 2013

Preface

This thesis is submitted in fulfilment with the requirements for obtaining a PhD degree at the Niels Bohr Institute, Faculty of Science, University of Copenhagen. The PhD study has been conducted under the supervision of associate professor Kim Lefmann and co-supervision of adjoint professor Ken Andersen, at the Niels Bohr Institute. It was initiated in February 2011 and ends in August 2013. In the two years preceeding this, I was employed as a research assistant in the ESS-Copenhagen simulations group, and I have including some results from this period in the thesis.

The thesis includes four peer-reviewed papers Klenø et al.[1], Klenø et al.[2], Klenø et al.[3], and Lefmann et al.[4], one submitted paper Klenø et al.[5], one paper in progress Klenø et al.[6], and two official reports Klenø et al.[7] and Lefmann et al.[8]. In the publication list full references for all papers are listed.

Abstract

In this thesis I have explored the challenges of long guides and instrumentation for the long pulsed European Spallation Source.

I have derived the analytical description needed for quantifying the performance of a guide using brilliance transfer. With this tool it is easier to objectively compare how well different guides perform the same task.

In comparing different guide geometries, I have shown that for transporting thermal or highly divergent neutrons over medium to long distances, elliptic and parabolic guides are significantly better in terms of brilliance transfer than simpler guides. I have also shown that the transport of a neutron beam over a very long distance is quite feasible, even for highly divergent, thermal neutrons.

I have investigated various methods for blocking the direct line of sight between the neutron source and the sample area, in order to reduce the fast neutron background. I have shown that blocking line of sight is feasible, even for advanced guide geometries, such as elliptic and parabolic guides. I have also looked into how guide imperfections affect the brilliance transfer, and shown that long elliptic guide are robust against imperfections at the levels we expect to see.

I have also detailed the simulations and optimisations of one particular instrument, the Compact SANS, on which I have worked on the design of the guide, collimation, and chopper systems.

Dansk Resume

I denne afhandling har jeg set på udfordringerne ved lange guides og instrumentering til den langpulsede Europæiske Spallationskilde.

Jeg har udledt den analytiske beskrivelse til kvantificering af en neutronguides kvalitet med brug af brilliansoverførsel. Med dette værktøj er det nemmere objektivt at sammenligne hvor godt forskellige guides løser den samme opgave.

Ved at sammenligne forskellige guidegeometrier, har jeg vist at elliptiske og parabolske guides er signifikant bedre end simplere guides, til transport af termiske eller stærkt divergente neutroner over medium til lange afstande, målt i brilliansoverførsel. Jeg har også vist at transport af en neutronstråle over meget lange afstand er praktisk muligt, selv for højdivergente, termiske neutroner.

Jeg har undersøgt forskellige metoder til at blokere for den direkte synslinie mellem neutronkilden og prøveområdet, med det formål at reducere den hurtige neutronbaggrund. Jeg har vist at det kan lade sig gøre, selv for avancerede guidegeometrier, som elliptisk og parabolsk. Jeg har også undersøgt hvordan guideimperfektioner påvirker brilliansoverførslen, og vist at lange elliptiske guides er robuste overfor imperfektioner på de niveauer vi forventer at se.

Desuden har jeg beskrevet detaljerne af simuleringerne og optimiseringerne af et bestemt instrument, "Compact SANS", hvor jeg har arbejdet på designet af guide-, kollimations- og choppersystemerne.

Contents

1. Introduction

This thesis deals with neutron instrumentation for the European Spallation Source studied by Monte Carlo simulations. Specifically I focus on neutron guides, with elliptic guides being the main interest.

The European Spallation Source, shown in figure 1.0.1 will be a long pulsed source, which is unique among neutron sources. Using this long pulse requires changes in instrumentation, such as unusually long instruments. This poses new challenges for guides, not just in delivering a high number of neutrons, but also delivering a smooth beam, blocking the background from what will be the worlds most powerful neutron source, and dealing with guide misalignment over a long distance.

In the following I will give a brief introduction to neutron science and the fundamentals in neutron instrumentation, and give the necessary definitions. Since the simulations were made using the software McStas, this package will also be described.
Section 2 will give a theoretical basis for beam transport, which is useful in describing neutron guides and quantifying their performance.

After this I will present my yet unpublished work, followed by an introduction to my published work, which is reprinted in the appendix.

1.1. Introduction to Neutron Scattering

Neutron science traces its beginning back to the first experiments by James Chadwick in 1932 with a polonium activated beryllium source[11].

With the development of the nuclear reactor by Enrico Fermi in 1942, much more powerful neutron sources became available[12]. With the end of WWII, nuclear reactors could be used for non-military purposes, which allowed the field of neutron scattering to develop in the 1950s and 1960s, resulting in the 1994 Nobel Price in Physics to Bertram Brockhouse and Clifford Shull for pioneering the techniques of neutron spectroscopy and neutron diffraction[13]. With the construction of powerful dedicated neutron sources such as the Institut Laue-Langevin (ILL) reactor facility in France and the ISIS spallation neutron source in the United Kingdom in the 1960s and 1970s, neutron scattering reached a greater level of maturity which allowed it to become a powerful scientific tool used in a wide range of fields, from fundamental physics and magnetism through life science and archaeology[14].

1.2. The State of a Neutron

In neutron instrumentation, a precise knowledge of neutron trajectories is essential, so to describe the neutron we start by defining a coordinate system with (0,0,0) in the centre of the moderator face. The x-axis is the horizontal, transverse direction, the y-axis is the vertical direction, and the z-axis is the longitudinal direction.
We define the divergence, $\vec{\eta}$, as the deviation of the velocity vector from the nominal flight direction, usually the z-axis. Usually the divergence is expressed in terms of the angle it makes with the z-axis. I.e. η_x is the angle between the z-axis and the projection of the velocity vector onto the x, z-plane, and similarly η_y is the angle

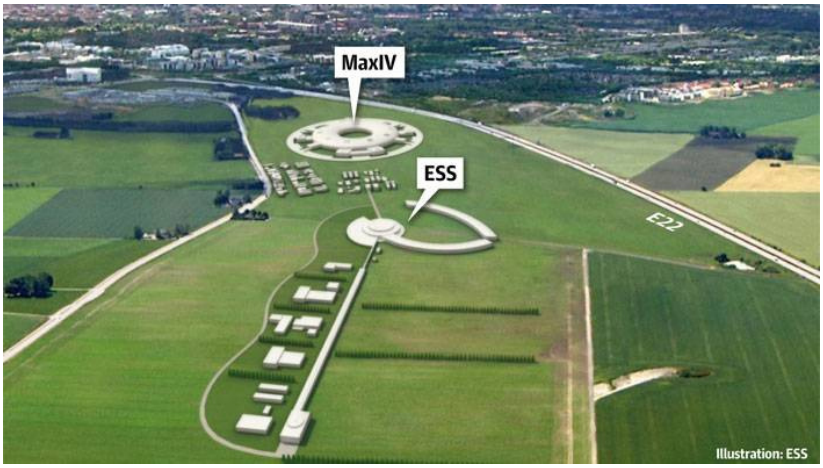

Figure 1.0.1: Model of the ESS superimposed on an aerophoto of North East Lund. The photo also shows the Max IV X-ray source[9] currently under construction[10].

between the z-axis and the projection of the velocity vector onto the y, z-plane.

With this we can express the state of a neutron with the parameters:

$$(x, y, z, \eta_x, \eta_y, \lambda)$$

Where λ is the wavelength of the neutron. Note that neutron spin is not included in this definition, and will not be used in this thesis.

To describe the number of neutrons in a beam, 3 different terms will be used, which I will define here:

- Intensity, I, is given in terms of neutrons per second (n/s). This describes the total number of n/s arriving at a particular area per unit time. It is a useful definition for quantifying the number of neutrons that will hit a sample of a certain size.
- Flux, Φ, is the same as intensity, but normalised to a 1 cm^2 area. This is useful for quantifying the amount of neutrons available at the sample position, irrespective of the sample size.
- Brilliance, Ψ, is given in terms of neutrons within a particular volume of time, area, divergence, and wavelength. It is usually given in units of n/s/cm^2/sr/Å. It is a useful term to quantify the power of a neutron source, and Liouville's Theorem makes it highly useful for instrumentation, as will be demonstrated later.

We can thus calculate flux from brilliance:

$$\Phi = \int_{\eta_{x0}}^{\Delta\eta_x} \int_{\eta_{y0}}^{\Delta\eta_y} \int_{\lambda_0}^{\Delta\lambda} \Psi d\lambda d\eta_y d\eta_x \tag{1.2.1}$$

And intensity from flux:

$$I = \int_{x_0}^{\Delta x} \int_{y_0}^{\Delta y} \Phi dx dy \tag{1.2.2}$$

We define the brilliance transfer, B, of an optical system between the positions z_1 and z_2 as the ratio of the brilliance at some point along the z axis to the brilliance at another point closer to the source:

$$B(z_1, z_2) = \frac{\Psi(z_2)}{\Psi(z_1)} \tag{1.2.3}$$

This value allows us to quantify the effectiveness of neutron transport, e.g. in a guide system.

1.2.1. Momentum and Energy Transfer

When performing neutron experiments, one often needs to measure the energy shift or the momentum transfer that occurs when a neutron interacts with the sample. These are denoted as $\hbar\omega$ and $\vec{q}$ respectively, and are defined as:

$$\vec{q} = \vec{k}_i - \vec{k}_f \tag{1.2.4}$$

$$\hbar\omega = E_i - E_f = \frac{h^2}{2m}\left(\frac{1}{\lambda_i^2} - \frac{1}{\lambda_f^2}\right) \tag{1.2.5}$$

where h is Planck's constant and m is the neutron mass; $\vec{k}_i, \vec{\eta_i}, \lambda_i, E_i$ are respectively the momentum vector, the divergence vector, the wavelength, and the energy of the ingoing neutron; and $\vec{k}_f, \vec{\eta_f}, \lambda_f, E_f$ are respectively the momentum vector, the divergence vector, the wavelength, and the energy of the outgoing neutron.

1.3. The European Spallation Source

While nuclear reactors are a comparatively cheap way to make a steady state neutron source, nuclear spallation neutron sources have in recent years begun to overtake reactor sources as the world leading facilities. Not only are spallation sources more readily made pulsed, which makes them far more suited for time of flight (ToF) instrumentation, but in many countries non-reactor based sources are more politically feasible.

The European Spallation Source (ESS), scheduled to be operational by the end of the decade, will be the world's brightest neutron source, though the time integrated neutron flux is at about the level of the world's most powerful reactor based source, the ILL[14, 10]. The unique feature of the ESS the that it is a long pulsed source, as seen in figure 1.3.1. This allows for a much greater time integrated neutron flux over the pulse than other pulsed sources, but to use the full pulse length with ToF-instrumentation, very long instruments will be required. Otherwise pulse shortening by mechanical choppers will be required to give a good time resolution, by shaping the

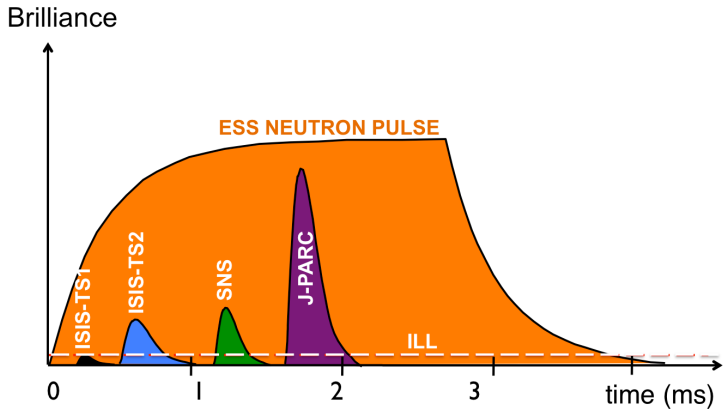

Figure 1.3.1: The brilliance and time structure of the ESS source pulse compared to other major neutron sources[10].

pulse. This gives unprecedented challenges for neutron optics, which this thesis will attempt to explore.

1.4. Neutron Instrumentation

There are 5 common classes of neutron instruments: SANS (small angle neutron scattering), reflectometers, diffractometers, imaging instruments, and spectrometers:

- SANS instruments are used to measure small q-values.
- Diffractometers are used for measuring large q-values.
- Reflectometers are used for measuring small q-values when scattering off a surface.
- Imaging instruments measure the shadow cast by a sample placed in a neutron beam.
- Spectrometers are used to measure both $\hbar\omega$ and q, but typically with poorer q resolution than a diffractometer.

The first 4 instrument classes do not measure the neutron energy transfer. They need a broad λ-range delivered onto the sample, as is also the case for indirect spectrometers. Direct spectrometers send monochromatic pulses to the sample. However new techniques use several wavelengths simultaneously[15, 16, 17], which means that the guide needs to be able to transport at broad λ-range.

The class of instrument does not directly influence the guide design, which is determined by the desired neutron phase space and the instrument length. However SANS instruments, diffractometers, and reflectometers tend to require a phase space with a narrow divergence interval, while spectrometers and imaging instruments tend to accept a larger divergence. For these reasons I have concentrated most of my work on guide design on guides that transport a broad λ-range and high divergences, as this is the most difficult problem.

In the following I will describe the time of flight method used at pulsed sources to determine the ingoing and outgoing wavelength of neutrons, and how spectrometers use this to determine $\hbar\omega$.

1.4.1. Time of Flight Instrumentation

Using the conversion factor $\alpha = \frac{m_n}{h} = 252.7\ \mu\text{s/Å/m}$ between neutron wavelength [Å] and inverse velocity [μs/m], the basic equation for neutron flight time, t, and flight distance, L, reads:

$$t = \alpha L \lambda \tag{1.4.1}$$

The uncertainty in λ, i.e. the wavelength resolution of a ToF instrument, is

$$\delta\lambda = \frac{\delta t}{L\alpha} \tag{1.4.2}$$

where δt is the time frame where neutrons are emitted, smaller than or equal to the pulse width, τ, of the neutron source (2.86 ms at the ESS[14, 4]). Pulse shaping using mechanical beam choppers improve resolution by reducing δt at the cost of flux.

We can calculate the maximum bandwidth that can be used, without neutrons from adjacent pulses overlapping in time at the detector position.

$$\Delta\lambda = \lambda_{\max} - \lambda_{\min} = \frac{T - \tau}{L\alpha} \tag{1.4.3}$$

where $T = 1/(14\ \text{Hz}) = 71.4$ ms is the moderator period at the ESS[14, 4].

We thus see that improved resolution in equation 1.4.2 by increasing the instrument length will result in a reduced wavelength band.

1.4.2. Neutron Spectroscopy

To illustrate the use of the ToF method and to motivate why the long pulse of the ESS will require long guides, I will here show an example of a class of neutron instruments, the neutron spectrometer.

Neutron spectroscopy can be used to investigate excitations in sample by measuring the change in energy, $\hbar\omega$, of neutrons scattering on the sample. From equation 1.2.5 this requires knowing both the ingoing (λ_i) and outgoing (λ_f) wavelength, which can both be done using the ToF method. We consider a very simple setup consisting of 4 elements placed in the following order: a pulsed neutron source, a mechanical beam chopper, an inelastically scattering sample, and a neutron detector. If the neutron pulse is emitted at time t_0 and arrive at the sample, which is placed at a distance from the source of L_1, at time t_1, equation 1.4.1 tells us that the ingoing wavelength must be:

$$\lambda_i = \frac{t_1 - t_0}{\alpha L_1} \tag{1.4.4}$$

t_1 is not directly measurable, but instead the beam chopper is used to restrict the time when neutrons can arrive at the sample, thereby defining t_1. The biggest contribution to uncertainty in this equation is typically in t_0, where the uncertainty can be as large as the pulse width, τ, for a pulsed neutron source.

λ_f is calculated in an analogous way, from the measured arrival time of the neutron in the detector, t_2, the distance between the sample and the detector, L_2, which is ofter much smaller than L_1, and the arrival time at the sample, t_1:

$$\lambda_f = \frac{t_2 - t_1}{\alpha L_2} \tag{1.4.5}$$

Here the biggest contribution to uncertainty is typically in t_1, but this can be adjusted by controlling the duration of the mechanical chopper's opening time. Reducing the opening time will naturally lead to a corresponding reduction in the amount of neutrons allowed through, but this can partly be mitigated by allowing multiple pulses through the chopper within the time frame of the repetition rate of the neutron source, using the Repetition Rate Multiplication (RRM) scheme [15, 16, 17], as shown in figure 1.4.1. Taken together, this gives us an energy transfer of:

$$\hbar\omega = \frac{h^2}{2m}\left(\frac{1}{\lambda_i^2} - \frac{1}{\lambda_f^2}\right) = \frac{h^2}{2m}\left(\frac{1}{\left(\frac{t_1 - t_0}{\alpha L_1}\right)^2} - \frac{1}{\left(\frac{t_2 - t_1}{\alpha L_2}\right)^2}\right) \tag{1.4.6}$$

However, for the second term, the uncertainty in t_0 from the pulse width can be changed by introducing a pulse shaping chopper, which will correspondingly reduce the amount of neutrons arriving at the sample. Instead the uncertainty can be reduced by increasing L_1, at the cost of a reduced wavelength band. So for a neutron source with a very large pulse width, such as the ESS[14, 4], a very large flight distance, above 100 m from the neutron source to the sample position, is foreseen for instruments where a wavelength band of around $\Delta\lambda = 2$ Å is preferable[14].

1.5. Monte Carlo Ray Tracing Simulations

Monte Carlo (MC) ray tracing simulations essentially consists of using a computer to generate a ray with a random set of parameters, within some specified volume of the parameter space, and tracing its evolution through interactions with pre-modelled surroundings. For those interactions that are stochastic, another weighted random choice is made. By repeating a MC process sufficiently many times, to allow a representative sampling of the initial parameter space and any stochastic interactions, we can learn valuable and accurate insights into the real world system, provided the modelling is sufficiently accurate[18]. This has been used for many years with success in the field of neutron science[19, 20].

1.5.1. McStas

All simulations for this thesis was performed using the software McStas[21, 22, 23]. McStas uses MC ray tracing for neutron instrumentation and virtual experiments.

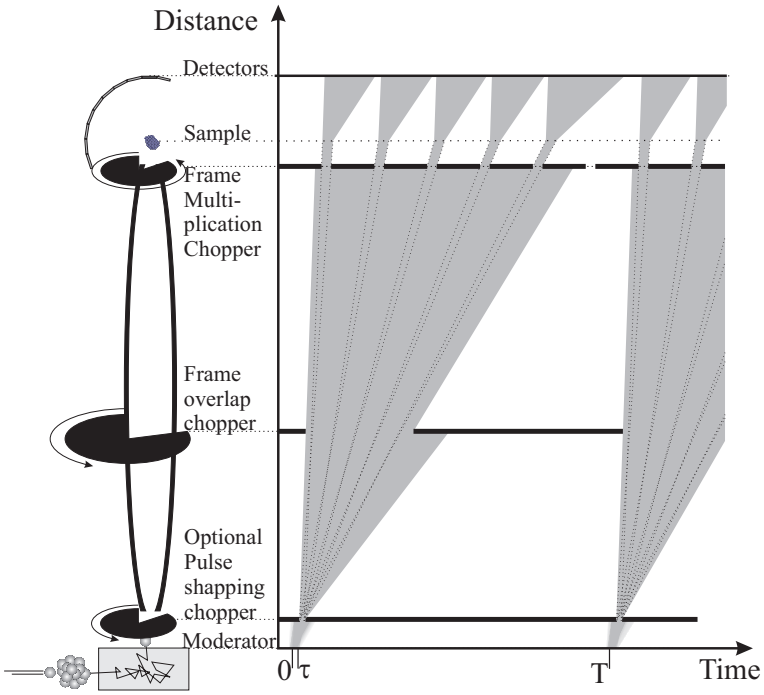

Figure 1.4.1: Layout of a simple time of flight instrument, with a time-distance diagram showing a chopper running in a RRM scheme.

An instrument is constructed in McStas using the available components, by placing them sequentially in a list. Typically a user would start by placing a source and define the size, wavelength spectrum, and divergence interval it will emit neutrons in. Optical components such as guides and mechanical beam choppers are placed after the source, which can be set to 'focus' on the guide opening, so it only emits neutrons that will hit the guide. A virtual sample component can be inserted, to do virtual experiments. An example of a virtual sample included in McStas is one that has a probability distribution of $\hbar\omega$ so that inelastic scattering can be simulated e.g. for a spectrometer. Monitors can be placed to measure the scattered beam from the sample, and to monitor the development of the beam through the optical components. As McStas currently has many (142) different components included[22], it can be used to simulate a wide range of instruments.

McStas performs MC simulations by generating rays from the virtual neutron source with a randomised set of initial parameters, including a weight factor so that a weighted source with e.g. a specific wavelength distribution can be simulated. The rays are then propagated through the components of the instrument. In stochastic interactions that have a non-zero probability that a ray is absorbed, such as a reflection on a mirror, the weight factor of the ray is instead reduced by the probability of absorption, thereby reducing the computing time needed for simulations. The intensity of the neutron beam can be calculated by summing the weight factors of all the rays that fall within the boundaries of a monitor. This is then repeated a high number of times, typically between 10^6 and 10^{10} in my simulations, in order to attain sufficient statistics. When the user specifies the number of rays to be simulated, the weight factor of each ray is

normalised.

Using McStas I have simulated numerous instruments and many different guide configurations. I have used the computing cluster provided by the interim computing centre at the ESS Data Management and Software Centre. This is a 42 node cluster, and each node has 12 processor cores. This has allowed me significantly speed up simulations compared to running them on a laptop computer. A simulation on the cluster typically took anywhere between a few seconds to several hours, depending on the complexity of the simulated instrument and the desired number of repetitions. Optimisations usually took several hundred times longer.

Besides the weight factor, McStas defines the state of a neutron ray with its position and velocity, i.e.

$$(x, y, z, v_x, v_y, v_z) \tag{1.5.1}$$

Naturally it is possible to transform from the neutron state given in section 1.2 to this one:

$$\begin{aligned} \eta_x &= \sin\left(\frac{v_x}{v}\right) \approx \frac{v_x}{v} \\ \eta_y &= \sin\left(\frac{v_y}{v}\right) \approx \frac{v_y}{v} \\ \lambda &= \frac{1}{\alpha v} \end{aligned} \tag{1.5.2}$$

Where $v = \sqrt{v_x^2 + v_y^2 + v_z^2}$, and the small angle approximation has been used in the two first lines.

McStas also includes the spin in the state of the neutron[24], but this will not be used here, as previously mentioned.

2. Neutron Transmission and Guides

In this section, I will derive an analytical framework for beam transport using neutron guides. First I will describe phase space density and Liouville's Theorem, followed by examples on how to use this for understanding neutron guides.

2.1. Phase Space Density

If we consider a closed system of N identical and non-interacting particles, the density of the particles at any given point in phase space is given by the distribution function, $D(\vec{r},\vec{v})$, which we define as:

$$\begin{aligned} N &= \int\int\int\int\int\int D(\vec{r},\vec{v})\ dxdydzdv_xdv_ydv_z \\ \Rightarrow D(\vec{r},\vec{v}) &= \frac{d^6N}{dxdydzdv_xdv_ydv_z} = \frac{d^6N}{dxdydzd\eta_xd\eta_yd\lambda}\cdot|\beta| = D(\vec{r},\vec{\eta},\lambda)\cdot|\beta| \end{aligned} \tag{2.1.1}$$

Where β is the determinant of the Jacobian matrix corresponding to the coordinate transformation from v_x, v_y, v_z to η_x, η_y, λ, i.e.:

$$\beta = \begin{vmatrix} \frac{\partial\eta_x}{\partial v_x} & \frac{\partial\eta_y}{\partial v_x} & \frac{\partial\lambda}{\partial v_x} \\ \frac{\partial\eta_x}{\partial v_y} & \frac{\partial\eta_y}{\partial v_y} & \frac{\partial\lambda}{\partial v_y} \\ \frac{\partial\eta_x}{\partial v_z} & \frac{\partial\eta_y}{\partial v_z} & \frac{\partial\lambda}{\partial v_z} \end{vmatrix} \tag{2.1.2}$$

Using equation 1.5.2 and the differentials

$$\begin{aligned} \frac{\partial\left(1/\sqrt{v_x^2+v_y^2+v_z^2}\right)}{\partial v_x} &= -v_x(v_x^2+v_y^2+v_z^2)^{-3/2} = -v_xv^{-3} \\ \frac{\partial\left(v_x/\sqrt{v_x^2+v_y^2+v_z^2}\right)}{\partial v_x} &= (v_y^2+v_z^2)(v_x^2+v_y^2+v_z^2)^{-3/2} = (v_y^2+v_z^2)v^{-3} \\ \frac{\partial\left(v_x/\sqrt{v_x^2+v_y^2+v_z^2}\right)}{\partial v_y} &= -v_xv_y(v_x^2+v_y^2+v_z^2)^{-3/2} = -v_xv_yv^{-3} \end{aligned} \tag{2.1.3}$$

and the assumption that $v_z^2 \gg v_x^2 \wedge v_z^2 \gg v_y^2$ and thus $v_z \approx v$, β can be calculated:

$$
\begin{aligned}
\beta =& \frac{\partial \eta_x}{\partial v_x}\frac{\partial \eta_y}{\partial v_y}\frac{\partial \lambda}{\partial v_z} + \frac{\partial \eta_y}{\partial v_x}\frac{\partial \lambda}{\partial v_y}\frac{\partial \eta_x}{\partial v_z} + \frac{\partial \lambda}{\partial v_x}\frac{\partial \eta_x}{\partial v_y}\frac{\partial \eta_y}{\partial v_z} \\
& - \frac{\partial \lambda}{\partial v_x}\frac{\partial \eta_y}{\partial v_y}\frac{\partial \eta_x}{\partial v_z} - \frac{\partial \eta_y}{\partial v_x}\frac{\partial \eta_x}{\partial v_y}\frac{\partial \lambda}{\partial v_z} - \frac{\partial \eta_x}{\partial v_x}\frac{\partial \lambda}{\partial v_y}\frac{\partial \eta_y}{\partial v_z} \\
\approx& \frac{v_z^2 v_z^2 (-v_z)}{v^9} + \frac{(-v_x v_y)(-v_y)(-v_x v_z)}{v^9} + \frac{(-v_x)(-v_x v_y)(-v_y v_z)}{v^9} \\
& - \frac{(-v_x) v_z^2 (-v_x v_z)}{v^9} - \frac{(-v_y v_x)(-v_x v_y)(-v_z)}{v^9} - \frac{v_z^2 (-v_y)(-v_y v_z)}{v^9} \\
=& \frac{-v_z^5 - v_x^2 v_y^2 v_z - v_x^2 v_y^2 v_z - v_x^2 v_z^3 + v_x^2 v_y^2 v_z - v_y^2 v_z^3}{v^9} \\
\approx& \frac{-v_z^5}{v^9} \\
\approx& - v^{-4}
\end{aligned}
\tag{2.1.4}
$$

Assuming there are no inelastic processes in neutron transport, v, and thus β, is a constant. Equation 2.1.1 then becomes:

$$
D(\vec{r}, \vec{v}) = \frac{d^6 N}{dx dy dz dv_x dv_y dv_z} = \frac{d^6 N}{dx dy dz d\eta_x d\eta_y d\lambda}\frac{1}{v^4} = D(\vec{r}, \vec{\eta}, \lambda)\frac{1}{v^4} \tag{2.1.5}
$$

2.2. Liouville's Theorem

Using statistical mechanics, it can be shown [25, 26] that the time evolution of the 6 N dimensional phase space density, δ, of a system of N identical particles is given by:

$$
\frac{d\delta}{dt} = \sum_i^{3N} \left(\frac{\partial \delta}{\partial x_i}\dot{x_i} + \frac{\partial \delta}{\partial v_i}\dot{v_i} \right) = 0 \tag{2.2.1}
$$

Known as Liouville's Theorem. As neutrons are non interacting particles, this can be reduced from a $6N$ dimensional expression to only 6 dimensions, using the single particle density, $D = N\delta$:

$$
\frac{dD(\vec{r}, \vec{v})}{dt} = \sum_i^{3} \left(\frac{\partial D(\vec{r}, \vec{v})}{\partial x_i}\dot{x_i} + \frac{\partial D(\vec{r}, \vec{v})}{\partial v_i}\dot{v_i} \right) = 0 \tag{2.2.2}
$$

Assuming that the processes under which the phase space evolves does not change the wavelength of individual neutrons, e.g. expansion into free space or elastic reflections from a mirror, 2.1.5 means we also have:

$$
\frac{dD(\vec{r}, \vec{\eta}, \lambda)}{dt} = 0 \tag{2.2.3}
$$

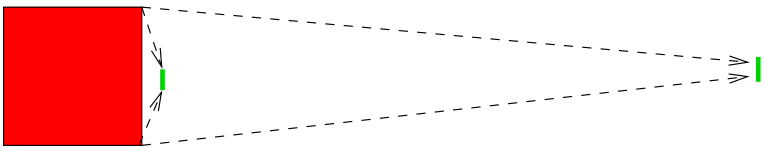

Figure 2.3.1: A neutron source (red) illuminating two $x, y, \vec{\eta}, \lambda$ integration boxes (green lines); one right at the source and one two meters away. The figure is not to scale.

2.3. Implications for Neutron Transmission

Since z is the nominal direction of propagation of the neutron beam, a displacement in z corresponds to a very good approximation of a displacement in time. Since we choose in the simulations to integrate over time, we will also integrate the phase space density over z:

$$D(x, y, \vec{\eta}, \lambda) = \int dz \; D(\vec{r}, \vec{\eta}, \lambda) \tag{2.3.1}$$

$D(x, y, \vec{\eta}, \lambda)$ then corresponds to the definition of brilliance given in section 1.2, which we can then conclude must be constant for a given set of $N, dx, dy, d\eta_x, d\eta_y, d\lambda$. I.e:

$$\begin{aligned} & D(x, y, \vec{\eta}, \lambda) = \Psi \\ \Rightarrow & \frac{d\Psi}{dt} = \frac{d\Psi}{dz} = 0 \end{aligned} \tag{2.3.2}$$

To exemplify this, we consider a $10 \times 10 \times 10$ cm^3 source radiating neutrons isotropically in a wavelength range $\Delta\lambda = 1$ Å wide. We measure the integrated brilliance in a phase space volume of $\Delta A = 1 \times 1$ cm$^2, \Delta\eta_x = 1^\circ, \Delta\eta_y = 1^\circ, \Delta\lambda = 1$ Å located right on the face of the source ($z = 0$) to be $\Psi = 1$ n/s/cm^2/Å/sr.
If we perform the same measurement at a distance of $z = 2$ m, as illustrated in figure 2.3.1, we would again measure 1 n/s/cm^2/Å/sr, i.e. a brilliance transfer of $B = 1$. This is of course because the narrow divergence area chosen to sample the phase space volume, is smaller than the $3^\circ \times 3^\circ$ size of the source at 2 m distance. If we were to sample over a much larger divergence area, we would measure a brilliance transfer of $B < 1$. This is because the sampled volume of phase space is not fully illuminated by the source, which leads to unusable measurements of the brilliance transfer.

Another example could be to imagine a system of focusing mirrors used to reflect the isotropically emitted neutrons from the above source onto a small area of real space. This will not increase the brilliance measured above, as the 'extra' neutrons will have a divergence outside the relevant phase space volume. What it will do is to increase the illuminated area of phase space. This is the primary purpose of neutron guides.

For a third example we imagine placing another identical source next to the first one. Again this will not increase the brilliance measured above, as the 'extra' neutrons will fall outside the phase space volume measured over. But if the second source emits neutrons in a different wavelength range than the first one, it is possible to use a

mirror to reflect extra long wavelength neutrons into the same position and divergence phase space volume, increasing the measured flux. This does not violate equation 2.2.2, as the extra neutrons measured comes by extending the wavelength interval in the phase space volume, thus D is unchanged. This is known as the bispectral approach[27, 28, 29, 30, 31].

Liouville's Theorem is highly useful for neutron transport as it gives a theoretical limit to this aspect of neutron instrumentation. If the phase space volume considered corresponds to the beam profile we would like to deliver to the sample, e.g. the cross section of the sample and the divergence area acceptable for the instrumental resolution, we can measure the ratio of the phase space density at sample position and at the source; Liouville's Theorem then tells us that this value can never be greater than one, assuming the phase space volume measured at the source is fully illuminated. It can however be lower than one if a system of mirrors is used to extend the illuminated phase space, but leaves unilluminated gaps in phase space, or if the mirrors have a non-perfect reflectivity, resulting in absorption and thus a reduced D.

2.4. Neutron Guides

Neutron guides are, as previously stated, a method of extending the volume of phase space at the sample position that is illuminated by the source, by using guides made of reflective surfaces. Figure 2.4.1 shows the evolution of the phase space of a neutron beam propagating through empty space. To restrict it to two dimensions, only x and η_x are shown, but since the beam is propagating freely through empty space, x and η_x are decoupled from y, η_y and λ. As the phase space of the beam evolves through time, and thus z, the part with a negative η_x will move in the negative x direction, while the part with a positive η_x will move in the positive x direction. This leads to a phase space that becomes more 'skewed' as shown in blue. Note though that the blue area maintains the volume. And since N is unchanged, we can conclude that D must also be unchanged. This form of visualisation of the phase space of a neutron beam is also known as an acceptance diagram[32, 33, 34, 35].
However the desired phase space (shown in black), e.g. the parts of the beam that will hit the sample and falls within an acceptable divergence range, is no longer fully overlapping with the phase space the beam occupies, i.e. it is no longer fully illuminated and we would measure a brilliance transfer of $B < 1$ when integrating over the black area.

I will here use the phase space diagrams for illustrating basic guide properties only. When it comes to advanced guide geometries, the use of diagrams become too difficult and I will rely on McStas simulations.

2.4.1. Straight Guide

To counter the loss of illumination of the desired phase space, we construct a simple guide composed of parallel mirrors on which neutrons will make total reflection. This will be referred to as a straight guide henceforth, and a McStas model of such a guide is shown in figure 2.4.3. In terms of phase space, these mirrors will constrict the x, y-range the beam can occupy and will switch the sign of the divergence of the phase

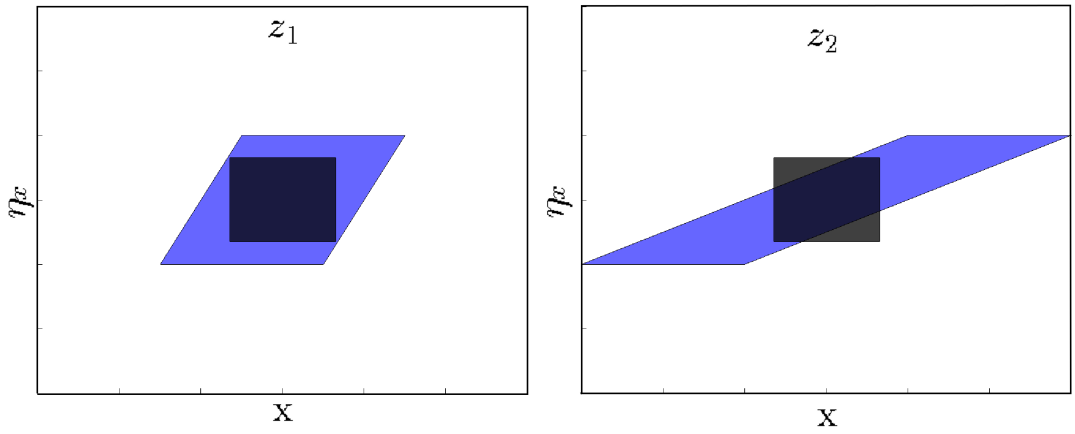

Figure 2.4.1: Phase space diagram with horizontal transverse position on the x-axis and horizontal divergence on the y-axis (both in arbitrary units) for a neutron beam expanding in vacuum. Blue: The phase space of the neutron beam. Black: The 'desired' phase space sampled when calculating the brilliance transfer. Left: At a $z = z_1$ close to the source. Right: At a $z = z_2$ further away from the source.

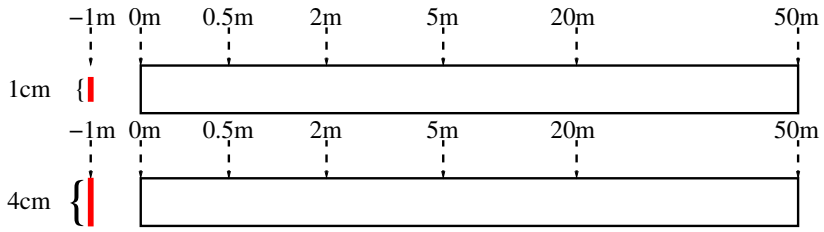

Figure 2.4.2: Diagrams of the simulation setup used to produce figures 2.4.4 and 2.4.7, showing the source, the guide, and the positions of the monitors. Note that the figures are not the scale.

space that touches it. This is shown in figure 2.4.4, which was produced with a McStas simulation of a 2×2 cm^2 guide placed 1 m after a 1×1 cm^2 source which is focused on the guide opening. Here we initially see a similar phase space as in figure 2.4.1, but as the beam moves through the guide we see at $z = 0.5$ m that the portions of the beam that has reflected on the guide has the sign of its divergence switched. Moving further through the guide, we see that the initial rhomboid shape is reflected into a number of thin lines, but the total area illuminated is still the same. At $z = 50$ m the lines are so numerous that they appear to fill the phase space, though in a sufficiently large and detailed diagram it would still be apparent that is it individual lines. Note that the initial rhomboid shape differs from that in figure 2.4.1, as that phase space shape was made by a source emitting neutrons within a fixed divergence interval.

As stated above, figure 2.4.4 was produced with a guide with total reflectivity. This is possible when transporting long wavelength neutrons with a low divergence, so that the q value they impact on reflections with the guide walls is less that the critical scattering value of nickel, which is $0.1°\text{Å}^{-1}$[36], or 0.02 Å^{-1} by equation 1.2.4. The latter value

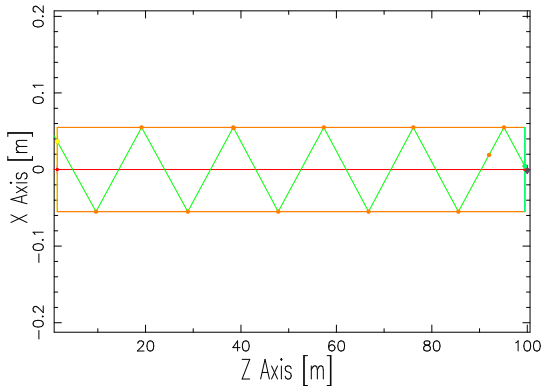

Figure 2.4.3: Cross-section in the horizontal plane of a McStas model of a straight guide. The green line is a neutron ray, the dots are reflections from the guide mirrors, the middle straight red line is the optical axis, and the lines at $x = \pm 5$ cm are the guide walls.

we define as $Q_c = 0.02$ Å^{-1}. Often the more precise value of $Q_c = 0.0217$ Å^{-1} is used[37], and this is also what has been used in the simulations.
A guide constructed according to the above principles is similar to the first neutron guides, which had their start in the 1960s[38]. They were intended to increase the flux at the sample position, and allow the sample to be moved further away from the source, which both reduces background from the source and opens up more space for the instrumentation.

2.4.2. Supermirror Coating

With the advent of supermirror coating more advanced guides became possible. Supermirror coating was first suggested in 1976[39] and became a mature process in the 1990s[40, 41, 42, 43, 44, 45, 46]. It is composed of multiple layers of alternating materials of different refractive indices, typically nickel and titanium. By stacking the layers with different spacings, overlapping Bragg peaks can be achieved, as shown in figure 2.4.5. In reality perfect reflection above the critical scattering angle cannot be achieved with a supermirror guide, and reflectivity drops off from nearly 1 at $q = Q_c$ to about 0.5 at $q = 7Q_c$[47]. The multiple of Q_c at which a supermirror can reflect neutrons is usually referred to as the m-value of the supermirror.

With the ability to reflect neutrons with a lower wavelength or greater divergence than was previously possible, supermirrors enabled more complicated guide geometries, such as a ballistic guide[16, 48].

If the beam from figure 2.4.4 moves through a 2×2 cm° guide with non-perfectly reflecting supermirrors, it will start losing neutrons in the high-divergence part of the beam, as seen in figure 2.4.7. Here we see from $z = 0$ to $z = 2$ m that the part of the beam with a divergence that falls outside the q interval that the mirror can reflect gets 'cut off' by absorption. At $z = 50$ m we see that the beam has been almost reduced to the region of divergence that falls below Q_c. The reason this happens is that if a ray with a certain $\vec{\eta}, \lambda$ impacts the mirrors n times in the q interval where the reflectivity

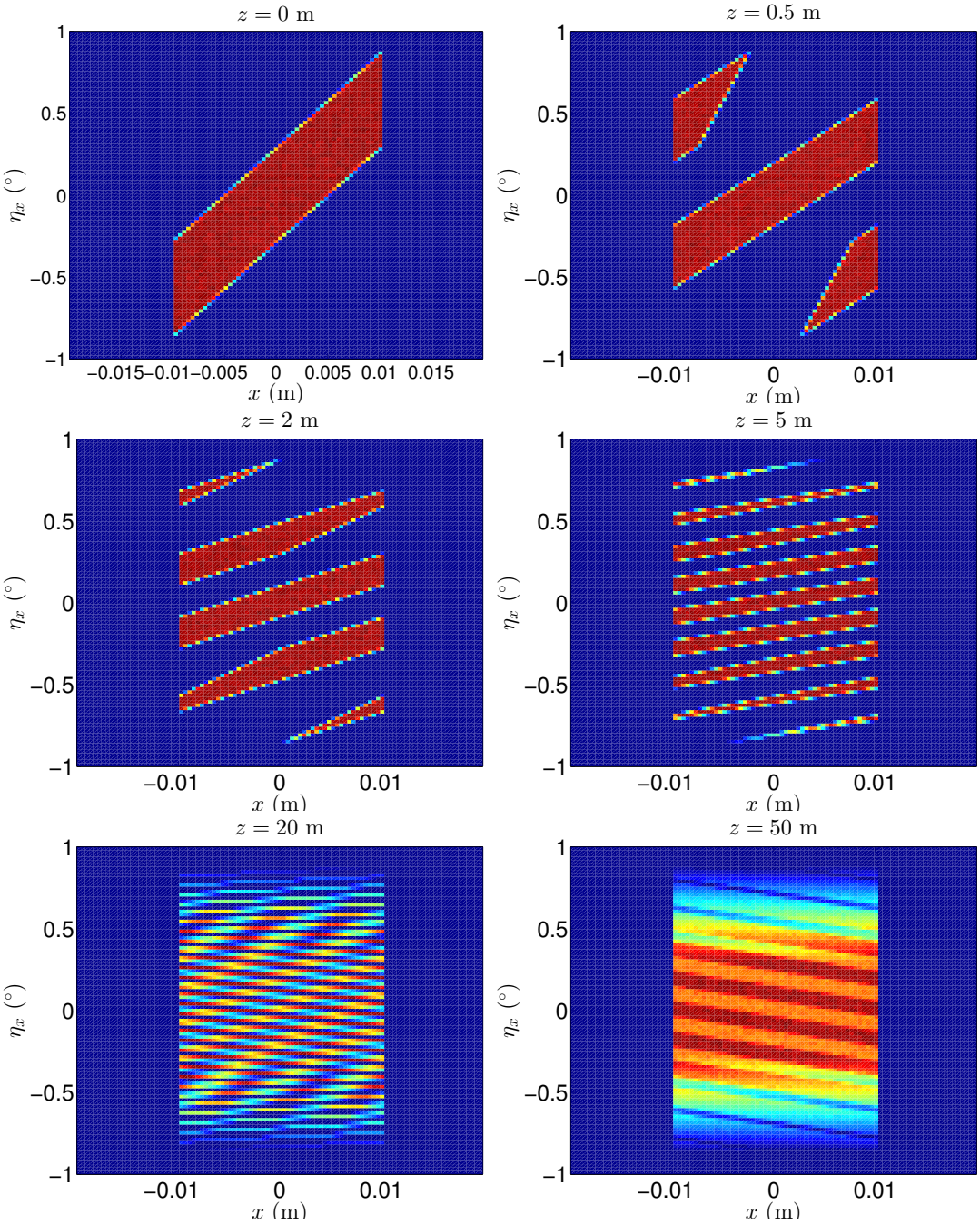

Figure 2.4.4: Phase space diagrams of a neutron beam moving through a straight guide with (artificially) perfectly reflecting mirrors. The guide starts at $z = 0$ and the source is positioned at $z = -1$ m, as shown in figure 2.4.2. Red denotes a brilliance transfer of 1 while dark blue is zero, graduated on a linear scale. As the mirrors are perfectly reflecting, this simplified example is valid for all wavelengths.

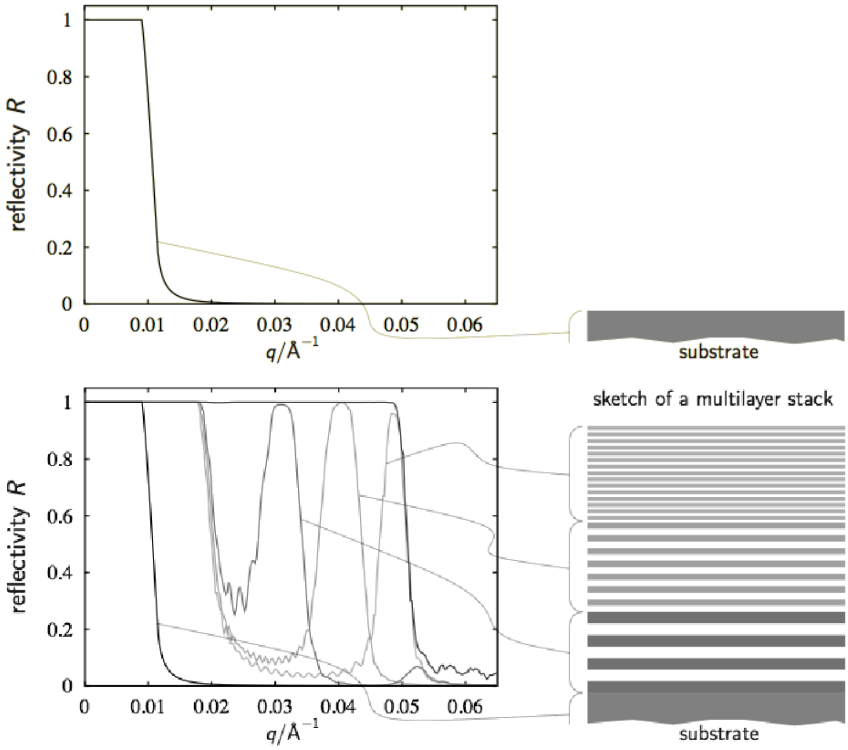

Figure 2.4.5: Reflectivity as a function of q for a neutron mirror. Top: A plain nickel mirror. Bottom: A multilayer supermirror with overlapping Bragg peaks. From [49].

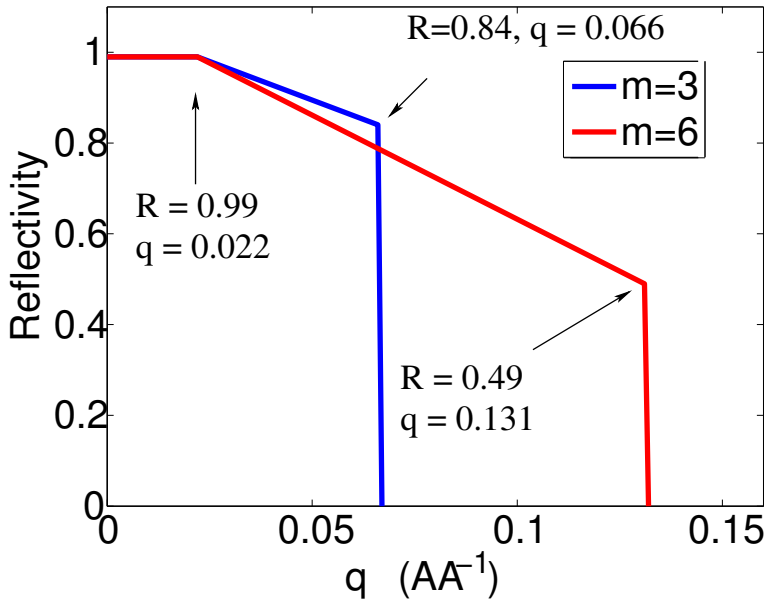

Figure 2.4.6: Model of neutron reflectivity as a function of q of two supermirror coatings with different m-values.

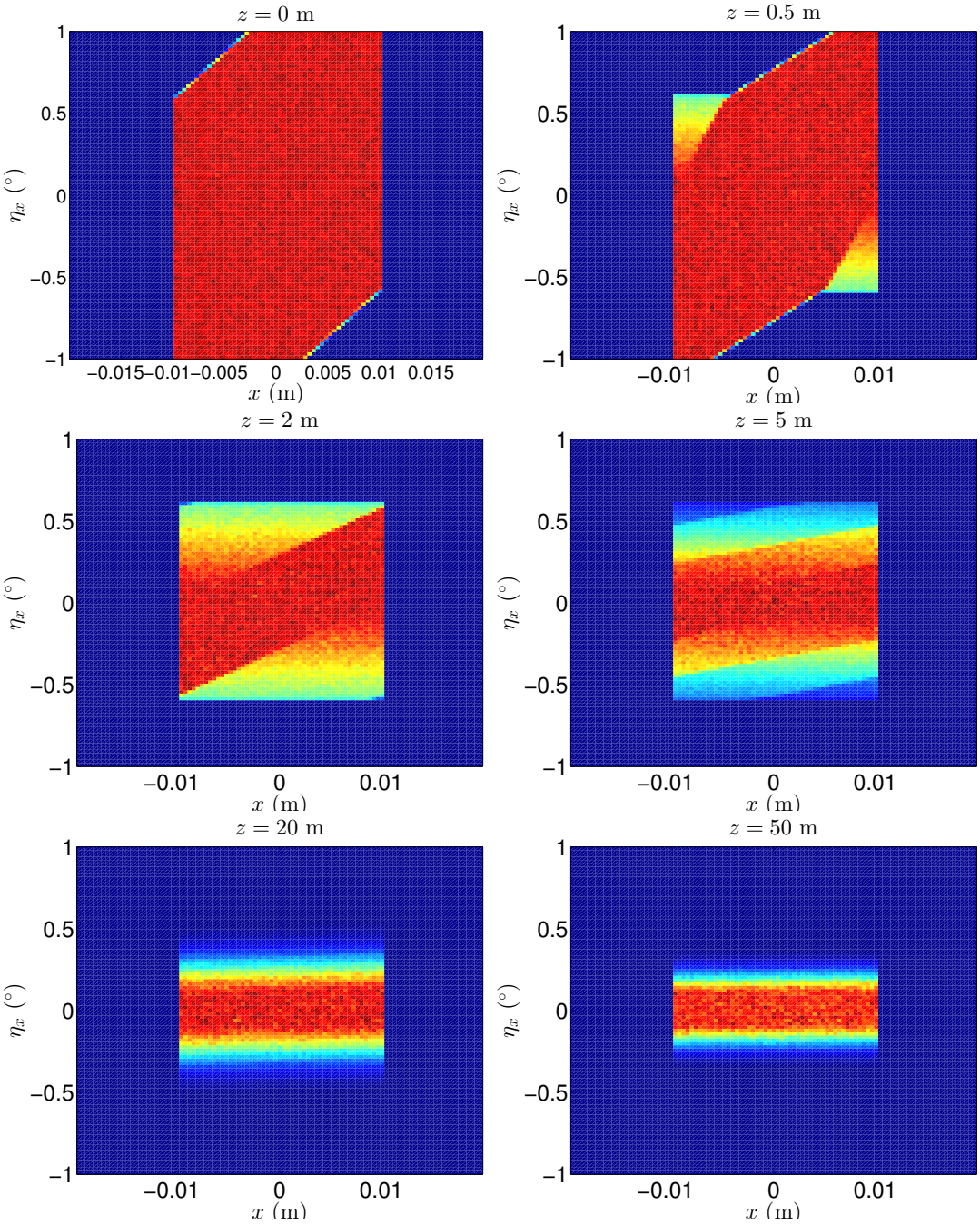

Figure 2.4.7: Phase space diagrams of a monochromatic neutron beam moving through a straight guide with non-perfectly reflecting mirrors. The guide starts at $z = 0$ and the source is positioned at $z = -1$ m. Red denotes a brilliance transfer of 1 while dark blue is zero, graduated on a linear scale. 1 Å neutrons were simulated, and the supermirror had the parameters $m = 6$ and $\alpha = 4.52$, cf. equation 2.4.2.

is $R < 1$, the transmission, T, of the ray will be severely attenuated if n is sufficiently high:

$$T = R^n \tag{2.4.1}$$

Note that the source used to produce figure 2.4.7 has been increased in size to 4×4 cm^2, in order to give more illumination to the initial phase space. This explains the difference in the $z = 0$ results for the two examples.

The model I have used for calculating the reflectivity of a supermirror is the following:

$$\begin{aligned} q < Q_c &: R = R_0 \\ Q_c < q < mQ_c &: R = R_0 - \alpha(m) \cdot (q - Q_c) \\ q > mQ_c &: R = 0 \end{aligned} \tag{2.4.2}$$

I. e. R_0 is the reflectivity for $q < Q_c$, and is usually set to either 1 or 0.99.

This will produce a reflectivity curve as in figure 2.4.6. $\alpha(m)$ is the slope of the reflectivity, and I have constructed a model for calculating this value, based on data from SwissNeutronics[47]:

$$\begin{aligned} m < 5 &: \alpha(m) = 3.5 \text{ Å} \\ m > 5 &: \alpha(m) = 3.5 \text{ Å} + 1.02 \text{ Å} \cdot (m - 5) \end{aligned} \tag{2.4.3}$$

Since this model was made, the guide quality from SwissNeutronics has improved, so that the above model yields a reflectivity that is too low. A new model was recently made by Henrik Jacobsen at the Niels Bohr Institute, that more accurately replicates the currently available reflectivity curves[27]. This will not be covered here.

2.4.3. Ballistic Guide

To counter the reduction in transmission from equation 2.4.1, it is possible to use a guide geometry that reduces the number of reflections, such as a ballistic guide.

The term 'ballistic guide' can describe any guide with a varying cross section[50], but is in this thesis defined as a guide that consists of a linearly expanding section, followed by a straight guide, and finally a converging section. A McStas model of such a guide shown in figure 2.4.8. The function of an expanding section is that as the guide allows the beam to expand in real space. Conservation of phase space density, and thus phase space volume, dictates that there will be a corresponding reduction in divergence. A beam with a lower divergence will on average have lower q when reflecting on the mirrors in the following straight section, thereby improving reflectivity, R, and reducing transmission losses for higher divergences. A lower divergence and a larger guide will naturally both reduce the number of reflections, n, in a guide of a given length. All 3 ingredients are essential for beam transport through a long guide[1], as per equation 2.4.1. The converging section is needed to refocus the beam onto the

Source size used with perfectly reflecting mirrors	1 cm^2
Source size used with non-perfectly reflecting mirrors	4 cm^2
Expanding section length	2 m
Guide opening width and height	2 cm
Midsection length	46 m
Midsection width and height	3.6 cm
Focusing section length	2 m
Guide end width and height	2 cm

Table 2.4.1: Geometrical parameters of the ballistic guide. The guide is symmetric in the x and y directions.

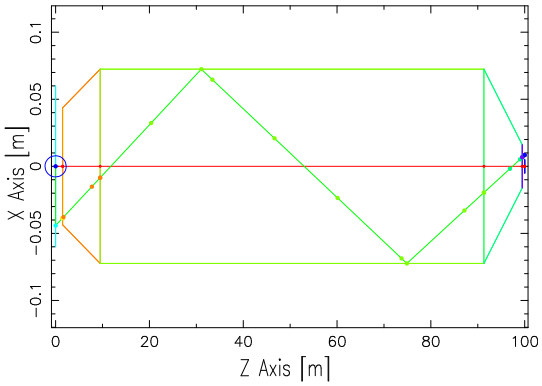

Figure 2.4.8: Cross-section in the horizontal plane of a McStas model of a ballistic guide. The green line is a neutron ray, and the dots denote interactions with a McStas component, such as a reflection from the guide mirrors or the transition from one guide section to another.

sample, at the same time restoring the original divergence.
The effect of this on the phase space of the beam can be seen in figure 2.4.9. This is similar to figure 2.4.4 except that it has been made with a ballistic guide, as described in table 2.4.1; the phase spaces at the guide entrances are identical. After the expanding section we see that the beam has expanded in real space and contracted in divergence space. After the straight section the phase space has been spread out in many thin lines, as in figure 2.4.4. After the converging section, the beam has been focused in real space and expanded in divergence space until it has the same dimensions as the final panel in figure 2.4.4, though there are two unilluminated triangles in the phase space. These are unfortunate side effects of using a ballistic guides, and show up as dips when plotting guide transmission as a function of divergence[1].

If we instead use a non-perfect mirrors and a larger source, as in figure 2.4.7, to produce figure 2.4.10, we still see the unilluminated triangles. Though unlike figure 2.4.7 there is only a slight reduction in the divergence space transported, which shows the advantage of using a ballistic guide instead of a straight guide.

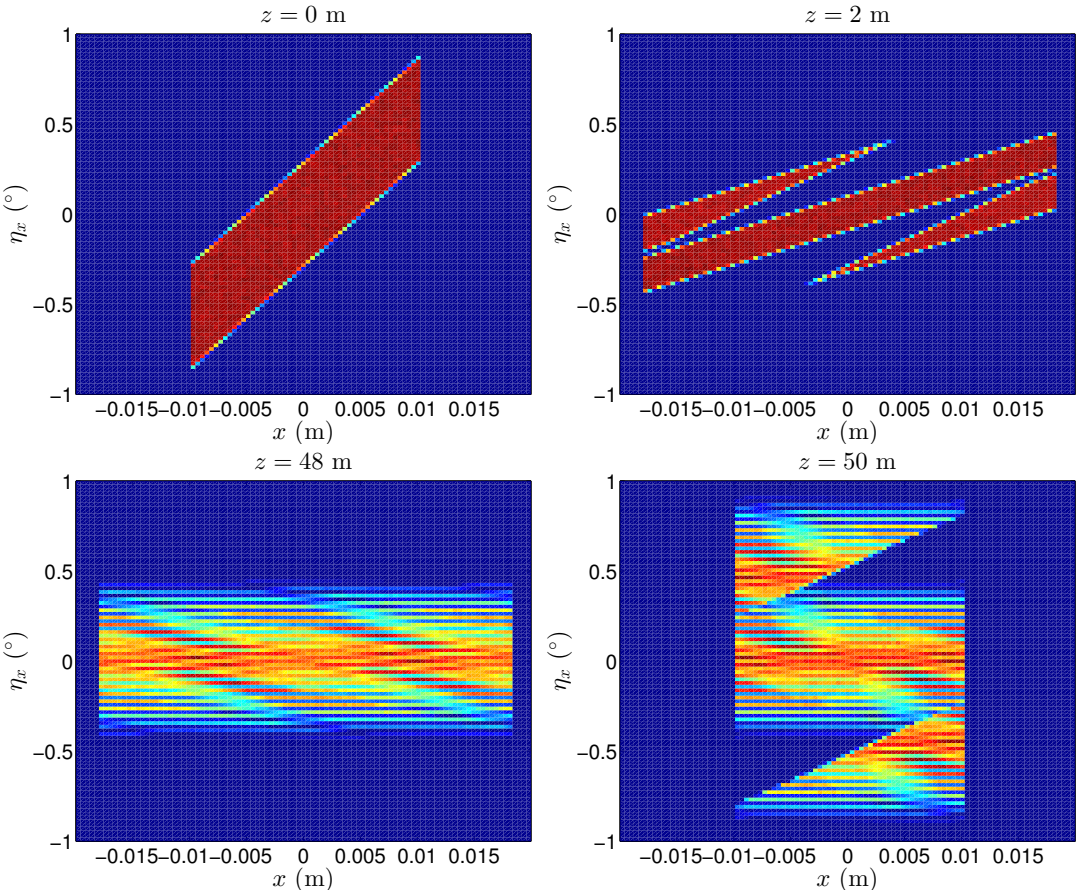

Figure 2.4.9: Phase space diagrams of a neutron beam moving through a ballistic guide with perfectly reflecting mirrors. The guide starts at $z = 0$ and the source is positioned at $z = -1$ m. Top left: at the guide entrance. Top right: after the expanding section. Bottom left: after the straight section. Bottom right: after the converging section.Red denotes a brilliance transfer of 1 while dark blue is zero, graduated on a linear scale. As the mirrors are perfectly reflecting, this result is valid for all wavelengths. Parameters for the guide are given in table 2.4.1.

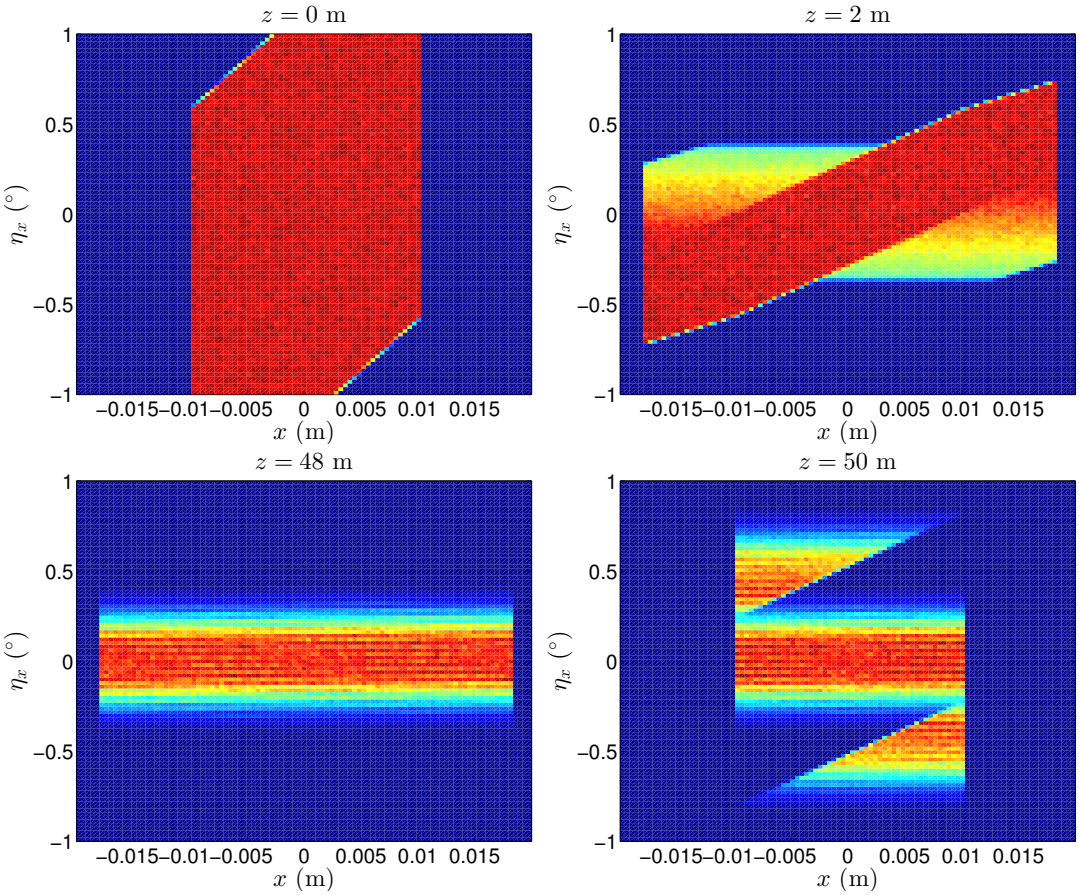

Figure 2.4.10: Phase space diagrams of a monochromatic neutron beam moving through a ballistic guide with non-perfectly reflecting mirrors. The guide starts at $z = 0$ and the source is positioned at $z = -1$ m. Top left: at the guide entrance. Top right: after the expanding section. Bottom left: after the straight section. Bottom right: after the converging section. Red denotes a brilliance transfer of 1 while dark blue is zero, graduated on a linear scale. 1 Å neutrons were simulated, and the supermirror had the parameters $m = 6$ and $\alpha = 4.52$, cf. equation 2.4.2. Parameters for the guide are given in table 2.4.1.

Source size used with perfectly reflecting mirrors	1 cm^2
Source size used with non-perfectly reflecting mirrors	4 cm^2
Guide length	48 m
Minor axis	72 mm
Initial focus point distance from guide start	1 m
Final focus point distance from guide end	1 m

Table 2.4.2: Geometrical parameters of the elliptic guide. The guide is symmetric in the x and y directions.

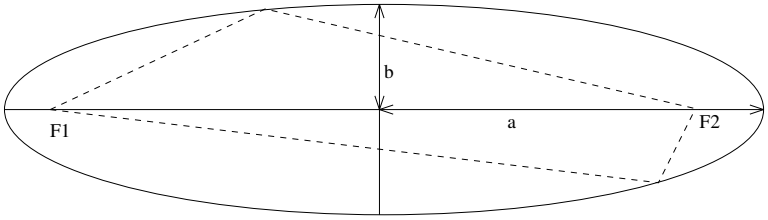

Figure 2.4.11: An ellipse showing point to point focusing of two rays from one focus point (F1) to the other (F2). a is the semi-major axis and b is the semi-minor axis.

2.4.4. Elliptic Guide

A more advanced version of a ballistic guide is to use non-linear expanding and contracting sections. Following an elliptic geometry is an apparent option, as an ellipse will reflect any ray emitted at one focus point onto the other focus point, as seen in figure 2.4.11.

An ellipse in the x, z plane with its centre in (0,0) is defined by the equation:

$$\left(\frac{x}{b}\right)^2 + \left(\frac{z}{a}\right)^2 = 1 \tag{2.4.4}$$

a is the length of the semi-major axis and b is the length of the semi-minor axis. The distance of the focal points from the centre of the ellipse, f, is given by:

$$f = \sqrt{a^2 - b^2} \tag{2.4.5}$$

A McStas model of such a guide shown in figure 2.4.12, and the parameters of the simulated elliptic guide are shown in table 2.4.2.

From simulations of an elliptic guide shown in figure 2.4.13, we see that such a guide is good at reducing the divergence of the beam for better transport through the guide, and the refocused beam has a 'smoother' phase space profile than that coming from a ballistic guide. Elliptic guides also have a brilliance transfer equal to or superior to that of ballistic guides, depending on the phase space volume transported[1].

Similar to figures 2.4.7 and 2.4.10, I have produced figure 2.4.14, which is a version of figure 2.4.13 with a larger source and non-perfectly reflecting mirrors. Here we see

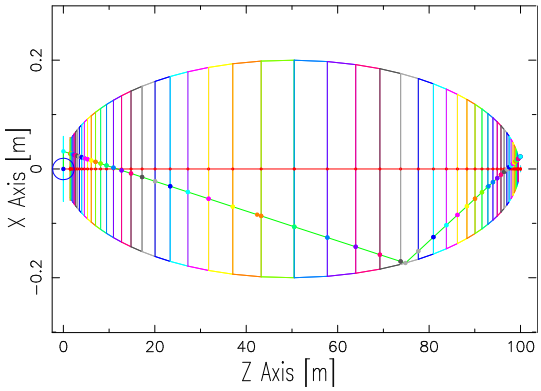

Figure 2.4.12: Cross-section in the horizontal plane of a McStas model of an elliptic guide. The green line is a neutron ray, and the dots denote interactions with a McStas component, such as a reflection from the guide mirrors or the transition from one guide section to another. The guide is constructed from 50 segments of straight guide, which are seen in the figure as isosceles trapezia of different colour with very long base lines.

that an elliptic guide can transport a much larger and smoother divergence space than a ballistic guide, in particular for an extended source.

Naturally the point to point focusing property of an ellipse is only possible with a point source. With a neutron source of finite size, the optical properties of an elliptic guide become more complicated[34, 51]. Despite this, the above advantages makes neutron guides using elliptic shaped mirrors highly useful for beam transport[1, 52, 3, 2], as is widely recognised in the literature[53, 54, 55, 56, 57, 58, 59, 60, 61, 62, 63, 64, 65, 66, 67, 68, 69, 70, 71, 72, 34, 73, 74].

For these reasons, this thesis will mainly focus on exploring aspects of elliptic guide design.

Parabolic guides should also be mentioned here, as they share many of the same transport abilities as elliptic guides, though they tend to have a slightly lower brilliance transfer[1]. I define a parabolic guide as a guide with a parabolically expanding section, followed by a long straight or curved midsection, and ending in a parabolically focusing section. A parabola can be constructed from an ellipse by setting one focus point to infinity, as such any ray coming from a point source in the other focus point will be reflected to have zero divergence.

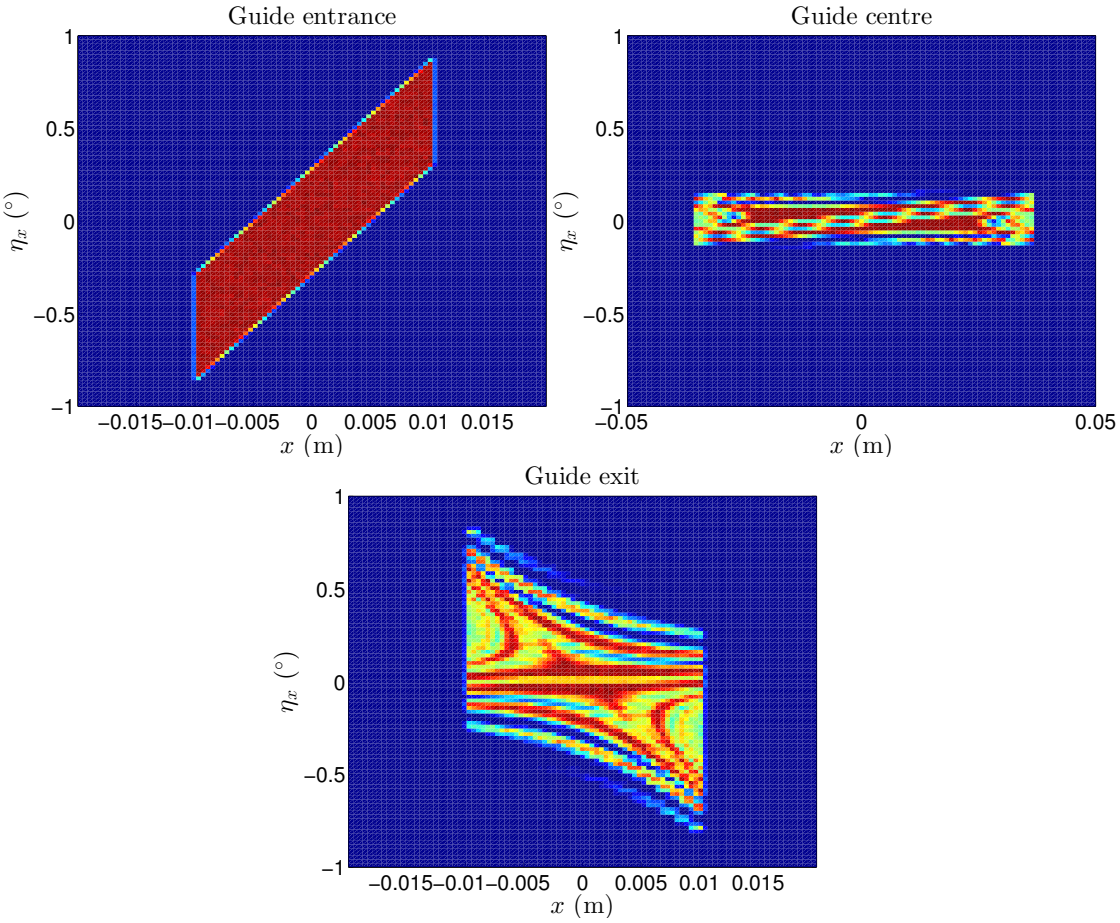

Figure 2.4.13: Phase space diagram of a neutron beam moving through an elliptic guide. Top left: at the guide entrance. Top right: at the guide centre. Note that the scale of the x-axis is bigger than in the other panels. Bottom: at the guide exit. Red denotes a brilliance transfer of 1 while dark blue is zero, graduated on a linear scale. As the mirrors are perfectly reflecting, this result is valid for all wavelengths. Parameters for the guide are given in table 2.4.2.

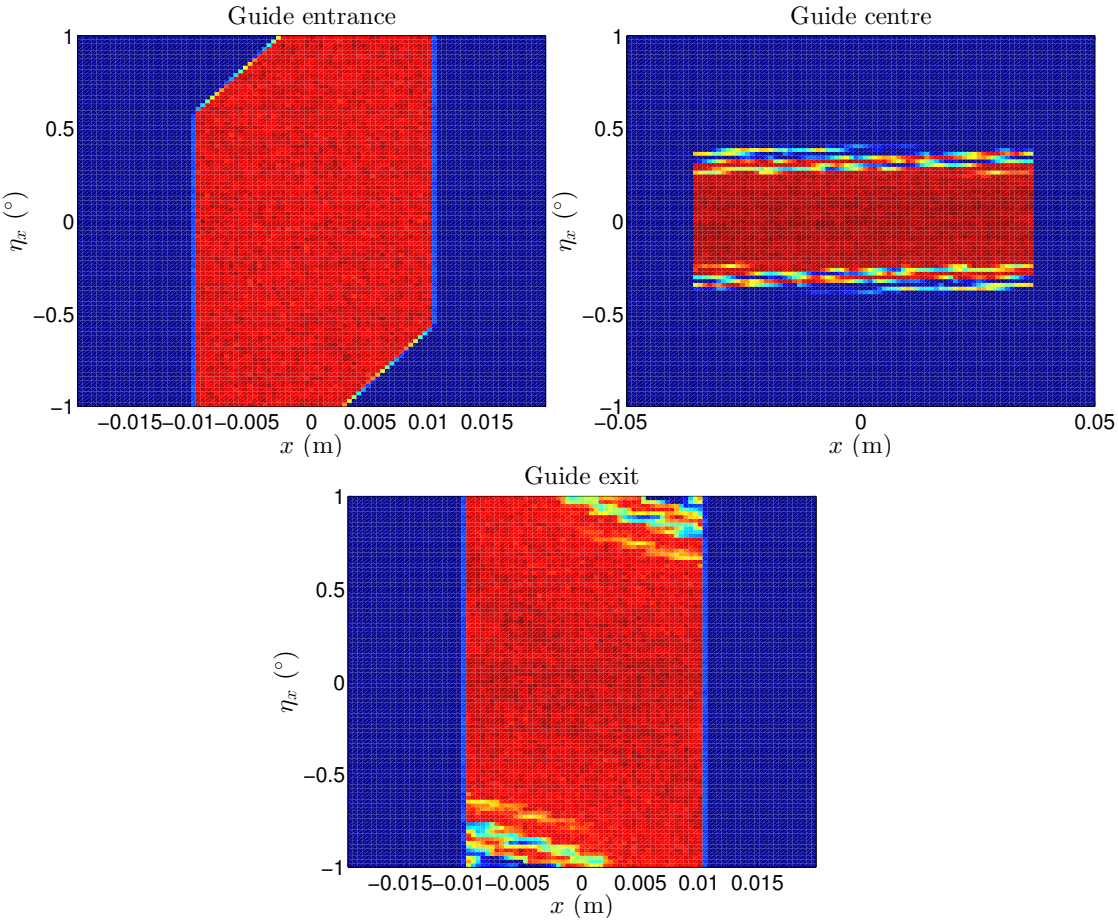

Figure 2.4.14: Phase space diagram of a neutron beam moving through an elliptic guide with non-perfectly reflecting mirrors. Top left: at the guide entrance. Top right: at the guide centre. Note that the scale of the x-axis is bigger than in the other panels. Bottom: at the guide exit. Red denotes a brilliance transfer of 1 while dark blue is zero, graduated on a linear scale. 1 Å neutrons were simulated, and the supermirror had the parameters $m = 6$ and $\alpha = 4.52$, cf. equation 2.4.2. Parameters for the guide are given in table 2.4.2.

3. Guide Simulations

In this section I will mostly present my unpublished work on guide simulations. Much of this was originally produced as reports that I wrote on request to the ESS for investigating some aspect of guide design. These are largely presented 'as is', with some reformatting.

Many of the results I have produced during my PhD have been published and are available in the appendix. They are briefly introduced in section 3.1.

Note that some of the early work was made with an older version of McStas (v. 1.12a), which means that these results may not be directly comparable to the rest. This is the case for sections 3.2.1, 3.4, and 3.6. The remainder was made with McStas version 1.12c, including the published work.

3.1. Published Work

In addition to the work listed below, I have also written or contributed to a number of papers and three large reports, all of which are detailed in the appendix. Here I will describe those that detail guide simulations.

3.1.1. Guide Geometry Comparison

A cornerstone of my work is published in the paper *Systematic Performance Study of Common Neutron Guide Geometries*[1], the results for which took months of work to produce and cross-compare between the software packages McStas and VITESS[75]. In this paper we did a thorough tabulating of the performance in transporting various areas of phase space over 4 different long distances, of the four guide geometries mentioned in section 2.4. We find that for long transport distances or low wavelengths of high divergences in the transported phase space, the parabolic and elliptic geometries perform almost equally, but much better than the two others. This is shown in figures 3.1.1 and 3.1.2, which respectively show the brilliance transfer as a function of radial divergence and wavelength for each of the 4 different geometries, and optimised for 4 different areas of phase space.

3.1.2. Blocking Line of Sight with Vertical Curvature

One thing we did not investigate in the paper[1], was the suitability of the different geometries to block the line of sight (LoS) from the neutron source to the sample and detector area. This is a subject of significant focus for instrumentation for the ESS[14], in order to reduce the fast neutron and gamma background at the sample position.

A long used method for blocking line of sight is to use a straight guide and curve it in the horizontal plane[38]. Another method that can be used with long guides that transport long wavelength neutrons, is to curve it to follow the ballistic trajectory of a neutron in free fall in the gravitational field, as shown in figure 3.1.3. I have explored and documented this for an elliptic guide in the paper *Eliminating line of sight in elliptic guides using gravitational curving*[3]. Analytical calculations are used to

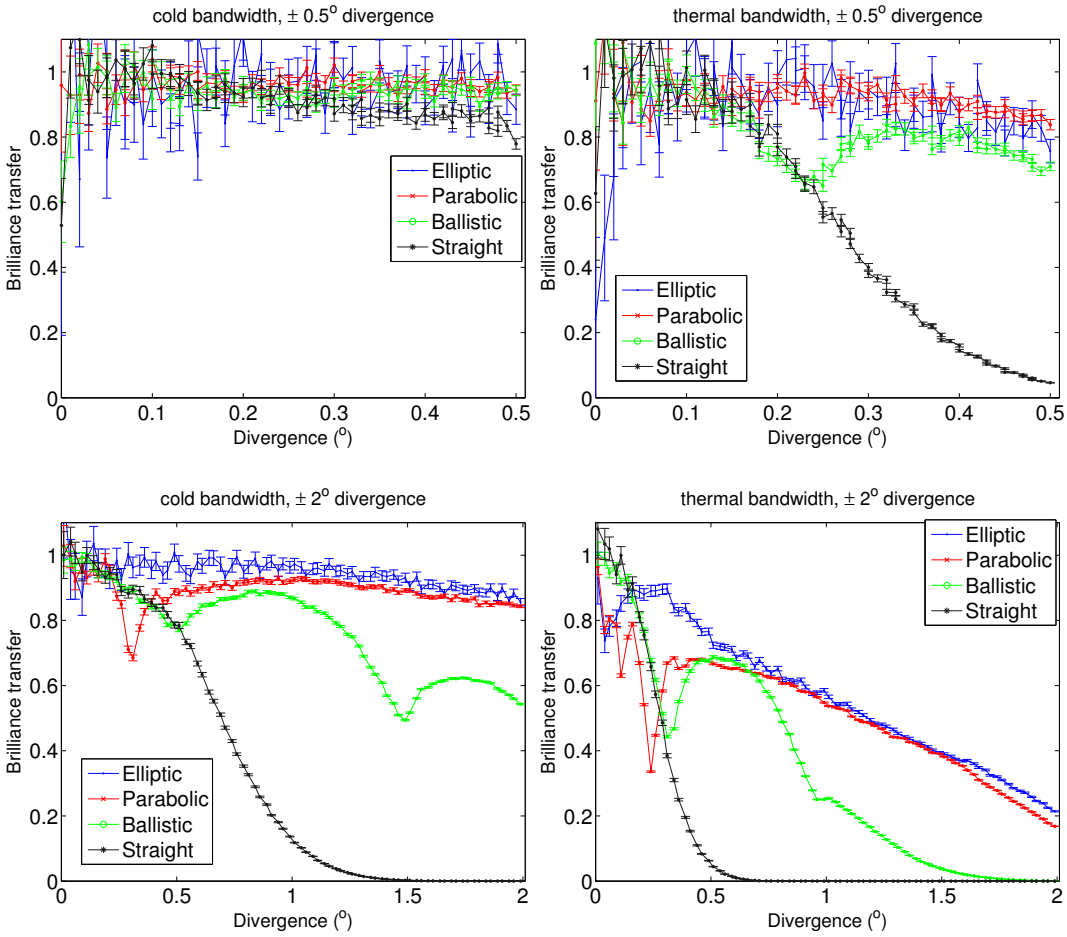

Figure 3.1.1: Brilliance (phase space density) transfer for the 4 different neutron guide geometries over a 150 m distance, plotted as a function of radial divergence. Left: Optimised for cold neutrons. Right: Optimised for thermal neutrons. Top: Optimised for 0.5 ° divergence. Bottom: Optimised for 2.0 ° divergence. Thermal is the wavelength interval 0.75-2.25 Å, and cold is 4.25-5.75 Å.

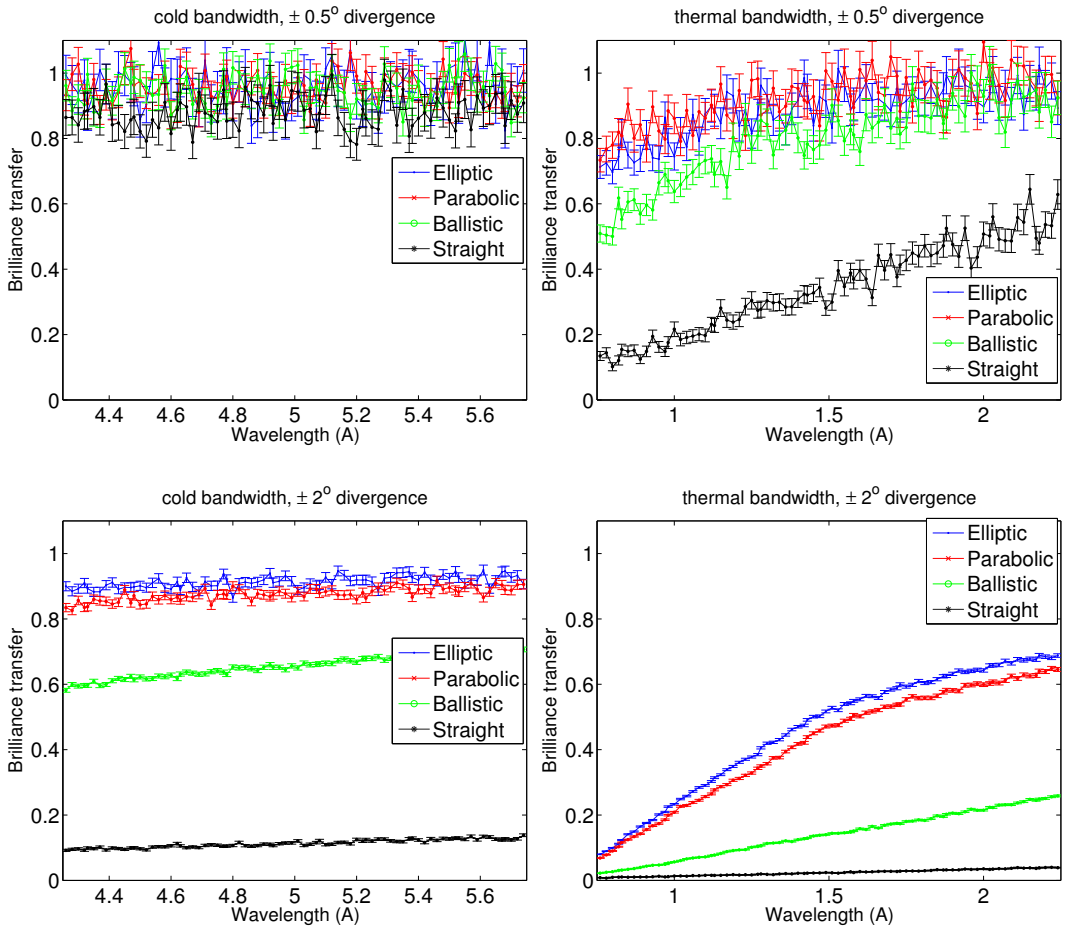

Figure 3.1.2: Brilliance (phase space density) transfer for the 4 different neutron guide geometries over a 150 m distance plotted as a function of wavelength, integrated over divergence. Left: Optimised for cold neutrons. Right: Optimised for thermal neutrons. Top: Optimised for 0.5 ° divergence. Bottom: Optimised for 2.0 ° divergence. Thermal is the wavelength interval 0.75-2.25 Å, and cold is 4.25-5.75 Å.

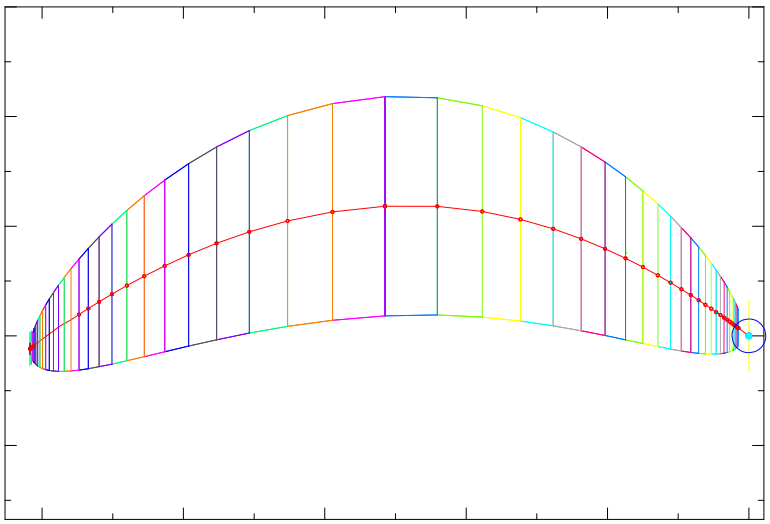

Figure 3.1.3: Sideways view of a 40 cm wide gravitationally curved guide, composed of 50 straight sections. The red line denotes the transverse centre of the guide. Please note that this figure is meant to give the reader a visual idea of the shape of a curved elliptical guide, and is not to scale.

calculate the correct curvature for a non-divergent monochromatic beam of the desired wavelength, but MC simulations are needed to quantify the effect such a geometry will have on a divergent, wide spectrum beam.

Figure 3.1.4 shows the transmission ration of a guide curved in such a way for 6.66 Å neutrons vs. an identical but uncurved guide, for 3 different guide lengths. From this we see that for long guides and long wavelengths, this is a useful method for blocking the line of sight with little loss in transmitted intensity. Note that transmitted intensity is calculated rather than brilliance transfer, as I had not yet begun to use the concept of brilliance transfer at the time this work was performed.

While this method will certainly block the direct line of sight, the actual effect in reduction of fast neutrons has not been quantified.

3.2. Blocking Line of Sight

In this section I will explore the effects of blocking line of sight for an elliptic guide and a parabolic-straight-parabolic guide, by curving them in the horizontal plane.

3.2.1. Curving elliptic Guides Horizontally to Block Line of Sight

While elliptic neutron guides are quickly gaining popularity due their increase in flux, techniques for eliminating the direct line of sight between the neutron source and the sample are still required. One method of doing this is to simply curve the guide in the horizontal plane, resulting in the banana-shaped guide shown in fig. 3.2.1. While this is a simple and effective method for eliminating line of sight, it will also destroy

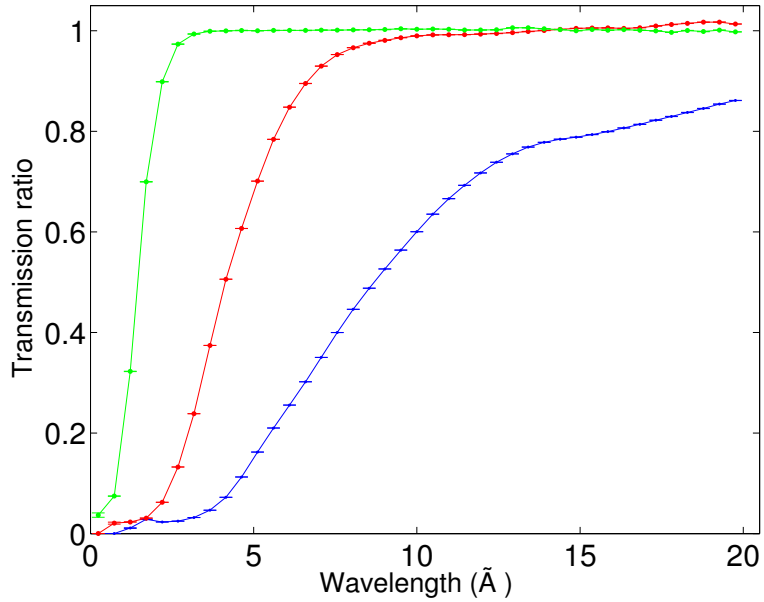

Figure 3.1.4: The simulated transmission ratio of a 40 cm wide elliptical guide, gravitationally curved to eliminate LoS, vs. an identical, but uncurved guide, as a function of wavelength. The green line represents a 300 m long guide, red is 100 m, and blue is 50 m. The sample size is 4×2 cm^2, and there are no divergence restrictions.

Guide length	100 m
Minor axis, horizontal	40 cm
Initial focus point distance from guide start, horizontal	0.73 m
Final focus point distance from guide end, horizontal	0.23 m
Minor axis, vertical	40 cm
Initial focus point distance from guide start, vertical	1.79 m
Final focus point distance from guide end, vertical	0.43 m

Table 3.2.1: Geometrical parameters of the elliptic guide.

the elliptic geometry, and might thus have a detrimental impact on the transmission of the guide. This effect I have investigated on an elliptical guide with the geometrical parameters given in table 3.2.1.
I will here briefly summarise simulation results of such guides. Note that the results are given in relative intensity, not brilliance transfer, as I had not yet begun to use the concept of brilliance transfer at the time these results where made and documented. The implication of this is that it is not the same phase spaces that are measured, but rather the sum of all neutrons arriving at the sample. Due to time constraints, I did not repeat these simulations in terms of brilliance transfer.

Simulations using $2 \cdot 10^8$ rays of epithermal neutrons found that a curvature of 1.1° is the minimum needed to successfully block all rays with a wavelength of 0.4 Å or below, for a 100 m long elliptic guide with a minor axis of 40 cm. This did however result in a 28% decrease in the intensity of 5 Å neutrons delivered to the sample, as

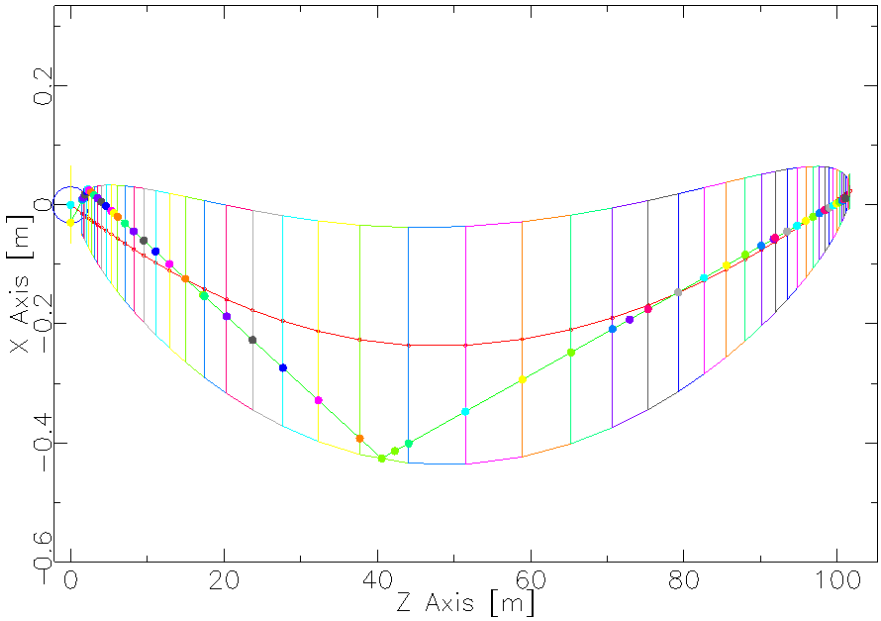

Figure 3.2.1: Top down view of an elliptic guide, horizontally curved by 1.1°. The vertical lines denotes the boundaries between the small guide elements comprising the total guide and red line is the transverse centre-line of the guide. The green line is a neutron ray, and the dots denote interactions with a McStas component, such as a reflection from the guide mirrors or the transition from one guide section to another.

seen in fig. 3.2.2.

This detrimental effect of curvature is more pronounced on an advanced non-uniform guide coating distribution with m-values up to 6 on the ellipse ends, where the intensity loss is 37%, than it is with a uniform m=2 guide coating, where the intensity loss is only 28 %, as seen in fig. 3.2.3. The non-uniform coating distribution does still deliver far more neutrons to the sample than an m=2 coating distribution though. For further details on non-uniform coating distributions, see [52]. As expected, this transmission loss is strongly dependent on wavelength, as seen in fig. 3.2.4. For example, the loss is almost 90% for 2 Å neutrons and 40% for 5 Å. Compared to this, curving an elliptical guide in the horizontal plane seems not to be the method of choice for eliminating LoS.

A less costly method for eliminating the line of sight uses a beamstop placed in the centre of the guide. For this wide guide, it will only cause 4% reduction in intensity on sample for 5 Å neutrons, as shown in fig. 3.2.5.

3.2.2. Curving a Parabolic Guide

In our paper *Systematic Performance Study of Common Neutron Guide Geometries*[1], parabolic guides were primarily included because of their promise to more readily allow for blocking the LoS than an elliptic guide, though investigating this claim fell outside the scope of that work. Instead I will show this here, by curving the straight section to block LoS. The criterion I will use for successfully blocking LoS is that no neutron

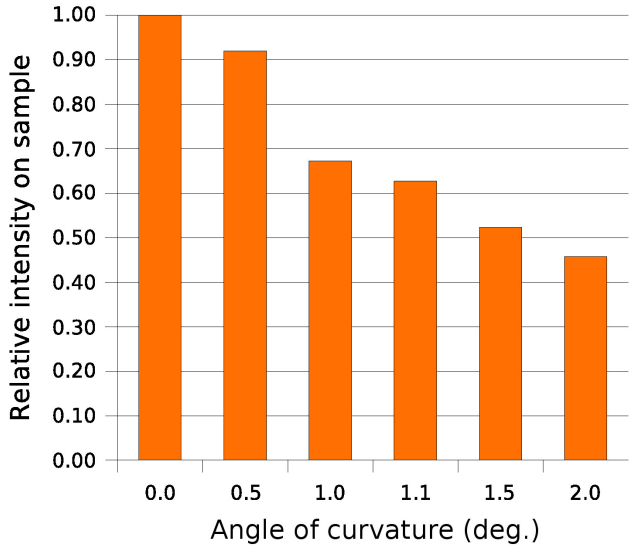

Figure 3.2.2: Relative intensity on sample for 5 Å neutrons, as a function of angle of curvature in the elliptical guide described in table 3.2.1. The statistical error is below 0.1 %. There are no divergence restrictions.

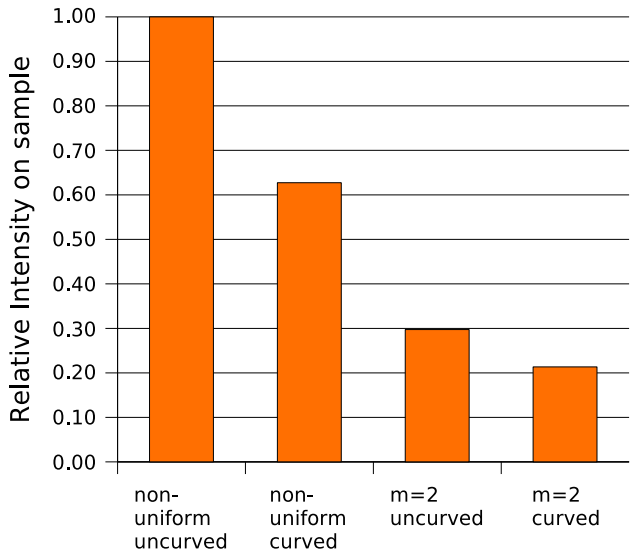

Figure 3.2.3: The effect of curvature on the elliptical guide described in table 3.2.1: Relative intensity on sample for 5 Å neutrons, for a guide with an advanced non-uniform coating distribution and for an m=2 coated elliptic guide, with and without curvature. The statistical error is below 0.1 %. There are no divergence restrictions.

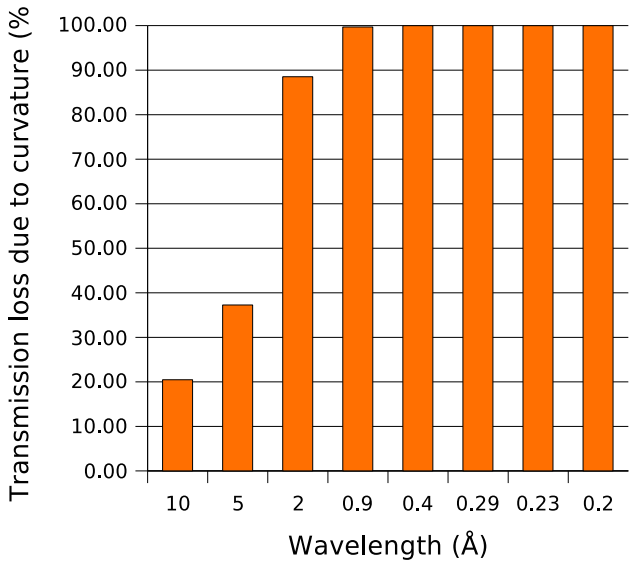

Figure 3.2.4: The dependence of transmission loss due to curvature on wavelength for the elliptical guide described in table 3.2.1. All wavelengths below 0.4 Å are completely blocked. The statistical error is below 0.2 %. There are no divergence restrictions.

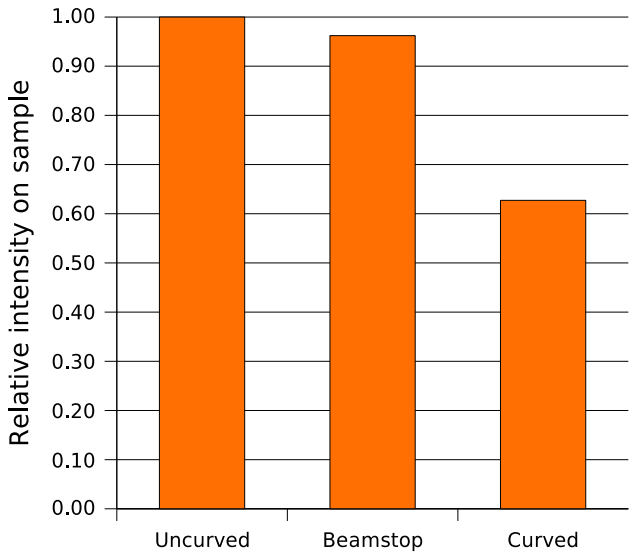

Figure 3.2.5: Two different methods for eliminating direct line of sight between source and sample: Relative intensity on sample for 5 Å neutrons, for an uncurved guide, an uncurved guide with a beamstop and a curved guide. The statistical error is below 0.1 %. There are no divergence restrictions.

with a wavelength of $\lambda < 0.1$ Å can reach the end of the straight section before being absorbed.

As previously stated, by a parabolic guide I refer to a guide that has a parabolically expanding section, followed by a straight section, and ending with a parabolically focusing section, just as in [1]. As the guides in [1] were optimised with no regard to LoS blocking, the parameters they ended up with tended to result in a relatively short and wide straight section.
So instead I simulated a parabolic guide where the expanding and focusing sections were each 20 m long, and the straight section is 108 m long, 10 cm wide and curved in the horizontal plane with a radius of curvature of 22 km, which fulfilled the above LoS criterion. The other parameters, such as supermirror coating, has been kept the same as [1]. After optimising the focal points of the parabolic sections, I have simulated the brilliance transfer of this guide, the results of which are shown in figures 3.2.6 and 3.2.7.

In figure 3.2.6 we see the brilliance transfer as a function of wavelength, within the integration box of 1×1 cm^2 and 0.5° of radial divergence: $\eta = \sqrt{\eta_x^2 + \eta_y^2}$. We see that for wavelengths of $\lambda > 0.6$ Å, curving the guide has little to no effect on the brilliance transfer. For wavelengths of $\lambda < 5$ Å, the curved guide has a significantly better brilliance transfer than an uncurved straight guide.

In figure 3.2.7 we see the brilliance transfer as a function of radial divergence, within the integration box of 1×1 cm^2 and a $\Delta\lambda$ of 0.75 Å $< \lambda <$ 2.25 Å. We see that curving the guide has little to no effect on the brilliance transfer for divergences up to 0.5°, and for divergences of $\eta > 0.2°$, the curved guide has a significantly better brilliance transfer than an uncurved, straight guide.

From this I will conclude that using a parabolic guide with a curved section in the middle, is indeed a viable method of blocking LoS while still having excellent brilliance transfer over a long distance, even for thermal neutrons.

The guides used for comparison are those from [1] that have been optimised for a 150 m distance, a divergence interval of $0 - 0.5°$, and a thermal wavelength band. The coatings used are the same as in the article: $m = 3$ for the straight guide and the straight guide sections of the parabolic guides, and a nonuniform coating distribution for the parabolic guide sections.

3.3. Smoothness of Divergence Distribution at the Sample Position

Some concerns have been raised over the smoothness of the divergence distribution coming from elliptic guides. While the increased beam transport through elliptic guides will inevitably produce a less smooth divergence distribution than a straight guide[34], simulation artifacts can exaggerate this, as I will demonstrate in this section. The guides models used here are those used in [1], with the same parameters for coating, source and sample size. The parameters for the guides used in this section are given in table 3.3.1.

The elliptic guide models I have developed - and which are widely used by the Copenhagen simulation group - approximate the elliptic shape by using 50 segments of piece-

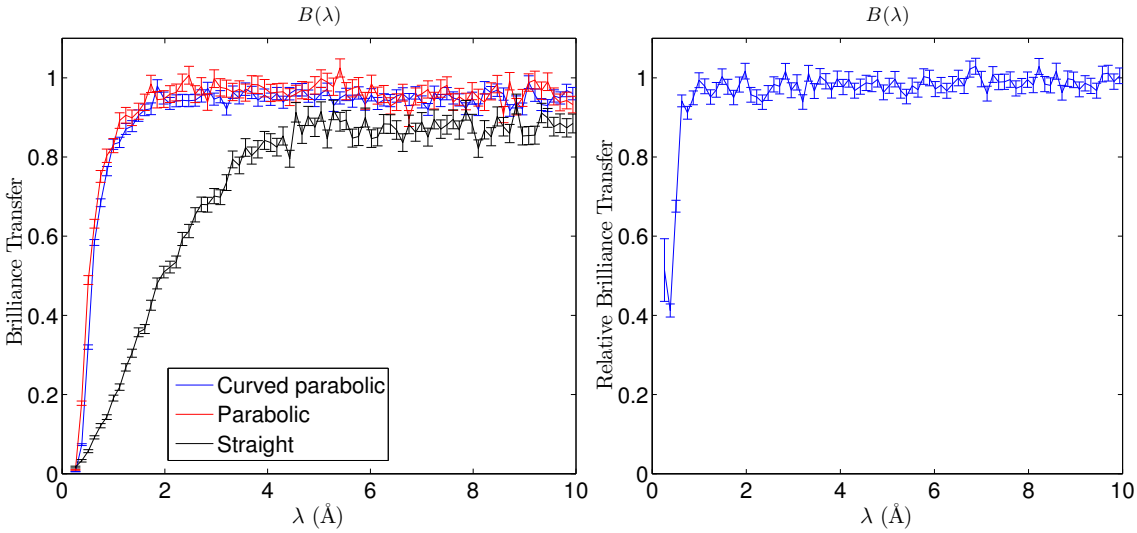

Figure 3.2.6: Brilliance transfer as a function of wavelength for a parabolic guide with a curved section in the middle. Left: Brilliance transfer compared to an uncurved parabolic guide and an uncurved straight guide. Right: The ratio of brilliance transfer of the curved parabolic guide to the uncurved parabolic guide. The divergence range is up to $\eta = 0.5°$

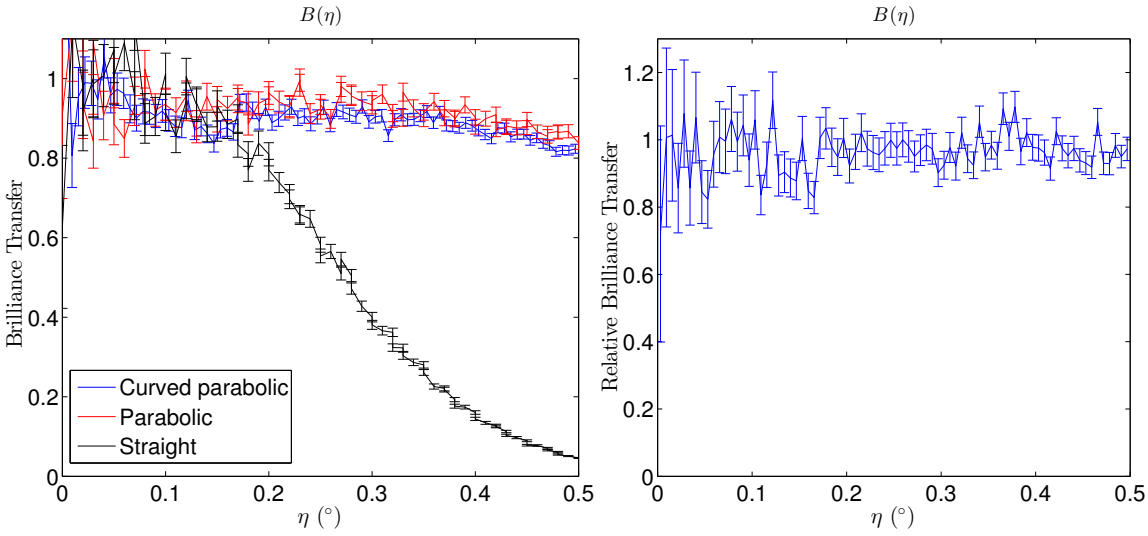

Figure 3.2.7: Brilliance transfer as a function of radial divergence for a parabolic guide with a curved section in the middle. Left: Brilliance transfer compared to an uncurved parabolic guide and an uncurved straight guide. Right: The ratio of brilliance transfer of the curved parabolic guide to the uncurved parabolic guide. The wavelength interval is 0.75 Å $< \lambda <$ 2.25 Å.

Phase space optimised for	T & 0.5°	C & 0.5°	T & 2°	C & 2°
Minor axis	27 cm	40 cm	40 cm	40 cm
Guide length	148 m	148 m	148 m	148 m
Initial focus p. dist. from guide start	3.45 m	2.32 m	2.39 m	2.26 m
Final focus p. dist. from guide end	0.64 m	1.79 m	0.34 m	0.47 m

Table 3.3.1: Geometrical parameters of the long elliptic guides used for 150 m instruments in [1]. Guides are listed by the wavelength interval and maximum divergence sampled over in the optimisation figure of merit. Thermal (T) is 0.75-2.25 Å and cold (C) is 4.25-5.75 Å. The realspace size of the figure of merit is 1×1 cm^2. The supermirror coating used with these guide is $m = 6$ for the first and last 10% of the guide length, and $m = 3$ for the middle 80%.

wise linearly tapering guide segments. This is a good compromise between accuracy and simulation feasibility in most cases[52]. However, for purposes of evaluating the smoothness of the divergence distribution, 50 segments is insufficient. This can be seen in figure 3.3.1, which shows the divergence distribution at the sample position for two 50 m long elliptic guides transporting 4 Å neutrons: one composed of 50 and one of 200 segments. Note that these guides have been optimised for transporting highly divergent neutrons. Figure 3.3.2 shows corresponding plots for guides optimised for low divergence. Here it can be seen that there is no noticeable change in the divergence distribution when going from 50 to 200 segments; this is not surprising, as low divergent neutrons are easier transported. Note that figure 3.3.2 is essentially a zoomed in version of figure 3.3.1.

For 100 m guides this difference is much less pronounced, as the divergence distribution is much more smooth, as seen in figure 3.3.3.

At 0.08° divergence, there is a dip to about 80% of the peak flux in figure 3.3.2. This divergence corresponds to neutrons that over a distance of 48.5 m has a transverse motion of 68 mm, when tracing their trajectory back from the sample towards the source. This means that they impact on the guide within the first meter of guide, as the guide starts 1.5 m from the source. The guide segment there is angled 1.1°, giving a total reflection angle of 1.2°. A neutron with a wavelength of 4 Å would then have a q-value of:

$$q = 2k\sin(1.2^\circ) = 4\pi\sin(1.2^\circ)/4\text{Å} = 0.066\ \text{Å}^{-1} \tag{3.3.1}$$

The coating I have used on the ends of the guide have a reflectivity at $q = 0.066$ Å of 79%, which completely explains the dip. Moving the source focus point changes the angles of the mirrors which are responsible for this dip, though this of course have other side effects. Thus the importance of smoothness of the divergence distribution needs to be quantified for the individual instrument, along with the other qualities of the beam, in order to find the most acceptable guide for each instrument.

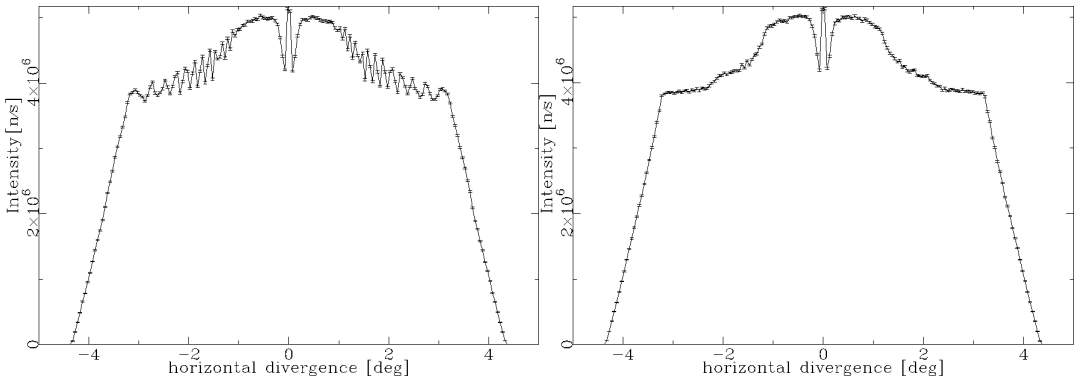

Figure 3.3.1: Divergence distribution at the sample position for 50 m long elliptic guides, transporting high divergence ($\eta \leq 2°$) 4 Å neutrons. Left: 50 guide segments. Right: 200 guide segments. The guide geometry is specified in table 3.3.1.

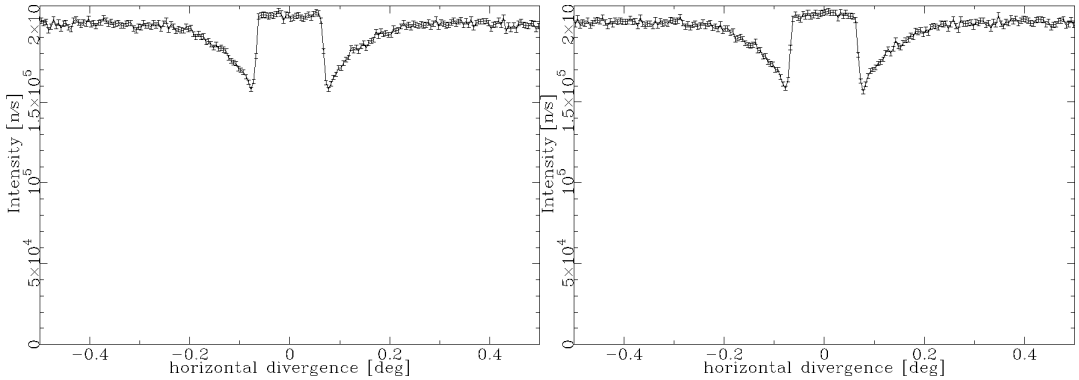

Figure 3.3.2: Divergence distribution at the sample position for 50 m long elliptic guides, transporting low divergence ($\eta \leq 0.5°$) 4 Å neutrons. Left: 50 guide segments. Right: 200 guide segments. The guide geometry is specified in table 3.3.1.

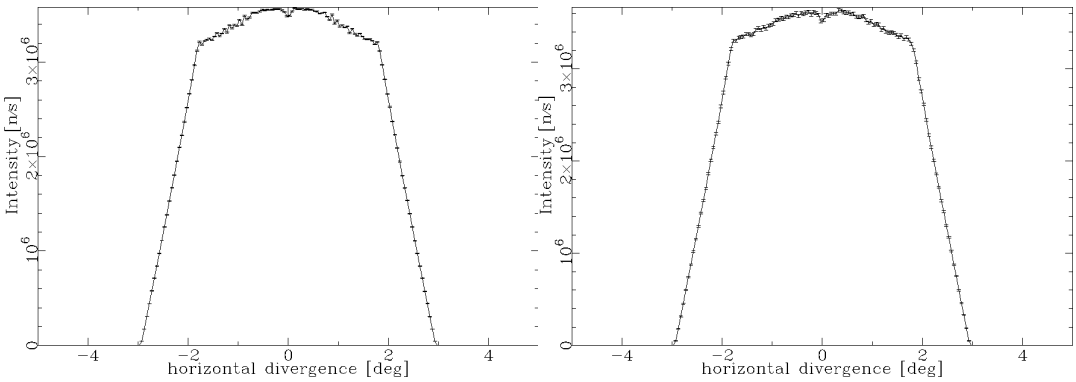

Figure 3.3.3: Divergence distribution at the sample position for 100 m long elliptic guides, transporting high divergence ($\eta \leq 2°$) 4 Å neutrons. Left: 50 guide segments. Right: 200 guide segments. The guide geometry is specified in table 3.3.1.

3.4. Waviness

Waviness describes an imperfection in the local angle of a mirror. It differs from misalignment in that waviness is an inaccuracy over a shorter length scale than misalignment, which concerns a full guide element. McStas models this in version 1.12a and 1.12c by adding or subtracting a random value from the angle of incidence, each time a neutron ray is incident on a guide wall. The random value is Gaussian, with the Gaussian width determined by the waviness parameter[22]. It should be noted that this model can give slightly incorrect results when looking at angles of incidence that are at the same order or smaller than the waviness value, and a more accurate algorithm is under testing[76].

I have used a waviness with a FWHM value of 0.01°, as this should be easily achievable by modern guide manufacturing processes[37]. This is also in good agreement with waviness measurements done on the guides at the D11 instrument at the ILL, which yielded a value of 0.012°[77].

For a 100 m long elliptic guide, focused on a 1×1 cm^2 sample, using this waviness value resulted in no discernible flux reduction at the sample position, for both 4 Å and 0.5 Å neutrons with a divergence below 2°. The geometrical parameters of the guide are given in table 3.4.1.

A qualitative way to interpret this result is that while waviness does have the effect of blurring the beam, the finite size of the moderator opening gives rise to an, apparently, more severe blurring. The blurring from the finite moderator size can be crudely quantified by considering the difference in angle of incidence of two neutrons impacting the far end of the guide; one from the centre of the moderator and one from the edge of the moderator, i.e. 6 cm off-centre:
$\arctan(0.06/100) = 0.034°$, which is 3 times the value of the waviness used.

As can be seen from fig. 3.4.1, noticeably detrimental effects on neutron transport only sets in at much higher waviness levels, around 0.1°.

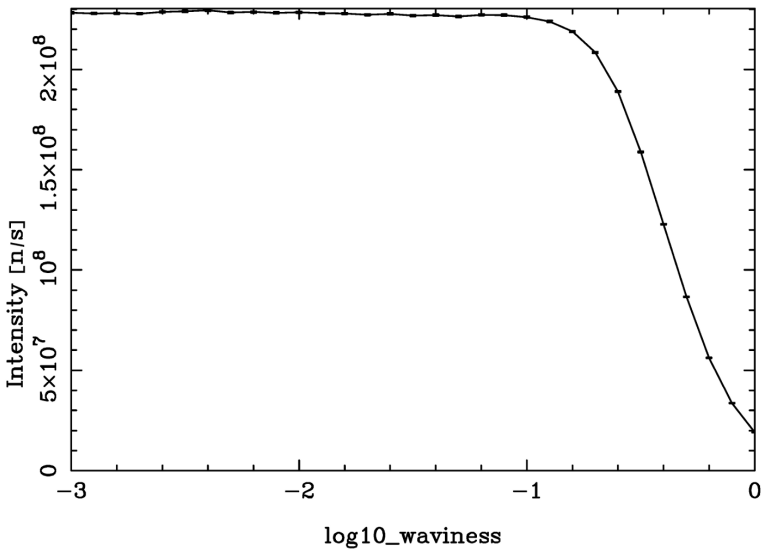

Figure 3.4.1: Flux on sample as a function of $\log_{10}$ waviness in degrees for 4 Å neutrons. The divergence restriction is $\eta \leq 2°$, and the geometrical parameters of the guide are given in table 3.4.1.

Minor axis	40 cm
Guide length	98 m
Initial focus p. dist. from guide start	1.8
Final focus p. dist. from guide end	0.33 m

Table 3.4.1: Geometrical parameters of the elliptic guide used for the waviness study. The supermirror coating used with these guide is $m = 6$ for the first and last 10% of the guide length, and $m = 3$ for the middle 80%.

3.5. Effects of Misalignment on Long elliptic Guides

Here I will explore the effects of misalignment on a long elliptic guide, using several different models, in order to give an estimate as to whether this is an issue that should be of concern for the ESS.

The guide used for most this study is a 148 m long elliptic guide, constructed from 50 straight segments in McStas, as shown in figure 3.5.1. The guide parameters, the figure of merit, and the method used to calculated the brilliance transfer, are for ease of comparison identical to those used in the previous study of neutron guide geometry[1], section 3.1. Specifically, the guide geometry used is the one optimised for 150m distance, 0.5° divergence, and cold spectrum (4.25-5.75 Å), as specified in table 3.3.1. As in the above study, a 12x12 cm^2 model of the ESS cold moderator is used as the source, the guide starts 1.5 m from the moderator, ends 0.5 m from a 1x1 cm^2 sample, and has a minor axis of 40 cm. All simulations were performed with gravity and a realistic guide waviness value of 0.01°[77].

Note that the elliptic guide models used are more proof-of-concepts than guides designed for an actual instrument. As such they are optimised for the brilliance transfer within a certain region of phase space, disregarding other areas of phase space. I.e. the optimiser was not punished for transporting neutrons to the sample area that fell outside of the integration box; rather these neutrons where simple not counted towards the optimisation figure of merit. One effect of this is that the guides transport a much larger area in both real space and divergence space than would realistically be required for most instruments. It is a reasonable assumption that this makes the guide models used here more robust to misalignment than a guide designed for the transport of a much smaller phase space.

A previous study of this kind has been made for straight neutron guides, where it was found that displacement misalignment values of 0.05 mm had a noticeable impact on the relative transmission of the guide, which is well above the manufacturers stated alignment limit of 0.01 mm[78].

3.5.1. Modelling Misalignment

I have modelled misalignment as a random variable on each of the 6 degrees of freedom of an individual guide segment: x (horizontal transverse), y (vertical), and z (longitudinal) displacement and pitch, yaw, and roll rotation, all relative to the previous guide segment. Specifically, the random misalignments are calculated so:

$$\begin{aligned} displacement_x &= rand \cdot x_{par} \\ displacement_y &= rand \cdot y_{par} \\ displacement_z &= rand \cdot z_{par} \end{aligned} \tag{3.5.1}$$

Where *rand* is a normal distributed random number generated for each degree of freedom in each individual guide segment, with $\sigma = 1$ and centred on 0. x_{par}, y_{par}, and z_{par} are the parameters used to control the size of that misalignment in the simulations. Similarly for the rotational misalignments we have:

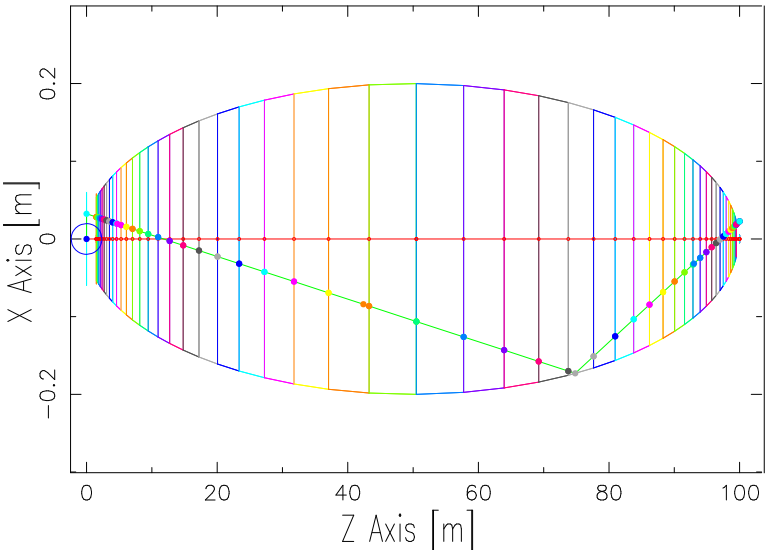

Figure 3.5.1: Cross-section in the horizontal plane of a McStas model of an elliptic guide. The green line is a neutron ray, and the dots denote interactions with a McStas component, such as a reflection from the guide mirrors or the transition from one guide section to another. The guide is constructed from 50 linear segments, which are seen in the figure as isosceles trapezia with very long base lines.

$$\begin{aligned} pitch &= rand \cdot pitch_{par} \\ yaw &= rand \cdot yaw_{par} \\ roll &= rand \cdot roll_{par} \end{aligned} \tag{3.5.2}$$

When these values have been calculated for each guide segment, they are added to the position and orientation of the segment relative to the previous segment. All negative values of $displacement_z$ are set to zero, as the segment cannot be displaced into the previous segment.

In figures 3.5.2 and 3.5.3 the effects of positional and rotational misalignment is visualised.

Limitations of the Model

- The guide segments used to construct the elliptic guide are of varying length, with very short segments used in the beginning and end of the guide, and longer segments (the longest almost 12 m) in the centre. This is done to better model the curvature in the ends of the ellipse while cutting down on simulation time in the less curved centre of the guide. However physical guides are typically constructed of 0.5 m segments, and the curved ends of elliptic guides can be made as continuously curved segments[37]. This impacts misalignment simulations as the effect of displacement misalignment is exaggerated by the many small segments in the beginning of the guide, while the effect of rotational misalignment

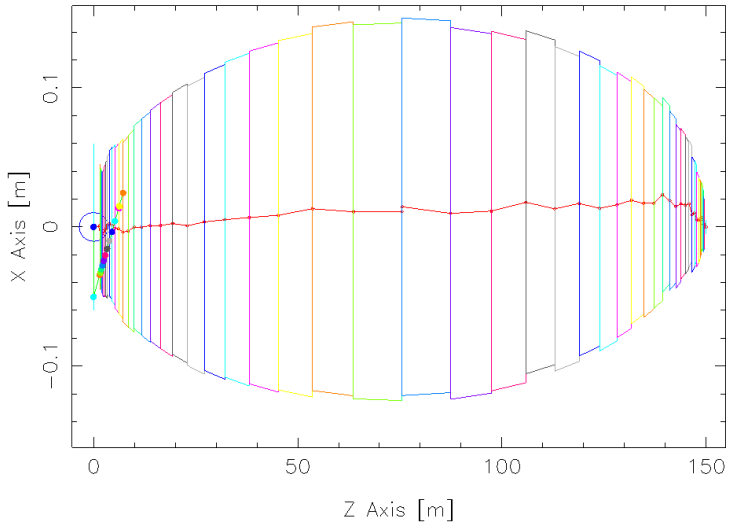

Figure 3.5.2: Cross-section in the horizontal plane of a McStas model of an elliptic guide, when setting positional misalignment to $x_{par} = 3$ mm. The green line is a neutron ray, and the dots denote interactions with a McStas component, such as a reflection from the guide mirrors or the transition from one guide section to another. The guide is constructed from 50 linear segments, which are seen in the figure as isosceles trapezia with very long base lines. The guide geometry used is the one optimised for 150m distance, 0.5° divergence, and cold spectrum (4.25-5.75 Å), as specified in table 3.3.1.

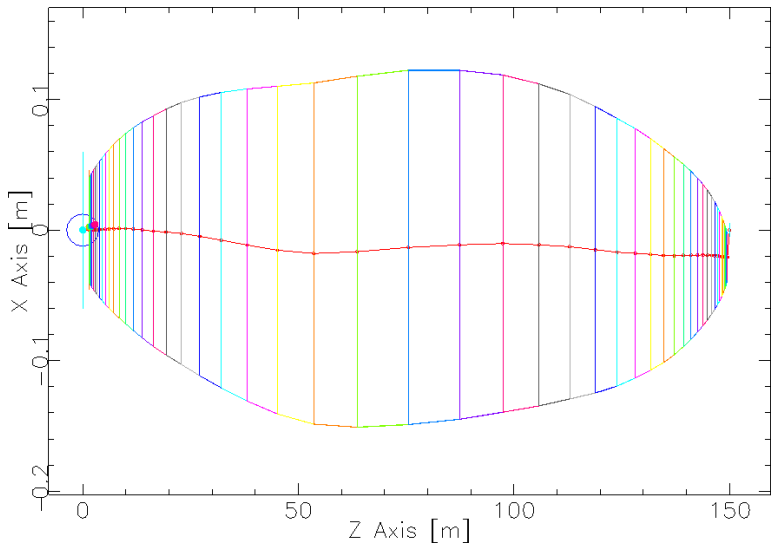

Figure 3.5.3: Cross-section in the horizontal plane of a McStas model of an elliptic guide, when setting rotational misalignment to $yaw_{par} = 0.01°$. The green line is a neutron ray, and the dots denote interactions with a McStas component, such as a reflection from the guide mirrors or the transition from one guide section to another. The guide is constructed from 50 linear segments, which are seen in the figure as isosceles trapezia with very long base lines. The guide geometry used is the one optimised for 150m distance, 0.5° divergence, and cold spectrum (4.25-5.75 Å), as specified in table 3.3.1.

is exaggerated by the long segments in the guide centre. This is addressed in section 3.5.5.

- Misalignment between the four mirrors composing a guide segment is not modelled, rather they are assumed to always be at a perfect 90° angle to each other.
- Large scale structure misalignment caused by e.g. ground movement of the instrument hall is not modelled.

3.5.2. Simulation Results

We performed a scan over each of the misalignment parameters to see how high a value is needed for it to significantly affect the brilliance transfer through the guide. The results are shown in figure 3.5.4. We see that the x and y displacements are quite noticeable at 1 mm, while the z (longitudinal) displacements have no effect even at 10 mm. The difference between longitudinal and transverse misalignment is not surprising, as the length of the guide is naturally much greater than the width, and as such transverse misalignment gives a much higher relative error for the same absolute displacement than longitudinal misalignment.
The rotational misalignments begins affecting the brilliance transfers for rotation values above 0.001° for pitch and yaw, while for roll the effect does not become noticeable until above 0.1°. This can be explained by the fact that roll does not affect either the longitudinal component of the neutrons velocity vector nor the sum of the transverse components. As the guide has transverse symmetry, changing the direction of the velocity vector from one transverse direction to another, should have little effect on transmission.
Note that there appears to be some incompatibility in the McStas 1.12c code between gravity and random pitch, therefore the simulations of pitch were performed without gravity. It is not expected that this affects the validity of this study.

Figure 3.5.5 shows the results of a scan of the transverse displacement in the range 0-1 mm, and shows that in this range the loss of brilliance transfer is proportional to the displacement value, with a loss of $\approx 10\%$ at 1 mm displacement.

This value is reassuring since these misalignments far exceeds the manufacturers specifications.

Beam Profile Brilliance transfer is not the only metric of a guide; a symmetric beam at the sample position in both real and divergence space is also a criteria. We here look at how misalignment affects this.
Figure 3.5.6 shows the beam cross-section at the sample position for a baseline setting of no misalignment and for 3 different settings of misalignment. The figure shows that almost no visible asymmetry in real space is caused by these values of misalignment.
Figure 3.5.7 shows the beam divergence profile at the sample position for a baseline setting of no misalignment and for 3 different settings of misalignment. It can be seen that a clear asymmetry in the horizontal direction occurs for a horizontal transverse displacement misalignment of 1 mm. For the more realistic value of 0.05 mm, no such asymmetry is noticeable.

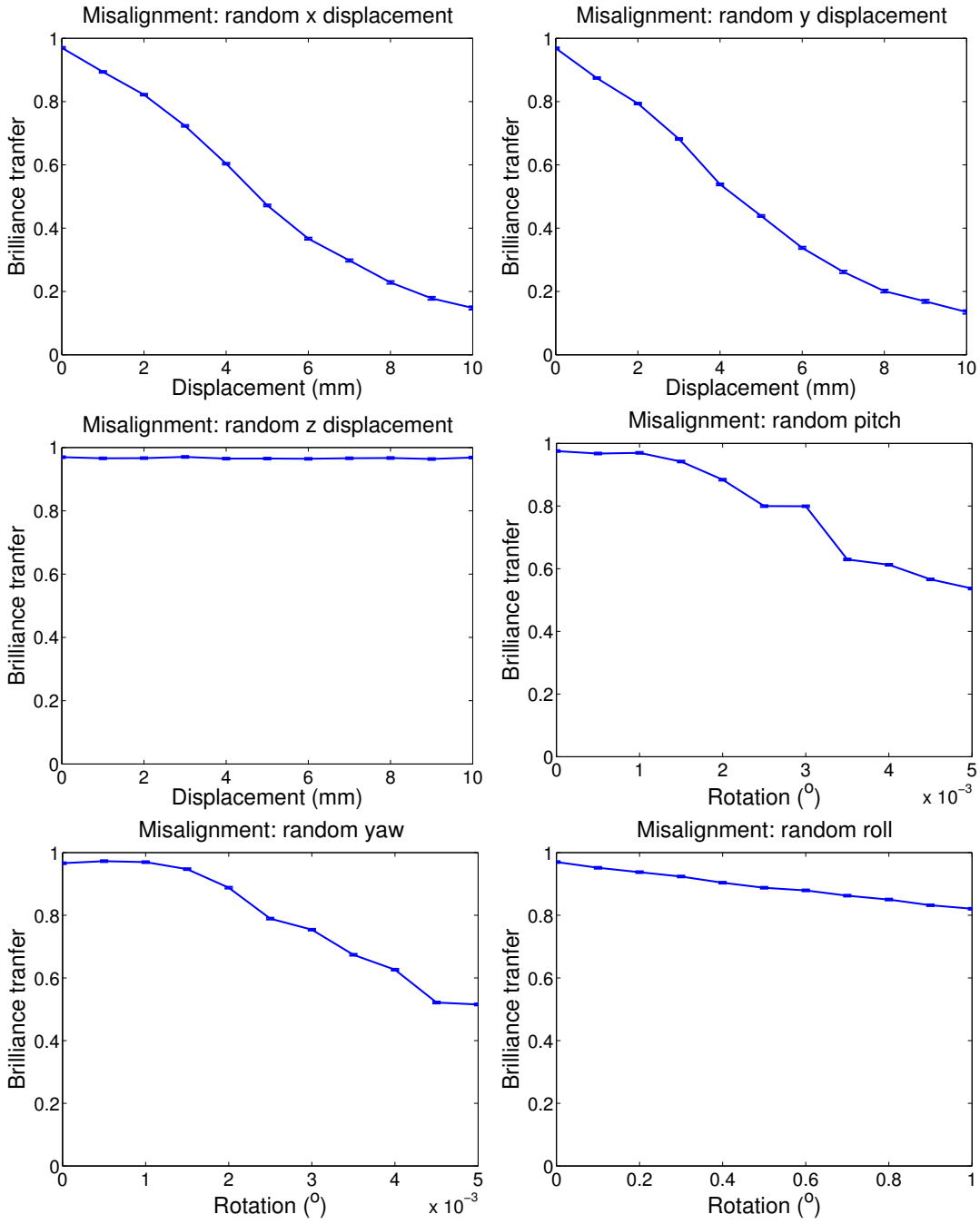

Figure 3.5.4: Brilliance transfer as a function of the 6 degrees of freedom used for misalignment. The divergence interval is $\eta \leq 0.5°$ and the wavelength interval is 4.25-5.75 Å. The guide geometry used is the one optimised for 150m distance, 0.5° divergence, and cold spectrum (4.25-5.75 Å), as specified in table 3.3.1.

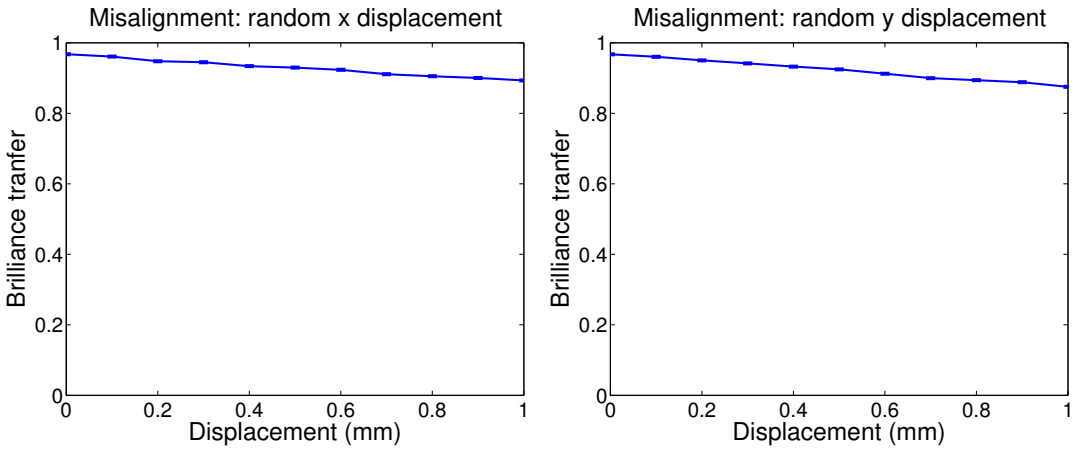

Figure 3.5.5: Brilliance transfer as a function of sub-millimetre transverse misalignment. A zoom in on figure 3.5.4. The divergence interval is $\eta \leq 0.5°$ and the wavelength interval is 4.25-5.75 Å. The guide geometry used is the one optimised for 150m distance, 0.5° divergence, and cold spectrum (4.25-5.75 Å), as specified in table 3.3.1.

3.5.3. Misalignment Relative to the Moderator

In the previous sections, it was assumed that each guide segment was aligned relative to the previous segment, which allowed misalignment to compound. If instead all guide segments are aligned relative to the moderator, this is avoided. Figures 3.5.8 and 3.5.9 shows the effect on the ellipse when modelling misalignment relative to the source. Note that the rotational misalignment value used in figure 3.5.8 is 10 times that used in figure 3.5.3, in order to make the drawing clearer.

Simulation Results Similar to in section 3.5.2, simulations of the brilliance transfer of the guide was made while scanning over the misalignment parameters. The results of this is shown in figure 3.5.10. Remember that for the rotational misalignment, the misalignment values scanned over are 10 times greater than those used for the results in figure 3.5.4. Also there are no simulations of longitudinal displacement misalignment here, as longitudinal displacement naturally require that the alignment is relative to the previous segment, to avoid overlap of the guide segments.
We see that the effect of rotational misalignment of brilliance transfer is much less severe when aligning relative to the source, and thus avoiding compound misalignment. The beam profile is shown in real space and divergence space in figure 3.5.11. Unlike in figure 3.5.7, no asymmetry can be seen due to misalignment.

3.5.4. Rotational Misalignment Calculated From Displacement

Random rotational misalignment tends to have an exaggerated effect on the long segments in the middle of the guide. As a more realistic description, I now let each end of each guide segment have an independent random displacement, and calculate the

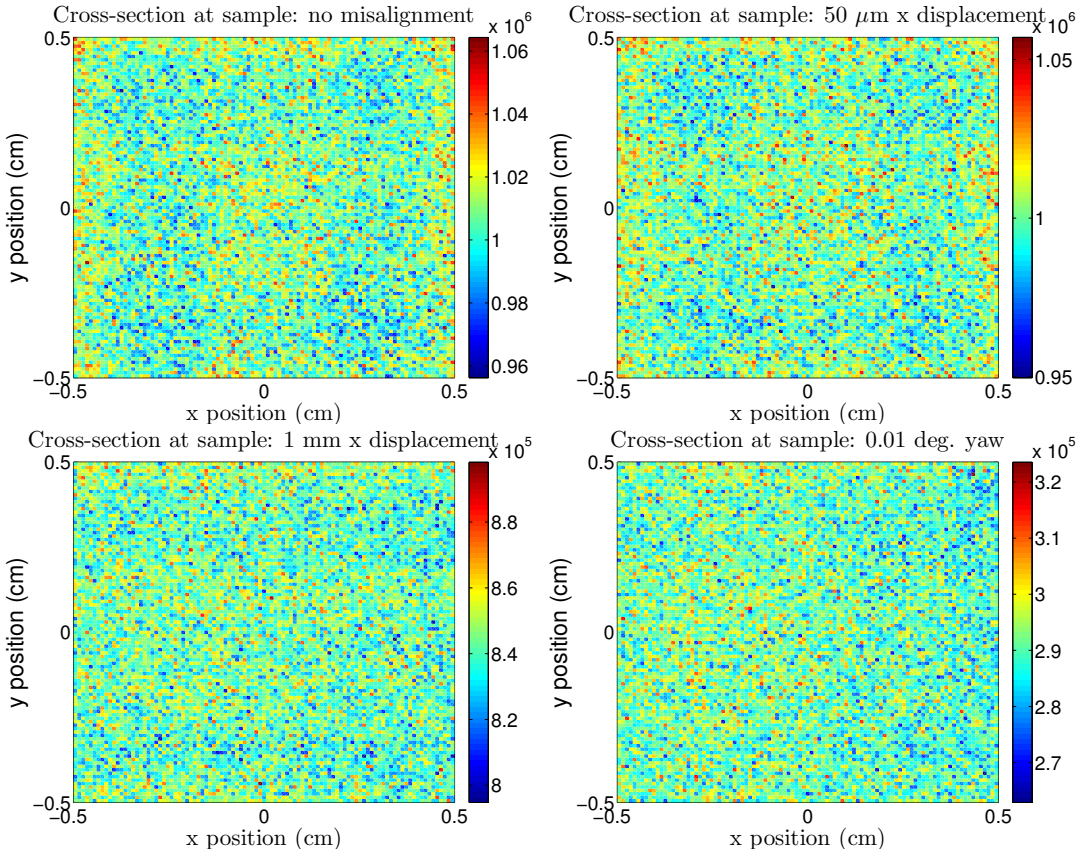

Figure 3.5.6: Beam cross-section at the sample position at various degrees of misalignment. The colour scale is n/s for each pixel. The divergence interval is $\eta \leq 0.5°$ and the wavelength interval is 4.25-5.75 Å. The guide geometry used is the one optimised for 150m distance, 0.5° divergence, and cold spectrum (4.25-5.75 Å), as specified in table 3.3.1.

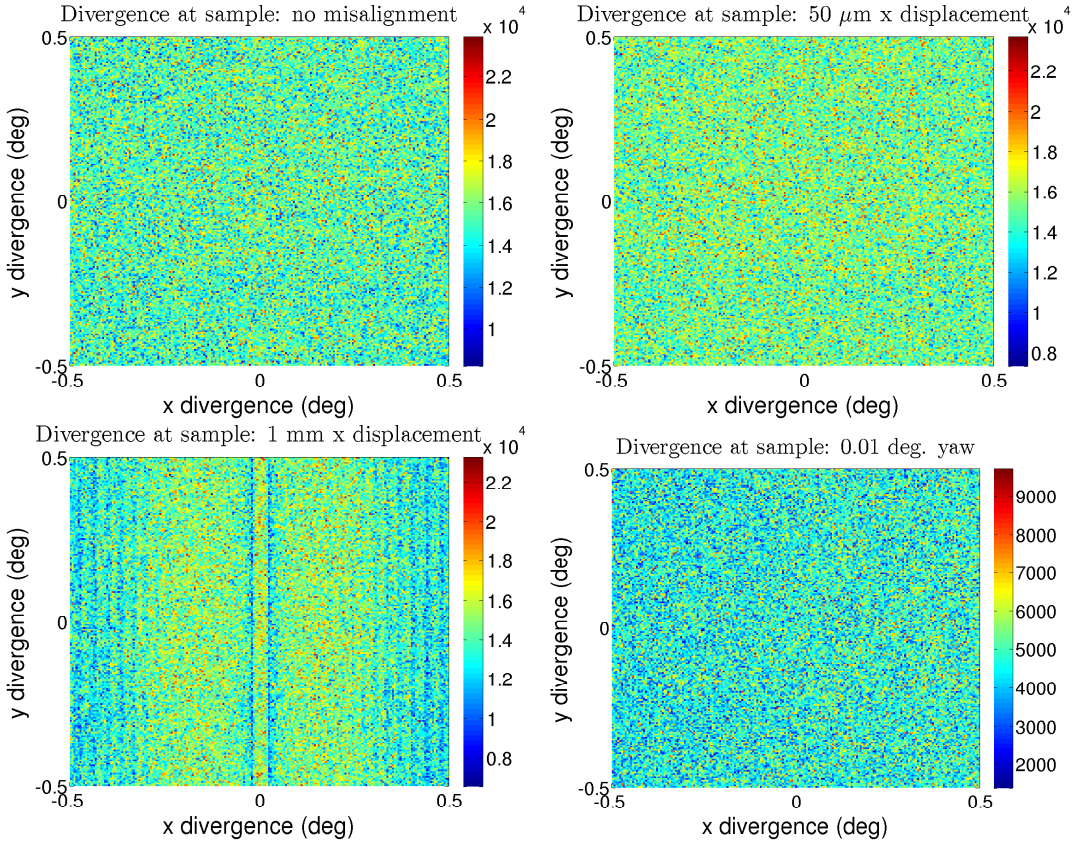

Figure 3.5.7: Divergence profile at the sample position at various degrees of misalignment. The colour scale is n/s for each pixel. The wavelength interval is 4.25-5.75 Å. The guide geometry used is the one optimised for 150m distance, 0.5° divergence, and cold spectrum (4.25-5.75 Å), as specified in table 3.3.1.

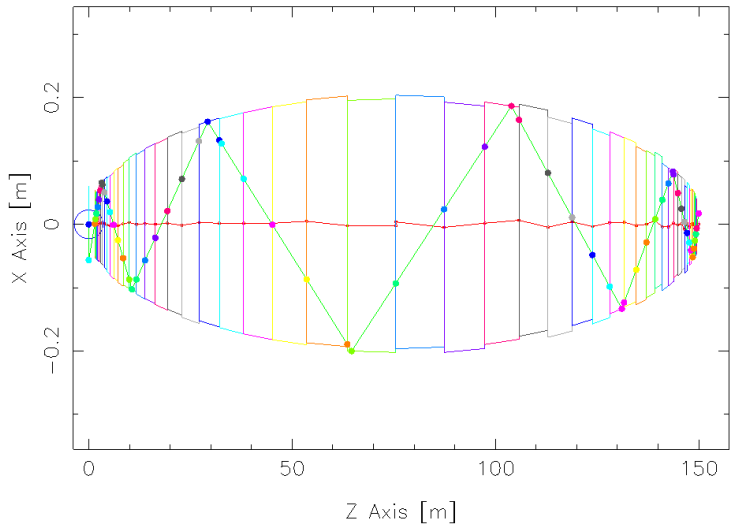

Figure 3.5.8: Cross-section in the horizontal plane of a McStas model of an elliptic guide, when setting positional misalignment to $x_{par} = 3$ mm and aligning relative to the moderator. The green line is a neutron ray, and the dots denote interactions with a McStas component, such as a reflection from the guide mirrors or the transition from one guide section to another. The guide is constructed from 50 segments of straight guide, which are seen in the figure as isosceles trapezia with very long base lines. The guide geometry used is the one optimised for 150m distance, 0.5° divergence, and cold spectrum (4.25-5.75 Å), as specified in table 3.3.1.

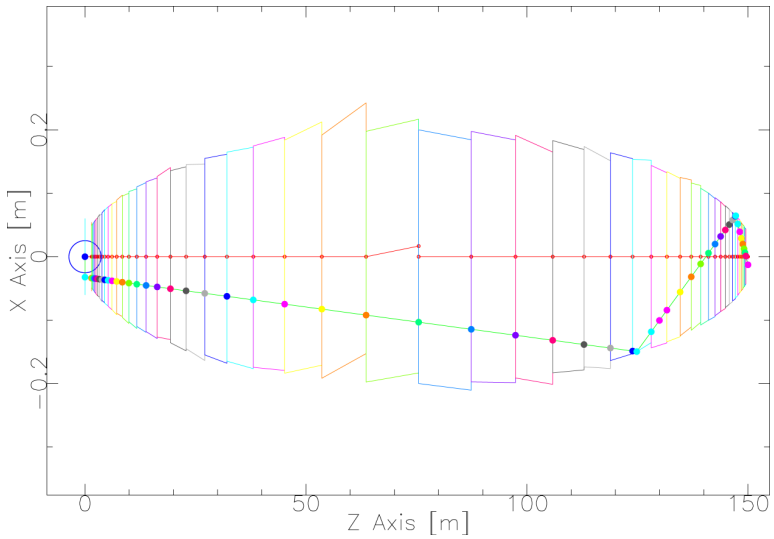

Figure 3.5.9: Cross-section in the horizontal plane of a McStas model of an elliptic guide, when setting rotational misalignment to $yaw_{par} = 0.1°$ and aligning relative to the moderator. The green line is a neutron ray, and the dots denote interactions with a McStas component, such as a reflection from the guide mirrors or the transition from one guide section to another. The guide is constructed from 50 segments of straight guide, which are seen in the figure as isosceles trapezia with very long base lines. The guide geometry used is the one optimised for 150m distance, 0.5° divergence, and cold spectrum (4.25-5.75 Å), as specified in table 3.3.1.

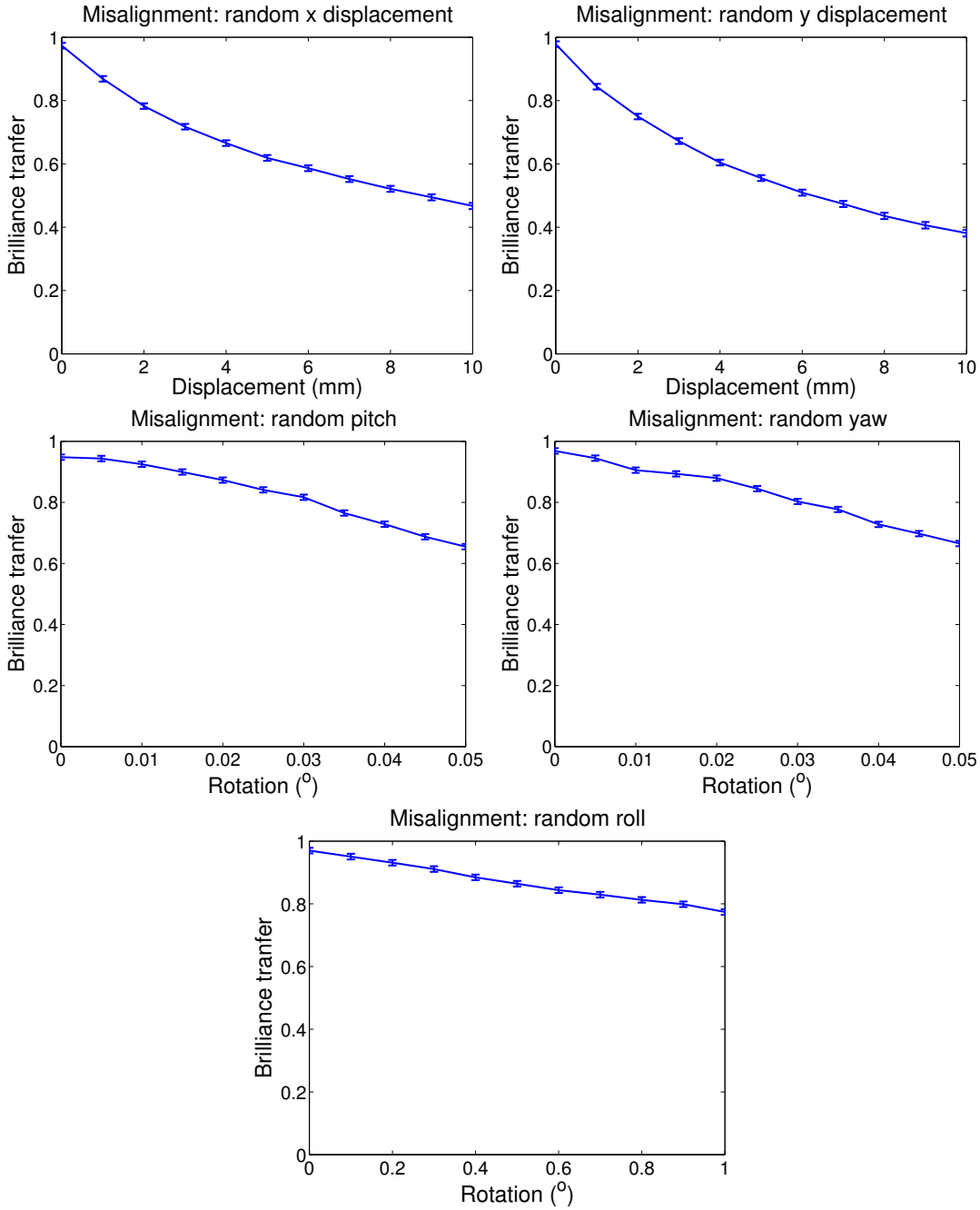

Figure 3.5.10: Brilliance transfer as a function of 5 of the degrees of freedom used for misalignment when aligning relative to the moderator. Longitudinal displacement is left out. The divergence interval is $\eta \leq 0.5°$ and the wavelength interval is 4.25-5.75 Å. The guide geometry used is the one optimised for 150m distance, 0.5° divergence, and cold spectrum (4.25-5.75 Å), as specified in table 3.3.1.

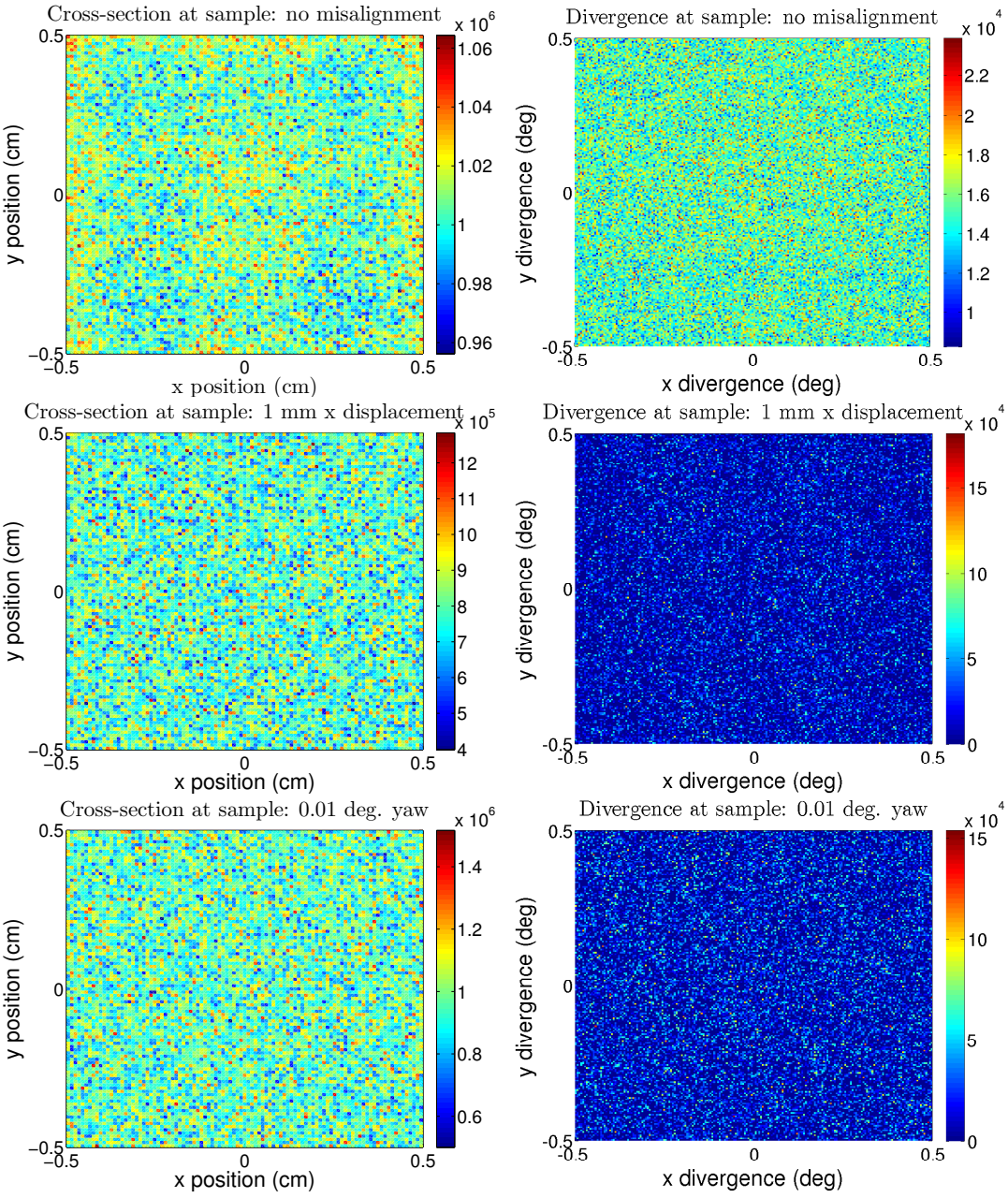

Figure 3.5.11: Left: beam cross-section at the sample position at various degrees of misalignment when aligning relative to the moderator. Right: divergence profile at the sample position at various degrees of misalignment. The colour scale is n/s for each pixel. The divergence interval is $\eta \leq 0.5°$ and the wavelength interval is 4.25-5.75 Å. The guide geometry used is the one optimised for 150m distance, 0.5° divergence, and cold spectrum (4.25-5.75 Å), as specified in table 3.3.1.

rotation of the segment as

$$\theta = \arctan\left(\frac{D_e - D_s}{L}\right)$$

where θ is the rotational displacement, D_e is the transverse displacement at the end of the segment, D_s is the transverse displacement at the start of the segment, and L is the length of the segment. The calculation is done separately for the two transverse rotations, yaw and pitch. Roll is unaffected by the length of the segment, and will hence be ignored in this section.

This model of misalignment is more accurate than the previous ones used, as physical alignment of guide segments will likely be done with the position of the ends of the segments using a laser.

The alignment of the guide segments is done relative to the moderator, as in section 3.5.3. Again this precludes longitudinal displacement misalignment.

Simulation Results Here 3 different 150 m elliptic guides have been simulated with misalignment: one for cold, low divergence neutrons, one for cold, high divergence neutrons, and one for thermal, low divergence neutrons. The geometries, accepted divergence space, and bandwidths are those used in [1] and listed in table 3.3.1.

Similar to section 3.5.2, simulations of the brilliance transfer of the guide was made while scanning over the misalignment parameters. The results of this is shown in figure 3.5.12. Note that for the displacement misalignment, the misalignment values scanned over are 10 times smaller than those used for the results in figure 3.5.10.

Comparing to figure 3.5.10, we see that the effect of misalignment on the brilliance transfer is a lot more severe when a displacement also causes a rotational misalignment.

3.5.5. Equidistant Space of Guide Segments

As described in the beginning of section 3.5, the guide used for these simulations is composed of 50 linear segments that together approximate part of an ellipse. The segments have varying lengths so that in the ends of the ellipse where the curvature is greatest, the segments are closely spaced, whereas in the middle of the ellipse much larger segments are used. This allows for a functionally good approximation of an ellipse while minimising the number of segments used, in order to improve computing time [52].
As mentioned in section 3.5.1, this causes problems with misalignment which we will here address.

For this section virtual guides have been constructed that are identical to those used in the previous section, except that they are composed of 300 sections of equal length. This makes it a lot more comparable to how it would be physically constructed, and thus also how the misalignment would affect an actual guide.

Simulation Results The same 3 elliptic guides as in the previous section has been simulated here, with the parameters given in table 3.3.1, and the misalignment is also modelled as in the previous section.

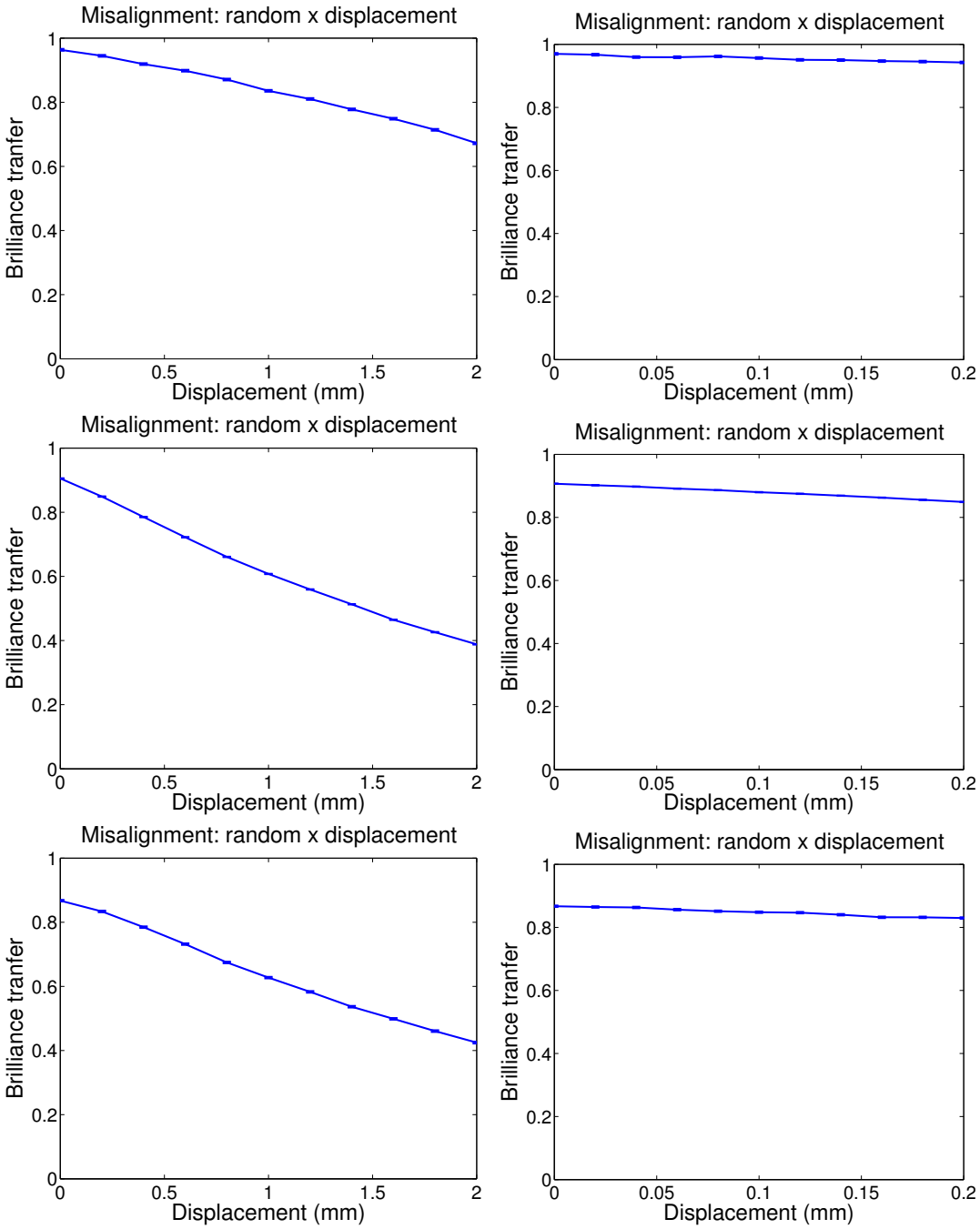

Figure 3.5.12: Brilliance transfer as a function of horizontal, transverse displacement misalignment when calculationg rotational misalignment from displacement. Top: cold neutrons with $\pm 0.5°$ divergence. Middle: cold neutrons with $\pm 2°$ divergence. Bottom: Thermal neutrons with $\pm 2°$ divergence. Left: 0-2 mm displacement. Right: 0-0.2 mm displacement. The guide geometries and wavelength intervals are specified in table 3.3.1.

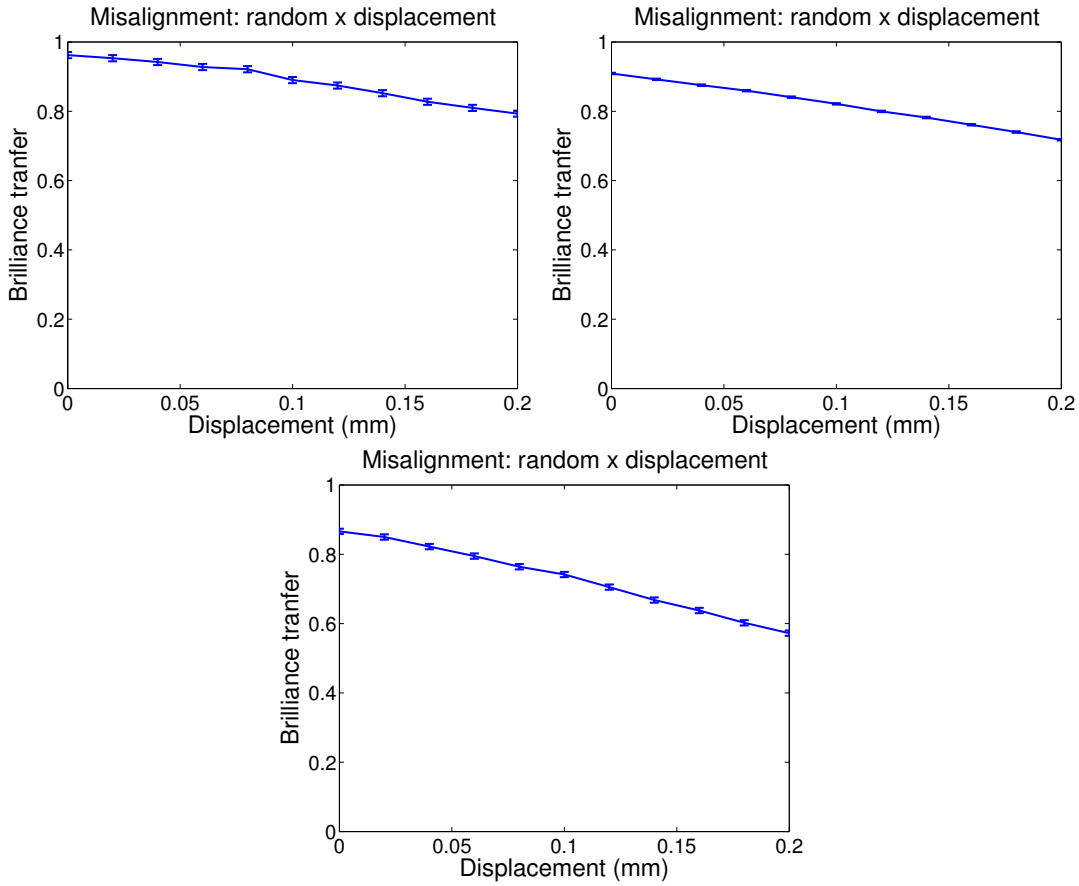

Figure 3.5.13: Brilliance transfer as a function of horizontal, transverse displacement misalignment when using equidistant guide segments. Top left: cold neutrons with ±0.5° divergence. Top right: cold (4.25-5.75 Å) neutrons with ±2° divergence. Bottom: Thermal (0.75-2.25 Å) neutrons with ±2° divergence. The guide geometries are specified in table 3.3.1.

Figure 3.5.13 shows that the effects of misalignment are much more severe when using this model. Not surprisingly the effect of the misalignment on the brilliance transfer is strongly dependent on the wavelength and divergence of the neutrons. Assuming an alignment precision of 20 μm, which is typical for present high precision installations[37], it is clear that the misalignment arising from the initial alignment of newly installed guides will not affect the brilliance transfer.

The beam profile at the sample position in figure 3.5.14 shows that a misalignment of 200 μm horizontal displacement has a noticeable effect on the shape of the profile. Figure 3.5.15 shows the horizontal divergence distribution at the sample position, and also here the misalignment is noticeable. Curiously, in the top row it appears that the misalignment smooths out a rather jagged divergence profile. The jaggedness is caused by the finite approximation of the elliptic shape, as shown in section 3.3.

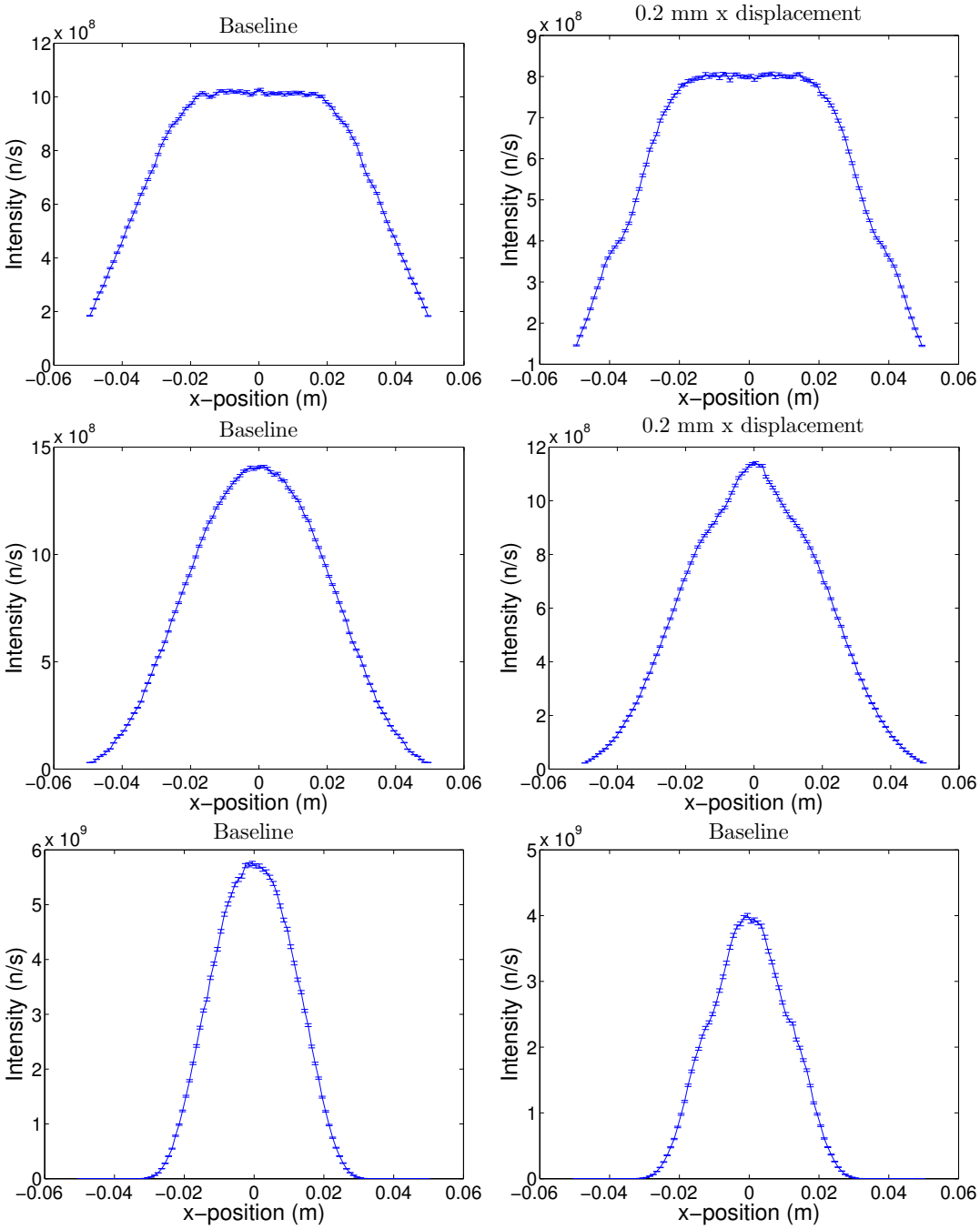

Figure 3.5.14: Horizontal beam profile at the sample position when using equidistant guide segments. Top: cold (4.25-5.75 Å) neutron guide optimised for ±0.5° divergence. Middle: cold (4.25-5.75 Å) neutron guide optimised fo ±2° divergence. Bottom: Thermal (0.75-2.25 Å) neutron guide optimised for ±2° divergence. Left: no misalignment. Right: 0.2 mm horizontal displacement. The guide geometries are specified in table 3.3.1.

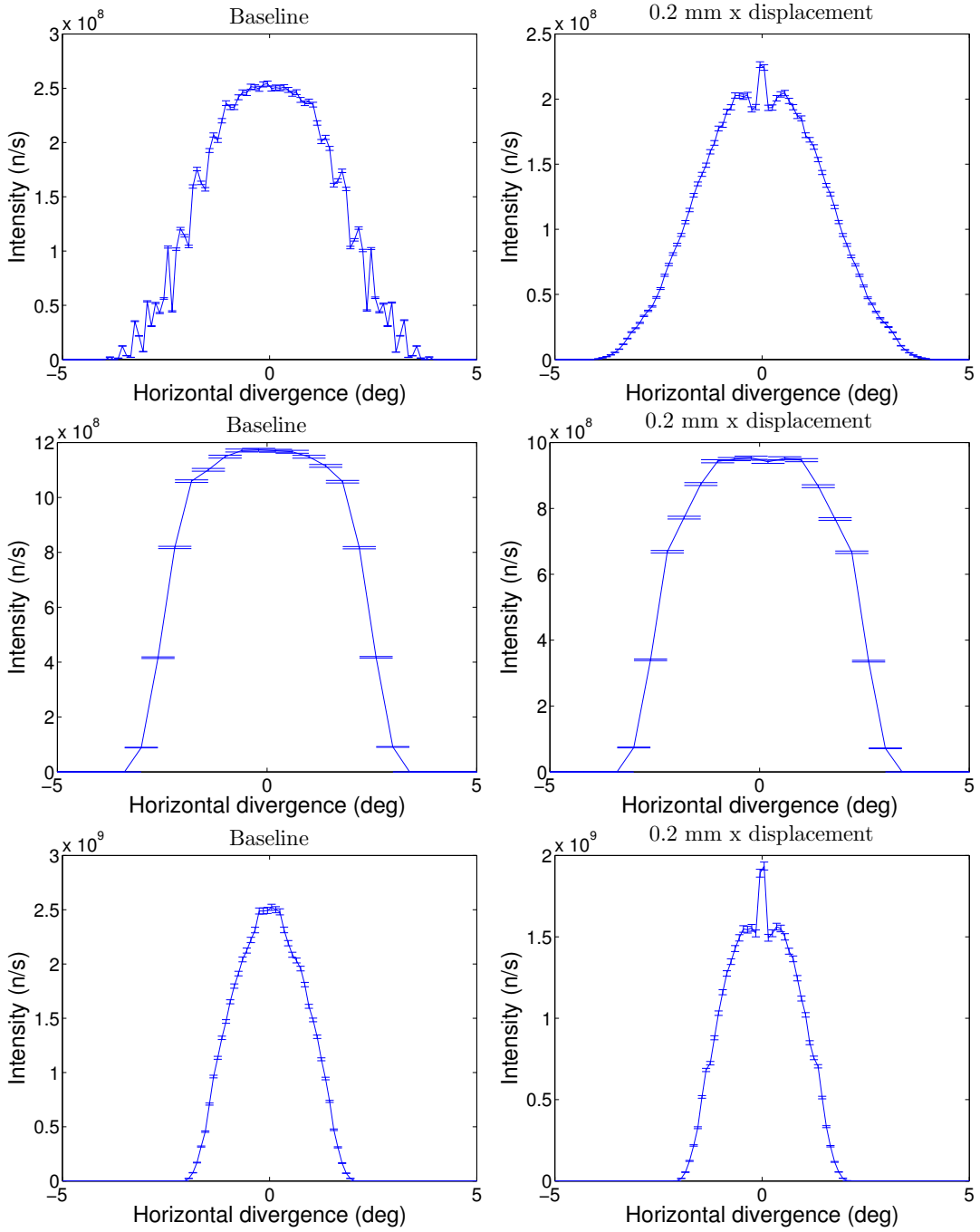

Figure 3.5.15: Horizontal divergence profile at the sample position when using equidistant guide segments. Top: cold (4.25-5.75 Å) neutrons with ±0.5° divergence. Middle: cold (4.25-5.75 Å) neutrons with ±2° divergence. Bottom: Thermal (0.75-2.25 Å) neutrons with ±2° divergence. Left: no misalignment. Right: 0.2 mm horizontal displacement. The guide geometries are specified in table 3.3.1.

3.5.6. Discussion on Misalignment

The results in section 3.5.5 shows that misalignment is a concern when constructing long elliptic guides, though the effect is strongly dependent on the wavelength and divergence of the neutrons being transported. At alignment accuracies of 50 μm, misalignment decreases the brilliance transfer with 4-9 %. It is therefore essential to use highly accurate alignment when constructing long elliptic guides, but at the manufacturer specified alignment limit of 10 μm, the misalignment effects are negligible. However, problems may appear subsequently by long term random guide movement, and this should be considered.

The findings in this study show an effect on guide transmission at similar levels of misalignment with those done in a previous study[78], but since that study was performed with a short straight guide, whereas this study was performed with a long elliptic guide, the findings are not directly comparable.

It is clear from the results that aligning relative to the moderator rather that the previous guide segment, is an effective method to reduce the impact of misalignment, as this avoids compound misalignment.

It is important to note that the elliptic guides investigated here are rather wide, with a 40 cm minor axis. It is a fair assumption that a guide designed to only accept the minimum necessary phase space would be more susceptible to misalignment.

It should also be stressed again that this study does not model large scale misalignment caused by e.g. ground movement of the instrument hall.

Later studies should also include the effect of producing guide elements in one single piece.

3.6. Miscellaneous

In this section I have collected some older guide simulation results, that does not fit in other sections.

3.6.1. Moderator size

A moderator face 12×12 cm^2 in size have been used in all simulations done so far; however a specially designed monitor (fig. 3.6.1b), which shows where on the moderator face a neutron reaching the sample originated from, reveals that the majority of the intensity on the sample originates from the inner 8×8 cm^2 section of the moderator. The guide used for this study is the one given in table 3.2.1.
Reducing the size of the moderator face to 8×8 cm^2 did indeed only reduce the intensity on target by 26%, as shown in fig. 3.6.2. This corresponds to an increase of 66% in intensity delivered to the sample pr. unit area of moderator face.
Generally the smaller the moderator face is, the higher a fraction of the emitted neutrons will be successfully transmitted, as an elliptic guide performs best when transmitting neutrons originating from a point source. However, as can be seen from the grey columns in fig. 3.6.2, this effect is more pronounced with a 8×8 cm^2 moderator, than with a 6×6 cm^2 moderator. This is an important result, as a smaller moderator

could give a higher brilliance[79].
Please note that the above simulation results where for a guide optimised to the 12×12 cm^2 moderator face. A guide optimised for a smaller moderator face will likely improve those figures.

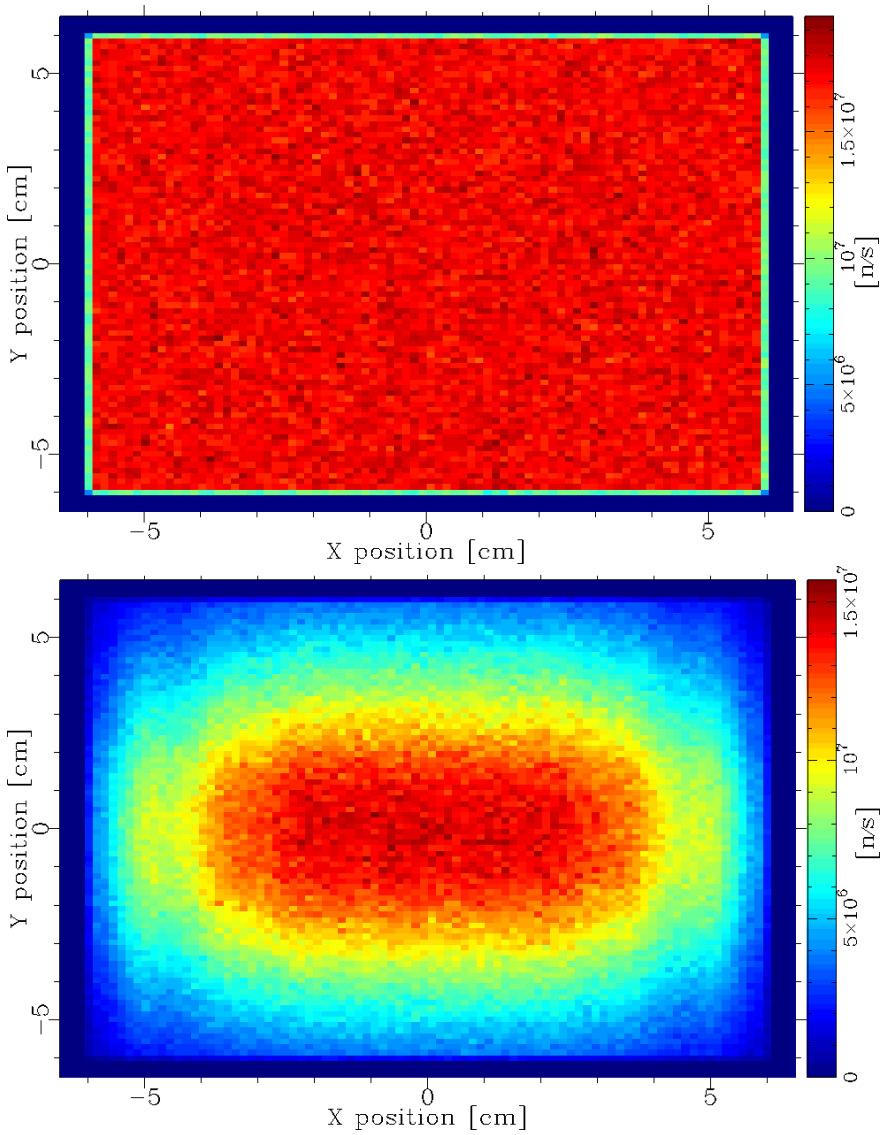

Figure 3.6.1: Top: The beam cross section immediately after the moderator. Bottom: The position on the moderator face where neutrons reaching the sample position originated from. The wavelength is 5 Å and there are no divergence restrictions. The guide geometry is specified in table 3.2.1.

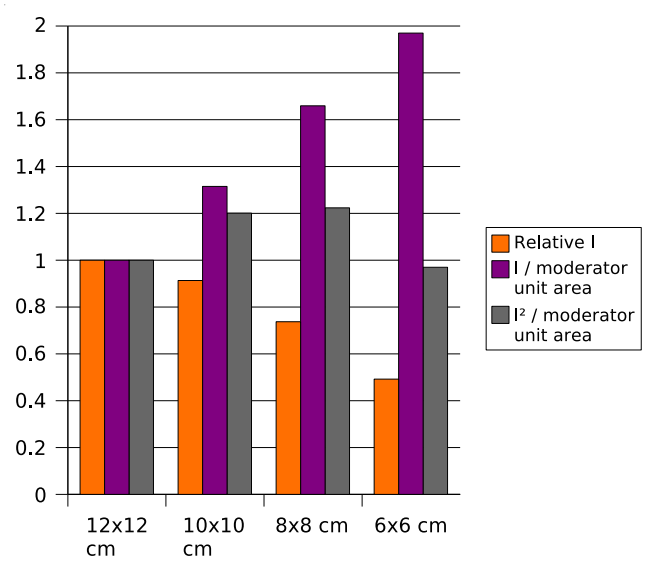

Figure 3.6.2: The relative intensity on sample, the intensity on sample pr. unit area of moderator face, and the intensity on sample squared pr. unit area of moderator face, for two different moderator sizes. The latter is included as the intensity on sample pr. unit area of moderator face will naturally increase for unrealistically small moderator surfaces, so it is a compromise between the first two figures of merit. The wavelength is 5 Å and there are no divergence restrictions. The guide geometry is specified in table 3.2.1.

3.6.2. Moderator Hotspots

This section investigates the effect it will have on guide design and instrument performance, if the ESS cold moderator can be designed with a "hotspot"; i.e. a grooved section of the moderator surface where the brilliance is higher than on the remainder of the surface. The guide used for this study is the one given in table 3.2.1.

For the purpose of these simulations, we have assumed a circular hotspot with a diameter of 3 cm. The brilliance in that area is multiplied by a factor 2, while the remainder of the 12×12 cm^2 moderator is normalised by a factor 0.95, so that the average brilliance of the moderator is unchanged.

Numerical optimisation of the elliptic guide for this non-uniform moderator results in an increase in intensity on a 1×1 cm^2 sample by $30\%\pm0.1\%$, again assuming that the average brilliance of the moderator is unchanged.

Fig. 3.6.3 shows origin data (See section 3.6.1 for more details on this.) for a guide focused on a uniform moderator and one focused on one with the hotspot, and the difference is evidently drastic. Due to the lower transmittance of the area outside the hotspot, it can be assumed that a lower background at the sample position will be a positive side effect.

The effects of moderator hotspots have also been investigated in our paper *Simulation of a suite of generic long-pulse neutron instruments to optimise the time structure of the European Spallation Source*[4] and report *Simulation of a suite of generic long-pulse neutron instruments to optimise the time structure of the ESS accelerator*[8].

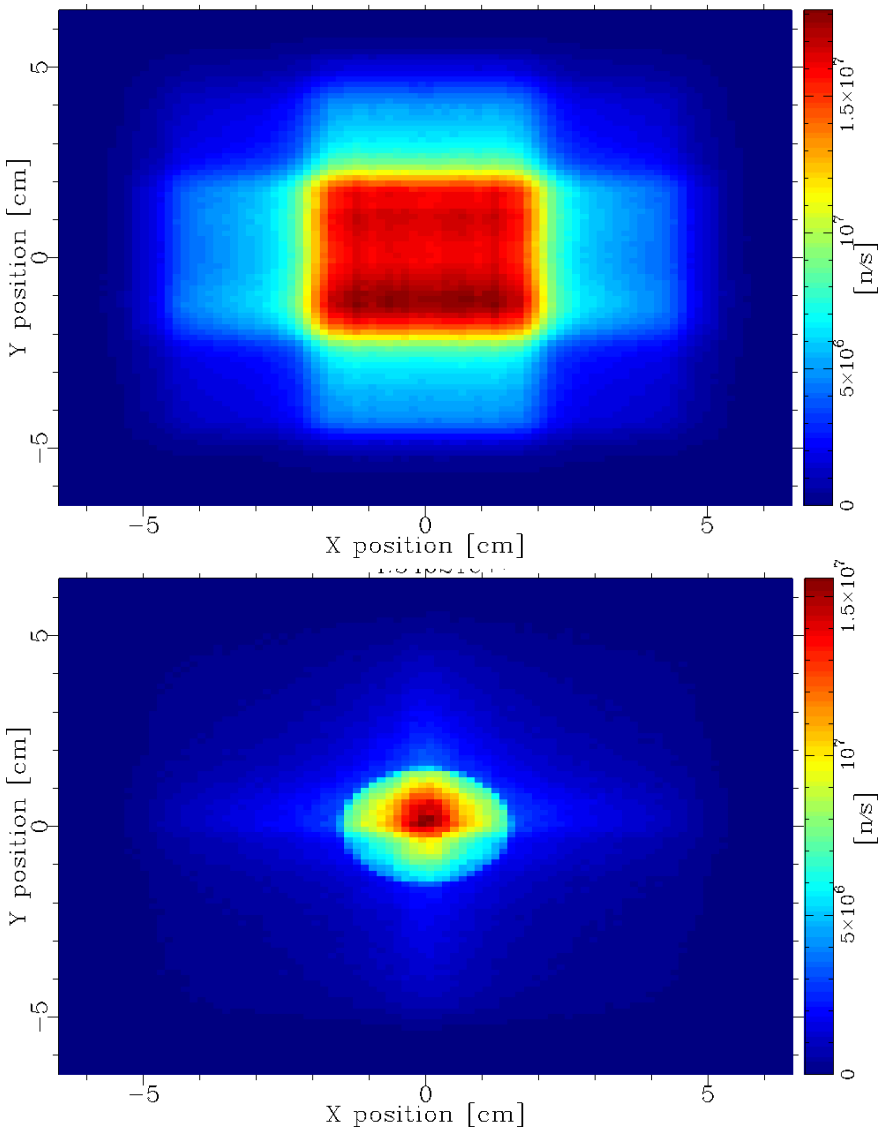

Figure 3.6.3: Left: Origin data using a uniform moderator. Right: Origin data using a moderator with a hotspot with a diameter of 3 cm. The wavelength is 5 Å and there are no divergence restrictions. The guide geometry is specified in table 3.2.1.

4. Results of Instrument Simulations

A large amount of my efforts the last years has been the simulation of full models of instruments related to the ESS. This work is an important part of this thesis and is documented in published articles or submitted manuscripts; all reprinted in the Appendix. I do not intent to rewrite these manuscripts here, and this chapter is merely a short introduction to my instrumentation work. Refer to the papers for a full explanation of the figures reprinted in this section.

4.1. Long Thermal-Neutron Spectrometer

My work on elliptic guides showed that it is possible to transport short wavelength neutrons over large distances with decent brilliance transfer. As an illustration of this result, I simulated two full thermal direct geometry ToF spectrometers for a presentation at the NASCES conference at J-PARC in 2011. The publication *Thermal Chopper Spectrometer for the European Spallation Source*[2] covers this work.

One spectrometer had a length of 180 m, the other was 300 m long. Both spectrometers use the Repetition Rate Multiplication method as described earlier and illustrated in fig. 1.4.1. My main result is that the very long thermal spectrometers are feasible and that the performance, due to the elliptic guide, does essentially not depend upon instrument length. Figure 4.1.1 documents this by showing the wavelength distribution of neutron flux on sample for the two instruments.

Note that the monochromating choppers are a pair of counter rotating choppers. As such a setup will open from the centre outwards and close from both edges simultaneously, the centre of the chopper window will, averaged over time, be open longer. This means the choppers will slightly affect the beam profile.

A full virtual experiment with a vanadium sample is shown for the two instruments in figure 4.1.2. For both instruments we obtain a decent energy resolution of 3.3 meV (RMS) with incident neutrons of 1 Å (82 meV).

The main importance of this work is the demonstration of feasibility for very long functioning instruments at ESS using neutrons down to 0.5 Å wavelength, an issue that was under discussion at the time of writing this paper.

4.2. Generic SANS instruments

As an input to the discussions of the optimal time structure (pulse length τ and pulse frequency $1/T$) for the ESS neutron source, our group performed a large piece of collective work by simulating and optimising 15 different instrument candidates, including 8 spectrometers and 4 diffractometers, at 20 different combinations of τ and T in the range $\tau = 1 - 2$ ms and $T = 10 - 25$ Hz. Our figure of merit was a weighted average of the neutrons on sample at these 15 instruments at fixed resolutions. The main result was that the figure of merit was proportional to the peak neutron flux from the moderator, multiplied by the factor $(\tau/T)^{0.3}$, see figure 4.2.1.

The time structures under discussion in the ESS accelerator and target/moderator groups at the time we finished this work all had the same peak flux and the same

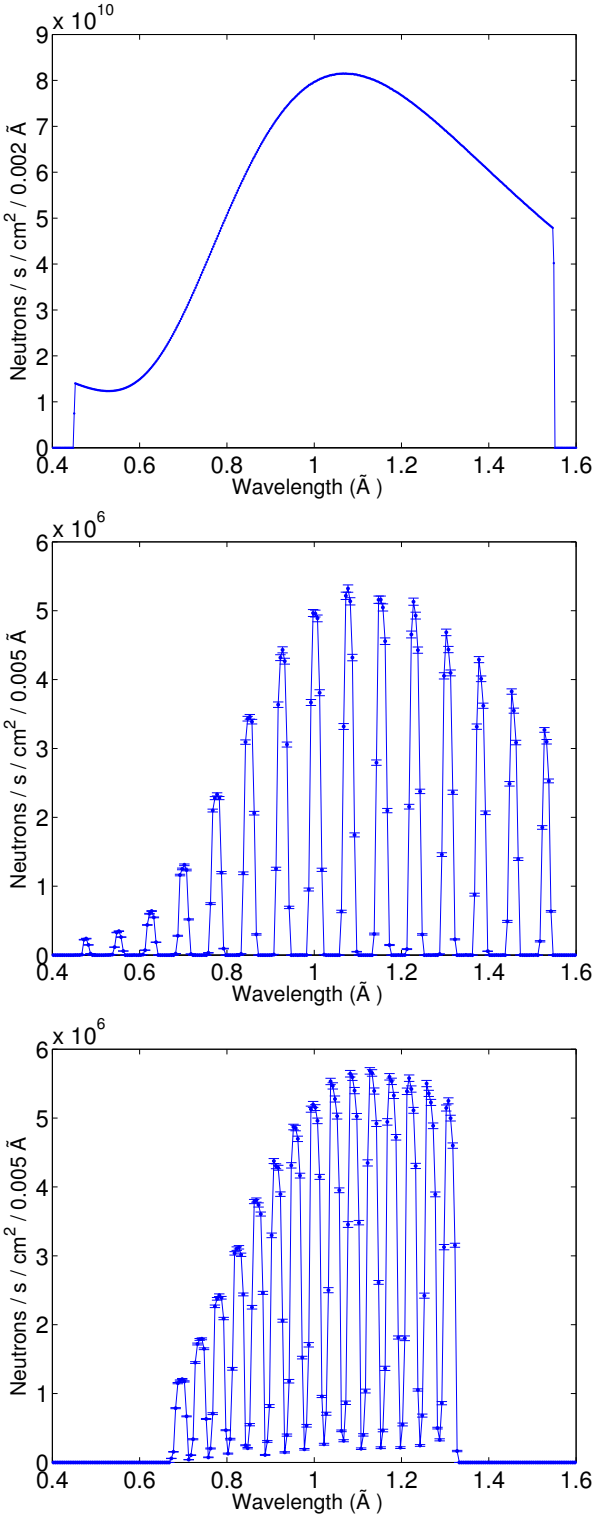

Figure 4.1.1: Wavelength distribution of the beam, and the effect of the resolution choppers. Top: at the entrance to the guide. Middle: at the sample position, just after the resolution choppers, with the 180 m guide system. Bottom: at the sample position, just after the resolution choppers, with the 300 m guide system. The sharp cut-offs at the 0.45 and 1.55 Å positions are caused by the bandwidth restrictions in the simulation.

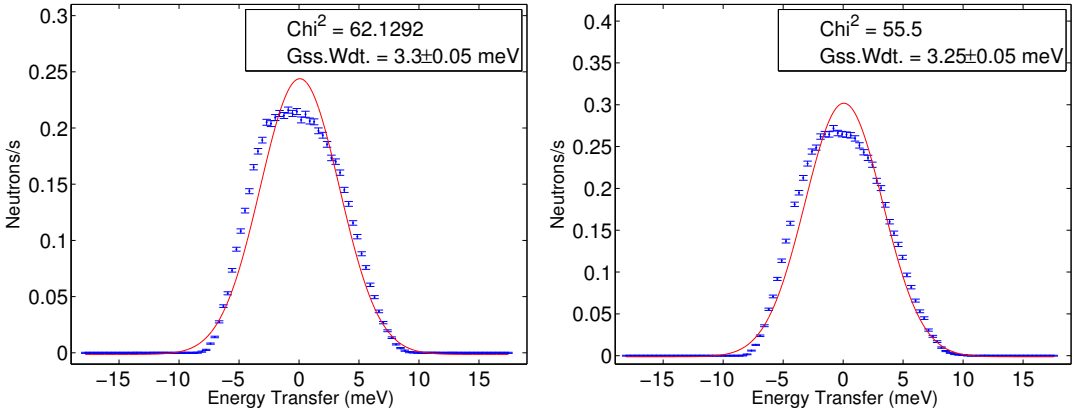

Figure 4.1.2: A virtual experiment with an elastically scattering sample, fitted to a Gaussian. Left: 180 m sample distance. Right: 300 m sample distance. The bin size is 0.36 meV and the initial energy is 82 meV.

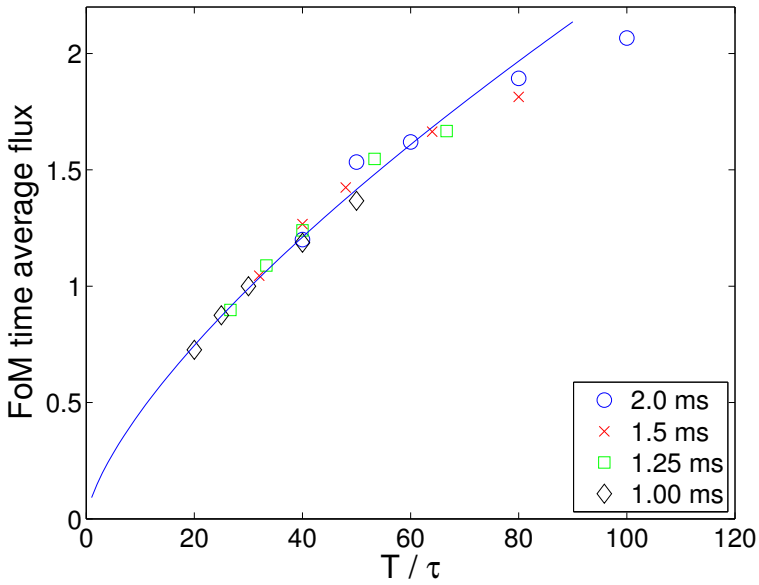

Figure 4.2.1: Average Figure-of-Merit for the generic ESS instrument suite at different time structures, plotted as a function of the inverse source duty cycle, under the assumption of constant time-average flux. Diamonds, squares, crosses, and circles represent pulse lengths of 2.0, 1.5, 1.25, and 1.0 ms, respectively. The solid line is a fit to a power law.

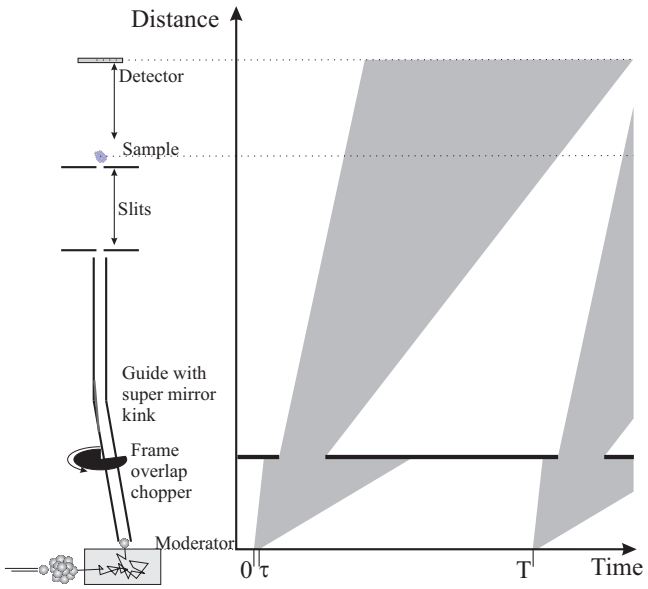

Figure 4.2.2: Left: Sketch of the main elements of the long SANS instrument. Details are not to scale. Right: Time-of-flight diagram illustrating the selection of wavelength band by choppers, with the spectrometer running in the (20 + 20) m setting.

values of the duty cycle τ/T. Hence, our result meant that the ESS was free to choose the time structure from accelerator/moderator technical considerations, without constraints from instrumentation requirements. Our work is documented in the article *Simulation of a suite of generic long-pulse instrument to optimise the time structure of the European Spallation Source*[4].

I performed a large part of the simulations in this article by taking care of the two chopper spectrometers and the 3 SANS instruments. I here show an interesting part of the simulations for the 20 m long SANS instrument, which is sketched in figure 4.2.2.

Apart from the flux number at sample, we investigated from where the neutrons reaching the sample originated at the moderator surface, in this guide system which is straight/curved and starts 1.5 m from the moderator. The results for the shortest collimation length (1 m pinhole collimation and 1 m between sample and detector) and the longest collimation length (10 m and 10 m) are shown in figure 4.2.3.

We see that at the best collimation, the useful area of the moderator has a diameter of only 2 cm. This means that this SANS instrument could increase its performance if the moderator flux could be increased locally in a "hot spot", e.g. by making a groove in the moderator surface[80]. A similar result was found for the 100 m cold-neutron chopper spectrometer, although the beneficial area here was a square 4×4 cm^2.

Details of the simulations I performed in the time structure work is reprinted in the report *Simulation of a suite of generic long-pulse neutron instruments to optimise the time structure of the ESS accelerator* and the attached "one-pager sheets", in the appendix.

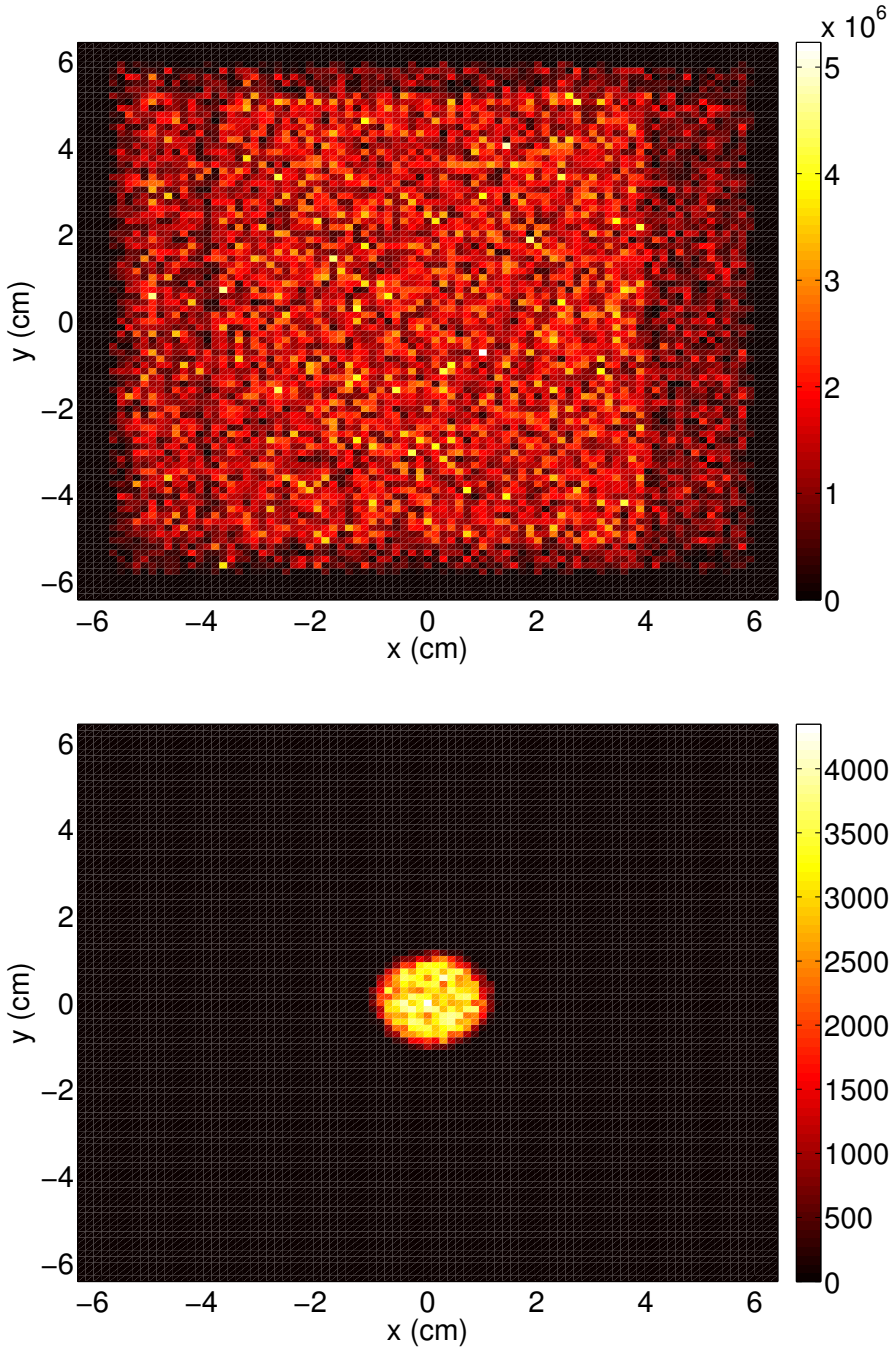

Figure 4.2.3: Simulated plots of the moderator surface showing the number of neutrons which reach the sample for the 20 m SANS instrument, as described in the text. The results are valid for any time structure. Top: Data for 2 m collimator-detector setting. Bottom: Data for 20 m collimator-detector setting.

4.3. A Bio-SANS Instrument for ESS

In 2012, I participated in the Danish-Swiss group that produced an official proposal for a bio-SANS instrument for ESS. My role was to perform many of the simulations and optimisations of the instrument, and the work is documented in the ESS instrument construction proposal[7] and in two articles[5, 6], all reprinted in the appendix.

The aim of the proposed instrument was to design a SANS that was optimised for biological experiments. This means an optimisation for flux and bandwidth, whereas the λ (or q) resolution of the instrument is of less importance. According to equations 1.4.2 and 1.4.3, this suggests that the instrument should be made as short as possible. Since the necessary bandwidth and frame-overlap choppers must be placed outside the biological shielding of the target monolith, 6 m from the moderator, we came to the conclusion that the shortest practical moderator-sample distance was 12 m. However, due to requirements of secondary shielding outside the monolith, it was later decided to change this length to 16 m.

Our original proposal contained a monochromating chopper option that could turn the SANS instrument to a low-energy-resolution spectrometer. This would mean that incoherent inelastic background from (primarily) water could be recognised and discarded. However, this would compromise the flux at the sample position so much that while it would increase the signal-to-noise ratio, the reduced statistics meant that the same resolution could be measured in less time without this chopper system. As a result, in the subsequent article on the proposal, we have omitted the inelastic option, after consultation with the ESS SANS Scientific and Technical Advisory Panel. However, the details of the inelastic SANS instrument are of interest for spectroscopy as such, which has led us to write another manuscript on this topic. Below I briefly present these two papers.

4.3.1. A classical ToF bio-SANS instrument

The instrument is 16 + 4 = 20 m long from source to detector, and has a 2×2 cm^2 9.9 m straight guide which has been curved in the horizontal plane with a radius of curvature of 280 m, designed to transport neutrons with wavelengths at 3 Å or above. This takes it twice out of LoS, i.e. the point there the LoS from the source is broken cannot be seen from the sample position, and allows for a minimum of 13.6 m of shielding to block any straight line from the source to the sample. These shielding considerations are due to concerns about fast neutrons from the spallation process and the instrument being rather short for an ESS instrument. The motivation for making a short instrument is that it allows for a broad q-range of up to 0.0080-2.02 Å^{-1}, which makes it possible to perform a full experiment using only one setting.
The collimation system uses pinhole collimation, is up to 4 m long, and is placed 10 cm before the sample.
The mechanical chopper system uses 2 bandwidth definition choppers to select the required bandwidth, and 3 resolution choppers to improve the wavelength resolution using wavelength frame multiplication[81, 82]. The positions and opening times of the choppers are given in table 4.3.1. The resolution chopper system is designed as a compromise between the higher resolution chopper system presented in [6] and the

	Source chopper distance	chopper openings [ms]			
1_{st} fr. over. chop.	6.5 m	6.36-27.71			
2_{nd} fr. over. chop.	9.5 m	8.91-39.44			
1_{st} res. imp. chop.	7 m	6.7-7.45	8.16-9.12	9.89-11.15	11.96-29.62
2_{nd} res. imp. chop.	10 m	9.26-10.18	11.35-12.42	13.83-15.16	16.78-41.4
3_{rd} res. imp. chop.	12 m	10.97-12	13.48-14.61	16.45-17.83	19.99-49.25

Table 4.3.1: Sample source distances and opening times for the various choppers used with the bio-SANS instrument.

need to allow more flux to reach the sample position.
Figure 4.3.1 shows the layout of the instrument. Figure 4.3.2 shows a schematic view of the curved guide and the brilliance transfer through the guide as a function of wavelength, which shows excellent transmission above 3 Å and a good cutoff for lower wavelengths.

In a virtual experiment, using a model of an isotropically scattering water sample, the instrument shows a gain of a factor of 20 in counting statistics over a wide q-range, using the 2 m collimation setting which allows a wavelength range of 3-18 Å, compared to the D22 instrument at the ILL using a velocity selector set to 4.5 Å, as shown in figure 4.3.3.

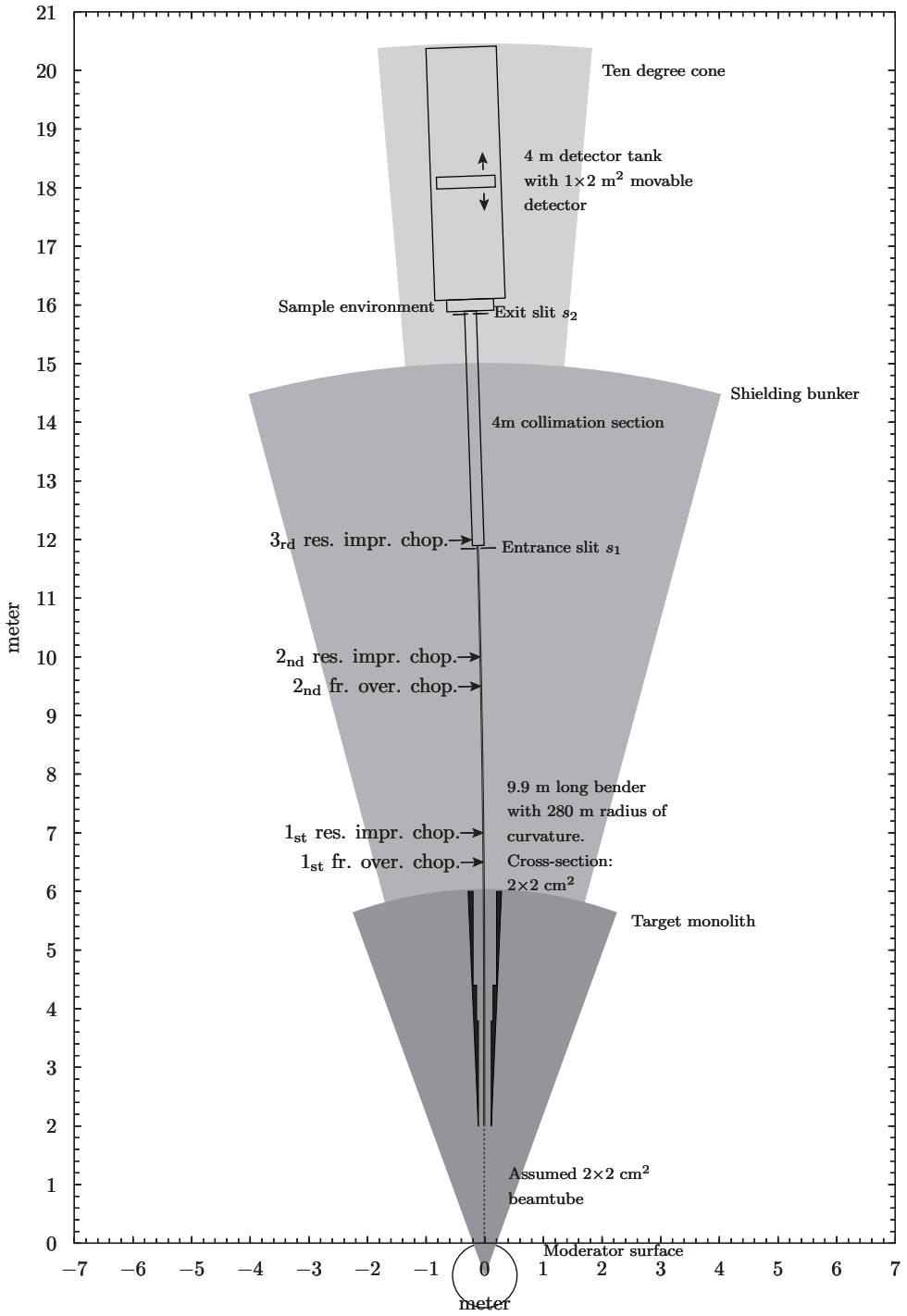

Figure 4.3.1: Schematic drawing of the Bio-SANS instrument. The source is at the bottom, with the moderator face at (0,0). The curved guide is shown as a line and the grey areas denote different sections of shielding. The positions of the choppers, collimation section, sample environment, and detector tank are indicated on the drawing.

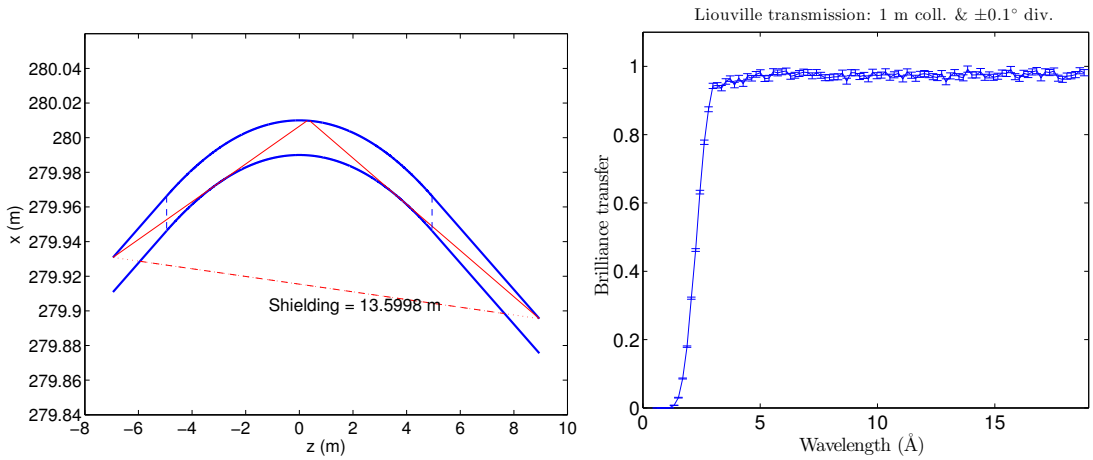

Figure 4.3.2: **Left:** Diagram showing the transport section with the bender and collimation section (blue) and line of sight from the moderator and sample positions (red). Since the two red lines do not overlap, line of sight is blocked twice. The dashed red line shows the direct line through the transport system that must penetrate the minimum amount of shielding. The moderator is at the left end of the transport system, and the sample position at the right end. The origin of the coordinate system is the centre of the bender circle. Note that the scale on the axes differ. **Right:** Brilliance transfer from source to sample as a function of wavelength within the phase space of 5×5 mm^2 and a 0.1° radial divergence, with the resolution choppers turned off and 1 m collimation length. As the transport section is designed for wavelengths of 3 Å or above, there is a steep cutoff below 3 Å.

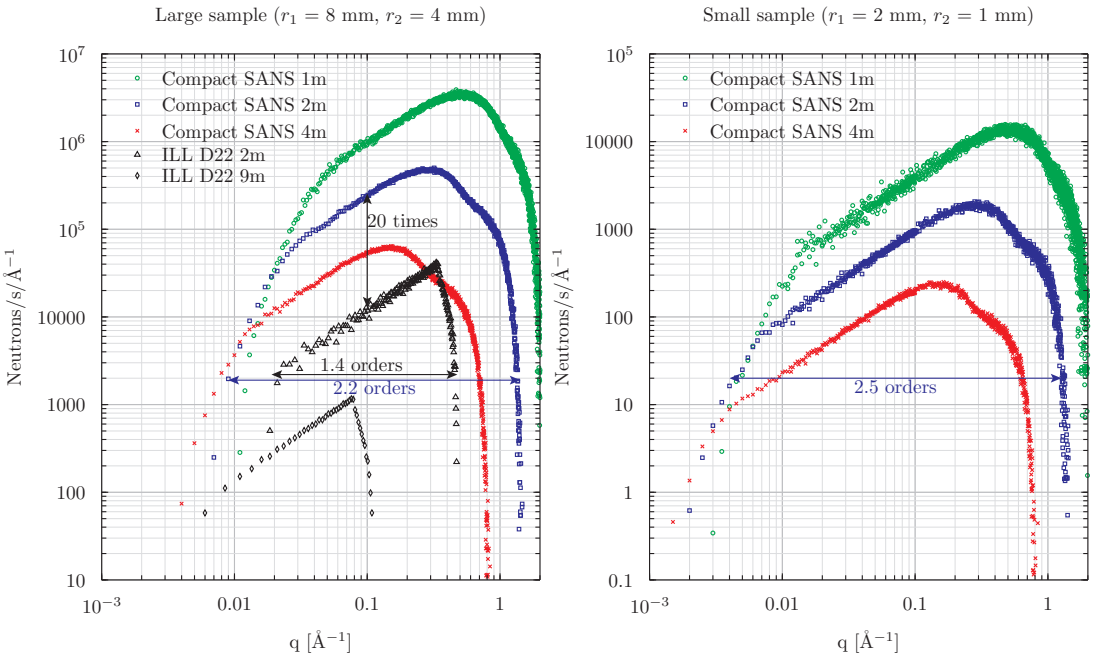

Figure 4.3.3: Monte Carlo simulation of instrument performance measured in neutrons reaching the detector per second per Å^{-1} as a function of q. The sample is a simple model of the isotropic scattering from 1 mm of H_2O. The wavelength range is 3.0-18.9 Å for the 1 m setting, 3.0-18.0 Å for the 2 m setting, and 3.0-16.5 Å for the 4 m setting. The D22 measurement has the velocity selector set to 4.5 Å.

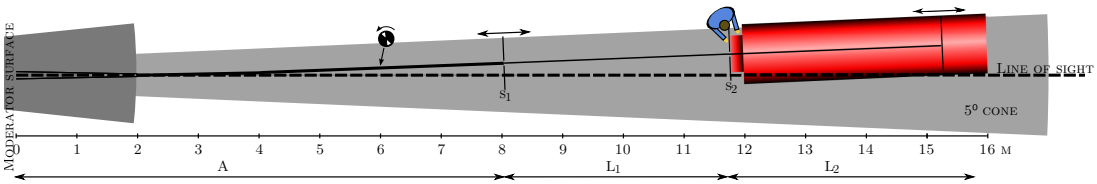

Figure 4.3.4: Schematic drawing of the proposed instrument. The source is on the left side, with the moderator face at 0. The kinked guide is shown as a solid line and the grey areas denote different sections of shielding. The positions of the choppers, slits, and detector tank are indicated on the drawing.

4.3.2. An ToF SANS spectrometer

We here present the inelastic option for the compact SANS instrument in our original proposal for the ESS. The instrument is quite similar to that presented in the previous section, except that the moderator-sample length here is the original value of 12 m. The layout of the instrument is shown in figure 4.3.4. We note the pulse-shaping chopper at 6 m and a monochromating chopper just before the sample, while the bandwidth choppers are omitted. The system uses the principles of repetition rate multiplication[16, 17, 15] and wavelength frame multiplication[81, 82] with $\Delta\lambda = 5.9$ Å. The resulting ToF diagram is shown in figure 4.3.5.

We show that by using the inelastic option with pulse-shaping and monochromating, we lose a factor 160 in flux compared to only having the frame overlap chopper running. Experiments at the PSI have shown that when scattering from water, the chopper system could realistically reduce the background by a factor 2-3. However, the instrument is certainly able to resolve low-energy, low-q scattering as shown in figure 4.3.6, which is the result of a virtual experiment on a phonon sample with the - extremely small - dispersion 1 meV Å, using an incoming neutron wavelength of 10 Å and a collimation-detector length of 1 m. The $q, \hbar\omega$ range of this instrument is to a large extent covered by cold-neutron chopper spectrometers, and will be of use only for special science cases where very small q's are needed. Hence, it is not likely to be among the first build for ESS.

Figure 4.3.7 shows the $\hbar\omega/q$ coverage of the instrument using a 4 m collimation distance and an ingoing wavelength of $\lambda_i = 10$ Å, compared with the lower limit of a typical cold chopper spectrometer using respectively $\lambda_i = 5$ Å and $\lambda_i = 10$ Å. The blue area to the left of the red curve is the area where the instrument will offer new possibilities. However it can be seen that much of this falls within the instrumental resolution, so it would have to be improved for the instrument to be useful.

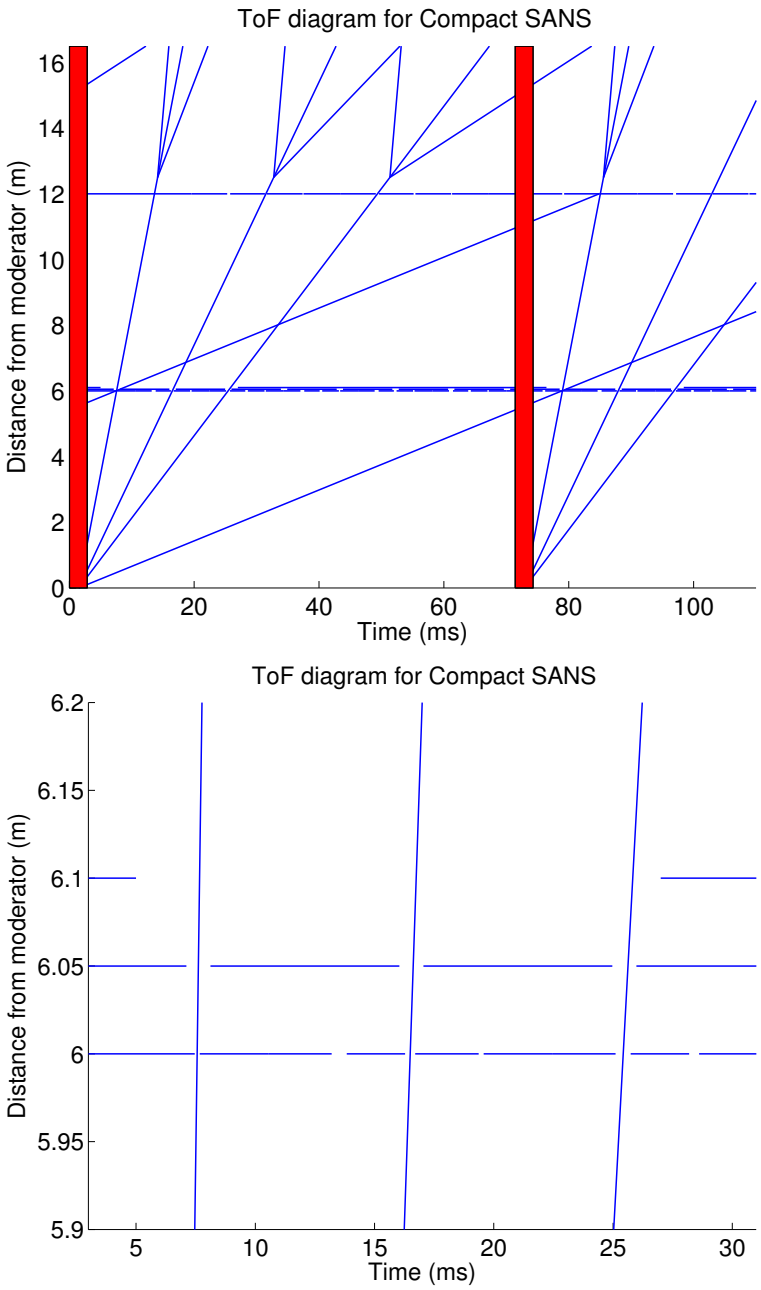

Figure 4.3.5: Top: Time of flight diagram of the chopper system of the ToF SANS spectrometer, with rays of 4.00, 9.89, and 15.78 Å neutrons going through, and the prompt pulse indicated in red. A long wavelength ray is seen that can get through the pulse shaping chopper system at 6 m, but is eliminated by the monochromating chopper at 12 m. Bottom: Closeup of the pulse shaping chopper system. At 6 m the pulse shaping chopper is placed, with 3 openings of variable sizes at the 0°, 90°, and 180° positions and moving at 6 times the pulse frequency, f. At 6.05 m the contaminant removal chopper is placed, with one opening and turning with 4/3 the speed of the pulse shaping chopper, i.e. $8f$. At 6.1 m the frame overlap chopper is placed, which defines the bandwidth. This chopper has one opening and moves with the source frequency.

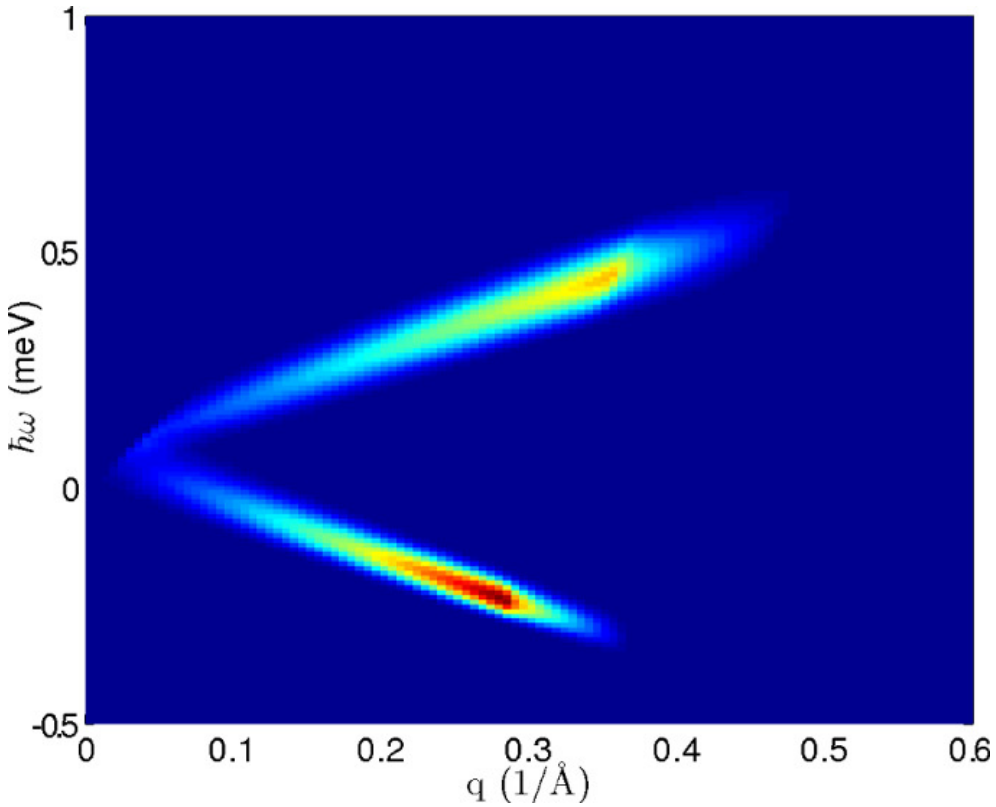

Figure 4.3.6: Results of virtual experiments with a phonon sample using the 10 Å peak and the resolution chopper set to a 75 μs opening. With a 1 m collimation distance and 1 m detector distance.

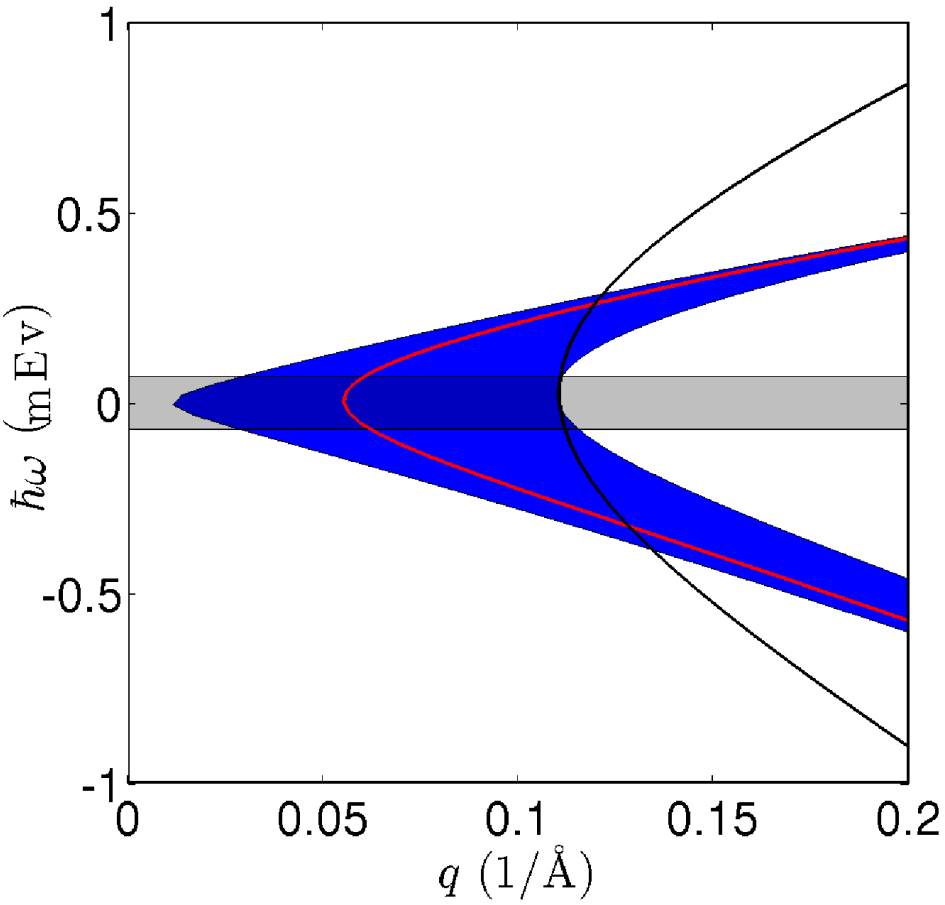

Figure 4.3.7: Calculation of the $\hbar\omega/q$ space that can be covered by the instrument. Blue: The instrument set in 4 m collimation mode, with the wavelength of the ingoing neutrons set to $\lambda_i = 10$ Å. Red: The lower limit for a cold chopper spectrometer with a scattering angle of $2\theta = 5°$ and $\lambda_i = 10$ Å. Black: The lower limit for a cold chopper spectrometer with $2\theta = 5°$ and $\lambda_i = 5$ Å. The shaded bars denote the width of the instrumental resolution.

5. Conclusion, Summary, and Discussion

In this thesis, I have investigated the need for and the possible use of long neutron guides for instruments at the ESS. The underlying assumption behind all the results presented is that my simulation models built with the McStas software gives correct and reliable results. I am confident that this assumption is valid, as McStas has been exhaustively tested and validated by comparisons both with other neutron simulation software and physical experiments, by - amongst others - Uwe Filges, Klaus Lieutenant, Peter Willendrup, and Emmanuel Farhi. I have also participated in such a test myself, where my results from McStas were confirmed by identical results by Klaus Lieutenant using VITESS[1].

In the following I will summarise my main results and discuss their implications:

Brilliance Transfer

Together with fellow simulators in the ESS group, I have defined the concept of brilliance transfer, which measures the guide transport properties relative to the maximally allowed by Liouville's Theorem. By this concept, it has been possible to quantify the quality of specific guide systems on a more detailed level than earlier, where guide simulators used merely the transported flux. This has now become a popular method in the community for presenting results of guide simulations.

Properties of Expanding Guide Systems.

In a common effort with the VITESS simulation group, we have optimised three different types of expanding guide systems: ballistic (or linear tapering), elliptic, and parabolic. By means of the brilliance transfer concept, we have quantified their transport properties for varying guide lengths, wavelengths, and divergences and found that elliptic and parabolic shapes behave almost equally. This can be understood by the observation that elliptic guides, due to the finite source and sample sizes, function more like guides than as optical focusing elements[51]. The implications for the ESS is that guide systems need not be constrained to be a supermirror focusing system by the elliptical or parabolic geometry, but can be tweaked to accommodate other considerations without sacrificing the brilliance transfer. These considerations could be focusing the beam down to fit in a small chopper window for a bandwidth definition chopper before transporting the beam the full length of the instrument, or to allow for breaking the line of sight. I expect that this flexibility is of critical importance, as a realistic guide would likely need to accommodate several such considerations.

As a by-product of this work, we were able to perform a cross-comparison between the McStas and VITESS packages to a much more detailed level than earlier.

Long Guides

Due to the long-pulse structure of the ESS, long guides are needed to achieve a good

wavelength resolution without using pulse shaping choppers. However the feasibility of long guides raised some concern, as they have never been built on the length needed by the ESS. I have investigated the transport properties of long guides and found that both elliptic and parabolic guide can achieve a high brilliance transfer and an acceptable phase space smoothness, even over very long distances and for highly divergent, thermal neutrons. This is an important result for ESS instrumentation, because it makes long instruments realistic. Long instruments makes it possible to 'focus' the bandwidth to allow a shorter wavelength range to have a higher flux at equal resolution, than would be possible with a short instrument.

The models I started out using for long guides were simplified models that did not take into account the non-idealities and constraints which I have expanded on below.

Non-ideal Guide Conditions

Relating to issues of how to construct long guide systems, I have investigated how real-world complications like misalignment and mirror waviness impact the transport properties. I have found that the long elliptic guide systems are robust to changes within realistic building constraints of 0.1° waviness and 50 μm of misalignment. However, it is recommended to open up the transported phase space slightly, as this makes the guide less susceptible to imperfections. Though this will of course need to be balanced against the need for background reduction.

During my investigations into waviness, a bug was discovered in the way McStas implements waviness. However this bug only affects simulations results of neutrons with divergences on the same order as the waviness value used. Therefore I consider the results presented in this thesis to be valid despite this.

In the misalignment study I began with the elliptical guide models I have used for my other work. These are composed of a number of straight guide segments of varying length, which allow for a good approximation of an ellipse for most purposes. However when studying misalignment, I found that this gave incorrect results when validated against a more realistic guide model constructed of equidistant 0.5 m long segments. With this more realistic model, I am confident of the results of the misalignment study.

Line of Sight

In spallation sources like the ESS, the fast neutrons produced by the proton beam will create a background signal that can travel down the guide channel. Therefore, it is desirable to avoid line of sight between the neutron source and the sample, something which conversations with ESS staff has revealed to be of high concern. I have investigated three methods for eliminating line of sight: curvature along the gravitational flight path, curving a parabolic or elliptic guide in the horizontal plane, and blocking the line of sight with a centrally placed beamstop. All can successfully block line of sight and all are useful in certain situations from a brilliance transfer perspective, but I expect that using a parabolic guide with a curved section in the centre will be the most commonly used method for long guides, because this gives a lower divergence

beam that can more easily be manipulated to allow breaking line of sight twice and allow spacing for large amounts of shielding.

This is an important result, as it goes a long way towards making expanding guide systems more feasible. It is of significant importance for the ESS, as the ESS reference instrument suite[14] contains 9 long instruments (> 100 m), 7 medium long instruments (~ 75 m), and 6 relatively short instruments (< 50 m), and the method of removing line of sight by curving the guide will almost certainly be used for the long instruments, and likely be used for the medium length instruments and possibly for some of the short instruments. As the question of line of sight is key to the shielding requirements, and as the shielding is a major driver of the cost of the ESS, this is a topic that warrants considerable study.

The ESS Instrument Suite

In the Copenhagen simulation group, we have used the elliptic guide concept to simulate an early version of the ESS instrument suite, many of which were simulated by me. By optimising the guide systems for a number of time structure parameters for the ESS source, we have quantified how different instrument types are affected by changes in the ESS time structure, as we found that the figure of merit for the instrument suite is proportional to $\left(\frac{T}{\tau}\right)^{0.3}$. This gave the ESS management important information in comparing the performance of the instrument suite with that of the accelerator and target for different time structures. This formed the basis for the decision change the time structure from the values of $T = 60$ ms and $\tau = 2$ ms used at the time of the this study, to the current values of $T = 71$ ms and $\tau = 2.86$ ms.

An Inelastic SANS Instrument for the ESS

As a part of the Danish-Swiss collaboration on instrument design for ESS, I have simulated and optimised a SANS instrument with an option for inelastic discrimination using an advanced system of mechanical choppers. This is a novel concept for SANS instruments, and would in theory allow for much more accurate measurements on samples with a high inelastic background. However, the inelastic option was later decided not to be included in the final instrument construction proposal, as my simulations showed it to be unfeasible because of the high cost in flux: Although experiments indicated that the proposed chopper system would be able to increase the signal to noise ratio for water samples by a factor 2-3, the loss in flux meant that the same resolution could be measured in less time without this chopper system, using the higher counting statistics. While the proposed chopper system would have allowed the instrument to resolve the inelastic scattering, there are doubts as to whether this presents enough of a science case to justify building it.

Another aspect to the ability to resolve inelastic scattering is that it could be used not just to cancel out the inelastic background, but to use the instrument for spectroscopy. This would allow for a much shorter spectrometer than are currently envisioned for the ESS, with an excellent q-range, but with a comparatively poor resolution.

Finally

As a final comment, I will summarise that ray-tracing simulations have been found to be extremely useful for the planning and design of the ESS, and I have made an important contribution in exploring the usefulness of elliptic guides and determining the feasibility of long guide.

Outlook

The field of neutron optics simulations is continually evolving, with the focus on more realistic simulations. A major step in this direction would be the inclusion of background and shielding considerations, as the current models assume that an absorbed neutron simply disappears. Including a proper nuclear physics treatment of the neutron in the neutron optics simulation models, would allow design and optimisation of guides for both transport and background reduction. Work on the implementation of this is currently undergoing at the Technical University of Denmark.

The bug we discovered in the implementation of waviness in McStas is currently being worked on, and when the new waviness model is ready it would be useful to investigate the effects of waviness on guides designed to transport phase spaces with a very low divergence area.

My study on misalignment only includes stochastic misalignment. Another study on systematic misalignment caused by e.g. ground motion should be done to quantify the tolerance of long guides to this.

When comparing different guide options for specific instruments, it would be useful in the future to include the above imperfections in the simulations, as this might favour less elegant but more robust guide designs.

The elliptic guide model I have created has inspired the design of a more accurate and computationally efficient model by Henrik Carlsen and Mads Bertelsen, which is currently being tested by the Copenhagen group. This holds promise to be highly useful not just in investigating elliptic guide, but also to model more complicated combinations of geometries.

One aspect of guide design I have not had time to investigate is the performance of a double ellipse, i.e. one ellipse following another, which is a concept that has some popularity in the community. Using the new model mentioned above, this has become much easier to do and should be investigated thoroughly.

My results show that fairly wide elliptic guides are optimal for brilliance transport. However this conflicts with the desire to have a narrow beam to better accommodate choppers, which makes such guides unrealistic for many instruments. One solution to this is to have an initial focusing section that narrows down the beam to the chopper, followed by a long guide for the transport.

Building on the methods I have used in this work, a generalised and automated guide optimisation tool is being developed by Mads Bertelsen, which holds promise to greatly speed up future work of this kind.

Another aspect that should be investigated further is the optimisation of supermirror coating, as this can be a major factor in the brilliance transfer and cost of a neutron guide. Such a project I expect to become significantly easier to complete, once the more efficient elliptic guide model is fully ready to use.

It is my opinion that the field of neutron guide study for the ESS has now reached a level of maturity, that detailed simulations and optimisations of specific instruments with demanding guide requirements should proceed.

Acknowledgements

First of all I would like to thank my supervisors, Kim Lefmann and Ken Andersen, for all their help and advice.

Secondly I would like to thank the people at SwissNeutronics and the ESS for providing data and answering questions, without which this thesis could not have been made.

I would like to thank all the guys and girls in the office, who have provided sparring on a daily basis.

I would like to thank all my colleagues around the world, for providing insights and inspiration over the years.

I would like to thank the people involved in the Danish-Swiss ESS instrumentation group for their collaboration in the work on the Compact SANS instrument.

Robert Feidenhans'l for providing help during my PhD, and for convincing me to embark on this project after a bottle of schnapps at the institute Christmas lunch.

Lastly I would like to thank my friends and family for support and patience during this last period of my PhD, where I have been quite busy. Most importantly I want to thank Louise for unwavering support and excellent proofreading.

References

[1] Kaspar Hewitt Klenø, Klaus Lieutenant, Ken H. Andersen, and Kim Lefmann. Systematic performance study of common neutron guide geometries. *Nuclear Instruments and Methods in Physics Research Section A: Accelerators, Spectrometers, Detectors and Associated Equipment*, 696(0):75 – 84, 2012.

[2] Kaspar Hewitt Klenø and Kim Lefmann. Thermal Chopper Spectrometer for the European Spallation Source. *Journal of the Physical Society of Japan*, 80:SB004, 2011.

[3] Kaspar H. Klenø, Peter K. Willendrup, Erik Knudsen, and Kim Lefmann. Eliminating line of sight in elliptic guides using gravitational curving. *Nuclear Instruments and Methods in Physics Research Section A: Accelerators, Spectrometers, Detectors and Associated Equipment*, 634(1, Supplement):S100 – S103, 2011. Proceedings of the International Workshop on Neutron Optics NOP2010.

[4] Kim Lefmann, Kaspar H Klenø, Jonas Okkels Birk, Britt R Hansen, Sonja L Holm, Erik Knudsen, Klaus Lieutenant, Lars von Moos, Morten Sales, Peter K Willendrup, et al. Simulation of a suite of generic long-pulse neutron instruments to optimize the time structure of the European Spallation Source. *Review of Scientific Instruments*, 84(5):055106–055106, 2013.

[5] K H Klenø, S Kynde, G Nagy, N Skar-Gislinge, K Mortensen, K Lefmann, J Kohlbrecher, and L Arleth. A Compact Time-of-Flight SANS Instrument Optimised for Measurements of Small Sample Volumes at the European Spallation Source. *Journal of Applied Crystallography*, 2013 (submitted).

[6] Kaspar Hewitt Klenø, Kim Lefmann, and Kell Mortensen. A Small Angle Pulsed Neutron Spectrometer. 2013 (in progress).

[7] K H Klenø, S Kynde, G Nagy, N Skar-Gislinge, K Mortensen, K Lefmann, J Kohlbrecher, and L Arleth. ESS Instrument Construction Proposal Compact SANS Optimised for Biological Samples. Technical report, European Spallation Source, March 2013.

[8] Kim Lefmann, Uwe Filges, Sonja L. Holm, Kaspar H. Klenø Erik Knudsen, Klaus Lieutenant, Lars von Moos, Morten Sales, and Peter K. Willendrup. Simulation of a suite of generic long-pulse neutron instruments to optimize the time structure of the ESS accelerator. Technical report, European Spallation Source, October 2010.

[9] Homepage of the MAX IV facility: www.maxlab.lu.se/maxiv, 2013.

[10] European Spallation Source website: www.esss.se, 2013.

[11] James Chadwick. Possible existence of a neutron. *Nature*, 129(3252):312, 1932.

[12] Stephane Groueff and Ralph E Lapp. Manhattan Project: The untold story of the making of the atomic bomb. *Physics Today*, 20:59, 1967.

[13] Gösta Ekspong. *Nobel Lectures in Physics 1991-1995*. World Scientific Publishing Company, 1997.

[14] S. Peggs and et. al. ESS Technical Design Report. Technical report, European

Spallation Source, April 2013.

[15] Kim Lefmann, Helmut Schober, and Feri Mezei. Simulation of a multiple-wavelength time-of-flight neutron spectrometer for a long-pulsed spallation source. *Measurement Science and Technology*, 19(3):034025, 2008.

[16] F Mezei. The raison detre of long pulse spallation sources. *Journal of Neutron Research*, 6(1):3–32, 1997.

[17] F Mezei, M Russina, and S Schorr. The multiwavelength cold neutron time-of-flight spectrometer project IN500 at LANSCE. *Physica B: Condensed Matter*, 276:128–129, 2000.

[18] Herman Kahn. Applications of Monte Carlo. Technical report, 1956.

[19] John RD Copley. Monte Carlo calculation of multiple scattering effects in thermal neutron scattering experiments. *Computer physics communications*, 7(6):289–317, 1974.

[20] DFR Mildner and JM Carpenter. Multiple scattering correction to neutron diffraction data of isotropic systems using optimized Monte Carlo techniques. *Acta Crystallographica Section A: Crystal Physics, Diffraction, Theoretical and General Crystallography*, 33(6):954–961, 1977.

[21] Kim Lefmann and K Nielsen. McStas, a general software package for neutron ray-tracing simulations. *Neutron News*, 10/3:20–23, 1999.

[22] Homepage of the McStas software: www.mcstas.org, 2013.

[23] Peter Willendrup, Emmanuel Farhi, Uwe Filges, and K Lefmann. User and Programmers Guide to the Neutron Ray-Tracing Package McStas. Technical report, 2012.

[24] Erik Knudsen, Linda Udby, Peter Kjær Willendrup, Kim Lefmann, and WG Bouwman. McStas-model of the delft SESANS. *Physica B: Condensed Matter*, 406(12):2361–2364, 2011.

[25] Lev Davidovich Landau and Evgenii Mikhailovich Lifshitz. *Statistical physics*, volume 5. Butterworth-Heinemann, 1951.

[26] Josiah Willard Gibbs. *Elementary principles in statistical mechanics: developed with especial reference to the rational foundation of thermodynamics*. Cambridge University Press, 2010.

[27] Henrik Jacobsen, Klaus Lieutenant, Carolin Zendler, and Kim Lefmann. Bi-spectral extraction through elliptic neutron guides. *Nuclear Instruments and Methods in Physics Research Section A: Accelerators, Spectrometers, Detectors and Associated Equipment*, 2013.

[28] F. Mezei and M. Russina. Neutronenoptische Bauelementenanordnung zur gezielten 242 spektralen Gestaltung von Neutronenstrahlen oder Pulsen. *Patent Germany Amtl. Aktz.*, 102 03 591 (2002), 2002.

[29] F. Mezei and M. Russina. Neutron-optical component array for the specific spectral shaping of neutron beams or pulses. *Patent US*, 7030397 B2 (2006), 2006.

[30] C. Zendler, K. Lieutenant, D. Nekrassov, L.D. Cussen, and M. Strobl. Bi-spectral

beam extraction in combination with a focusing feeder. *Nuclear Instruments and Methods in Physics Research Section A: Accelerators, Spectrometers, Detectors and Associated Equipment*, pages 1–8, December 2012.

[31] K. Lieutenant, J. Peters, and F. Mezei. Monte Carlo simulation of the new time-of-flight powder diffractometer EXED at the Hahn-Meitner-Institut. *Journal of Neutron Research*, 14(2):147–165, 2006.

[32] Phillip M Bentley and Ken H Andersen. Accurate simulation of neutrons in less than one minute Pt. 1: Acceptance diagram shading. *Nuclear Instruments and Methods in Physics Research Section A: Accelerators, Spectrometers, Detectors and Associated Equipment*, 602(2):564–573, 2009.

[33] JRD Copley. Acceptance diagram calculations of the performance of neutron removal mirrors. *Nuclear Instruments and Methods in Physics Research Section A: Accelerators, Spectrometers, Detectors and Associated Equipment*, 659(1):403–410, 2011.

[34] P. M. Bentley, S. J. Kennedy, K. H. Andersen, D. M. Rodriguez, and D. F. R. Mildner. Correction of Optical Aberrations in Elliptic Neutron Guides. *ArXiv e-prints*, January 2012.

[35] DFR Mildner. Acceptance diagrams for curved neutron guides. *Nuclear Instruments and Methods in Physics Research Section A: Accelerators, Spectrometers, Detectors and Associated Equipment*, 290(1):189–196, 1990.

[36] Albert-José Dianoux and GH Lander. *Neutron data booklet*. Old City Philadelphia, 2003.

[37] Peter Böni. personal communication, 2006-2013.

[38] H. Maier-Leibnitz and T. Springer. The use of neutron optical devices on beam-hole experiments on beam-hole experiments. *Journal of Nuclear Energy. Parts A/B. Reactor Science and Technology*, 17(4-5):217 – 225, 1963.

[39] F. Mezei. Novel polarized neutron devices: supermirror and spin component amplifier. *Communications on Physics*, 1:81 – 85, 1976.

[40] Peter Böni. Supermirror-based beam devices. *Physica B: Condensed Matter*, 234-236(0):1038 – 1043, 1997. Proceedings of the First European Conference on Neutron Scattering.

[41] Otto Schrpf. Thin-film devices and their role in future neutron spectroscopic investigations. *Physica B: Condensed Matter*, 174(14):514 – 527, 1991.

[42] Charles F Majkrzak and John F Ankner. Supermirror neutron guide coatings. *Proc. SPIE Neutron Optical Devices and Applications*, 1738, 1992.

[43] Th Krist, C Pappas, Th Keller, and F Mezei. The polarizing beam splitter guide at BENSC. *Physica B: Condensed Matter*, 213:939–941, 1995.

[44] Benedicte Ballot, Francois J Samuel, and Bernard Farnoux. Supermirror neutron guide. In *San Diego'92*, pages 159–165. International Society for Optics and Photonics, 1992.

[45] VG Syromyatnikov, AF Schebetov, and ZN Soroko. Fe Al neutron polarizing supermirror on a Si crystal substrate with antireflecting Cd layer. *Nuclear Instru-*

ments and Methods in Physics Research Section A: Accelerators, Spectrometers, Detectors and Associated Equipment, 324(1):401–403, 1993.

[46] O Elsenhans, P Böni, HP Friedli, H Grimmer, P Buffat, K Leifer, J Söchtig, and IS Anderson. Development of Ni/Ti multilayer supermirrors for neutron optics. *Thin Solid Films*, 246(1):110–119, 1994.

[47] SwissNeutronics, December 2010.

[48] F Mezei and M Russina. Neutron beam extraction and delivery at spallation neutron sources. *Physica B: Condensed Matter*, 283(4):318 – 322, 2000.

[49] Jochen Stahn. A neutron polariser based on magnetically remanent Fe/Si supermirrors, 2006. Slides of a talk given at the Institut Laue-Langevin, Grenoble, January 18th.

[50] Hartmut Abele, D Dubbers, H Häse, M Klein, A Knöpfler, M Kreuz, T Lauer, B Märkisch, D Mund, V Nesvizhevsky, et al. Characterization of a ballistic supermirror neutron guide. *Nuclear Instruments and Methods in Physics Research Section A: Accelerators, Spectrometers, Detectors and Associated Equipment*, 562(1):407–417, 2006.

[51] L.D. Cussen, D. Nekrassov, C. Zendler, and K. Lieutenant. Multiple reflections in elliptic neutron guide tubes. *Nuclear Instruments and Methods in Physics Research Section A: Accelerators, Spectrometers, Detectors and Associated Equipment*, 705(0):121 – 131, 2013.

[52] Kaspar Hewitt Klenø. Simulating Neutron Guides for the European Spallation Source. Master's thesis, Niels Bohr Institute, Copenhagen, Denmark, 2008.

[53] Christian Schanzer, Peter Böni, Uwe Filges, and Thomas Hils. Advanced geometries for ballistic neutron guides. *Nuclear Instruments and Methods in Physics Research Section A: Accelerators, Spectrometers, Detectors and Associated Equipment*, 529(1-3):63 – 68, 2004. Proceedings of the Joint Meeting of the International Conference on Neutron Optics (NOP2004) and the Third International Workshop on Position-Sensitive Neutron Detectors (PSND2004).

[54] T Hils, P Boeni, and J Stahn. Focusing parabolic guide for very small samples. *Physica B: Condensed Matter*, 350(1):166–168, 2004.

[55] Garrett E Granroth, David H Vandergriff, and Stephen E Nagler. SEQUOIA: A fine resolution chopper spectrometer at the SNS. *Physica B: Condensed Matter*, 385:1104–1106, 2006.

[56] Stefanus Harjo, Takashi Kamiyama, Shuki Torii, Toru Ishigaki, and Masao Yonemura. The Ibaraki prefecture materials design diffractometer for J-PARCDesigning neutron guide. *Physica B: Condensed Matter*, 385:1025–1028, 2006.

[57] Ryoichi Kajimoto, Mitsutaka Nakamura, Toyotaka Osakabe, Taku J Sato, Kenji Nakajima, and Masatoshi Arai. Study of converging neutron guides for the cold neutron double-chopper spectrometer at J-PARC. *Physica B: Condensed Matter*, 385:1236–1239, 2006.

[58] Sebastian Mühlbauer, Martin Stadlbauer, Peter Böni, Christan Schanzer, Jochen

Stahn, and Uwe Filges. Performance of an elliptically tapered neutron guide. *Physica B: Condensed Matter*, 385:1247–1249, 2006.

[59] MV Gubarev, BD Ramsey, DE Engelhaupt, JM Burgess, and DFR Mildner. An evaluation of grazing-incidence optics for neutron imaging. *Nuclear Instruments and Methods in Physics Research Section B: Beam Interactions with Materials and Atoms*, 265(2):626–630, 2007.

[60] Peter Böni. New concepts for neutron instrumentation. *Nuclear Instruments and Methods in Physics Research Section A: Accelerators, Spectrometers, Detectors and Associated Equipment*, 586(1):1–8, 2008.

[61] P Kudejova, G Meierhofer, K Zeitelhack, J Jolie, R Schulze, A Türler, and T Materna. The new PGAA and PGAI facility at the research reactor FRM II in Garching near Munich. *Journal of radioanalytical and nuclear chemistry*, 278(3):691–695, 2008.

[62] S Mühlbauer, PG Niklowitz, M Stadlbauer, R Georgii, P Link, J Stahn, and P Böni. Elliptic neutron guides focusing on tiny samples. *Nuclear Instruments and Methods in Physics Research Section A: Accelerators, Spectrometers, Detectors and Associated Equipment*, 586(1):77–80, 2008.

[63] Ryoichi Kajimoto, Kenji Nakajima, Mitsutaka Nakamura, Kazuhiko Soyama, Tetsuya Yokoo, Kenichi Oikawa, and Masatoshi Arai. Study of the neutron guide design of the 4SEASONS spectrometer at J-PARC. *Nuclear Instruments and Methods in Physics Research Section A: Accelerators, Spectrometers, Detectors and Associated Equipment*, 600(1):185–188, 2009.

[64] Hiroshi Arima, Kazuki Komatsu, Kazuaki Ikeda, Katsuya Hirota, and Hiroyuki Kagi. Designing an elliptical supermirror guide for the high-pressure material science beamline of J-PARC. *Nuclear Instruments and Methods in Physics Research Section A: Accelerators, Spectrometers, Detectors and Associated Equipment*, 600(1):71–74, 2009.

[65] JC Cook. Design and estimated performance of a new neutron guide system for the NCNR expansion project. *Review of Scientific Instruments*, 80(2):023101–023101, 2009.

[66] Richard M Ibberson. Design and performance of the new supermirror guide on HRPD at ISIS. *Nuclear Instruments and Methods in Physics Research Section A: Accelerators, Spectrometers, Detectors and Associated Equipment*, 600(1):47–49, 2009.

[67] PG Niklowitz, C Pfleiderer, S Mühlbauer, P Böni, T Keller, P Link, JA Wilson, M Vojta, and JA Mydosh. New angles on the border of antiferromagnetism in NiS2 and URu2Si2. *Physica B: Condensed Matter*, 404(19):2955–2960, 2009.

[68] M Janoschek, P Böni, and M Braden. Optimization of elliptic neutron guides for triple-axis spectroscopy. *Nuclear Instruments and Methods in Physics Research Section A: Accelerators, Spectrometers, Detectors and Associated Equipment*, 613(1):119–126, 2010.

[69] B Khaykovich, MV Gubarev, Y Bagdasarova, BD Ramsey, and DE Moncton. From x-ray telescopes to neutron scattering: Using axisymmetric mirrors to focus

a neutron beam. *Nuclear Instruments and Methods in Physics Research Section A: Accelerators, Spectrometers, Detectors and Associated Equipment*, 631(1):98–104, 2011.

[70] DFR Mildner and MV Gubarev. Wolter optics for neutron focusing. *Nuclear Instruments and Methods in Physics Research Section A: Accelerators, Spectrometers, Detectors and Associated Equipment*, 634(1):S7–S11, 2011.

[71] J Stahn, T Panzner, U Filges, C Marcelot, and P Böni. Study on a focusing, low-background neutron delivery system. *Nuclear Instruments and Methods in Physics Research Section A: Accelerators, Spectrometers, Detectors and Associated Equipment*, 634(1):S12–S16, 2011.

[72] Damian Martin Rodriguez, Shane J Kennedy, and Phillip M Bentley. Properties of elliptical guides for neutron beam transport and applications for new instrumentation concepts. *Journal of Applied Crystallography*, 44(4):727–737, 2011.

[73] Andreas Houben, Werner Schweika, Thomas Brückel, and Richard Dronskowski. New neutron-guide concepts and simulation results for the POWTEX instrument. *Nuclear Instruments and Methods in Physics Research Section A: Accelerators, Spectrometers, Detectors and Associated Equipment*, 2012.

[74] J Stahn, U Filges, and T Panzner. Focusing specular neutron reflectometry for small samples. *The European Physical Journal Applied Physics*, 58(01), 2012.

[75] M. Sanchez del Rio, editor. *Neutron instrument simulation and optimization using the software package VITESS*. SPIE, 2004.

[76] Ursula B. Hansen. personal communication, 2013.

[77] Antonio Perillo-Marcone. D11 waviness measurements. personal communication, 2011.

[78] Peter Allenspach, Peter Böni, and Kim Lefmann. Loss Mechanisms in Supermirror Neutron Guides. *Proc. SPIE*, 4509, 2001.

[79] K. Batkov, A. Takibayev, L. Zanini, and F. Mezei. Unperturbed moderator brightness in pulsed neutron sources. *Nuclear Instruments and Methods in Physics Research Section A: Accelerators, Spectrometers, Detectors and Associated Equipment*, 2013.

[80] D.J. Picton, S.M. Bennington, T.A. Broome, and T.D. Beynon. Design options for coupled cold moderators on a low power spallation source. *Nuclear Instruments and Methods in Physics Research Section A: Accelerators, Spectrometers, Detectors and Associated Equipment*, 545(12):363 – 374, 2005.

[81] Ferenc Mezei and Margarita Russina. Multiplexing chopper systems for pulsed neutron source instruments. In *International Symposium on Optical Science and Technology*, pages 24–33. International Society for Optics and Photonics, 2002.

[82] K. Lieutenant and F. Mezei. Monte Carlo simulations of a powder diffractometer installed on a long pulse target station using wavelength frame multiplication. *Journal of Neutron Research*, 14(2):177–191, 2006.

A. List of Publications

The publications I have contributed to are listed here and ordered after publication date, with the newest first. The publications are listed with their title, authors, and abstract. All are published, unless otherwise stated.

All the publications are appended to this thesis in the order they are listed here, except from the ESS Technical Design Report, due to the length of this. It can be accessed on the ESS website at:
http://europeanspallationsource.se/scientific-technological-documentation

A.1. First author papers that are a part of this thesis

A Small Angle Pulsed Neutron Spectrometer

Kaspar Hewitt Klenø, Kim Lefmann, and Kell Mortensen, in progress

This paper will detail the chopper system used in the original construction proposal of the Compact SANS instrument for the ESS, and how it allows the instrument to be used as a spectrometer despite its short source-sample distance.

My contribution: I have designed the guide and collimation system, performed all the simulations, most of the analytical work, and written most of the paper.

A Compact Time-of-Flight SANS Instrument Optimised for Measurements of Small Sample Volumes at the European Spallation Source

Kaspar Hewitt Klenø, Søren Kynde, Gergely Nagy, Kell Mortensen, Kim Lefmann, Joachim Kohlbrecher, and Lise Arleth, submitted to Journal of Applied Crystallography.

The high flux at European Spallation Source (ESS) will allow for performing experiments with relatively small beam-sizes while maintaining a high intensity of the incoming beam. The long pulsed nature of the source makes the facility optimal for time-of-flight small-angle neutron scattering (ToF-SANS). We find that a relatively compact SANS instrument becomes the optimal choice in order to obtain the widest possible q-range in a single setting, the best possible exploitation of the neutrons and hence obtaining the highest possible flux at the sample position. The instrument proposed in the present article is optimised for performing fast measurements of small sample volumes, typically down to $2 \times 2 \times 2$ mm^3, while covering a q-range from about 0.005 1/Å to 0.5 1/Å in a single instrument setting. This q-range corresponds to that available at a typical good BioSAXS instrument and is relevant for a wide set of biomacromolecular samples. A central advantage of covering the whole q-range in a single setting is that each sample has to be loaded only once. This makes it convenient to use the fully automated high-throughput flow-through sample changers commonly applied at modern synchrotron BioSAXS-facilities. The central drawback of choosing a very compact instrument is that the resolution in terms of $\Delta\lambda/\lambda$ becomes significantly worse than what is usually the standard at state-of-the-art SANS instruments. Our McStas based simulations of the instrument performance for a set of characteristic biomacromolecular samples show that the smearing effects still have relatively minor

effects on the obtained data and can be compensated for in the data analysis. However, in cases where a better resolution is required in combination with the large simultaneous q-range characteristic of the instrument, we show that this can be obtained by inserting a set of choppers.

My contribution: I have designed the guide and collimation system, performed all the instrument simulations, some of the analytical work, and written about half of sections 2 and 4 and most of section 3.

ESS Instrument Construction Proposal Compact SANS Optimised for Biological Samples

K. Klenø, S. Kynde, G. Nagy, N. Skar-Gislinge, K. Mortensen, K. Lefmann, J. Kohlbrecher, L. Arleth, 2013.

Formal and detailed instrument construction proposal, submitted to the ESS instrument division and the Scientific and Technical Advisory Panel.

My contribution: I have designed the guide and collimation system, performed all the instrument simulations, some of the analytical work, and written most of sections 3 and 5.

Systematic Performance Study of Common Neutron Guide Geometries

K. H. Klenø, K. Lieutenant, K. Andersen, and K. Lefmann, Nuclear Instruments and Methods in Physics Research Section A, 696, 75-84,2013.

In this paper, we present the results from a systematic benchmarking of 4 different long neutron guide geometries: elliptic, parabolic, ballistic (piecewise linearly focusing/defocusing), and straight, for various wavelength, divergence restriction, and guide length settings. In this work, we mapped relevant parts of the neutron phase space to show where advanced guide geometries have significant transport advantages over simple guide geometries. The primary findings are that the elliptic and parabolic geometries perform almost equally well, and they are considerably superior to the other geometries, except for low-divergence, cold neutrons. In addition, it was observed that transporting thermal neutrons more than 100 m using elliptic guides was possible with only a 10 percent loss in the phase space density for divergences up to ± 0.5 degrees, which enables the construction of very long thermal neutron instruments. Our work will allow instrument designers to use tabulated, standard geometries as a starting point for optimising the guide required for the particular instrument.

My contribution: I have done half the work in developing the conceptual basis for the paper, performed most of the simulations, all of the analytical work, and written the entire paper except section 3.

Thermal Chopper Spectrometer for the European Spallation Source

Kaspar Hewitt Klenø and Kim Lefmann, Journal of the Physical Society of Japan, 80, SB004, 2011.

One of the instruments being considered for the ESS is a thermal chopper spectrometer, intended for the study of lattice vibrations and magnetic excitations. However, as the ESS will be a long pulsed source, we propose a very long instrument (180 m - 300 m). We here present a guide system that can achieve a flux of 3.47×10^8 n/s/cm^2 and a resolution of $\frac{dE}{E} = 5.3$ % for 1 Å neutrons on the sample with a transport efficiency of 80%. Furthermore, we demonstrate the efficiency of the instrument using a virtual experiment measuring an elastic line width.

My contribution: With some help from my coauthor, I have done most of the work in developing the conceptual basis for the paper, performed all of the simulations, all of the analytical work, and written the entire paper.

Eliminating line of sight in elliptic guides using gravitational curving

Kaspar H. Klenø, Peter K. Willendrup, Erik Knudsen, and Kim Lefmann, Nuclear Instruments and Methods in Physics Research Section A, 634, S100-S103, 2010.

Eliminating fast neutrons ($\lambda < 0.5$ Å) by removing direct line of sight between the source and the target sample is a well established technique. This can be done with little loss of transmission for a straight neutron guide by horizontal curving. With an elliptic guide shape however, curving the guide would result in a breakdown of the geometrical focusing mechanism inherent to the elliptical shape, resulting in unwanted reflections and loss of transmission.

We present a new and yet untried idea by curving a guide in such a way as to follow the ballistic curve of a neutron in the gravitational field, while still retaining the elliptic shape seen from the accelerated reference frame of the neutron. Analytical calculations and ray-tracing simulations show that this method is useful for cold neutrons at guide lengths in excess of 100 m.

We will present some of the latest results for guide optimization relevant for instrument design at the ESS, in particular an off-backscattering spectrometer which utilizes the gravitational curving, for 6.66 Å neutrons over a guide length of 300 m.

My contribution: With some help from my coauthors, I have done most the work in developing the conceptual basis for the paper, performed all of the simulations, all of the analytical work, and written the entire paper.

A.2. Coauthor papers that are a part of this thesis

Simulation of a suite of generic long-pulse neutron instruments to optimize the time structure of the ESS

Kim Lefmann, Kaspar H. Klenø, Jonas Okkels Birk, Britt R. Hansen, Sonja L. Holm, Erik Knudsen, Klaus Lieutenant, Lars von Moos, Morten Sales, Peter K. Willendrup, and Ken H. Andersen, Review of Scientific Instruments, Review of Scientific Instruments, 84, 55106-55106, 2013

We here describe the result of simulations of 15 generic neutron instruments for the long-pulsed European Spallation Source (ESS). All instruments have been simulated

for 20 different settings of the source time structure, corresponding to pulse lengths between 1 ms and 2 ms; and repetition frequencies between 10 Hz and 25 Hz. The relative change in performance with time structure is given for each instrument, and an unweighted average is calculated. The performance of the instrument suite is proportional to a) the peak flux and b) the duty cycle to a power of approx. 0.3. This information is an important input to determining the best accelerator parameters. In addition, we find that in our simple guide systems, most neutrons reaching the sample originate from the central 3-5 cm of the moderator. This result can be used as an input in later optimization of the moderator design. We discuss the relevance and validity of defining a single Figure-of- Merit for a full facility and compare with evaluations of the individual instrument classes.

My contribution: I have performed the simulations for 7 of the 15 instruments investigated, compiled the tables used in the paper, some of the figures used, and developed the 'hotspot' simulations.

Simulation of a suite of generic long-pulse neutron instruments to optimize the time structure of the ESS accelerator

Kim Lefmann, Uwe Filges, Sonja L. Holm, Kaspar H. Klenø, Erik Knudsen, Klaus Lieutenant, Lars von Moos, Morten Sales, and Peter K. Willendrup, Technical report for the ESS, October 2010.

We here describe the result of simulations of 16 generic neutron instruments for the long-pulsed European Spallation Source. All instruments have been simulated for 17 different settings of the accelerator time structure, corresponding to pulse lengths between 1 ms and 2 ms; and repetition frequencies between 10 Hz and 25 Hz. The relative change in performance with accelerator settings is given for each instrument, and an unweighted average is calculated. In combination with estimations of flux numbers for the different accelerator settings, this can be used to obtain the best accelerator parameters. In addition, the effect of a hot spot on the moderator is calculated, which will be used to optimize the moderator design.

My contribution: I have performed some or all of the simulations for 9 of the 16 instruments investigated, compiled the tables used in the paper, developed the 'hotspot' simulations, and written some or all of 9 of the attached 'one pagers'.

A.3. Papers not included as a part of this thesis

This sections lists publications that should not be evaluated by the thesis committee, but are listed here in the interest of comprehensiveness as I have made contributions to them during my PhD project.

Simulations of Chopper Jitter at the LET Neutron Spectrometer at the ISIS TS2

Kaspar Hewitt Klenø, K Lefmann, P K Willendrup, P Christiansen, and R Bewley, accepted for publication by Journal of Neutron Research.

The effect of uncertainty in chopper phasing (jitter) has been investigated for the

high-resolution time-of-flight spectrometer LET at the ISIS second target station. The investigation is carried out using virtual experiments, with the neutron simulation package McStas, where the chopper jitter is found to cause a Lorentzian tail in the resolution function. We find that jitter up to the unrealistic value of 2 μs can be tolerated without any noticeable degradation of resolution or incident intensity. The results are supported by simple analytical estimates and are believed to be general for chopper spectrometers.

ESS Technical Design Report

S. Peggs et. al., April 2013, European Spallation Source

Official ESS report, forming the technical basis for deciding to fund the ESS construction. The report lists the scientific case for the ESS, details the proposed instruments, and gives a technical review of the proposed ESS accelerator, target station, and support facilities. NOTE: This is not appended to this thesis, due to the length.

Optimal shape of a cold-neutron triple-axis spectrometer

K. Lefmann, U. Filges, F. Treue, J.J.K. Kirkensgård, B. Plesner, K.S. Hansen, K.H. Klenø, Nuclear Instruments and Methods in Physics Research Section A, 634, S1-S6, 2010

We have performed a McStas optimization of the primary spectrometer for a generic 40 m long, cold-neutron triple-axis spectrometer with a doubly focusing monochromator. The optimal design contains an elliptically focusing guide, a virtual source point before a low-grade PG monochromator, and non-equidistant focusing at the monochromator. The flux at 5 meV shows a gain factor 12 over the classical design with a straight $3 \times 12cm^2$, $m = 2$ guide and a vertically focusing PG monochromator. In addition, the energy resolution was found to be improved. This unexpectedly large design improvement agrees with the Liouville theorem and can be understood as the product of many smaller gain factors, combined with a more optimal utilization of the beam divergence within the guide. Our results may be relevant for a possible upgrade of a number of cold-neutron triple-axis spectrometersand for a possible triple-axis spectrometer at the European Spallation Source.

Virtual experiments: the ultimate aim of neutron ray-tracing simulations

K. Lefmann, P. K. Willendrup, L. Udby, B. Lebech, K. Mortensen, J. O. Birk, K. Klenø, E. Knudsen, P. Christiansen, J. Saroun, J. Kulda, U. Filges, M. Konnecke, P. Tregenna-Piggott, J. Peters, K. Lieutenant, G. Zsigmond, P. Bentley & E. Farhi, Journal of Neutron Research, 16, 97-111, 2008.

We define a virtual neutron experiment as a complete simulation of an experiment, from source over sample to detector. The virtual experiment (VE) will ideally interface with the instrument control software for the input and with standard data analysis packages for the virtual data output. Virtual experiments are beginning to make their way into neutron scattering science with applications as diverse as instrument

design/upgrade, experiment planning, data analysis, test of analysis software, teaching, and outreach. In this paper, we summarize the recent developments in this field and make suggestions for future developments and use of VEs.

A Small Angle Pulsed Neutron Spectrometer

K. Klenø[1], K. Lefmann[1], and K. Mortensen[1]
[1]*Nanoscience Center, Niels Bohr Institute, University of Copenhagen, Denmark*

1 Introduction

The European Spallation Source (ESS) [1] will be the first long-pulsed spallation neutron source built. This has spawned a wealth of ideas for novel instrumentation concepts [11, 14, 7], and more are still to be evaluated. This paper presents a concept for adding spectrometer capabilities to a compact small-angle neutron scattering (SANS) instrument, and discusses which additional value it will add to the facility.

The compact SANS instrument is envisioned for high throughput studies of biological and soft matter. Its standard mode of operation is the high flux mode, fully utilising the high flux pulse produced by the ESS. Due to the short distance from the source this gives rise to relatively poor resolution in terms of $\frac{\delta\lambda}{\lambda}$ on the instrument, but for typical biological macromolecules, this is acceptable with the resulting gain in flux. This type of the instrument was recently proposed as a day-one instrument for ESS [6, 5]. This paper is based on the original proposal from October 2012 of an instrument with a 12.5 m sample distance, not the revised proposal from February 2013.

A second mode of operation is the "SANS spectrometer mode". Here a series of choppers are used to "monochromatise" and shape the incoming pulse. This improves the energy and q-resolution of the instrument considerably, although with a trade off in flux. The rationale behind this option is twofold: a) to lower the inelastic background, *e.g.* from water, and b) to open up for spectroscopic studies in the low-angle region.

This article presents the spectrometer mode of operation for a TOF SANS instrument. First, we briefly summarize the general setup of the instrument as proposed for ESS, including the High Flux operation mode. Then, we present the Chopped SANS operation mode. Finally, we discuss the merits and usefulness of the spectrometer mode, including SANS (Brillouin) spectroscopy and the possibility to suppress inelastic incoherent background in the elastic SANS signal.

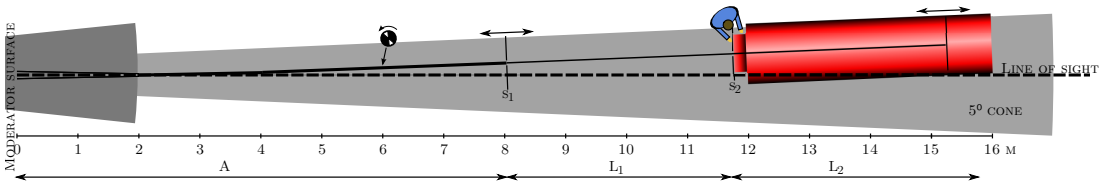

Figure 1: *Schematic drawing of the proposed instrument. (The dimensions are to scale.)*

2 Basic Instrument Layout

The proposed instrument consists of an initial transport section, a chopper system, a collimation section, a sample environment, and a detector tank. See figure 1. In this chapter we describe the general layout of the instrument, while the chopper system will be described in the following chapter.

2.1 Transport Section

Beginning at the moderator surface, the first two meters of the transport section is a channel through the shielding of the moderator. The width of the channel is 12 cm × 12 cm at the moderator surface narrowing down to 4 cm × 4 cm at the guide entrance, 2 m from the moderator. The first guide section is 2 m long and has a cross-section of 4 cm × 4 cm. It has an angle of 1.15° relative to the beamtube from the moderator. Hence, we denote it the "kinked" section. The next section is 4.4 m long and is placed in an angle of 2.3°. In effect, the direct line of sight from the moderator is blocked by this kink. The guide coating used is m=4.2 in the kink and m=2.1 for the remainder of the guide. These values were obtained by requiring that 3 Å neutrons with a divergence low enough to be accepted by the collimation system can be reflected through the guide. The simulations detailed in section 4 show that these values give an excellent transmission through the guide across a wide bandwidth. Note that these coating values will have to be finally optimised based on the reflectivity of the coating available at the time of construction. The optimisation should balance the transmission of the low wavelength neutrons in the most relaxed collimation mode. This requires a high m-value, while higher wavelength neutrons will benefit from a lower m-value coating due to a higher reflectivity.

2.2 Collimation Section

The 4 m long collimation section starts at 8.4 m from the moderator surface and consists of four 1 m elements. Each element can be exchanged with extra guide

sections allowing for collimation lengths of 4 m, 3 m, 2 m, or 1 m. KASPAR: Er det nødvendigt med guides: kollimeringen tager vel neutronerne alligevel? The extra guides are inserted vertically to make room for maximal shielding on the sides. The two defining slits are circular and denoted s_1 and s_2 as indicated on figure 1. For the standard setup, the slit radii are set to 8 mm and 4 mm.

2.3 Detector Tank

The detector tank is 4 m long and has room for a 1 m $\times$ 1 m detector, with a pixel size of 5×5 mm^2. The detector is movable so that the sample-detector distance can vary between 1 m and 4 m.

2.4 Performance of Time-of-Flight SANS

In the following L denotes the full length of the instrument from moderator to detector, A is the distance from the moderator to the collimator and L_1 is the collimation length. $A + L_1$ is 12.4 m in the proposed setup. The sample-detector distance is denoted L_2. The radii of the pinhole apertures are denoted s_1 and s_2.

We consider three settings of $L_1 = L_2 = 1$ m, $L_1 = L_2 = 2$ m and $L_1 = L_2 = 4$ m.

Using the conversion factor α=252.7 µs/Å/m between neutron wavelength [Å] and inverse velocity [µs/m], the basic equation for neutron time-of-flight (TOF) reads:

$$t = \alpha L \lambda. \tag{1}$$

The uncertainty in λ is

$$\delta\lambda = \frac{\tau}{L\alpha}, \tag{2}$$

where $\tau = 2.86$ ms is the pulse width at ESS and L is the total instrument length from moderator surface to detector. The width of the wavelength band is

$$\Delta\lambda = \lambda_{\text{max}} - \lambda_{\text{min}} = \frac{T - \tau}{L\alpha}, \tag{3}$$

where $T = 1/14$ Hz $= 71.4$ ms is the moderator period at the ESS. The minimum wavelength used is always $\lambda_{\text{min}} = 3$ Å and the maximum wavelength is calculated from (3). In table 1, we show the values of $\delta\lambda/\lambda$ and $\Delta\lambda$ for characteristic settings and wavelengths.

2.5 Introduction to simulations

The instrument performance has been calculated with Monte Carlo ray-tracing simulations. We have built an model of the ESS time-of-flight SANS spectrometer

Instrument length: $L = A + L_1 + L_2$	$\delta\lambda/\lambda$ @ 4 Å	$\delta\lambda/\lambda$ @ 8 Å	$\delta\lambda/\lambda$ @ 12 Å	Bandwidth [Å] $\Delta\lambda$
13=11+1+1	21%	11%	7%	20.8
14=10+2+2	20%	10%	7%	19.3
16=8+4+4	17%	9%	6%	16.9

Table 1: *Calculated wavelength resolutions for the SANS spectrometer at different values of colllimation lengths and wavelengths.*

with the package McStas [8]. Simulations were performed on the 1000-node computer cluster of the ESS Data Management and Software Center [2]. Typical runs required ?? CPU hours for the guide simulations and ?? CPU hours for the full inelastic simulations.

3 Time-of-flight SANS spectroscopy

In the following, we will sketch and discuss considerations on the inelastic option for the ESS Compact SANS, while the simulations of this option will be performed in section 4.

The principal idea behind the chopped SANS option is to be able to discriminate between inelastically and elastically scattered neutrons, thus reducing the inelastic background of the SANS signal.Adding a flexible pulse shaping chopper system will allow for improved q and E resolution on demand[4]. The chopper layout is very similar to that used for chopper spectrometers. The resulting instrument could be used for small-angle spectroscopy (Brillouin scattering) as well. In order to evaluate the applicability of this spectroscopy mode in combination with small angle scattering, the predicted instrument performance could be compared to the BRISP instrument at ILL (Grenoble) [3].

3.1 Discrimination of Inelastic Scattering

For the inelastic option, we need to determine independently the initial and final energy (or wavelength). In the direct geometry, this is done by pulsing the beam at a position just before the sample, using a set of choppers. These choppers generate a number of bursts of neutrons with different wavelengths within one time frame (the repetition-rate multiplication - RRM - principle[9, 11, 13]).

We denote the primary flight time before the chopper t_1, and the secondary flight time t_2, corresponding to the primary and secondary flight lengths $L_1 + A = 12.5$ m and $L_2 = 4$ m. Using (1), we can then deduce λ_1 and λ_2.

We will here consider mostly the option of $L_2 = 4$ m, since this is the most optimal for discriminating inelastically scattered neutrons.

The Secondary Neutrons

The most desired effect of this instrument mode is to be able to discriminate the elastic scattering of cold neutrons from the inelastic scattering due to (in particular) water at ambient temperatures. This inelastic scattering will most often be a thermalisation process (in this case an energy gain), resulting in neutrons of wavelengths around $\lambda_f = 2$ Å, depending on sample thickness.

The sub-frame for each burst must hence contain the faster neutrons. Since the energy gain scattering is compressed into a short time, the intensity peak will be fairly close to a secondary flight time of $t_2 = 0$. This value we then take as the starting point of the time frame.

As for the slower neutrons (energy loss scattering), the longest secondary flight time is in principle infinite. In chopper spectroscopy, one often uses a cut-off around twice the wavelength of the incoming neutrons, as the intensity beyond that becomes very weak. Doing this would ensure that this SANS instrument can be used for true inelastic experiments as well (dynamics of large structures in polymers, biology, or magnetism).

The slowest secondary neutrons we possibly need to consider are in this case the 53.2 Å ones, where $t_2 = 53.8$ ms. Since this fills out almost the whole time frame, we need to compromise somewhat, as will be discussed below. We here also discuss a few possibilities for designing this timing and the corresponding chopper system.

Constant Burst Time of Monochromating Chopper

We start by discussing the most simple scheme, where the bursts are identical and equidistant in time. We place the monochromating chopper system shortly before the sample position, at $A + L_1 - L_{\mathrm{MS}}$, where the monochromator-sample length is $L_{\mathrm{MS}} = 0.5$ m. This system consists of one chopper with one opening in front of the sample, which rotates with a frequency of $f_{\mathrm{m}} = n_{\mathrm{m}} f_{\mathrm{ESS}}$, where n_{m} is an integer.

Using a t_2 of more than 30 ms would allow only two bursts in each frame, which is on the low side when balancing inelastic discrimination with the desire for a broad wavelength range and a high flux. Hence, we could compromise to use 3 bursts at the detector position. However, we need to take care of the longer secondary flight times of the later pulses. Hence, the closest solution is $n_{\mathrm{m}} = 4$, where we block the 4th burst by a slow chopper, as shown in Fig. 2. This would give $t_2 = T/n_{\mathrm{m}} = 17.9$ ms and a difference between the incoming wavelengths of 5.89 Å, in this case 4.00, 9.89, and 15.78 Å. As seen in figure 2, the blocking

λ_1	E_1	τ_1	τ_2	$\delta\lambda_1/\lambda_1$	δE_1	δE_2	δE
4.00 Å	5.11 meV	2.86 ms	950 μs	23.6%	2.41 meV	2.41 meV	3.41 meV
9.89 Å	0.84 meV	2.86 ms	950 μs	9.5%	160 μeV	160 μeV	226 μeV
15.78 Å	0.33 meV	2.86 ms	950 μs	6.0%	39 μeV	39 μeV	56 μeV

Table 2: *Key numbers and results for the constant burst time option with no pulse shaping.*

of the last pulse gives sufficient time for the slowest neutrons from the longest wavelength pulse. With these wavelengths, none of the elastic lines will overlap with possible contaminants from the prompt pulse, as seen in figure 2.

We use the three wavelengths mentioned above for examples of the calculations of this mode, although this is of course only one specific choice. The results of these calculations are shown in table 2 and are discussed below.

Since the neutron energy is $E \sim \lambda^{-2}$, we can relate the relative uncertainties (to first order):

$$\frac{\delta E}{E} = 2\frac{\delta\lambda}{\lambda}. \tag{4}$$

The energy resolution is also calculated and mentioned in Table 2.

In this example, we use the full pulse of the source, $\tau_1 = \tau$. Hence, the wavelength resolution of the incoming neutrons, $\delta\lambda$, is given directly by (2).

We denote the opening time (FWHM) of the monochromating chopper by τ_2 and calculate the resolution of the outgoing wavelength using the general equation (2). When we require that the incoming and outgoing resolutions must match for the elastic line ($\lambda_1 = \lambda_2$), we find $\delta\lambda_1 = \delta\lambda_2$, or

$$\tau_2 = \tau_1\frac{L_2}{A + L_1} = \frac{\tau}{3} = 950\,\mu\text{s}. \tag{5}$$

As we see in Table 2, the energy resolutions match for all three wavelengths simultaneously. However, the energy resolution for in particular the 4 Å wavelength neutrons is relatively coarse.

Estimating the intensity, the monochromating chopper is open in total 2.8 ms, or around 4% of the time frame. Hence, in rough terms we lose around a factor 25 in flux compared to the standard SANS instrument.

3.2 Improving Resolution by a Pulse Shaping Chopper

To improve the energy resolution, we insert a pulse shaping chopper at $L_{\text{ps}} = 6$ m from the source. Instead of having just a single burst per frame, as for the long ESS instruments, this chopper will burst once for each of the 3 wavelengths we

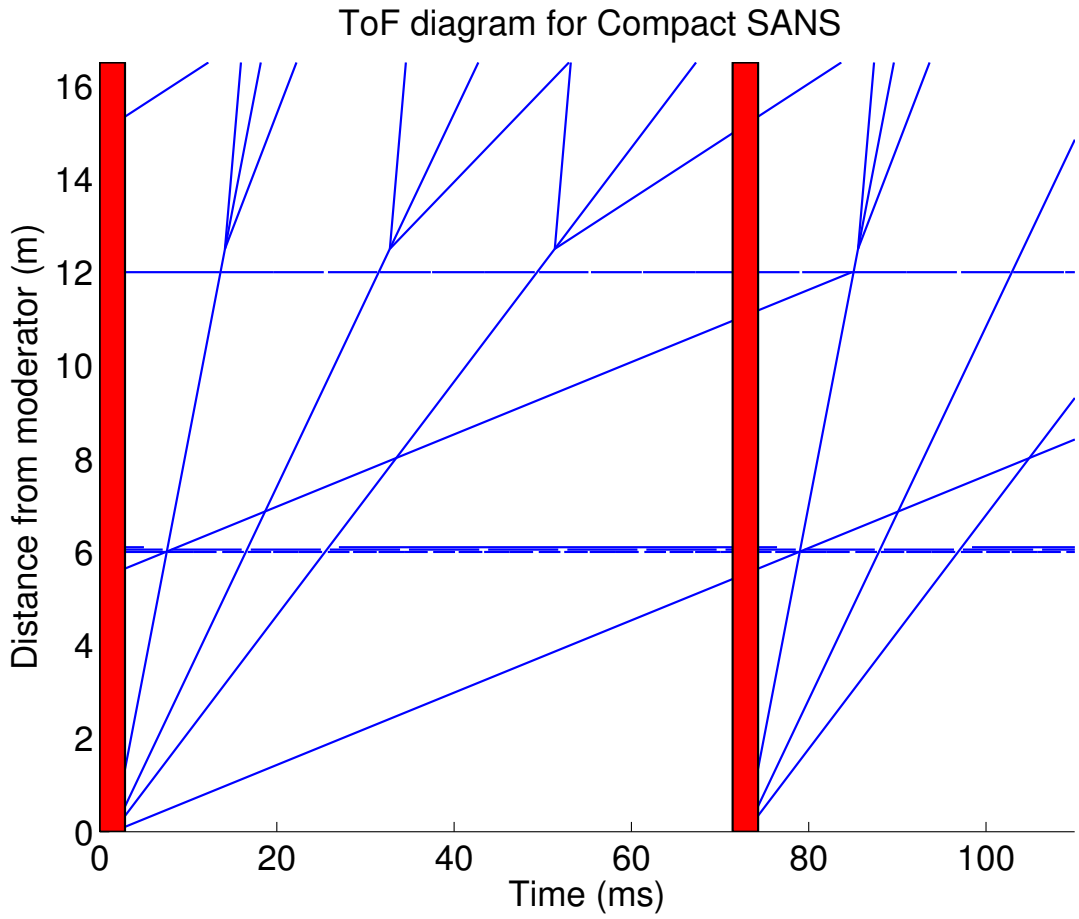

Figure 2: *Time of flight diagram of the variable-burst time scheme of the chopper ToF SANS for ESS. The position of the pulse-shaping chopper, the contaminant removal chopper, and the frame overlap chopper is at 6 m, and the monochromating chopper is at 12 m. The red areas indicate the prompt pulse. See figure 3 for a closer look at the chopper system at 6 m.*

λ_1	E_1	$\tau_{\rm ps}$	τ_2	$\delta\lambda_1/\lambda_1$	δE_1	δE_2	δE
4.00 Å	5.11 meV	210 μs	140 μs	3.46%	354 μeV	354 μeV	501 μeV
9.89 Å	0.84 meV	210 μs	140 μs	1.40%	23 μeV	23 μeV	33 μeV
15.78 Å	0.33 meV	210 μs	140 μs	0.88%	5.8 μeV	5.8 μeV	8.2 μeV

Table 3: *Key numbers and results for the constant burst time option with a pulse shaping chopper.*

use (the wavelength frame multiplication, or WFM, scheme[10, 12]). The time between bursts will then be $t_{\rm ps} = (T/n)(L_{\rm ps}/(A + L_1 - L_{\rm MS})) = T/8 = 8.93$ ms.

The opening time of the pulse shaping chopper can be freely adjusted. For calculating an example, we here aim for an improved energy resolution of 10% at 4.0 Å wavelength, where equation (2) is here used with the length $L' = A + L_1 - L_{\rm ps} - L_{\rm MS} = 6$ m. We calculate a burst time of the pulse shaping chopper of $\tau_{\rm ps} = 210$ μs. Again, to match the primary and secondary resolutions, we decrease τ_2 to 140 μs.

The results are shown in table 3. We see that the resolution of the 4 Å neutrons has improved to 500 μeV as required, while the longer wavelengths have an amazingly good resolution, 8.2 μeV at 15.78 Å, despite the short length of the instrument. However, this comes at a price. The monochromating chopper is open only around 0.6% of the time frame, and the pulse shaping chopper has shortened the effective pulse length to around 15% of the original. Hence, three orders of magnitude in intensity is lost in this scheme, corresponding to the general experience from ToF spectroscopy that the intensity is proportional to the square of the energy width of the elastic line.

3.3 Variable Chopper Burst Times

Table 3 illustrates the common experience that the energy resolution improves for the long-wavelength neutrons. However, the intensity is lowest just at these long wavelengths. Therefore, it will often be of advantage to relax the resolution selectively at the long wavelengths to gain intensity there.

We propose a pulse shaping chopper consisting of a chopper with three openings, where the openings have the ratio 1:2:3. If this chopper spins with 6 times f, they have moved 3/4 turn for each of the 8 sub-pulses. We can then use a coarse, asymmetric contaminant removal chopper to discard the "wrong" openings from the pulse shaping chopper. This is illustrated in figure 3.

For the monochromating chopper, we use a similar scheme with pulse-shaping and contaminant removal choppers. We obtain the results given in table 4, where we keep the requirement $\delta E/E = 10\%$ for the 4.0 Å neutrons. It is seen that

λ_1	E_1	$\tau_{\rm ps}$	τ_2	$\delta\lambda_1/\lambda_1$	δE_1	δE_2	δE
4.00 Å	5.11 meV	210 μs	140 μs	3.46%	354 μeV	354 μeV	500 μeV
9.89 Å	0.84 meV	420 μs	305 μs	2.80%	47 μeV	58 μeV	75 μeV
15.78 Å	0.33 meV	630 μs	469 μs	2.63%	17 μeV	23 μeV	29 μeV

Table 4: *Key numbers and results for the variable burst time option with variable pulse shaping.*

Setup	I (n/s)
NC	2.0×10^7
PS	3.9×10^6
VC	1.2×10^5

Table 5: *Comparison of intensity on a 5×5 mm^2 sample for 3 versions of the SANS spectrometer: no choppers (NC), a simple chopper system consisting only of a pulse shaping chopper that improves the wavelength resolution by a factor 2 compared to the unchopped version (PS), and the chopper system described in section 3.3 (VC). All versions are with the 4 m collimation setting with $S_1 = 8$ mm and $S_2 = 4$ mm.*

the line widths broadened by a factor 2 and 3 for 9.89 Å and 15.78 Å neutrons, respectively. Hence, their respective intensities increase by factors 4 and 9.

We can estimate the intensity loss from the choppers compared to the unchopped instrument by the ratio of the opening time of the pulse shaping chopper to the full pulse width and the ratio of the opening time of the monochromating chopper to the ESS pulse period. By multiplying these two loss factors and summing over the 3 chopper pulses, we arrive at an estimate of the total loss caused by the chopper system:

$$\Sigma_i \frac{(\tau_{1_i} \cdot \tau_{2_i})}{\tau(T-\tau)} = 0.23\% \tag{6}$$

Table 5 shows that the simulations give a figure of 0.60 % intensity compared to the unchopped version of the instrument. This discrepancy might be explained by the fact that the above rough calculation does not take into account the non-uniformity of the wavelength distribution from the source.

4 Monte Carlo Simulations

In order to determine the usefulness of this SANS instrument for spectroscopy, we here demonstrate its performance by ray-tracing simulations. First, however,

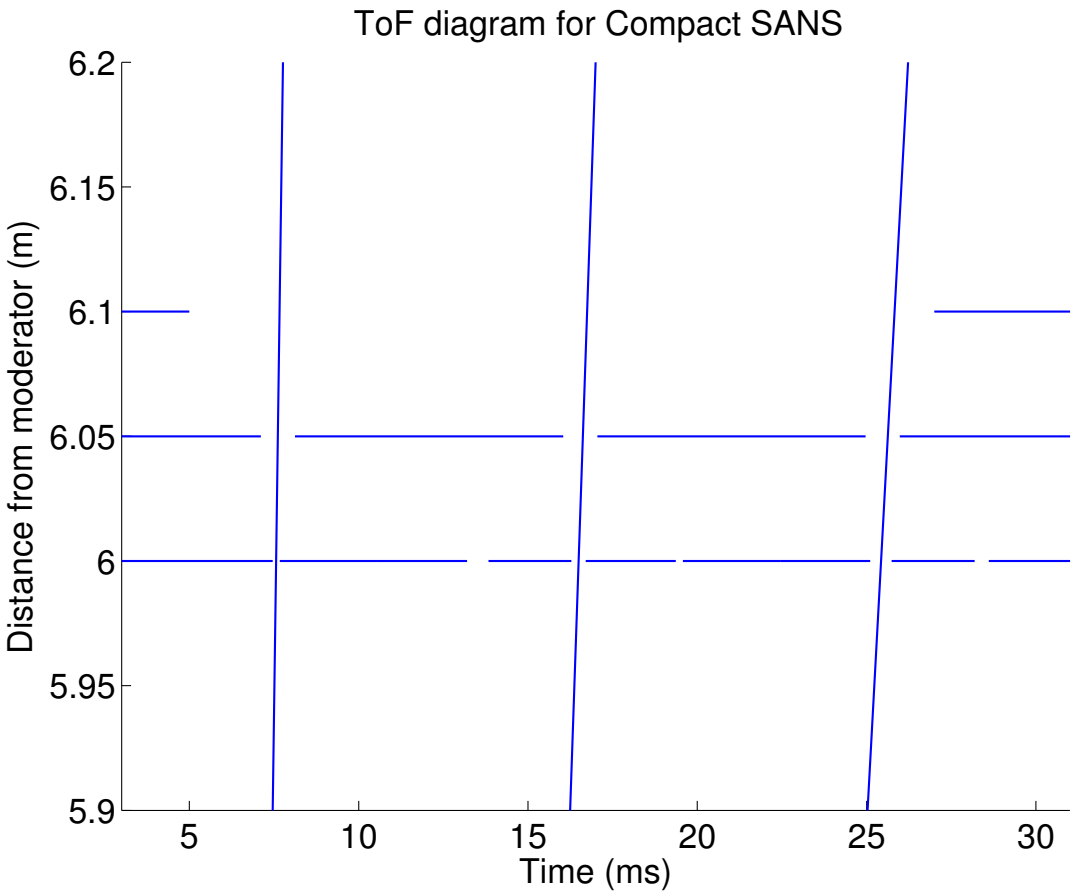

Figure 3: *Time of flight diagram closeup of the variable-burst pulse shaping chopper system, with rays of 4.00, 9.89, and 15.78 Å neutrons going through. At 6 m the pulse shaping chopper is placed, with 3 openings of variable sizes at the 0°, 90°, and 180° positions and moving at 6 times the pulse frequency, f. At 6.05 m the contaminant removal chopper is placed, with one opening and turning with 4/3 the speed of the pulse shaping chopper, i.e. $8f$. At 6.1 m the frame overlap chopper is placed, which defines the bandwidth. This chopper has one opening and rotates with the source frequency.*

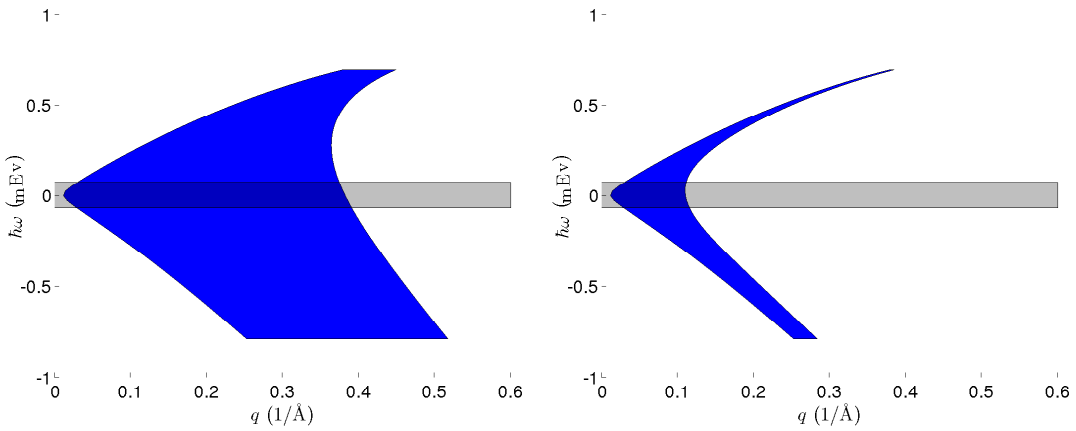

Figure 4: *Calculations of the $\hbar\omega/q$ space that can be covered with the instrument. The shaded bars denote the width of the instrumental resolution. Left: 1 m detector distance. Right: 4 m detector distance. The wavelength of the ingoing neutrons is set to $\lambda_i = 10$ Å. ($E_i = 0.82meV$)*

we must establish the connection between (angle, time-of-flight) raw data and the desired (q, ω) picture, where (q) is the scattering angle and $(\hbar\omega)$ the energy transfer:

$$\hbar\omega = \frac{\hbar^2}{2m_{\mathrm{n}}}(k_i^2 - k_f^2) \tag{7}$$

$$q = \sqrt{(k_f sin(2\theta))^2 + (k_f cos(2\theta) - k_i)^2}, \tag{8}$$

where k_i wavenumber of the ingoing neutron, determined by the resolution chopper, k_f is the wavenumber of the scattered neutron, and 2θ is the scattering angle constrained by the ingoing beam divergence and the detector size and position.

Using (7) and (8) above and considering k_f's in the interval $0.4k_i < k_f < 1.4k_i$, we can create the plots in figure 4 which show the $(q, \hbar\omega)$ area that can be covered by the instrument.

While our chopper system is sufficient to discriminate between elastic and some inelastic scattering, improved resolution will often be needed to properly resolve elastic scattering for spectroscopy. In this example, we decrease the opening times of the resolution chopper by a factor 4, so that for the 10 Å pulse the opening time is now 75 μs.

4.1 Virtual Experiments

Using a model of the ESS long pulsed source, the instrument has been simulated with McStas in order to gauge its performance. Using the results of the simu-

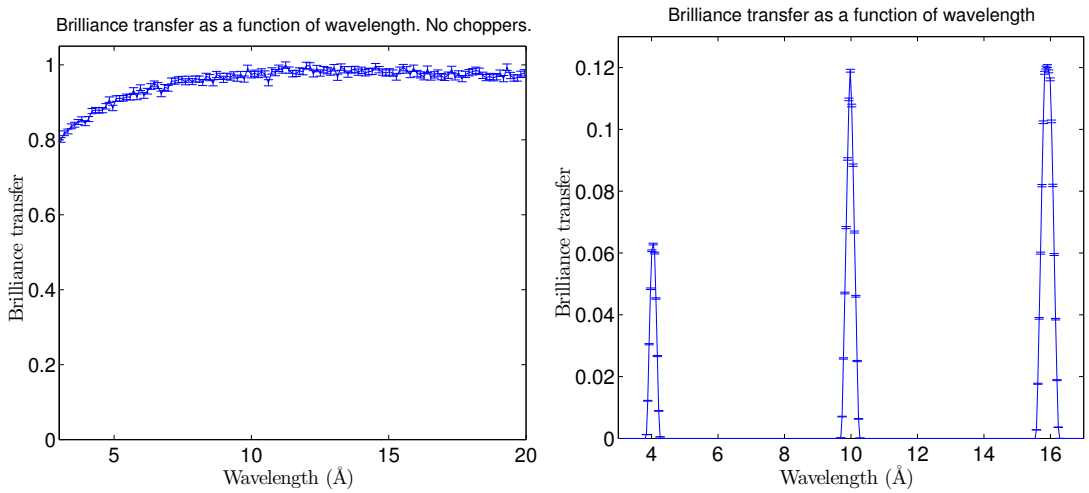

Figure 5: *Brilliance transfer from source to sample as a function of wavelength. Left: without choppers. Right: with choppers in variable burst mode.*

Instrument length: $L = A + L_1 + L_2$	Flux on sample (n/s/cm^2)	Neutrons on 50.3 mm^2 sample (n/s)
13=11+1+1	14×10^8	7.0×10^8
14=10+2+2	3.6×10^8	1.8×10^8
16=8+4+4	0.94×10^8	0.47×10^8
ILL D22 A+2+2	0.28×10^8	0.11×10^8

Table 6: *Simulated flux on sample for.*

lation, the brilliance transfer from the source to the sample position has been calculated and is shown in figure 5. The left graphs shows the brilliance transfer

For the virtual experiments we simulated an inelastically scattering sample using the McStas component 'Phonon_simple' with the following parameters:

This section is not complete yet.

5 Conclusion

This section is not ready yet.

References

[1] European Spallation Source.

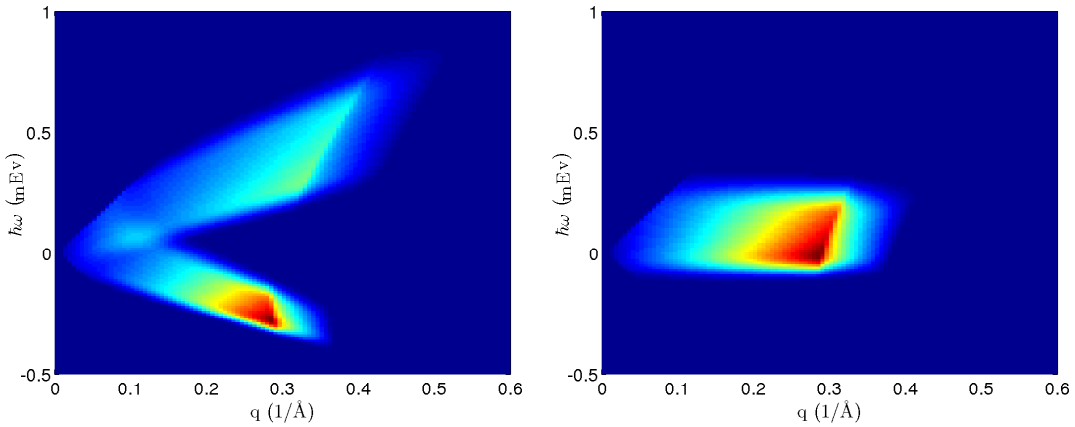

Figure 6: *Results of virtual experiments with a phonon sample using the 10 Å peak and a 1 m collimation and detector distance. Left: Inelastically scattering phonon sample. Right: Elastically scattering vanadium sample.*

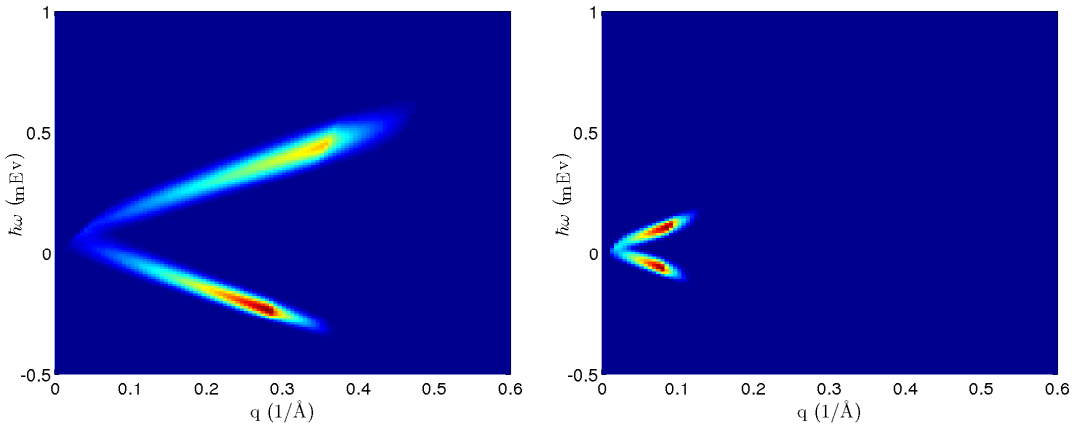

Figure 7: *Results of virtual experiments with a phonon sample using the 10 Å peak and the resolution chopper set to a 75 µs opening. Left: 1 m collimation distance and 1 m detector distance. Right: 1 m collimation distance and 4 m detector distance.*

[2] European Spallation Source - Data Management and Software Centre.

[3] De Francesco, A., Laloni, A., Formisano, F., Orecchini, A., Aisa, S., Guarini, E., Petrillo, C., Pilgrim, W., Suck, J., Sani, L., et al. Brisp: The new brillouin spectrometer at ill's high flux reactor. *Neutron News 19*, 4 (2008), 10–13.

[4] Heenan, R., Penfold, J., and King, S. Sans at pulsed neutron sources: present and future prospects. *Journal of applied crystallography 30*, 6 (1997), 1140–1147.

[5] Klenø, K. H., Kynde, S., Nagy, G., Skar-Gislinge, N., Mortensen, K., Lefmann, K., Kohlbrecher, J., and Arleth, L. Ess instrument construction proposal: Compact sans optimised for biological samples. Tech. rep., Niels Bohr Institute, October 2012.

[6] Klenø, K. H., Kynde, S., Nagy, G., Skar-Gislinge, N., Mortensen, K., Lefmann, K., Kohlbrecher, J., and Arleth, L. Ess instrument construction proposal: Compact sans optimised for biological samples. *J. Appl. Cryst. (submitted)* (2013).

[7] Lefmann, K., Klenø, K. H., Birk, J. O., Hansen, B. R., Holm, S. L., Knudsen, E., Lieutenant, K., von Moos, L., Sales, M., Willendrup, P. K., et al. Simulation of a suite of generic long-pulse neutron instruments to optimize the time structure of the european spallation source. *Review of Scientific Instruments 84*, 5 (2013), 055106–055106.

[8] Lefmann, K., and Nielsen, K. Mcstas, a general software package for neutron ray-tracing simulations. *Neutron News 10/3* (1999), 20–23.

[9] Lefmann, K., Schober, H., and Mezei, F. Simulation of a multiple-wavelength time-of-flight neutron spectrometer for a long-pulsed spallation source. *Measurement Science and Technology 19*, 3 (2008), 034025.

[10] Lieutenant, K., and Mezei, F. Monte carlo simulations of a powder diffractometer installed on a long pulse target station using wavelength frame multiplication. *Journal of Neutron Research 14*, 2 (2006), 177–191.

[11] Mezei, F. The raison d'etre of long pulse spallation sources. *Journal of Neutron Research 6*, 1 (1997), 3–32.

[12] Mezei, F., and Russina, M. Multiplexing chopper systems for pulsed neutron source instruments. In *International Symposium on Optical Science and Technology* (2002), International Society for Optics and Photonics, pp. 24–33.

[13] Mezei, F., Russina, M., and Schorr, S. The multiwavelength cold neutron time-of-flight spectrometer project in500 at lansce. *Physica B: Condensed Matter 276* (2000), 128–129.

[14] Schober, H., Farhi, E., and Mezei, F. Tailored instrumentation to long pulse neutron spallation sources. *Nuclear Instruments and Methods in Physics Research A 589* (2008), 34–46.

A Compact Time-of-Flight SANS Instrument Optimised for Measurements of Small Sample Volumes at the European Spallation Source

Kaspar Hewitt Klenø,[a] Søren Kynde,[a] Gergely Nagy,[b] Kell Mortensen,[a] Kim Lefmann,[a] Joachim Kohlbrecher[b]* and Lise Arleth [a]*

[a]*Niels Bohr Institute, University of Copenhagen, Denmark, and* [b]*SINQ, Paul Scherrer Institute, Switzerland. E-mail: joachim.kohlbrecher@psi.ch, arleth@nbi.ku.dk*

(Received 0 XXXXXXX 0000; accepted 0 XXXXXXX 0000)

Abstract

The high flux at European Spallation Source (ESS) will allow for performing experiments with relatively small beam-sizes while maintaining a high intensity of the incoming beam. The long pulsed nature of the source makes the facility optimal for time-of-flight small-angle neutron scattering (ToF-SANS). We find that a relatively compact SANS instrument becomes the optimal choice in order to obtain the widest possible q-range in a single setting, the best possible exploitation of the neutrons and hence obtaining the highest possible flux at the sample position. The instrument proposed in the present article is optimised for performing fast measurements of small sample volumes, typically down to $2 \times 2 \times 2$ mm^3, while covering a q-range from about 0.005 1/Å to 0.5 1/Å in a single instrument setting. This q-range corresponds to that available at

a typical good BioSAXS instrument and is relevant for a wide set of biomacromolecular samples. A central advantage of covering the whole q-range in a single setting is that each sample has to be loaded only once. This makes it convenient to use the fully automated high-throughput flow-through sample changers commonly applied at modern synchrotron BioSAXS-facilities. The central drawback of choosing a very compact instrument is that the resolution in terms of $\Delta\lambda/\lambda$ becomes significantly worse than what is usually the standard at state-of-the-art SANS instruments. Our McStas based simulations of the instrument performance for a set of characteristic biomacromolecular samples show that the smearing effects still have relatively minor effects on the obtained data and can be compensated for in the data analysis. However, in cases where a better resolution is required in combination with the large simultaneous q-range characteristic of the instrument, we show that this can be obtained by inserting a set of choppers.

1. Introduction

Small angle neutron scattering (SANS) holds a great promise for the investigation of a large range of crucial and yet poorly explored biomolecular systems. However, SANS studies of such systems are presently limited by the large-volume requirements of typically 200-800 μL, along with problems with poor signal-to-noise ratios due to the large incoherent scattering from samples that are inherently rich in Hydrogen. In the context of biomolecular systems, the European Spallation Source (ESS) will provide a unique opportunity to combine the high flux of a next generation neutron source with new instrument concepts to study small samples of exciting new biomolecular materials.

The X-ray based sister-technique of SANS; Synchrotron Small-Angle X-ray Scattering, SAXS, has undergone a tremendous development during the last five years.

Internationally, this has resulted in several dedicated and scientifically highly productive so-called BioSAXS beamlines (Pernot *et al.*, 2010; Roessle *et al.*, 2007). These are beamlines where the required sample volume is minimised to about 10 μL and where the signal-to-background has been optimised such that it is now possible to obtain good data out to about 0.6 1/Å, thus allowing for much better structural resolution. These beamlines also strive to automate everything that can be automated. This includes fast automated sample loading and cleaning of the sample cuvette as well as fully automated data collection, reduction and preliminary data analysis (Franke *et al.*, 2012).

Despite from a few cases (Lynn *et al.*, 2006; Dewhurst, 2008), such a development is not yet visible in the SANS instrumentation community, where a large flexibility of the instrument is almost always prioritised over automation and user-friendliness of the data collection process. However, the instrument planning process at the ESS allows for a much more coordinated strategy towards the instrumentation than what has typically been the case at other facilities. This allows for a more optimal focusing of the different envisioned SANS instruments to different scientific applications right from the early phase of designing the instrument.

The proposed compact SANS instrument may be seen as the neutron based answer to the large scientific demand that has been driving Bio-SAXS development within X-ray science. By designing a SANS instrument that is rather short, it becomes possible to obtain a very high neutron flux with a large bandwidth on a small sample, thus at the same time effectively increasing the signal and the dynamic range in terms of momentum transfer, q. The goal of the present work is an instrument that is optimised for SANS measurements of biological samples with volumes down to $2 \times 2 \times 2$ mm^3, while covering, with a single instrument setting, a q-range comparable to that available at a typical synchrotron based BioSAXS instrument.

Based on neutron ray-tracing simulations using McStas (Lefmann & Nielsen, 1999; Willendrup *et al.*, 2004), we find that an instrument with a 12 m bend guide followed by a 4 m collimation section and an up to 4 m sample detector distance has a very attractive performance with respect to typical biomacromolecular samples in solution. Simulations of the instrument performance are performed for a typically sized biomacromolecular sample of Insulin hexamers, a 1 mm H_2O sample and an artificial sample with logarithmically spaced Bragg peaks. The simulations of the insulin Hexamer show that despite the relatively poor q-resolution intrinsic for such a compact instrument ($\delta\lambda/\lambda$ of up to 20% at the lowest wave-lengths), we find that the q-resolution of the instrument is more than sufficient for investigating the biomacromolecular samples.

However, several cases can be thought of where a better wavelength resolution is required. Some of these cases are probably better investigated at one of the longer and more classical SANS instruments that are present at several existing facilities (E.g. ILL and FRM-II). To accommodate the scientific cases where a large simultaneous q-range is required in combination with an instrument with better wavelength resolution we have investigated how the resolution may be improved "on demand" by inserting a set of choppers. We find that the resolution $\delta\lambda/\lambda$ can be improved down to about 10 % at the cost of reducing the neutron flux to about 40 % of the original level.

As usual, the typical measurement times will be highly dependent on the sample in terms of its molecular mass and its excess scattering length density. However taking a traditional difficult example of weakly scattering Insulin Hexamers in the challenging situation where a combination of a small sample size of $2\times2\times2$ mm^3, low molar mass (36 KDa) and relatively weak contrast ($\Delta\rho \approx 3 \times 10^{10} 1/\mathrm{cm}^2$ in D_2O) applies, then typical measurement times of about 1000 seconds will be required in order to obtain data with sufficiently good signal-to-noise ratio in a q-range from 0.008 to 0.35

1/Å. While this is definitely fast as compared to what can be obtained at present SANS facilities for this type of sample, much shorter measurement times can easily be obtained for other types of samples.

2. Theory and Methods

Wavelength Resolution

The instrument uses the time of flight (ToF) method (Heenan *et al.*, 1997), where the arrival time of a neutron in the detector is used to determine wavelength:

$$t = \alpha L \lambda, \tag{1}$$

where L is the moderator-detector distance, λ the neutron wavelength, and $\alpha = 252.7$ μs/Å/m. This gives us the uncertainty in the ToF determination of the wavelength:

$$\frac{d\lambda}{\lambda} = \frac{dt}{t} = \frac{\tau}{\alpha L \lambda} \tag{2}$$

where τ is the pulse width. So with the ESS pulse length, $\tau = 2.86$ ms, $\lambda = 10$ Å , and the instrument configuration with 4 m collimation, corresponding to a L of 20 m, we get a wavelength resolution (FWMH) of:

$$\frac{d\lambda}{\lambda} = 6.0\% \tag{3}$$

Other examples of $\frac{d\lambda}{\lambda}$ are provided in table 1.

Bandwidth

The bandwidth available can be calculated from the constraint that we avoid frame overlap by restricting the measuring time to the pulse period minus the pulse length:

$$T - \tau = \alpha \ \Delta\lambda \ L, \tag{4}$$

which for the 1 m collimation configuration gives us the bandwidth

$$\frac{T-\tau}{\alpha L} = \Delta\lambda = 15.9 \text{ Å} \tag{5}$$

Other examples of $\Delta\lambda$ are provided in table 2.

Momentum Transfer Range

The momentum transfer, q, of a scattered neutron is related to the scattering angle 2θ as:

$$q = \frac{4\pi}{\lambda}\sin\theta. \tag{6}$$

The angle θ is defined as

$$\theta = \frac{1}{2}\arctan\left(\frac{d}{L_2}\right), \tag{7}$$

where d is the distance on the detector from the beam centre to the pixel where the neutron was detected and L_2 is the sample-detector distance.

The maximum q-value accessible to the instrument is obtained when the neutrons with the smallest wavelengths are detected at the largest possible angle, i.e. the furthest corner of the detector.

The minimum q-value is obtained when the longest wavelengths are detected as close to the beam as possible. In this paper we take this distance to be

$$d_{min} = 1.5\left(r_2 + (r_1 + r_2)\frac{L_2}{L_1}\right), \tag{8}$$

where r_1 and r_2 are the slit radii of the entrance and exit pinholes of the collimator respectively, L_1 is the collimation length and L_2 is the sample-detector distance. The factor of 1.5 is a margin to compensate for the fact that a real beamstop will likely be slightly larger than the beam, and that some of the pixels very close to the beam may be half covered by the beamstop.

Virtual Experiments

A virtual model of the instrument was constructed and simulated using the McStas neutron ray-trace simulation package (Lefmann & Nielsen, 1999). Only standard components were used and the virtual source, *ESS_moderator_long*, is a model of the ESS long pulsed source, with the baseline ESS pulse period of 71.14 ms (14 Hz) and pulse width of 2.86 ms. The simulations where performed at the ESS-DMSC 1000-core cluster, using typically 100 cores for 5 hours.

To demonstrate the intensity performance, q-range and resolution of the instrument we have performed full virtual experiments on various samples with different characteristics. The investigated examples are:

- A completely isotropic scatterer corresponding to the isotropic contribution from 1mm of H_2O.
- A purely mathematical "powder-sample" featuring an $I(q)$ curve with logarithmically spaced sharp peaks to illustrate the instrument resolution in q-space.
- A more realistic biomolecular sample based on an elaborate scattering model of a 5 mg/ml solution of insulin hexamers in D_2O buffer.

Signal to Noise Ratio

For each kind of scattering profile we have ordered the detected neutron events into q-bins based on their time-of-flight and position on the detector (Seeger & Hjelm Jnr, 1991). Since the intensity unit in McStas is neutrons/second, the resulting quantity becomes differential count-rate $\frac{\partial^2 S(q)}{\partial q \partial t}$. From this the expected number of neutrons in a q-bin of width Δq during a measurement of time Δt can be calculated:

$$S(q) = \frac{\partial^2 S(q)}{\partial q \partial t} \Delta q \Delta t. \tag{9}$$

Assuming Poisson statistics, the level of statistical noise can be estimated as:

$$N(q) = \sqrt{\left(\frac{\partial^2 S(q)}{\partial q \partial t} + \frac{\partial^2 B(q)}{\partial q \partial t}\right) \Delta q \Delta t}, \tag{10}$$

where $\frac{\partial^2 B(q)}{\partial q \partial t}$ is the differential count rate of the background.

Combining equations (9) and (10), the expected measurement time associated with a given scattering profile and desired signal to noise ratio (S/N) can be estimated:

$$\Delta t = \left(\frac{S}{N}\right)^2 \frac{\frac{\partial^2 B(q)}{\partial q \partial t} + \frac{\partial^2 S(q)}{\partial q \partial t}}{\frac{\partial^2 S(q)}{\partial q \partial t}^2 \Delta q}. \tag{11}$$

3. Proposed Instrument Layout

Guide

The guide system begins at 2 m from the source, and starts with a 9.9 m long curved guide with a cross-section of 2 cm × 2 cm. It is curved with a radius of 280 m which breaks the line of sight from the moderator to the sample twice; i.e. the point where the line of sight from the moderator is broken, cannot be seen from the sample position. After the bend guide follows the collimation section, which for a neutron transport optimisation perspective is a 3 m long straight guide with a 2 cm × 2 cm cross-section, when the instrument is in the 1 m collimation mode. In total this guide system blocks line of sight from the moderator to the sample with a minimum of 13.6 m of shielding for any straight line.

The m-values of the coating required for this guide system is as follows: m=2.4 for the outer wall of the curved guide, m=1 for the inner wall of the curved guide, and m=2.1 for the top and bottom of the curved guide and the guide in the collimation section.

Figure 1 (left) shows the layout of the guide system and how the line of sight is blocked, and figure 1 (right) shows that the performance of the guide system in terms of brilliance transmission over the entire wavelength range used.

Collimation Section

The 4 m long collimation section starts at 11.9 m from the moderator surface and consists of four 1 m elements. The first three elements can be exchanged with extra guide sections allowing for collimation lengths of 4 m, 3 m, 2 m, or 1 m. The extra guides are inserted vertically to make room for maximal shielding on the sides. The two defining slits are circular and denoted s_1 and s_2 as indicated on figure 2.

This gives a maximum divergence at the sample position of $\phi_{max} = \arctan \frac{r_1+r_2}{L_1}$, where L_1 is the collimation distance used and r_1 and r_2 are the slit radii.

Chopper System

Two bandwidth definition choppers are required to select the bandwidth calculated in section 2. Additionally, in order to improve the wavelength resolution of the instrument, it is possible to reduce the effective pulse width using choppers. In order to minimise the flux loss caused by chopping the beam, we employ a system inspired by wavelength frame multiplication (Lieutenant & Mezei, 2006; Mezei & Russina, 2002) using 3 resolution choppers placed at 7, 10, and 12 m from the source, as shown in figure 3. Refer to table 3 for a full list of the chopper positions and opening times.

This chopper system represents what we feel is a good compromise between resolution and flux, but it is important to note that it can be 'turned off' to allow for the full flux when a more relaxed resolution is acceptable, so that only the bandwidth definition choppers are active.

Sample Environment

Immediately after the collimation there will be 20 cm space for the sample environment. See figure 4.

As this instrument is optimised for weakly scattering soft samples it is important

that as much as possible of the neutron flight path takes place in vacuum. We anticipate that one of the standard sample environments will be a flow-through sample holder placed with vacuum on either side of the windows. This will minimise the background as well as the sample consumption and allow for automatic sample changing procedures similarly to what is already seen on dedicated synchrotron bio-SAXS beamlines.

Another characteristic sample environment will be an array of standard 1 cm $\times$ 1 cm $\times$ 2mm Helma quartz cuvettes for measurements of samples where several hundreds of μl are available. Again we suggest that the sample should be placed immediately in front of the detector tank window and the vacuum should be extended all the way to the sample with a prolonged flight tube after the second collimation pinhole.

As this is a specialised instrument intended for doing a few things good, there will be no option to include very space consuming sample environments, such as large electromagnets and cryostats. However if needed, the prolonged vacuum tube can be removed and the entire 20 cm sample space can be used. This should be enough to accommodate e.g a permanent magnet or a small custom made cryostat or rheometer.

Detector Section

The detector simulated is 1 m wide and 2 m tall. It is kept under vacuum in a 4 m long detector tank. The beam is centred on the lower square meter of the detector. For the flow through sample environment no window is needed, rather the flight tube is attached directly to the detector tank. For the other environments we imagine that the neutrons enter through a 25 cm diameter beryllium window.

In the simulations, it is for simplicity assumed that the detector efficiency is 100%, i.e. all incoming neutrons are detected. The pixel size is set to be 5 $\times$ 5 mm^2. To be able to make use of the centre of the detector for settings with very small beam sizes

the central 20 × 20 cm^2 of the detector is a assumed to have pixels of 2 × 2 mm^2. As usual for SANS instruments, the detector is movable, and for the simulations, its distance from the sample always mirrors that of the collimation length. A beamstop protects the detector from the direct beam, and is placed 1 cm in front of the detector.

Due to the rapid development in detector technologies we have not decided on any specific type of detector for this instrument, but we consider the requirements to be relatively modest.

4. Results

Instrument Performance

Using Monte Carlo simulations, the parameters of the transport system where tweaked to optimise the flux on sample for 3 Å neutrons, as the low wavelengths are the most challenging to transport. By optimising for low wavelengths, we get excellent transport performance for the whole bandwidth, as seen from figure 1 (right).
The simulated flux on sample is presented in table 1 together with the wavelength resolution, q-range, and bandwidth (table 2), which are calculated as discussed in section 2.

Intensity and q-range

The intensity performance is best seen in the simulation of isotropic scattering from H_2O, see figure 5. The settings shown have sample detector distances of 1 m, 2 m or 4 m which in all instances are equal to their respective collimation lengths. For the left plot an entrance pinhole of the collimation section of radius $r_1 = 8$ mm has been used and an exit pinhole of radius $r_2 = 4$ mm. For the right a setup intended for small samples has been used, with $r_1 = 2$ mm and $r_2 = 1$ mm. The beamsize of this setting is only 8mm at the detector (equation (8)). This gives rise to an extended q-range at

low q, but requires that the pixels near the beam is smaller than 5×5 mm^2.

The plots show the differential count rates $\frac{\partial^2 S(q)}{\partial q \partial t}$. The actual number of neutrons recorded in a given q-bin and measurement time can be estimated with equation (9).

For comparison, curves are also shown for ILL beamline D22 with the setting $r_1 =$ 8 mm, $r_2 = 4$ mm, $L_1 = L_2 = 2$ m. A velocity selector with a wavelength resolution of 10% has been used and a 1×1 m^2 detector assumed. We have furthermore assumed the peak intensity wavelength at $\lambda = \lambda_{\rm min} = \lambda_{\rm max} = 4.5$ Å. The performance of D22 is also shown in a setting that is suited for lower q-values. This setting uses 9 m collimation and the velocity selector aimed at 4.5 Å neutrons. The performance is not much different when using a longer wavelength and shorter collimation.

Note that between the curves of the same collimation length there is approximately a factor of 16^2 difference in intensity between the left (large sample) and right (small sample) plots. This corresponds to the reduction of each of the collimation pinholes of a factor of 16 in the small sample configuration. Using e.g. a $r_1 = 8$ mm entrance pinhole and a $r_2 = 1$ mm exit pinhole results in a configuration still suitable for small samples, but with a gain in intensity of a factor of 16 relative to the curves on the right. The intensity gain comes with the cost of the extended q-range towards low q apparent in the right plot. This setting has been used in the insulin hexamer example below.

Bio-molecules

To evaluate the performance of the instrument under conditions for which it has been optimised, a virtual experiment with a more realistic bio-molecular sample has been performed. It is based on an atomic model of an insulin hexamer in solution. The buffer is assumed to be 100% D_2O and the concentration is 5 mg/ml. The sample thickness is 2 mm and it is irradiated through the $r_2 = 1$ mm exit pinhole. This gives

an irradiated volume of less than 7 μl, which makes it realistic to keep the total sample consumption below 10 μl.

It is evident from figure 7 (left) that the important oscillatory features of the scattering curve are clearly resolved. Also a single instrument setting can cover the entire range from the low-q Guinier range to the very difficult high-q region, where the signal is two orders of magnitude lower than the incoherent background.

In figure 7 (right) we have plotted the differential neutron count rates for the signal and the background. These have been used to calculate the estimated measurement times needed to obtain a signal to noise ratio of 10 via equation (11) with $\Delta q = 0.1q$. In the region where the signal is more than 5% of the background it will be possible to make a good background subtraction with less than 1000 seconds of measurement. Sample volumes smaller than 100 l are rarely measured on existing beamlines The measuring time is inversely proportional to the irradiated volume, which means that 100 μl of insulin hexamer in D_2O could be measured in a few minutes on the proposed instrument. This is about 20 times faster than measuring in a single setting on e.g. D22 at ILL and with a significantly broader q-range.

Resolution

The short length of the proposed instrument makes it difficult to resolve the wavelength and hence the momentum transfer of the individual neutron. This is illustrated by the simulation results in figure 6. The sample features Bragg peaks around logarithmically spaced q-values. This does not correspond to any particular situation. As demonstrated above the limited resolution is not a problem for the biomolecular samples that the instrument is intended for. Especially not in the low q where most samples exhibit a flat Guinier region. However, in some cases a higher resolution is needed to resolve fine structure at high q, as seen from figure 7 (left). For these situ-

ations, we propose the chopper system presented in section 3. Our calculations show that this chopper system will improve the resolution of the low wavelengths by a factor 2, while reducing the overall flux with a relatively modest 60 %, as presented in table 1. Furthermore, this flux reduction mostly affects small wavelength neutrons, which are relatively abundant.

5. Conclusion

A ToF-SANS instrument is proposed that is optimised to exploit the source characteristics of the upcoming European Spallation Source towards getting the highest possible neutron flux at the sample position. We find that a relatively compact instrument instrument provides the best exploitation of the neutrons in the single pulses and allows for covering the broadest possible q-range in a single setting.

This flux may either be used for enabling SANS measurements of very small ($2\times2\times2$ mm^3/ 8 μl) and weakly scattering biological samples within realistic time frames of about 20 minutes. Or it may be used to perform SANS measurements on larger sample volumes ($8\times8\times2$ mm^3/ 128 μl) in an high throughput mode with total measurement times down to a minute or faster depending on the scattering power of the sample.

A compact ToF-SANS instrument will naturally have a less good wavelength resolution than a longer instrument. We show, by means of McStas based simulations, that the obtained $\delta\lambda/$ of up to 20 % (highly dependent on the neutron wavelength) is not critical for a typical protein in solution sample (insulin hexamers). Nevertheless, there will definitely be cases where a combination of the broad simultaneous q-range that can be obtained at the instrument will be desirable in combination with a better resolution. As an answer to this request, we propose that the instrument is equipped with a set of choppers that can be introduced on demand to produce a maximal $\delta\lambda/$ of 10 % while still maintaining 40 % of the flux of the standard high intensity setting.

While we are certain the combination of a high flux and a broad q-range in a single setting will be highly attractive for a rather broad user community, the proposed instrument will be particularly interesting for users with weakly scattering biological samples that are limited in sample quantity. For this group of users, the instrument will allow for obtaining the highest possible quality SANS data on samples that have so far been difficult or impossible to measure with SANS.

Acknowledgements

We appreciate useful discussions with the ESS STAP members and Andrew Jackson (ESS). The simulation software was supported by Peter Willendrup (DTU) and the hardware by ESS Data Management and Software Centre. We owe much thank to Emmanuel Farhi (ILL) for providing us his McStas implementation of the ILL-D22 instrument model. The project has been supported by the Danish Agency of Research and Innovation by grants supporting the ESS design update.

Table 1. *$d\lambda/\lambda$ stated in FWHM for selected wavelengths and collimation lengths of the proposed compact SANS instrument, and the flux on sample found by McStas simulations. Top: assuming the full pulse width is used. Bottom: assuming the resolution improving chopper system described in section 3. L_1: collimation length.*

L_1 (m)	$d\lambda/\lambda$ at 4Å	$d\lambda/\lambda$ at 8Å	$d\lambda/\lambda$ at 12Å	flux on sample (n/s/cm^2)
1	17%	8%	6%	12×10^8
2	16%	8%	5%	3.3×10^8
4	14%	7%	5%	0.88×10^8
1	9%	8%	6%	4.7×10^8
2	8%	8%	5%	1.3×10^8
4	7%	7%	5%	0.34×10^8

Table 2. *q-range of the proposed compact SANS instrument and the maximum bandwidth that avoids frame overlap. In the simulations and q-range calculations, we fixed the wavelength band with 3 Å as the minimum wavelength. The q-range calculations assume that the beam is centred in the lower square meter of the detector. L_1 collimation length.*

L_1 (m)	$q_{min}(Å^{-1})$	$q_{max}(Å^{-1})$	$\Delta\lambda$
1	8.0×10^{-3}	2.02	15.9 Å
2	4.2×10^{-3}	1.38	15.0 Å
4	2.3×10^{-3}	0.87	13.5 Å

Table 3. *Positions (in distance from source) and opening times for the choppers used.*

	Position (m)	chopper openings (from-to) (ms)			
1_{st} bandwidth def. chop.	6.5 m	6.36-27.71			
2_{nd} bandwidth def. chop.	9.5 m	8.91-39.44			
1_{st} resolution chop.	7 m	6.7-7.45	8.16-9.12	9.89-11.15	11.96-29.62
2_{nd} resolution chop.	10 m	9.26-10.18	11.35-12.42	13.83-15.16	16.78-41.4
3_{rd} resolution chop.	12 m	10.97-12	13.48-14.61	16.45-17.83	19.99-49.25

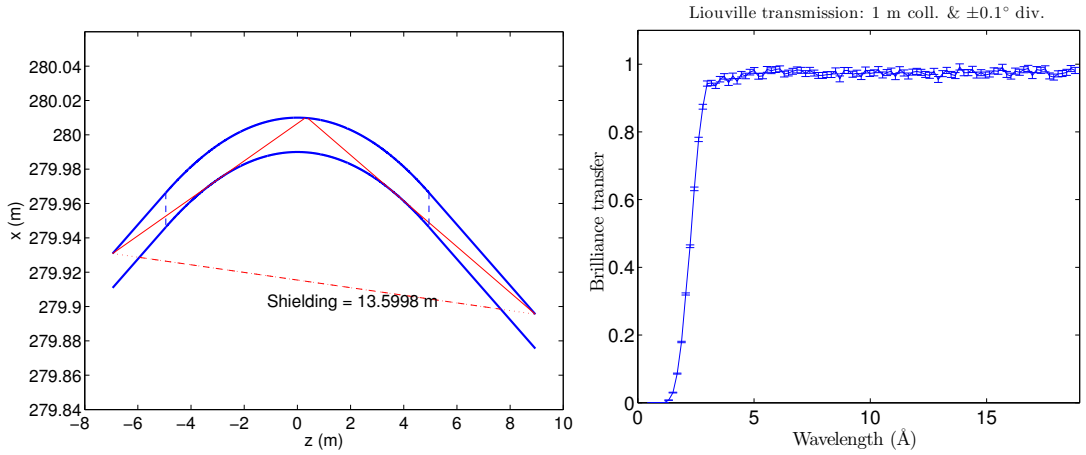

Fig. 1. **Left:** Diagram showing the transport section with the bender and collimation section (blue) and line of sight from the moderator and sample positions (red). Since the two red lines do not overlap, line of sight is blocked twice. The dashed red line shows the direct line through the transport system that must penetrate the minimum amount of shielding. The moderator is at the left end of the transport system, and the sample position at the right end. The origin of the coordinate system is the centre of the bender circle. Note that the scale on the axes differ. **Right:** Brilliance transfer from source to sample as a function of wavelength within the phase space of 5 mm × 5 mm and a 0.1 ° radial divergence, with the resolution choppers turned off and 1 m collimation length. As the transport section is designed for wavelengths of 3 Å or above, there is a steep cutoff below 3 Å.

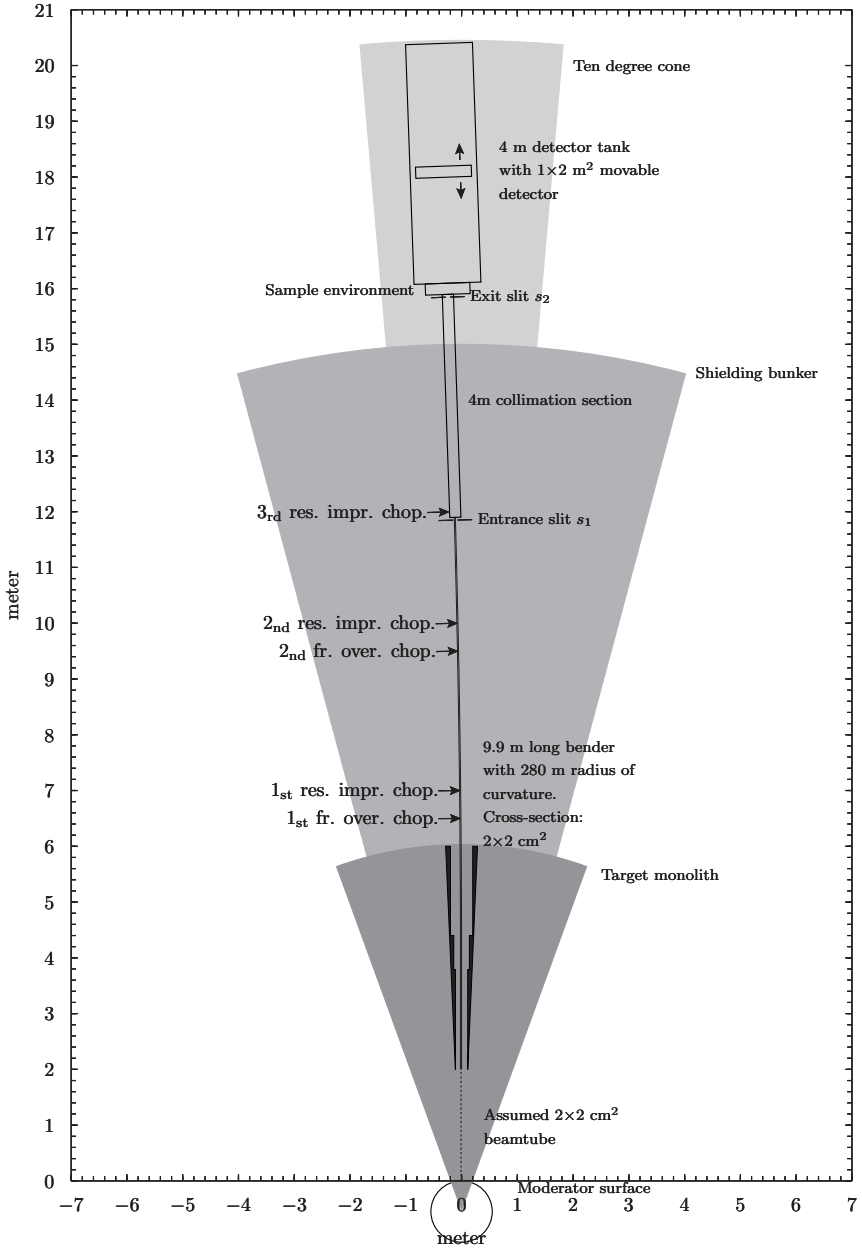

Fig. 2. Schematic drawing of the proposed instrument.

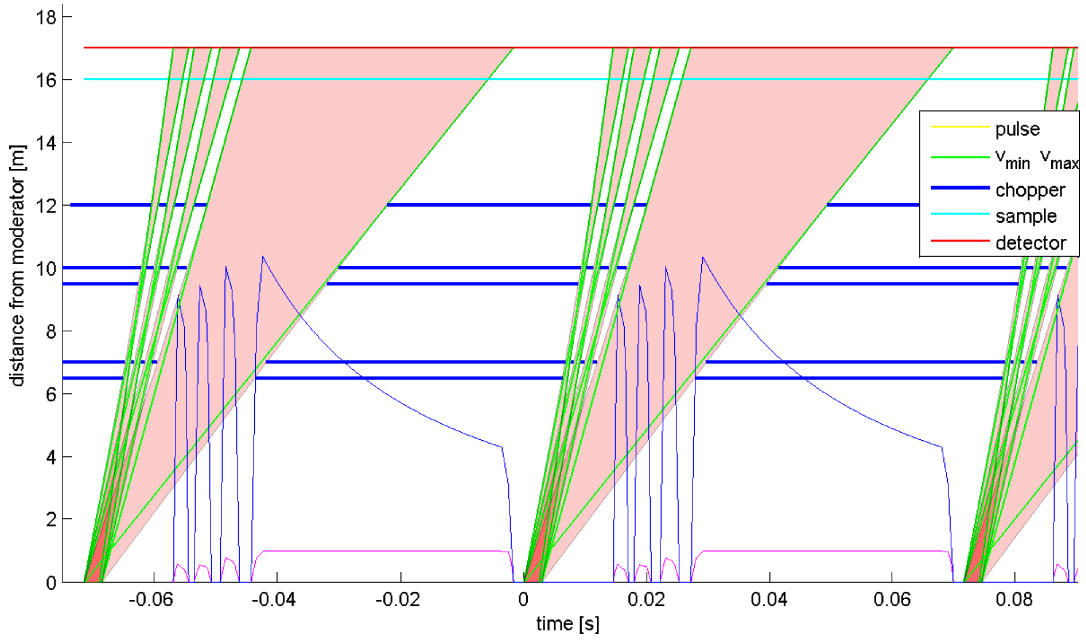

Fig. 3. Time of flight diagram showing the chopper system for improving the wavelength resolution, shown with a 1 m sample to detector distance. The calculated results (on the same y axes) is shown for wavelength resolution in percentage (blue line) and flux ratio relative to when only the bandwidth choppers are running (magenta line). The bandwidth shown here is 3-18.9 Å.

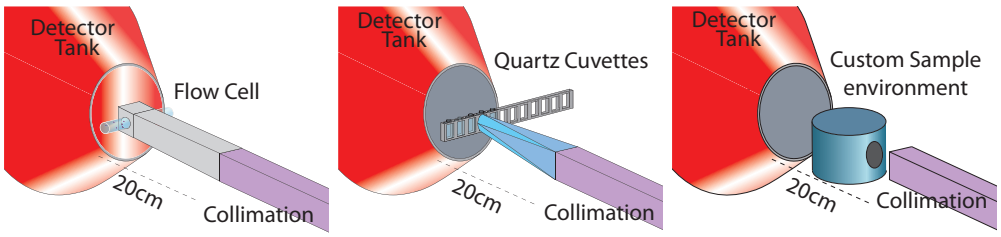

Fig. 4. Sketch of the three sample environment schemes. **Left:** the small sample flow through mode, where the flow cell is placed next to the detector tank window and connected to the collimation section via an unbroken vacuum. **Middle:** Standard quartz cuvette sample changer placed close to the detector tank window. A "nose" is inserted in order to extend the vacuum as close to the sample position as possible. **Right:** Here the 20 cm gap is used to house a custom fitted environment. It is important to note that the 20 cm gap is only a limitation between the detector tank window and the collimation section, there is more space available both above and below for the more bulky parts of the sample environment.

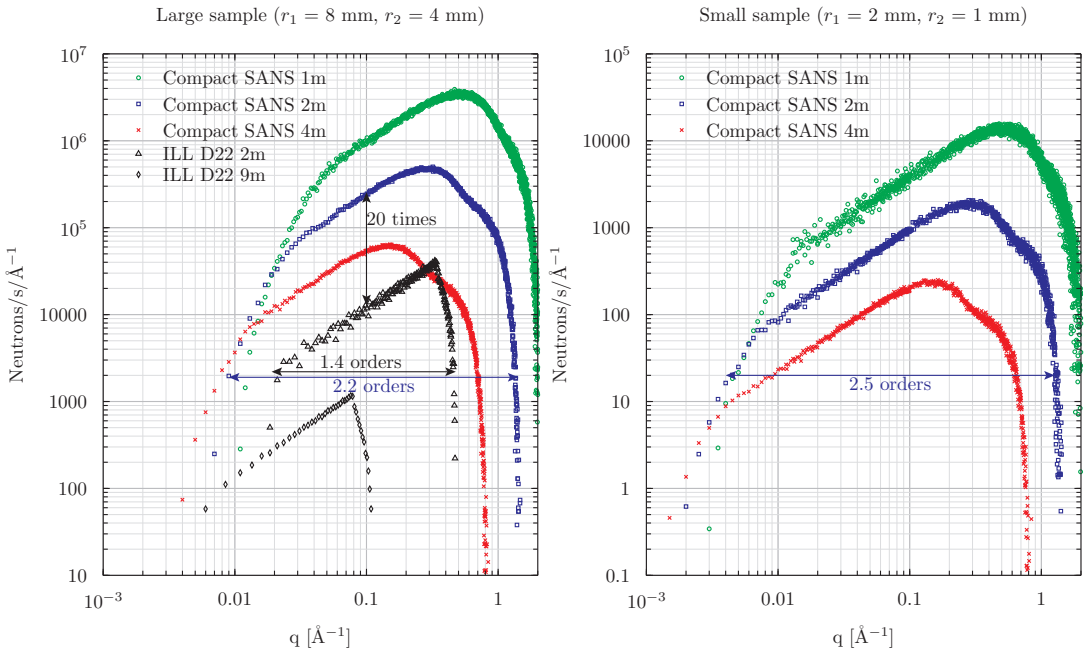

Fig. 5. Monte Carlo simulation of instrument performance measured in neutrons reaching the detector per second per Å^{-1} as a function of q. The sample is a simple model of the isotropic scattering from 1 mm of H_2O.

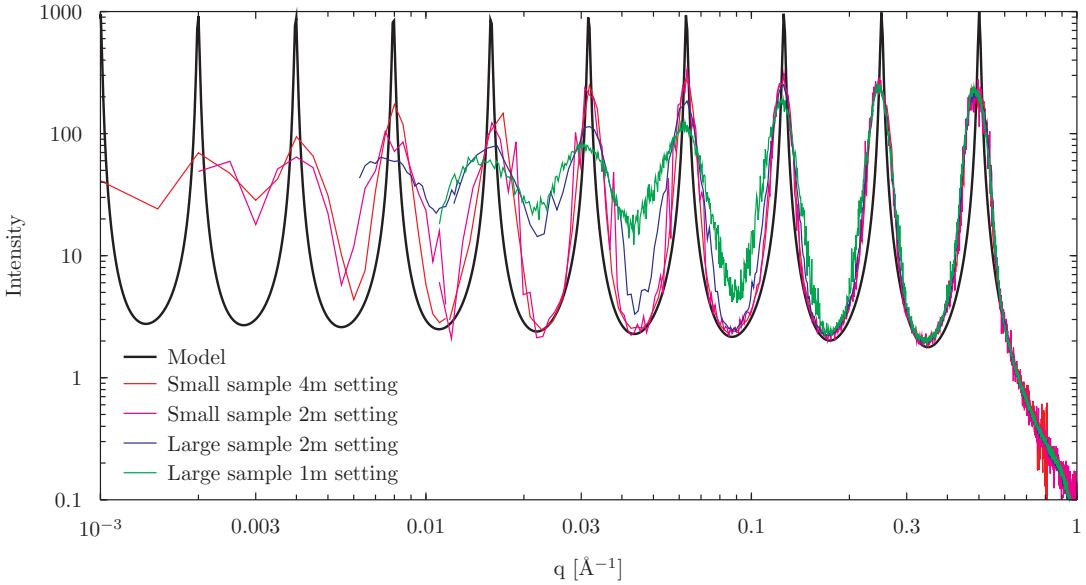

Fig. 6. Instrumental smearing at various settings. The resolution at different q-ranges is made clear by a Monte Carlo simulation of the scattering from a "sample" featuring logarithmically spaced sharp peaks.

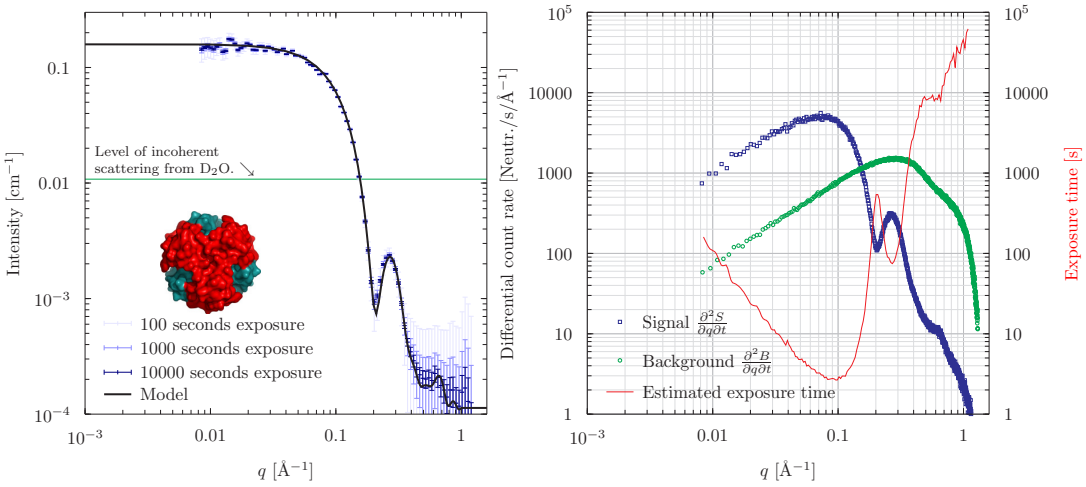

Fig. 7. Monte Carlo simulation of scattering signal from 5 mg/ml insulin in D_2O buffer. **Left:** The intensity curve without the background signal overlayed with the scattering curve of the model. The error bars expected after 100, 1000 and 10000 seconds measurement are shown. **Right:** Differential count rates that can be used to estimate the exposure times needed to get good statistics at various q (from equation (11)). This is shown in red, for $\Delta q = 0.1q$ and (S/N)=10.

References

Dewhurst, C. D. (2008). *Measurement Science and Technology*, **19**(3), 034007.

Franke, D., Kikhney, A. G. & Svergun, D. I. (2012). *Nuclear Instruments and Methods in Physics Research Section A: Accelerators, Spectrometers, Detectors and Associated Equipment*, **689**, 52–59.

Heenan, R., Penfold, J. & King, S. (1997). *Journal of applied crystallography*, **30**(6), 1140–1147.

Lefmann, K. & Nielsen, K. (1999). *Neutron News*, **10/3**, 20–23.

Lieutenant, K. & Mezei, F. (2006). *Journal of Neutron Research*, **14**(2), 177–191.

Lynn, G., Heller, W., Urban, V., Wignall, G., Weiss, K. & a.a. Myles, D. (2006). *Physica B: Condensed Matter*, **385-386**, 880–882.

Mezei, F. & Russina, M. (2002). In *International Symposium on Optical Science and Technology*, pp. 24–33. International Society for Optics and Photonics.

Pernot, P., Theveneau, P., Giraud, T., Fernandes, R. N., Nurizzo, D., Spruce, D., Surr, J., McSweeney, S., Round, a., Felisaz, F., Foedinger, L., Gobbo, a., Huet, J., Villard, C. & Cipriani, F. (2010). *Journal of Physics: Conference Series*, **247**, 012009.

Roessle, M. W., Klaering, R., Ristau, U., Robrahn, B., Jahn, D., Gehrmann, T., Konarev, P., Round, A., Fiedler, S., Hermes, C. & Svergun, D. (2007). *Journal of Applied Crystallography*, **40**(s1), s190—-s194.

Seeger, P. A. & Hjelm Jnr, R. P. (1991). *Journal of Applied Crystallography*, **24**(5), 467–478.

Willendrup, P., Farhi, E. & Lefmann, K. (2004). *Physica B: Condensed Matter*, **350**(1-3), E735–E737.

Synopsis

A ToF-SANS instrument is proposed that is optimised to exploit the source characteristics of the upcoming European Spallation Source towards getting the highest possible neutron flux at the sample position. We find that a relatively compact instrument instrument provides the best exploitation of the neutrons in the single pulses and allows for covering the broadest possible q-range in a single setting.

ESS Instrument Construction Proposal Compact SANS Optimised for Biological Samples

March 1, 2013

K. Klenø[1], S. Kynde[1], G. Nagy[2], N. Skar-Gislinge[1], K. Mortensen[1], K. Lefmann[1], J. Kohlbrecher[2], L. Arleth[1],

[1]*Niels Bohr Institute, University of Copenhagen, Denmark*

[2]*SINQ, Paul Scherrer Institute, Switzerland*

Overview

We hereby propose that a SANS instrument optimised for high throughput analysis of biological samples is constructed as one of the instruments in the SANS instrument suite at the ESS. In order to allow for minimising the sample volume, cover a broad q-range relevant for biological samples and obtain short measurement times, it turns out that a rather compact layout is the preferred one. The proposed instrument has a total maximal length of 20 meters from moderator surface to detector, it has the sample positioned at 16 meters from the moderator, and has a maximal collimation length and sample to detector distance of 4 meters each.

The resolution in terms of $\delta\lambda/\lambda$ at such a compact instrument is intrinsically less good than at a longer instrument. While our simulations show that the relaxed resolution is unproblematic for a broad range of biological samples, a better resolution may be required in several cases. In order to allow for this, a set of disc choppers may be build into the guide and collimation sections. By sacrificing some of the high neutron intensity, this allows for obtaining a very low $\delta\lambda/\lambda$ when required, while still maintaining the very broad q-range in a single setting that is achievable at the short instrument.

Being optimised for investigations of bio-molecular solutions, the proposed instrument has a small sample area compatible with a flow-through based sample handling robot. However, even with the small sample area, several other types of sample environment may easily be fitted in. This opens up for using the instrument for a broad range of applications within condensed colloidal and soft matter systems.

The proposal is developed by the SANS work group of the Swiss-Danish ESS workpackage. The main contributors are located at the Niels Bohr Institute at the University of Copenhagen in Denmark and at the SINQ at the Paul Scherrer Institute in Switzerland. The pre-investigations for the proposal have mainly been carried out in the period from February 1, 2012 to February 28, 2013. The instrument proposal is developed in collaboration with Dr. Andrew Jackson at the ESS and with scientific feed-back from the SANS Scientific and Technical Advisory Board at the ESS.

1 Scientific Impact

The high flux at European Spallation Source (ESS) allows for performing experiments with small beam-sizes while still maintaining a high intensity of the incoming beam. The central goal of the presently proposed instrument is to develop a Time-of-Flight based SANS instrument optimised for sample volumes of 8 µL ($2 \times 2 \times 2$ mm^3) while still covering a wide q-range in a single setting. The combined requirement of a small sample volume and a large dynamic range in a single setting makes a quite compact SANS instrument the most optimal choice. The q-range obtained with the proposed configuration is basically the same as that covered at SAXS instruments optimised for biological samples and has already proven to be highly relevant for a large user community.

The possibility of covering a large q-range in a single setting, and using only a small sample volume, suggests that the solution SANS experiments at the proposed instrument may optimally incorporate flow-through sample cell set-ups in combination with automated liquid handling robots. Such sample environments have recently been developed and implemented at synchrotron SAXS facilities. However, it should be emphasised that the proposed instrument layout, with a path length of the sample environment of 20 cm, is also compatible with several other types of sample environments typically used to investigate soft matter systems. Besides from the standard Hellma Quartz cuvettes, the sample region will allow for incorporation of a shear cell, a furnace, a pressure cell, a vacuum cell, a cold finger cryostat or a permanent magnet.

The proposed compact SANS instrument has a very high flux but at the cost of a relatively poor $\delta\lambda/\lambda$. While our simulations demonstrate that this relaxed

resolution is unproblematic for a broad range of typical biological of or soft matter samples, there are also several scientific cases where a better resolution will be required. The proposed instrument includes a set of choppers for exactly this purpose. These provide the opportunity of a $\delta\lambda/\lambda$ from 4% to 19% (depending on setting and wavelength) down to below 11 % at all wavelengths at the cost of a decrease in the neutron intensity at the sample down to around 40 % of the standard.

As a central part of optimising a SANS instrument for weakly scattering biological samples, different means for increasing the signal-to-noise ratio was investigated in the preparation phase of this project. Our central idea was to use the choppers for discriminating between the elastic and inelastic signal and potentially to suppress the inelastic part of the incoherent contribution to the scattering background. Our calculations and simulations showed that the approach might indeed allow for suppressing part of the background. However, the cost of the suppression, in terms of loss in counting statistics, made the solution unattractive for almost all practical purposes. Consequently, this idea has been abandoned in this final version of the instrument proposal.

SANS on Biological Samples The primary target for which the proposed instrument has been optimised are biological and colloidal samples in solution. Most existing SANS instruments were originally designed with many different applications in mind corresponding to the broad range of needs defined by the general user community. The instrument planning process at the ESS allows for a much more coordinated strategy towards the instrumentation than what has typically been the case at other facilities. This allows for a more optimal focusing of different SANS instruments to different scientific applications right from the early phase of designing the instrument.

Such a more narrow scientific focusing have become more common in the SANS community during the last few years. Examples are the BioSANS instrument at the HFIR reactor facility at Oak Ridge National Laboratory which is optimised for biological applications, and the D33 instrument at Institut Laue Langevin, which is primarily optimised for studies in magnetism. At the HFIR-BioSANS instrument, very important lessons have already been learnt with respect to securing that the potentially very large biological user community is sufficiently well prepared and trained for optimally exploiting the potential of such a dedicated SANS instrument. The ILL-D33 instrument is still too young to be fully evaluated, but based on the strong and well-established community that performs SANS on magnetic systems at the ILL, a strong performance is expected for this instrument right from the beginning.

The proposed instrument will allow for addressing a science case that is very similar to that of the BioSAXS instruments at e.g. Petra-III in Hamburg (P12) and

the BM29 BioSAXS instrument at ESRF, Grenoble, as well as to the recently decommissioned X33 beamline at the old DORIS synchrotron in Hamburg. At these instruments, a strong scientific focus of both the instrument and the beamline staff has allowed for optimising and automating the data acquisition process to a level that goes far beyond what is available at any SANS instrument. This involves keeping the sample consumption at a minimum as well as using fully automated routines for both the data reduction and first part of the data analysis (e.g. automated background subtraction, indirect Fourier transform and ab initio bead model fitting). All this allows the user to focus on the samples and on the results of the SAXS experiment as the experiment takes place. This improved user friendliness has opened up the SAXS technique for a quickly growing user community originating from structural biology. The resulting scientific output, in terms of publications, is very impressive.

At most SANS facilities, on the other hand, many users with non-physicist backgrounds have to place a major part of their attention in operating the instrument and making the initial processing of the data. The means that the experimental feed back during the experiment may become very weak and that users may limit themselves to do measurements of preplanned series regardless of the sample quality. A situation where the users quickly obtain the information to focus their experiment on the good-quality samples and maybe even can perform experiments that actually helps solving the problems with the remaining samples would be much more desirable.

The solution SAXS approach to investigate bio-molecules is particularly successful in the study of the large group of water soluble proteins, where SAXS complement protein crystallography data very well. However, a very important topic in structural biology is the large group of membrane proteins. Despite remarkable breakthroughs in this field during the last few years, including the award of the 2012 Nobel Price in Chemistry, very little is still known about the structure and functioning of membrane proteins and how they incorporate and interact with the lipid membrane. As the majority of medical drugs target membrane proteins, and as we are only just beginning to understand how this takes place, it is strongly anticipated that this will remain a very important research topic in the decades to come with continued very large scientific impact.

While SANS will clearly never be able to compete with SAXS in terms of beam-brightness, SANS in combination with contrast variation, opens up new possibilities when it comes to the study of membrane proteins and other more complex biological samples. However, as these the most exiting samples are typically limited to very small quantities, it is in many cases not practically possible to run the measurements at present SANS instruments which typically require 200-300 µL sample volumes. With the proposed instrument we will be able to target these and many other types of samples that are limited in volume much better

than today. The increase in neutron intensity provided by the ESS, will make it attractive to work with beam diameters of about 2 mm and hence sample volumes at 10-20 µL. Our simulations show that a very broad q-range can be covered in a single setting at a small-volume sample, while maintaining the same measurement time, typically a few minutes, that is required to obtain a single setting measurement at the D22 at ILL.

In the many cases where the sample volumes are less restricted and sample volumes of 200 µL may easily be obtained, the SANS instrument may be operated in a truly high-throughput fashion and with sub-minute measurement times depending on the sample. The ≈ 3 orders of magnitude that can be covered in a single experimental configuration in combination with the high neutron intensity, opens up for running fast time-resolved experiments much more optimally than at present pulsed and continuous source based instruments.

An important lesson to be learnt from both the BioSAXS facilities and from BioSANS experiments is that the sample preparation is generally significantly more demanding than anticipated from the point of view of the users prior to the experiments. In most protein systems it is necessary to perform a careful pre-optimisation of the formulation conditions in order to produce a well-defined protein-in-solution sample, that are sufficiently good to allow for a careful SAXS analysis. While this is already an issue in the H_2O-based buffers typically used in SAXS experiment, the problem becomes even more predominant when changing to the D_2O-based buffers in SANS experiments. In Europe much of this initial user-training as well as the development of more optimal sample preparation facilities and sample handling expertise is already taking place in connection with the SAXS beamlines and as a natural result of the growing BioSAXS community. While most protein systems have to be handled on a one by one basis, it is anticipated that the general awareness of the problem and the experience in solving it, that have been generated via the BioSAXS community should make the task somewhat smaller in the BioSANS community.

SANS on non-biological samples The proposed instrument is optimised with biological samples in mind. Assuming typical beamtimes of 12-24 hours it will allow for hosting a very high number of user experiments each year. Even though there is a good potential for a very large SANS user community in Life Sciences - simply based on the overall size of this scientific community as a whole as well as on the quickly emerging BioSAXS community - it may become difficult to fill all the available beamtime with Life Science users from the beginning of the operations.

Fortunately, the proposed instrument may easily be adapted to a very attractive more general purpose SANS instrument by simply changing the sample environment as described in section 3. While this scientific "de-focusing" will obviously

give a less high level within BioSANS, mainly due to the associated reprioritisation of the beamline staff, it may alleviate the major part of the risk associated with focusing a SANS instrument on a scientific area that is still not strongly represented in the present SANS community.

The proposed instrument, if operated in a more standard SANS mode, will be at least a factor of 20 faster than the benchmark instrument D22 at ILL while at the same time cover a broader q-range. This opens up for new and exciting experiments in time-resolved SANS. Furthermore, the fact that a typical beamtime will be around 24 hours, will automatically open up for a very high scientific throughput, production and impact of this beamline.

2 User Base and Demand

The aim of the proposed instrument is to address some of the needs and requests of the user community in Structural Biology. The Structural Biology community has been extremely successful from a scientific point of view during the last decades. This is reflected in the Nobel Price in chemistry in 2009 (for the determination of the ribosome structure) and in 2012 (for the determination of a class of G-protein coupled receptors, GPCRs), that are both based on Synchrotron X-ray crystallography work. But also reflected in a strong overall representation in Nature and Science journals. These breakthroughs would not have been possible without synchrotron X-ray instruments dedicated to the biological samples studied. As an example, the work on the GPCRs (2012 Nobel Prize) heavily relied on the availability of microfocus X-ray beams, which were co-developed with a strong user-community and with a rather narrow range of applications in mind.

While there is a strong potential for investigations of biological systems with neutrons, the potential is until now far from being reached and the life science user community are very underrepresented at most neutron scattering facilities when seen in relation to their strong representation at the synchrotron X-ray facilities and in academia and industry more generally. The present proposal is based on the presumption that if a SANS instrument optimised for biological samples becomes available and accessible to the users, then the user community, the strong scientific cases, and the high impact publications will naturally follow.

As mentioned in the previous section, such BioSANS instruments are not yet available in Europe. However, during the last decade a dedicated BioSAXS instrument has gradually been developed and optimised by Dmitri Svergun's group at the X33 beamline at the second generation synchrotron DORIS at DESY in Hamburg, and it is instructive to have a look at some of their statistics (see figure 1). The graphs illustrate two central points: 1) Despite that the group has focused almost entirely on growing a user community with a rather narrow

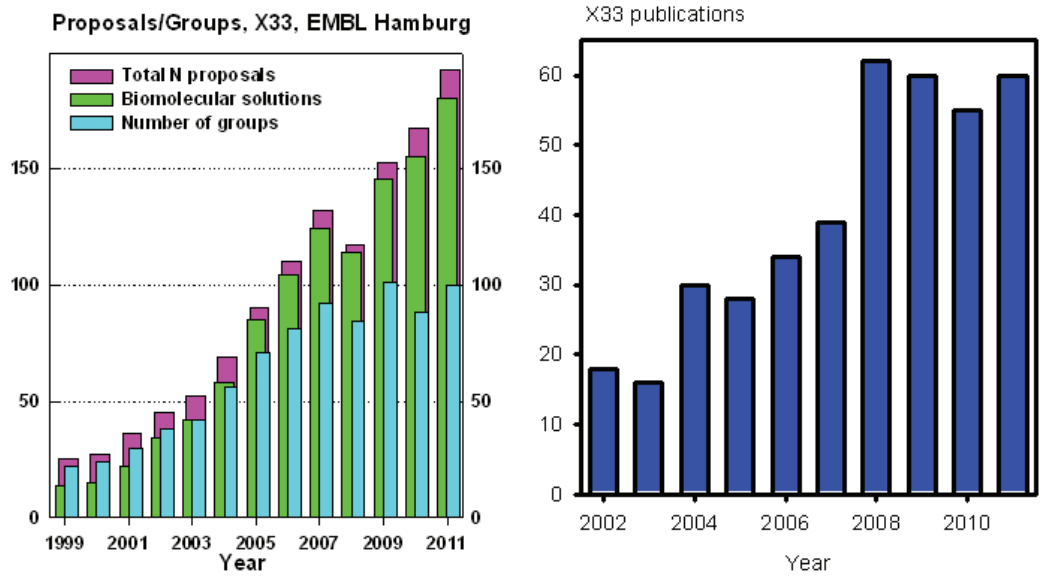

Figure 1: *User and publication statistics from the X33 beamline at the Doris synchrotron in Hamburg. Reproduced with permission from D. Svergun, EMBL Hamburg.*

central interest in investigating samples that can be categorised as "proteins in solution", there have been no problems filling the available beamtime. 2) The beamline focus on bio-molecular solutions, both with respect to instrumentation and scientific staff, has significantly payed off in terms of scientific publications. The annual number of publications resulting from the beamline has increased from about 20-30 per year in the first half of the ten year period to about 60 per year in the second half. In this context, it should be emphasised that the publications include several high impact publications like Nature, Science, PNAS and EMBO Letters publications. This demonstrates that the beamline, even though it was placed at a second generation synchrotron, has been able to contribute significantly to the solving of many central problems in the area of life sciences.

Similar scientifically focused BioSAXS beamlines have been developed several places in the world in the last few years. Both at the Petra-III in Hamburg and at the ESRF, but also at less high intensity synchrotrons such as at CHESS at Cornell University and at Lawrence Berkeley National Laboratory. After a bit of maturation time, all facilities look very promising with respect to scientific production and there are not yet any indications that the user community has reached its saturation level. The typical time for a full measurement (including sample handling and background measurement) is about 5-10 minutes at ESRF and at Petra-III and the typical beamtime is 8-24 hours or less. This implies that

the facilities can host at least 200 user groups annually and obtain a very strong scientific production.

While the proposed SANS instrument will naturally have less flux than a modern BioSAXS instrument, the SANS instrument comes with the intrinsic advantage of the option of contrast variation. As discussed above, most of the work from Dmitri Svergun's group is based on systems of proteins in solution. While this is a very important scientific case, it will not be advantageous to use SANS instead of SAXS for these investigations. However, many of the cutting edge biological applications deal with more complex biological structures, such as membrane proteins in cell membranes, protein-DNA/protein-RNA complexes or quaternary protein structures. In all these systems, the option of contrast variation SANS on very small samples volumes has the potential of becoming the key to determining the structures.

It is clear that all of the bioSAXS community will not be directly transferable to a future BioSANS community. On the other hand, there are several experiments among the above mentioned that are not performed at the present BioSAXS beamlines due to the lack of opportunities within contrast variation. So while it is expected that there will be significant overlaps between the emerging BioSAXS community and a future BioSANS community at the ESS, a dedicated ESS BioSANS instrument is also expected to foster its own unique user community.

It is impossible to give a reliable quantitative estimate of the future user base for the proposed instrument. At present, however, it is very clear that the otherwise enormous Life Science area is very under-represented in the SANS community as compared to e.g. the communities for much more specialised scientific areas such as polymer science, colloids and surfactants, and condensed materials. This is clear from the Figure 1 of the LoKI SANS instrument proposal from the ESS, which shows that only about 6% of the present SANS experiments may be categorised as Life Sciences. Only a decade ago, the situation was comparable in the SAXS community. But with the emergence of more user-friendly SAXS instruments as well as better and more robust data analysis software, the user community has gradually matured and are now to a much larger extent able to benefit from the available instruments and produce high impact science.

3 Description of Instrument Concept and Performance

The proposed compact SANS instrument is envisioned for high throughput studies of biological and soft matter. It essentially has two modes of operation: One is a high flux mode, fully utilising the high flux pulse produced by the ESS. Due

to the short distance from the source this gives rise to relatively poor resolution in terms of $\frac{\delta\lambda}{\lambda}$ on the instrument, but as we will show, for typical examples of biological macromolecules, this does not pose a significant problem.

The second mode of operation is the chopped SANS mode. Here a series of choppers are used to "monochromatise" and shape the incoming pulse. This improves the resolution of the instrument considerably, although with a trade off in intensity.

First, the general setup of the instrument is described. This is followed by an account of the expected performance of the high flux and small sample operation modes. Finally the Chopped SANS operation mode is described.

3.1 Basic Instrument Layout

The instrument consists of an initial transport section, a collimation section, a sample environment, and a detector tank. See figure 2.

3.1.1 Transport Section

The transport section begins at 2 m from the source, and starts with a 9.9 m long bender with a cross-section of 2 cm $\times$ 2 cm. It is curved with a radius of 280 m which breaks the line of sight from the moderator to the sample twice; i.e. the point where the line of sight from the moderator is broken, cannot be seen from the sample position. After the bend guide follows the collimation section, which for a neutron transport optimisation perspective is a 3 m long straight guide with a 2 cm $\times$ 2 cm cross-section, when the instrument is in the 1 m collimation mode. In total this guide system blocks line of sight from the moderator to the sample with a minimum of 13.6 m of shielding for any straight line.
Note that for the purpose of line of sight calculations, it has been assumed that in the 2 m space between the moderator and the guide, there is a 2 cm $\times$ 2 cm beamtube. If this is not the case, the transport system may have to be slightly modified to meet desired line of sight requirements.

The m-values of the coating required for this transport section is as follows: m=2.4 for the outer wall of the bender, m=1 for the inner wall of the bender, and m=2.1 for the top and bottom of the bender and the guide in the collimation section.

Figure 3 shows the layout of the transport section and how the line of sight is blocked, and figure 4 shows the brilliance transfer through the guide system as a function of wavelength, when using the 1 m collimation setting.

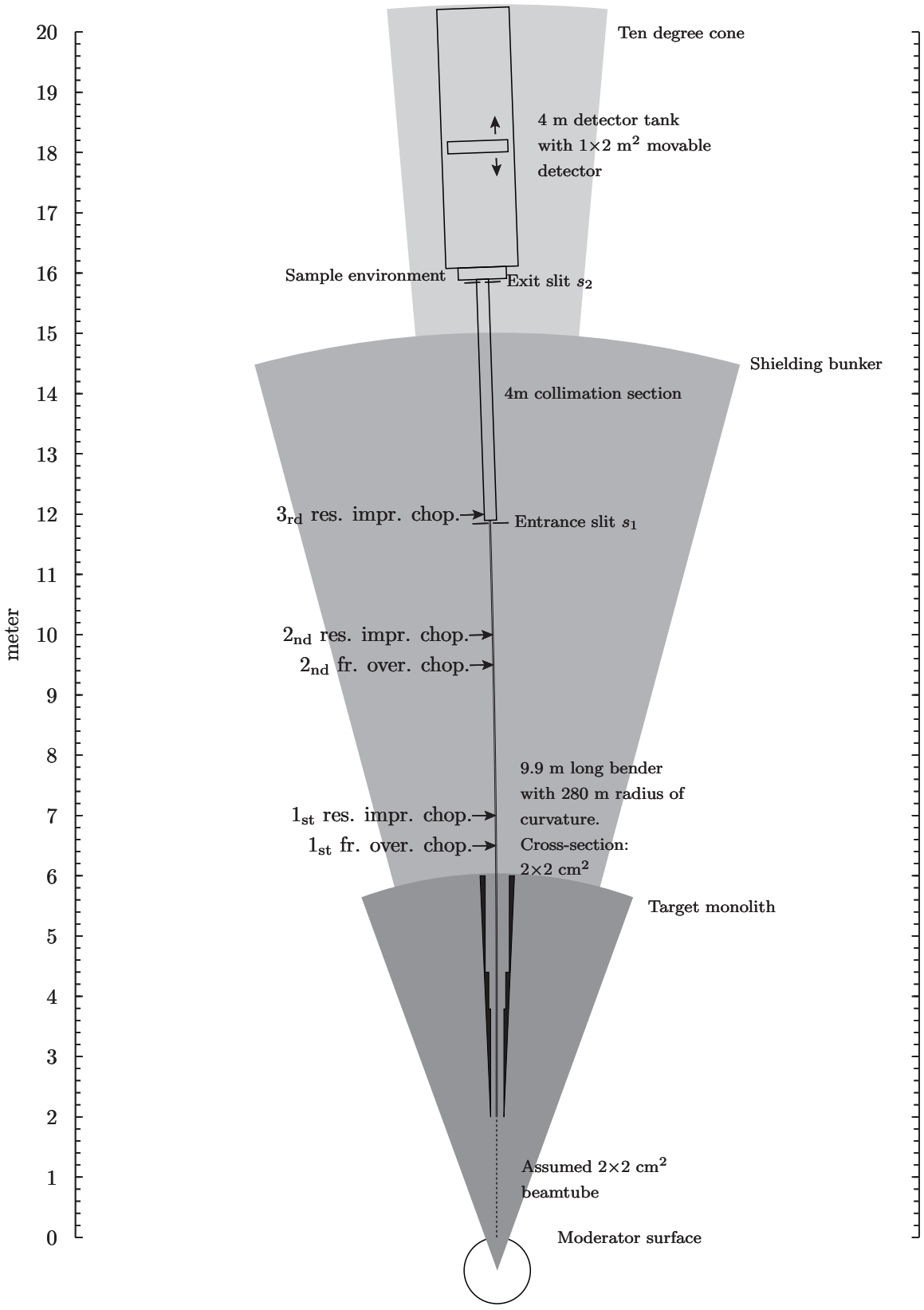

Figure 2: *Schematic drawing of the proposed instrument. (1 cm corresponds to 1 m)*

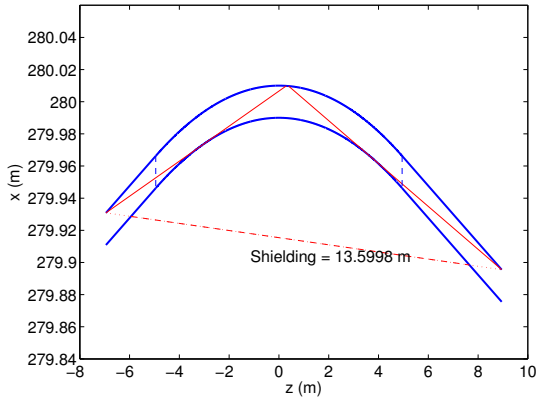

Figure 3: *Diagram showing the transport section with the bender and collimation section (blue) and line of sight from the moderator and sample positions (red). Since the two red lines do not overlap, line of sight is blocked twice. The dashed red line shows the direct line through the transport system that must penetrate the minimum amount of shielding. The moderator is at the left end of the transport system, and the sample position at the right end. The origin of the coordinate system is the centre of the bender circle. Note that the scale on the axes differ.*

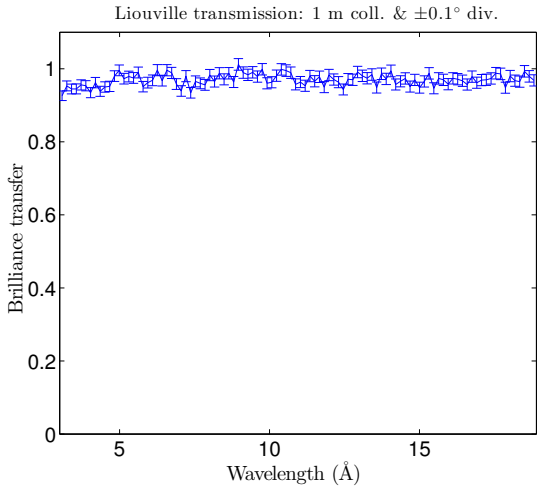

Figure 4: *Brilliance transfer from source to sample as a function of wavelength within the phase space of 5 mm × 5 mm and a 0.1 ° radial divergence. Left: without choppers. Right: with choppers in variable burst mode.*

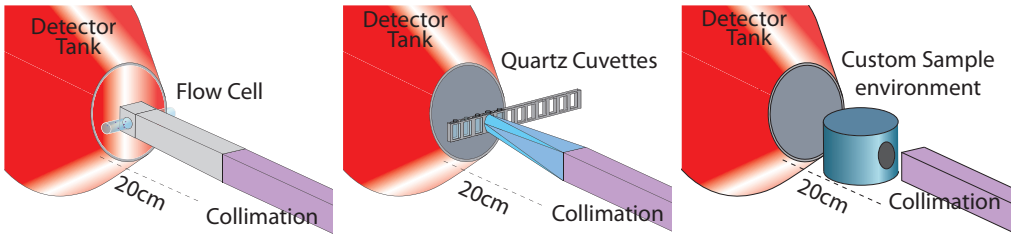

Figure 5: *Sketch of the three sample environment schemes. Left: the small sample flow through mode, where the flow cell is placed next to the detector tank window and connected to the collimation section via an unbroken vacuum. Middle: Standard quartz cuvette sample changer placed close to the detector tank window. A "nose" is inserted in order to extend the vacuum as close to the sample position as possible. Right: Here the 20 cm gap is used to house a custom fitted environment. It is important to note that the 20 cm gap is only a limitation between the detector tank window and the collimation section, there is more space available both above and below for the more bulky parts of the sample environment.*

3.1.2 Collimation Section

The 4 m long collimation section starts at 11.9 m from the moderator surface and consists of four 1 m elements. The first three elements can be exchanged with extra guide sections allowing for collimation lengths of 4 m, 3 m, 2 m, or 1 m. The extra guides are inserted vertically to make room for maximal shielding on the sides. The two defining slits are circular and denoted s_1 and s_2 as indicated on figure 2.

As an alternative to movable guide elements, additional movable slits could be used to 'deactivate' the unwanted guide elements. Which option is preferable is left to engineering considerations.

3.1.3 Bandwidth Definition Choppers

The bandwidth will be defined using the time-of-flight principle using two disk choppers. These will rotate with a frequency of 14 Hz and be located at 6.5 and 9.5 m from the source. This will ensure that long wavelength neutrons from previous pulses does not interfere with the measurement.

3.1.4 Sample Environment

In the envisioned instrument a gap of 20 cm between the collimation section and the detector tank is available for the sample environment. When only very small sample volumes are available a flow cell will be placed in an unbroken vacuum

extending all the way from the beginning of the collimation section to the detector tank. This scheme is outlined in figure 5, left. The cell can be loaded with a robotic sample changer allowing for fully automated, high throughput measurements. This type of setup is currently available and tested at most dedicated BioSAXS beamlines.

In case of a more conventional sample environment using quartz cuvettes, the samples are placed immediately before the detector tank and the collimator is prolonged with a 19 cm nose extending the vacuum all the way to the sample. This scheme is shown in figure 5, middle.

Finally the whole 20 cm gap can be used for a custom fitted sample environment, for example a rheometer, a permanent magnet, a pressure cell, or a cold finger cryostat. These may have to be custom fitted into the 20 cm gap, which should be technically feasible for all the proposed sample environments. The scheme is shown in figure 5, right. It is important to note that the space available above and directly below the 20 cm gap is considerably larger and should easily accommodate the motor and control hardware for, for example a rheometer.

3.1.5 Detector Tank

The detector tank is 4 m long and has room for a 1 m $\times$ 2 m detector with 5 mm pixels. Preferably, a 20 cm $\times$ 20 cm area in the middle of the detector has 2 mm pixels. We envisage the detector mounted on rails to make it possible to move it forth and back in the direction of the beam to optimise the covered q-range. We are aware that development several places is going in the direction of multi-detector setups. Both at SANS2D (ISIS) and D33 (ILL) such solutions have been implemented. It is expected that this instrument will also benefit from such a solution, but for the ease of comparison to the benchmark instrument D22 (ILL) we have simply assumed a single flat detector. If required, it will also be straight forward to place the entire detector tank on rails, allowing for a larger sample environment. But at present we do not see the need for this option.

3.2 Instrument Performance

In the following L denotes the full length of the instrument from moderator to detector, A is the distance from the moderator to the collimator and L_1 is the collimation length. The 20 cm sample space is centred at 16 m from the source and $A+L_1$ is 15.9 m in the proposed instrument. The sample to detector distance is denoted L_2. The radii of the pinhole apertures are denoted s_1 and s_2.

Calculations are shown for two sample sizes. The first uses s_1= 8 mm and s_1= 4 mm intended for samples in standard 1 cm wide Hellma quartz-cuvettes. The second uses s_1= 2 mm and s_2= 1 mm intended for <10 µl samples loaded into the

flow through cell. Small sample volumes like this can not be handled routinely at any existing SANS beamlines. The large pinholes allow for short measurement times and high throughput measurements while the small pinholes allow for measuring small sample volumes at comparable measurement times as D22 (ILL) at present.

For each sample size we consider three standard settings of $L_1 = L_2 = 1$ m, $L_1 = L_2 = 2$ m and $L_1 = L_2 = 4$ m.

3.2.1 Analytical Considerations

The key performance characteristics presented in tables 1, 2 and 3 are calculated in the following way: Using the de Broglie conversion factor α=252.7 µs/Å/m between neutron wavelength [Å] and inverse velocity [µs/m], the uncertainty in λ is

$$\delta\lambda = \frac{\tau}{L\alpha}, \tag{1}$$

where $\tau = 2.86$ ms is the pulse width at ESS and L is the total instrument length from moderator surface to detector. The width of the wavelength band that can be accommodated without frame overlap is

$$\Delta\lambda = \lambda_{\max} - \lambda_{\min} = \frac{T - \tau}{L\alpha}, \tag{2}$$

where T=71.4 ms is the source period at the ESS. If we set the minimum wavelength to $\lambda_{\min} = 3$ Å, the maximum wavelength is calculated from (2). The radius of the direct beam spot size on the detector is

$$S = s_2 + (s_1 + s_2)\frac{L_2}{L_1}. \tag{3}$$

Assuming that the usable part of the detector starts 1.5 S away from the beam centre, this gives a minimum q-value of

$$q_{\min} = \frac{4\pi}{\lambda_{\max}} \sin\left(\frac{1}{2}\text{atan}\left(\frac{1.5S}{L_2}\right)\right) \approx \frac{3\pi}{\lambda_{\max}}\left(\frac{s_2}{L_2} + \frac{s_1 + s_2}{L_1}\right). \tag{4}$$

The maximum-q-value is set to

$$q_{\max} = \frac{4\pi}{\lambda_{\min}} \sin\left(\frac{1}{2}\text{atan}\left(\frac{D}{L_2}\right)\right), \tag{5}$$

where D is the distance from the beam centre to the furthest corner of the detector. With the beam centred on a 1×1 m^2 square detector we have $D = 0.5\sqrt{2}$ m. For the 1×2 m^2 detector we use $D = \sqrt{1.5^2 + 0.5^2}$ m, corresponding to a beam centred on the lower square of the detector. The numbers for the large detector are given in parentheses in tables 2 and 3.

Instrument length: $L = A + L_1 + L_2$	$\delta\lambda/\lambda$ @ 4 Å	$\delta\lambda/\lambda$ @ 8 Å	$\delta\lambda/\lambda$ @ 12 Å	Bandwidth [Å] $\Delta\lambda$
17=15+1+1	17%	8%	6%	15.9
18=14+2+2	16%	8%	5%	15.0
20=12+4+4	14%	7%	5%	13.5

Table 1: *Wavelength resolution at selected wavelengths and settings, and the corresponding bandwidth of the pulse.*

3.2.2 Monte Carlo Simulations

A model of the instrument has been implemented in McStas, and the number of neutrons/second on the sample has been calculated with this.

The flux on sample is just this number divided by the aperture area of the second pinhole.

For comparison, numbers are also shown for ILL beamline D22 with the setting s_1=4 mm, s_2=8 mm, $L_1 = L_2$=2 m. A velocity selector with a wavelength resolution of 10% has been used and a 1×1 m^2 detector assumed. We have furthermore assumed the peak intensity wavelength at $\lambda = \lambda_{\rm min} = \lambda_{\rm max} = 4.5$ Å. In figure 7 we have also shown the performance of D22 in a setting that is suited for lower q-values. This setting uses 9 m collimation and the velocity selector aimed at 4.5 Å neutrons. The performance is not much different when using a longer wavelength and shorter collimation. A McStas implementation of the source and guide system of ILL/D22 has kindly been provided by Emmanuel Farhi.

In the small sample configurations where s_1 =2 mm, s_2=1 mm and $L_1 \approx L_2$, we will have a spot radius of only 4 mm at the detector. To utilise the lowest q values of these settings, pixel sizes of about 2 mm will be needed at least in the centre of the detector. If this is not possible one will probably want to use a larger collimation entry, e.g. s_1=8 mm to get same flux on sample and q-range as in the large sample case. This setting may also be preferred in situations where lowest q-values are not crucial.

In the following we show how scattering from various samples will appear in the proposed instrument. In the simulation a detector efficiency of 100% has been assumed, with pixels of 5×5 mm^2. In the large sample configuration a circular beam stop of radius 2.6 cm has been assumed. For the small sample configuration a beam stop of 7 mm radius has been used. In this configuration we also assumed a smaller pixel size of 2×2 mm^2 at the centre of the detector. For simplicity and ease of comparison a 100% detector efficiency was assumed for both the proposed instrument and the benchmark instrument. It should however be remembered that a real detector typically has an energy dependent measurement efficiency.

Instrument length: $L = A + L_1 + L_2$	$q_{\min}$ (Å^{-1})	$q_{\max}$ (Å^{-1})	Flux on sample (n/s/cm^2)	Neutrons on 50.3 mm^2 sample (n/s)
17=15+1+1	0.0080	1.27 (2.02)	12×10^8	5.9×10^8
18=14+2+2	0.0042	0.71 (1.38)	3.3×10^8	1.7×10^8
20=12+4+4	0.0023	0.37 (0.78)	0.88×10^8	0.44×10^8
ILL D22 A+2+2	0.0168	0.47	0.28×10^8	0.11×10^8

Table 2: *Instrument performance with the Large Sample configuration: s_1=8 mm, s_2=4 mm and 1×1 m^2 detector. Numbers in parenthesis correspond to the 2×1 m^2 detector*

Instrument length: $L = A + L_1 + L_2$	$q_{\min}$ (Å^{-1})	$q_{\max}$ (Å^{-1})	Flux on sample (n/s/cm^2)	Neutrons on 3.14 mm^2 sample (n/s)
17=15+1+1	1.9×10^{-3}	1.27 (2.02)	9.3×10^7	29×10^5
18=14+2+2	1.0×10^{-3}	0.71 (1.38)	2.3×10^7	7.3×10^5
20=12+4+4	5.7×10^{-4}	0.37 (0.78)	0.57×10^7	1.8×10^5

Table 3: *Instrument performance for the Small Sample configuration: s_1=2 mm, s_2=1 mm and 1×1 m^2 detector. Numbers in parenthesis correspond to the 2×1 m^2 detector*

Intensity and q-range Figure 6 and 7 plots the scattering from an isotropic scatterer. The isotropic scattering corresponds to the elastic incoherent contribution from 1 mm of H_2O.

In figure 6 the resulting detector image for the integrated pulse is shown using the maximum flux setting of 1 m collimation and large apertures. With the proposed pixel size of 5×5 mm^2 1500 counts per sec. per cm^2 gives 370 counts per sec. per pixel. In the centre where the pixels size is 2×2 mm^2 this gives 60 counts per sec. per pixel. Though it is possible to think of more strongly scattering samples, this gives a good impression of the numbers of events that it will typically be necessary to handle.

In figure 7 we plot the number of neutrons hitting the 2×1 m^2 detector as a function of q. In order to estimate the number of neutrons recorded in an interval of 1/100 Å^{-1} around q=0.1Å^{-1}, in 1800 seconds, the value of the intensity should be read off at q=0.1Å^{-1} and multiplied with 1/100 Å^{-1} · 1800 s. For the small sample configuration with 2 m collimation this example gives 1/100 Å^{-1} · 1800 s 1000 neutrons/s/Å^{-1}=18000 neutrons.

For comparison we also show the performance of the D22 beamline at ILL with a 2 m collimation and pinhole radii of s_1=8 mm and s_2=4 mm. The use of the very broad bandwidth gives an intensity that is approximately a factor of 20 higher

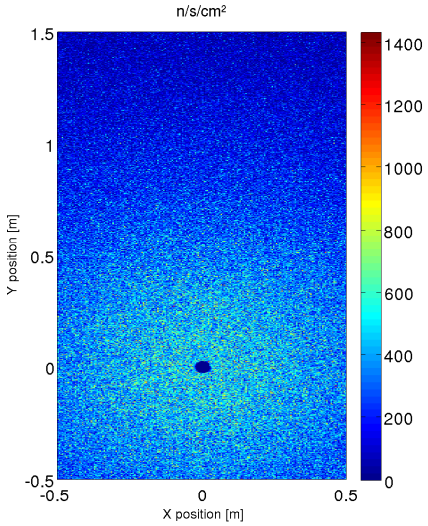

Figure 6: *Monte Carlo simulation of isotropic scattering from 1 mm of H_2O in the large sample configuration with 1 m of collimation. The figure shows the full detector image. The colours denote the number of neutrons per second per cm^2 in the different areas of the detector.*

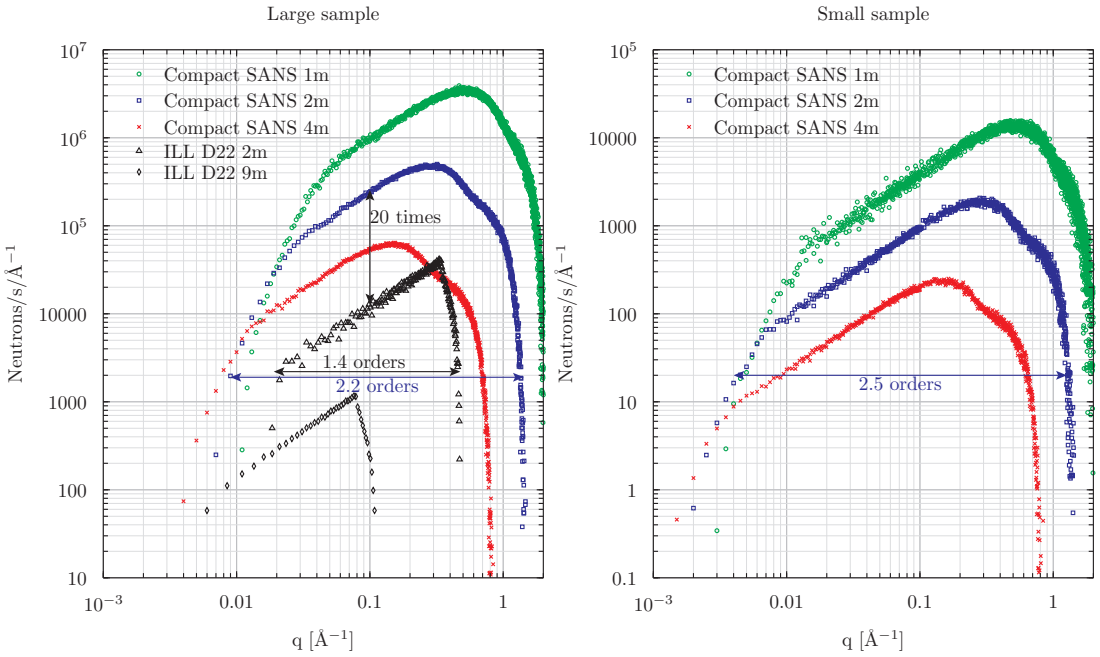

Figure 7: *Monte Carlo simulation of instrument performance measured in neutrons reaching the detector pr. second pr. Å as a function of q. The sample is a simple model of the isotropic scattering from 1 mm of H_2O.*

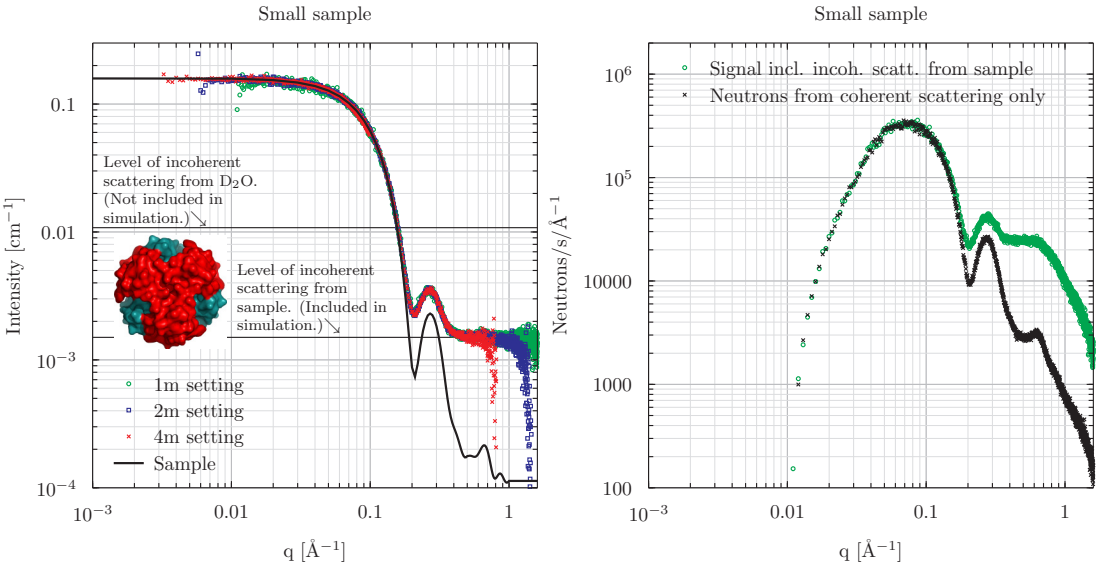

Figure 8: *Left: Scattering solution of insulin hexamers at 5 mg/ml in D_2O buffer and placed in a 2 mm path length cuvette. The model takes into account absorption from solvent and sample and incoherent scattering from the hexamers. The black line is the coherent signal from the sample without instrumental smearing. Right: Number of neutrons hitting the detector pr. time pr. q-range. In black is the number of neutrons stemming from the coherent signal only. The collimation apertures are s_1=8 mm, s_2=4 mm.*

than at D22 for comparable configurations. Combined with the large detector we furthermore cover 2.2 orders of magnitude in q reducing the need for multiple settings.

Note that between the curves of the same collimation length there is approximately a factor of 16^2 difference in intensity between the curves in the left (large sample) and right (small sample) plot. This corresponds to the reduction of each of the collimation pinholes of a factor of 16 in the small sample configuration. Using e.g. a s_1=8 mm entrance pinhole and a s_2=1 mm exit pinhole results in a configuration still suitable for small samples, but with a gain in intensity of a factor of 16 relative to the curves on the right. This comes with the cost of the extended q-range apparent in the right plot. In the examples below, we have chosen to show only the extreme configurations.

The next examples shown in figure 8 and 9 gives an impression of the type of samples that the instrument is optimised for. Figure 8 shows an insulin hexamer, a close to spherical molecule of a diameter of approximately 40 Å. The scattering curve that serves as input for the simulation is calculated from an atomistic bead model and includes high q structure. As seen, the oscillatory soft features of the curve is easily recognisable in all three settings, meaning that the $\frac{\delta\lambda}{\lambda}$ resolution

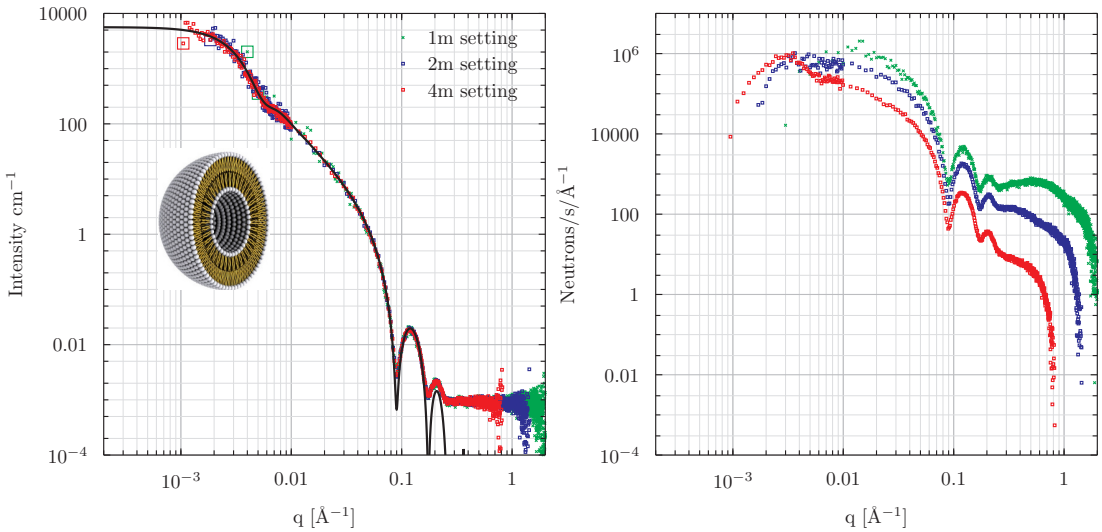

Figure 9: *Left: Scattering from solution of phospholipid liposomes in 100% D_2O at a volume concentration of 2% and placed in a 2 mm path length cuvette. Right: The number of neutrons hitting the detector pr. time pr. q-range. The collimation apertures are s_1=2 mm, s_2=1 mm.*

is sufficiently good to get the necessary information about the sample. The high intensity can be utilised to yield a high throughput or even time resolved studies of conformational changes. In the right part of the figure we show the number of neutrons collected at each q-value, both with and without the elastic incoherent scattering from the hexamer. It is apparent that a few seconds of measurement will be sufficient for a good statistics measurement. These simulations have been carried out using the "large sample" configuration giving the highest possible flux of the instrument. If the beam size is decreased to 2 mm samples the measurement time will increase to a few minutes.

Figure 9 shows the scattering profile from a solution of phospholipid liposomes, modelled as a three layer shell with an outer radius of 400 Å. The very narrow "small sample" collimation have been used in this simulation. The entire q-range of table 3 can be used with pixels of 2 mm. These are about the largest objects for which the Guinier-region can still be measured with this instrument. Despite the small beam, we still have decent count rates in the whole q-range and good measurements are obtained in a few minutes or less depending on the sample size.

Resolution The performance of the instrument when measuring sharply featured samples, has been investigated by inserting a sample consisting of logarithmically spaced peaks (figure 10). Above q>0.1 Å^{-1} the resolution is primarily governed by wavelength spread. The well collimated beam (red line) does not perform much better than the high intensity beam (green line). The proposed

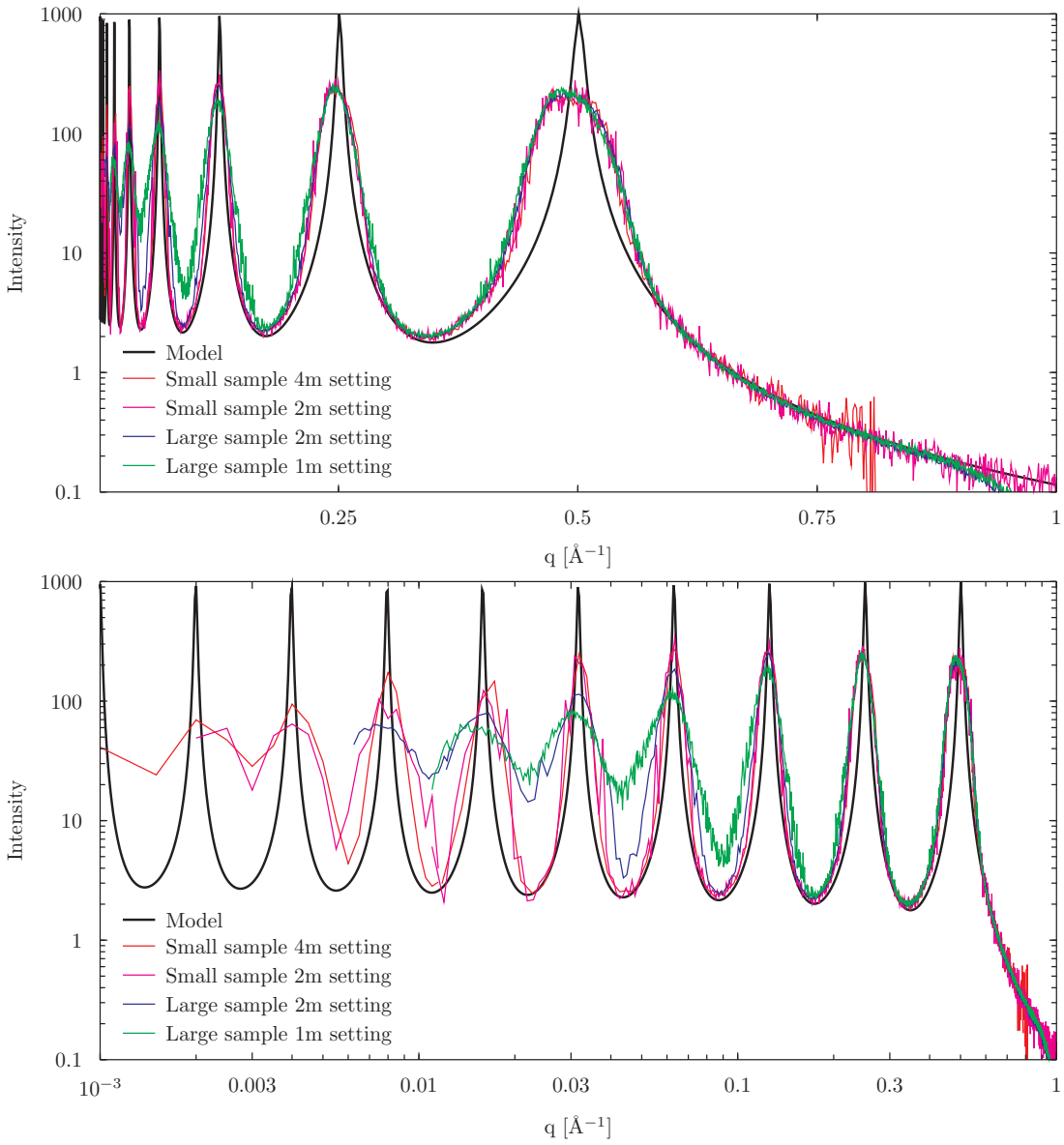

Figure 10: *Instrumental smearing at various settings. The resolution at different q-ranges is made clear by a Monte Carlo simulation of the scattering from a "sample" featuring logarithmically spaced sharp peaks. The same calculations are shown on a linear scale (above) and logarithmic scale (below).*

instrument is not optimised for good resolution in the low q-range, where biomolecular solution samples will normally exhibit a (flat) Guinier-region.

3.3 Chopper-based improvement of the wavelength resolution

As shown by the simulations in the previous section, the limited wavelength resolution of the proposed instrument does not pose a problem for the type of measurements that are of primary focus for the instrument. However, there are nevertheless several experiments where a better wavelength resolution is desirable. The experiments where the majority of the measurements call for a better resolution are more naturally conducted at one of the two other proposed SANS instrument. However, there may be cases where only a part of the experiment calls for better resolution or cases where the combination of a broad q-range in a single setting and a good resolution is desired. In order to enable these types of measurements we propose that a set of choppers for improving the wavelength resolution is incorporated in the presently proposed instrument.

The chopper system is designed such that the choppers can be "turned OFF" in the many cases where they are not required. In this case the instrument has the performance described in the first part of this section. The choppers can also be "turned ON", such that a better wavelength resolution is obtained in the part of the experiment where it is required. The proposal is inspired by the ideas published in [12, 13], which selectively reduces the 2.86 ms pulse width for wavelengths, in order to improve the resolution.

The proposed chopper arrangement results in a neutron flux loss of only approximately 60% compared to the basic instrument setup, considering a realistic wavelength distribution. The obtained results were calculated by Matlab. The wavelength resolution was approximated for every detector time using:

$$\delta\lambda/\lambda = \frac{v_{max} - v_{min}}{\frac{v_{max}+v_{min}}{2}}, \tag{6}$$

where v_{max} and v_{min} are the maximal and minimal velocities of neutrons arriving to the detector at a given time.

The calculated relative magnitude of integrated flux for the normal and the improved resolution setup was calculated as follows: For simplification we considered that the neutron flux is evenly distributed in time during the pulse length of 2.86 ms. For taking into account the wavelength distribution from the source, output from the McStas component ESS_moderator_long in cold source setting was used. At any given detector time the choppers in both the normal and in the improved resolution mode are defining a virtual pulse, which can vary from

Sample-to-detector distance:	1 m	2 m	4 m
Resolution in Basic mode	19 %	18 %	16 %
Improved resolution	11 %	10 %	9 %
Accompanied flux loss	61 %	61 %	61 %

Table 4: *Maximal wavelength resolution values ($\delta\lambda/\lambda$) in normal and improved resolution mode for different sample to detector distances. Flux loss in the improved resolution mode, compared to the normal mode.*

Instrument length: $L = A + L_1 + L_2$	$\delta\lambda/\lambda$ @ 4 Å	$\delta\lambda/\lambda$ @ 8 Å	$\delta\lambda/\lambda$ @ 12 Å
17=15+1+1	9%	8%	6%
18=14+2+2	8%	8%	5%
20=12+4+4	7%	7%	5%

Table 5: *Wavelength resolution at selected wavelengths and settings for the improved resolution mode. Compare with table 1.*

the pulse being blocked (virtual pulse length = 0) to the full ESS pulse (virtual pulse length = 2.86 ms). The ratio of the virtual pulse lengths in the improved resolution mode and that in the normal mode, weighed at every detector time using the wavelength distribution file, provides a good approximation for the flux difference in the two modes of operation.

The influence of the chopper setup on the resolution and time integrated flux is summarised in table 4.

The present setup is considering a 16 m sample source distance. Frame overlap choppers are situated at 6.5 and 9.5 m. In the presented design the frame overlap choppers theoretically has no influence on the improved resolution mode (i.e. they could also be stopped in the open position), however for background reducing purposes they should preferentially be operated also in this mode.

The resolution improving choppers are situated at 7, 10 and 12 m. In the presented design each of the choppers is rotating with ESS frequency. The parameters for this setup are shown in 6. In order to reduce the required size of the choppers, the 7 and 10 m choppers can be designed to be rotated with double of the ESS frequency. In this case the frame overlap choppers are crucial also in the improved resolution mode.

Since the signal, detected at the time of the next ESS pulse, is expected to be dominated by background from epithermal neutrons, the acceptable wavelength band can be further reduced. In this case the resolution improving chopper,

	Source chopper distance	chopper openings [ms]			
1_{st} fr. over. chop.	6.5 m	6.36-27.71			
2_{nd} fr. over. chop.	9.5 m	8.91-39.44			
1_{st} res. imp. chop.	7 m	6.7-7.45	8.16-9.12	9.89-11.15	11.96-29.62
2_{nd} res. imp. chop.	10 m	9.26-10.18	11.35-12.42	13.83-15.16	16.78-41.4
3_{rd} res. imp. chop.	12 m	10.97-12	13.48-14.61	16.45-17.83	19.99-49.25

Table 6: *Sample source distances and opening times for the various choppers*

situated at 7 m can be rotated with 3 times the ESS frequency, allowing for further reduction of the chopper diameter.

If required each chopper can be substituted with inversely rotating double choppers, where the chopper openings are placed in an opposite order.

Figures 11, 13 and 15 show the time characteristics of the proposed choppers, the resulting wavelength bands and resolution in the normal mode, while Figures 12, 14 and 16 show the time characteristics of the proposed choppers, the resulting wavelength bands, resolution, and the flux relative to the normal mode in the improved resolution mode.

We would like to emphasise that the proposed chopper design may be further refined, in order to reduce the flux loss, reduce the time gap between the consecutive wavelength bands or to extend the wavelength range towards smaller values. However it shows the feasibility of obtaining an increased resolution without substantial loss of flux of long wavelength neutrons at the Bio-SANS instrument, since the proposed chopper design reduces the number of neutrons reaching the sample, exclusively in the small wavelength range.

4 Strategy and Uniqueness

In order to cover the huge range of science that SANS can address in the most effective fashion, the vision for SANS at the ESS calls for three SANS instruments:

1. Broad Band Small Sample SANS: Aimed at the soft matter, biophysics and materials science communities, with a wide simultaneous q range at least 3 orders of magnitude in q, through the use of large area of detectors and a wide wavelength band. Designed to maximise the integrated intensity on the sample, at the cost of resolution.

2. General Purpose Polarised SANS: Aimed at the hard matter and industrial process users, with a flexible sample area, flexible optics, polarisation and

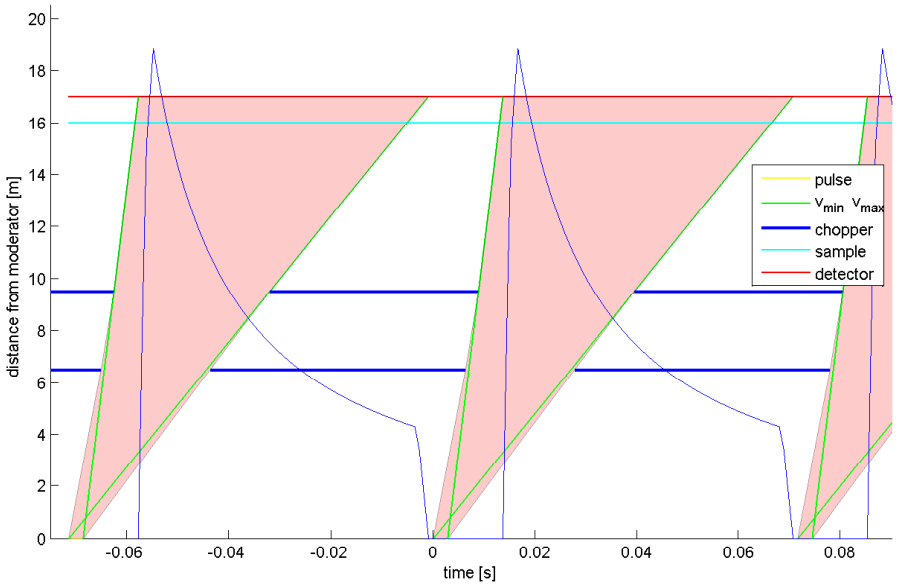

Figure 11: *Normal mode for 1 m sample to detector distance with calculated results (same y axes) for resolution in percentage (blue line).*

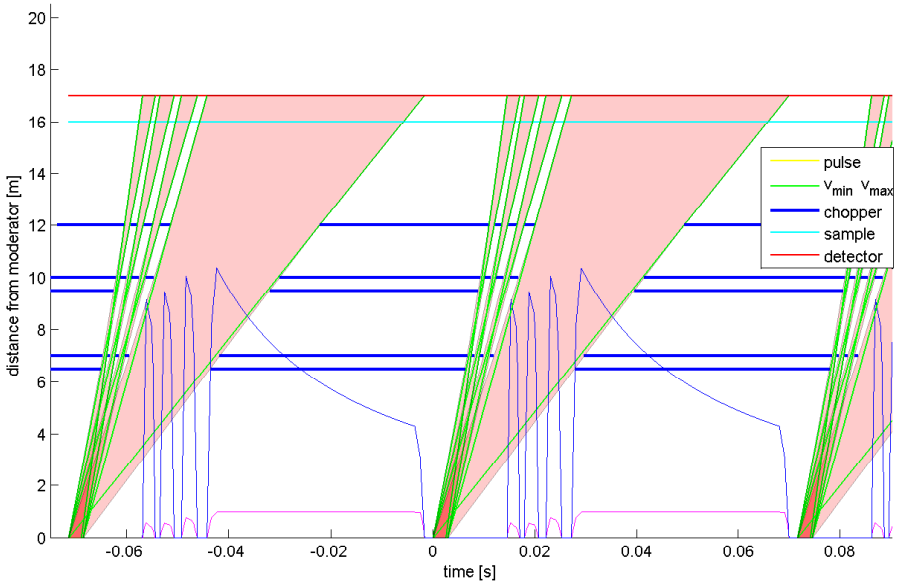

Figure 12: *Improved resolution mode for 1 m sample to detector distance with calculated results (same y axes) for flux ratio (magenta line) and resolution in percentage (blue line).*

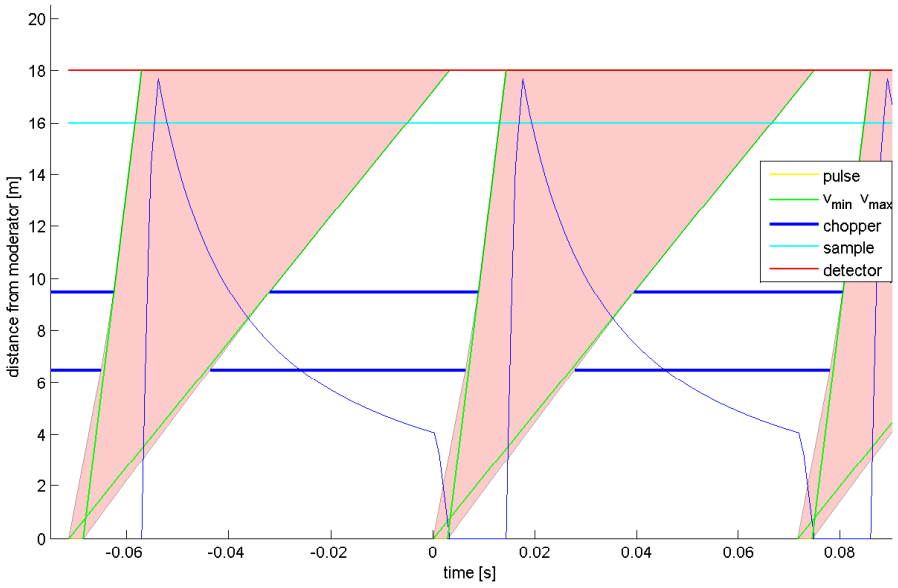

Figure 13: *Normal mode for 2 m sample to detector distance with calculated results (same y axes) for resolution in percentage (blue line).*

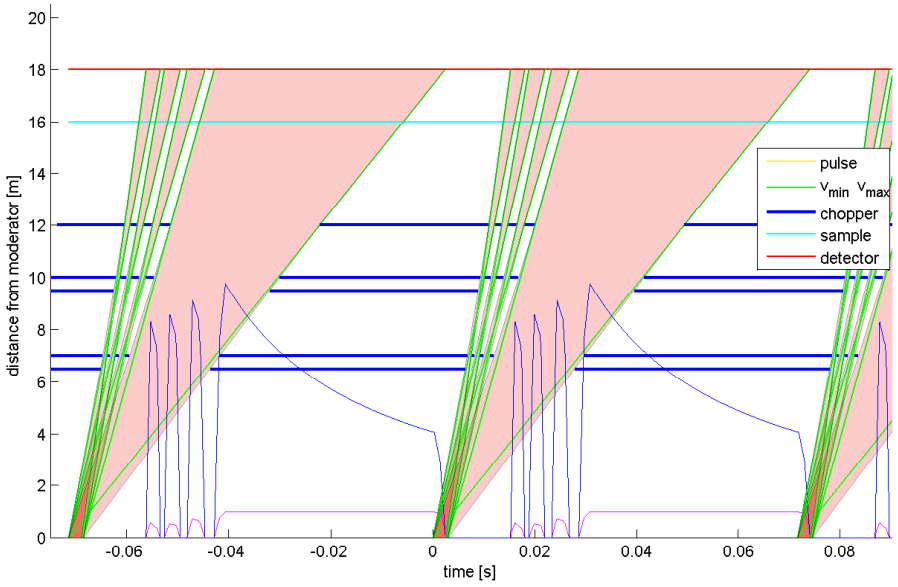

Figure 14: *Improved resolution mode for 2 m sample to detector distance with calculated results (same y axes) for flux ratio (magenta line) and resolution in percentage (blue line).*

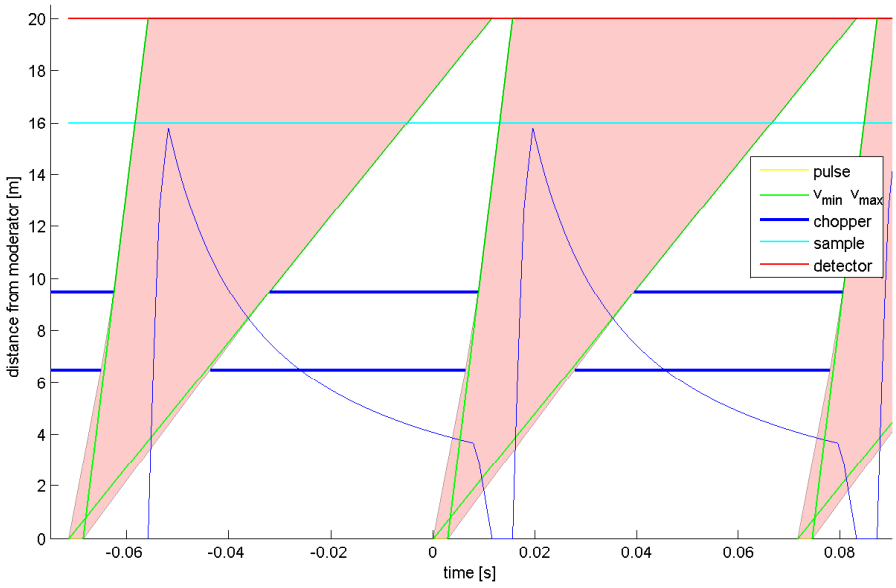

Figure 15: *Normal mode for 4 m sample to detector distance with calculated results (same y axes) for resolution in percentage (blue line).*

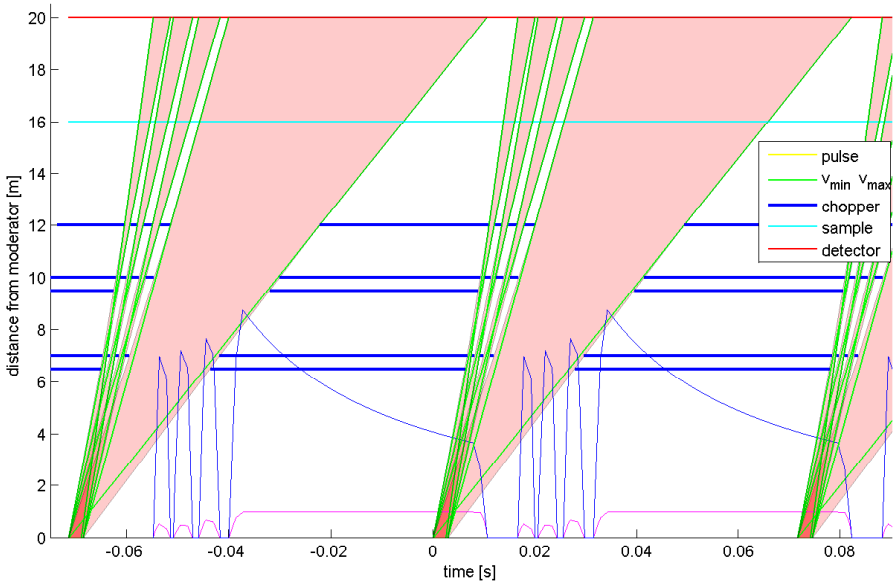

Figure 16: *Improved resolution mode for 4 m sample to detector distance with calculated results (same y axes) for flux ratio (magenta line) and resolution in percentage (blue line).*

polarisation analysis. Multiple detector banks for at least 2 orders of magnitude simultaneous q range. Higher resolution with options for GISANS and VSANS.

3. High Throughput Small Sample SANS / BioSANS: Aimed at the structural biology community, being a compact instrument with a biologically relevant length scale. Optimised for small samples and high throughput (e.g. flow through cells). The instrument should have end-to-end automated processing and initial analysis of data (cf BioSAXS beamlines).

The proposed instrument is the Danish-Swiss workpackage bid on the third category of instruments. The instrument will complement the two other SANS instruments at the ESS and provide a natural entrance point for users from the Life Science community. In order to benefit maximally from a good solution SANS instrument, it would be desirable to have a complementing SAXS instrument located at the nearby MAX-IV facility. This will allow for investigating exactly the same bio-samples with X-rays and neutrons during the same experiment, thus minimising typical sources of error associated with transportation (e.g. as a result of freezing the samples). Similarly combined access to SAXS and SANS are becoming more and more common e.g. at ESRF/ILL in Grenoble. However, the full potential of combining the two techniques is still far from being reached.

The Bio-SANS instrument also calls for good in-house sample deuteration facilities as well as good and nearby bio-sample preparation laboratories and sample quality control procedures.

The proposed instrument, with its small sample volume, its broad bandwidth achievable in a single setting and its standardised experimental setup, has been optimised for investigations of bio-molecular and colloidal solutions. The relatively small sample area (total path-length of 20 cm), implies that the instrument loses some of the flexibility characteristic for a more classical multipurpose instrument. However, despite the limited space, it is possible to incorporate custom fitted sample environments for e.g. rheology, furnace requiring experiments, as well as pressure, vacuum cells or perhaps a small cold finger cryostat. The ability to cover a broad q-range in very quick experiments will be a strong advantage also in the category of soft condensed matter experiments.

The limited sample access implies that it will be difficult or impossible to incorporate large cryostats, large magnets, etc. into the sample area. These are more easily incorporated into the other proposed SANS instruments, for example the general purpose polarised SANS instrument which is designed with exactly these applications in mind.

5 Technical Maturity and Risk Management

This section will discuss the technological challenges involved in meeting the demands of the different components, as well as explore the potential problems the instrument might encounter if some of the assumptions made in previous sections turn out to be incorrect.

5.1 Feasibility and Risk Assessment - Instrument

The proposed instrument is based on an existing and well-proven concept for small-angle neutron scattering. However, the optimisation for biological samples by means of the very compact design of the instrument has, to our knowledge, not been tried before at existing facilities. Nevertheless, we regard the overall design as unproblematic, technically mature and associated with a very low risk with respect to feasibility. In the few cases where there are issues with respect to feasibility, good back-up solutions can be implemented without a significant decrease of the instrument performance. The central risks identified for the instrument are the following:

1. That we have under- or overestimated the radiation background level from the source, which would make a 16 m sample position non-optimal.
2. That a sufficiently good detector with a pixel-size down to 2 mm near the beam centre is not available in 2019.
3. That the user base for a BioSANS instrument is not sufficiently strong.

Regarding point 1: Final estimates of the background radiation levels are not yet available from the ESS. However, based on the available information and advice from the ESS the sample position has been moved from the originally proposed 12.5 m out to 16 m. If however it turns out that either the radiation level is low enough that the sample position can safely be moved closer to the source, or so high that it is necessary to move further away, the instrument concept is flexible enough that this can be accommodated in the detailed design phase.

Risk: Non-negligible.
Consequences: Moving the sample position impacts the wavelength resolution, the flux, and the bandwidth (and thus the q-range).
It can be seen from equation (1) that increasing the moderator to detector distance by (in this example) a factor 1.2, will improve the resolution by the same factor, as seen when comparing tables 7, 8, and 9.

Instrument length: $L = A + L_1 + L_2$	$\delta\lambda/\lambda$ @ 4 Å	$\delta\lambda/\lambda$ @ 8 Å	$\delta\lambda/\lambda$ @ 12 Å	Bandwidth [Å] $\Delta\lambda$
13=11+1+1	21%	11%	7%	20.8
14=10+2+2	20%	10%	7%	19.3
16=8+4+4	17%	9%	6%	16.9

Instrument length: $L = A + L_1 + L_2$	$q_{\min}$ (Å^{-1})	$q_{\max}$ (Å^{-1})	Flux on sample (n/s/cm^2)
13=11+1+1	0.0061	1.27	14×10^8
14=10+2+2	0.0033	0.71	3.6×10^8
16=8+4+4	0.0018	0.37	0.94×10^8

Table 7: *Wavelength resolution, bandwidth, q-range, and flux if the sample position is at 12 m, with s_1=8 mm, s_2=4 mm and no choppers.*

Instrument length: $L = A + L_1 + L_2$	$\delta\lambda/\lambda$ @ 4 Å	$\delta\lambda/\lambda$ @ 8 Å	$\delta\lambda/\lambda$ @ 12 Å	Bandwidth [Å] $\Delta\lambda$
17=15+1+1	17%	8%	6%	15.9
18=14+2+2	8%	8%	5%	15.0
20=12+4+4	7%	7%	5%	13.5

Instrument length: $L = A + L_1 + L_2$	$q_{\min}$ (Å^{-1})	$q_{\max}$ (Å^{-1})	Flux on sample (n/s/cm^2)	
17=15+1+1	0.0080	1.27 (2.02)	12×10^8	5.9×10^8
18=14+2+2	0.0042	0.71 (1.38)	3.3×10^8	1.7×10^8
20=12+4+4	0.0023	0.37 (0.78)	0.88×10^8	0.44×10^8

Table 8: *Wavelength resolution, bandwidth, q-range, and flux if the sample position is at 16 m, with s_1=8 mm, s_2=4 mm and no choppers.*

The flux will be affected two-fold by moving the sample position further out: Both by the reduced bandwidth and by greater transmission losses. Figure 4 shows that the transmission losses are very low for the baseline design, and since the instrument uses cold, low divergent neutrons, transmission losses should still be quite low given the proper guide, independent of instrument length[11]. The loss due to reduced bandwidth is harder to estimate, but it can be simulated. As we can see from comparing the flux numbers listed in tables 7, 8, and 9, the total decrease in flux by elongating the instrument to a sample position of 20 m is about 10 %.
The bandwidth will be reduced by a longer instrument, and consequently also the q-range as pr. equations (2), (4), and (5). Tables 7, 8, and 9 list the q-ranges for a sample sample position at 12 m, 16 m, or 20 m.

Instrument length: $L = A + L_1 + L_2$	$\delta\lambda/\lambda$ @ 4 Å	$\delta\lambda/\lambda$ @ 8 Å	$\delta\lambda/\lambda$ @ 12 Å	Bandwidth [Å] $\Delta\lambda$
21=19+1+1	13%	7%	4%	13.4
22=18+2+2	13%	6%	4%	12.8
24=16+4+4	12%	6%	4%	11.7

Instrument length: $L = A + L_1 + L_2$	$q_{\min}$ (Å^{-1})	$q_{\max}$ (Å^{-1})	Flux on sample (n/s/cm^2)
20=19+1+1	0.0094	1.27	10×10^8
22=18+2+2	0.0048	0.71	2.8×10^8
24=16+4+4	0.0026	0.37	0.82×10^8

Table 9: *Wavelength resolution, bandwidth, q-range, and flux if the sample position is at 20 m, with s_1=8 mm, s_2=4 mm and no choppers.*

Regarding point 2: A detector will be required that has the capacity for measuring count rates at the order of 10^8 neutrons/second. Additionally, in order to benefit from the tight collimation and resolve the low q-values, a detector that has improved resolution with a pixel size of 2 mm, at least in the region around the direct beam, will be required.
Risk: The risk of this problem is assumed to be very low. The consequences of not having sufficiently good detectors will have severe consequences for several instruments at the ESS. It is therefore anticipated that finding a good solution to the problem will have high priority at the ESS-project and that a solution will be found.
Consequences: The proposed SANS instrument will still be functional and highly competitive even if all the neutrons can not be counted and the low q can not be sufficiently well resolved. However, the access to very short measurement times with the large beam (D=8 mm) will not be exploitable nor will the access to measuring the very lowest q-values proposed in fig. 7 (right).

Regarding point 3: As mentioned in section 2, the Life Science areas are underrepresented as users at most present neutron scattering facilities when seen in relation to their representation at the X-ray Synchrotron facilities and in academia more generally. In order to fully exploit the capacity of the proposed instrument, the user community for SANS investigations of biological systems has to be strengthened significantly. Today, many "Bio-users" at the neutron scattering facilities have a physics background or rely heavily on close collaborations with physicists. In order to exploit the scientific potential of the proposed instrument, it is necessary to have an instrument that is more easily accessible for scientists with a non-physicist background and where the measurements themselves become a routine operation while the samples receive the focus. As it is also very clearly demonstrated by the example from the user community devel-

opment performed at Dmitri Svergun's X33 beamline at EMBL Hamburg (see fig. 1 and discussions in sections 1 and 2), a potentially very strong user community for performing interesting Life Science with small-angle scattering does exist, provided that an instrument and the associated data analysis tools are adapted to their needs.
Risk: The risk associated with this point is impossible to assess reliably. While it is clear that there is a potential for an extremely strong user community within the life science area, it is also clear that the community needs to be further nurtured and that new concepts for automated SANS data analysis software need to be developed in order to benefit maximally from the large capacity of the proposed instrument.
Consequences: If it turns out that the proposed instrument is not sufficiently demanded by the Life Sciences user community, the flexibility of the sample area implies that the instrument may be re-furnished to become a more general purpose SANS instrument at a relatively low cost and effort. In this situation, the main selling point will be the access to high intensity, broad q-range and small samples, hence allowing for e.g. time resolved measurements. For this type of instruments, there is a documented very large user community already today, and at most facilities the SANS instruments are heavily oversubscribed.

5.1.1 Feasibility of Neutron Guide

The guide uses low coating values that have been commercially available for many years. The guide geometry is a commonly used bender, with straight segments in the collimation section, and as such is relatively simple to assemble.

If the heat and radiation environment requires that all or part of the guide is made with a metal substrate, SwissNeutronics assures us that this will not pose a problem with the coating values required.

5.2 Shielding of the Proposed Instrument

In order to fully assess the shielding requirements of the instrument a detailed simulation will have to be performed. As the cost of the area detector and the shielding is expected to dominate the overall costs of the instrument, such a simulation is necessary before a reliable instrument cost estimate can be performed. A more careful analysis will also allow for evaluating which choices of the shielding material are most optimal, both with respect to keeping the background radiation level sufficiently low at the facility and with respect to minimise the costs of the shielding. The required resources for performing such a more careful analysis has not been part of the present Swiss-Danish work-package and will be handled by the radiation safety unit at the ESS.

Up to now we have only made a rough, conservative estimate of the shielding requirements for the case that we block the full beam at the exit of the neutron guide outside the main biological shielding of the ESS (i.e. between the first set of choppers and the collimation section). For this we assumed that all choppers stay in the open position and that the whole spectrum of neutrons from the cold source arrive at the end of the $40 \times 40 \mathrm{mm}^2$ neutron guide. In this case we need to absorb 1.4×10^{12} n/s. The thickness of the shielding depends strongly of the absorbing isotope. We assumed that all neutrons will be absorbed by Boron as it emits γ-rays with an energy of 478 keV upon neutron absorption, which is much lower than emitted energy of Cadmium or Gadolinium and therefore less requiring to shield. To shield 1.4×10^{12} emitted γ-rays per second one needs a 45 cm thick Fe-shielding to decrease the radiation level at the shielding surface to about 10μSv/h. In case of Pb as shielding material the thickness would only need to be around 25 cm. These values have been obtained by assuming that all neutrons are absorbed in a point 10 cm from the surface of the biological shielding. The Gamma-Ray-Flux-to-Dose-Rate conversion factors have been taken from [10].

It should be emphasised that the estimated shielding thickness of 45 cm Fe is the worst case scenario and that this will most likely only be necessary at the instrument beam shutter position and maybe at the pulse-shaping chopper system (at 6 meters from the source). Along the neutron guide, the shielding can most likely be thinner as the neutron loss is expected to be minimal here. Around the apertures and other neutron absorbing elements, the shielding will have to be strengthened again.

We also estimated the required shielding at the sample position for the maximum flux of 14×10^8 n/s/cm^2 obtained at the 1 m collimation (see table 2). If this flux is blocked with Boron the shielding required in 3 m distance would still need to be about 30 cm thick in order to reduce the dose rate down to <10 μSv/h. The required shielding thickness will strongly depend on the detailed design and the space available and needs to be verified by a more elaborate simulation. As discussed above, the cost estimate for the shielding and hence the entire instrument will be strongly affected by the outcome of this simulation.

6 Costing

The cost estimate presented in table 10 in this section is partly based on our knowledge about the cost of similar devices at existing instruments and partly on qualified guesses. A column stating the estimated required manpower for the implementation of the devices is also provided. This estimate does not include the work of the instrument scientist.

It should be emphasised that the calculated cost is only a first estimate. A more

accurate costing of the instrument will be made if the instrument is forwarded for construction and as a result of the detailed engineering plans.

The biggest uncertainty in price is expected to be associated with the costing of the shielding where an important part of the price is due to the large amounts of Iron (Fe) which we have assumed used for the shielding. The world market prices for Fe are subject to quite significant fluctuations. For example, the iron prices have increased from a price of 0.11 k€ per ton ten years ago to 0.7 k€ per ton today, but with a maximum of 1.37 k€ ton in the middle of 2011. Hence, we anticipate that the ESS will need a systematic approach to the acquisition of this raw material, and this approach lies outside our field of expertise.

It should also be emphasised that intensive research and development into the shielding optimisation is presently taking place at the ESS. Consequently, the materials choices for the shielding are not yet decided upon.

The cost estimate does not include the joint costs of the shielding bunker around the target monolith.

The cost estimate does also not include research and development costs for the detector and for the different types of sample environment.

Based on the presented cost estimate, we end up on a total instrument price close to 8 million € plus the cost of 12-14 man-years for the instrument construction.

Component	Price /k€ of hardware	Manpower (months)
Shielding		
Shielding for first chopper		2
Shielding for neutron guide system		6
Shielding of sample area		3
Shielding of detector vessel		3
Total main shielding	>1500	
N-shielding with Boral-Al with 4.5% ^{10}B (2k€/m^2)	200	
Detector		
2D detector	3000	12
Trolley for detector & beamstop	300	6
Detector cooling incl. infrastructure	80	3
Detector vessel	600	2
Large VAT gate valve (DN 800)	55	
Neutron Optics		
Pulse shaping choppers (electronics incl)	500	2
Frame overlap choppers (electronics incl)	200	2
Neutron guide system	120	2
Collimation system	400	2
Attenuators	10	1
Instrument beam shutter	80	4
Sapphire windows	15	
Monitors		
2 fission chambers	14	
Amplifiers	6	
Vacuum system		
Detector vessel vacuum	150	
Collimation system vacuum	50	
Sample environment		
Sample table	80	6
Standard sample changer with T-control	50	3
Pressure cell	100	4
Rheometer	130	0.5
Flow through cell	300	1
Small 1.5 Tesla E-Magnet	100	1
Support		
Motor controllers	200	6
Power supplies	100	2
Instrument control software&hardware	10	4
Basic analysis software	10	12
General beamline construction		
		60
Total	>8295	151.5

Table 10: *Cost estimate for the different elements of the compact SANS instrument.*

References

[1] De Francesco, A. et al. (2008) BRISP: the new Brillouin Spectrometer at ILL's High Flux Reactor. *Neutron News.* 19: 10-13.

[2] Nelkin, M. (1960) Scattering of slow neutrons by water. *Phys. Rev.* 119: 741-746

[3] May, R. P. et al. (1982) The forward scattering of cold neutrons by mixtures of light and heavy water. *J. Appl. Cryst.* 15: 15-19

[4] G. Nagy, K. Kleno, S. Kynde, K. Mortensen, J. Kohlbrecher and L. Arleth, Suppression of incoherent, inelastic scattering in a chopped SANS instrument, Progress report to the ESS, August 15th, 2012

[5] Pellionisz, P. (1971) Statistical chopper method for separation of elastic and inelastic scattered neutrons in time-of-flight experiments. *Nucl. Instr. Meth.* 92: 125-135

[6] von Jan, R. and Scherm, R. (1970) The statistical chopper for neutron time-of-flight spectroscopy. *Nucl. Instr. Meth.* 80: 69-76

[7] Price, D. L. and Sköld, K. (1970) A detailed evaluation of the mechanical correlation chopper for neutron time-of-flight spectrometry. *Nucl. Instr. Meth.* 82: 208-222

[8] Gukasov, A. G. et al. (1992) Cross-correlation polarized neutron spectrometer *Phys. B: Condensed Matter* 180-181: 1007-1010

[9] Rosenkranz, S. and Osborn, R. (2008) Corelli: Efficient single crystal diffraction with elastic discrimination. *PRAMANA - J. Phys.* 71: 705-711

[10] Laurie M. Unger and D. K . Trubey (1982) Specific Gamma-Ray Dose Constants for Nuclides Important to Dosimetry and Radiological Assessment, ORNL/RSlC-45

[11] K. H. Klenø et al. (2012) Systematic Performance Study of Common Neutron Guide Geometries. *NIMA (in press)*

[12] M. Russina and F. Mezei (2010) Implementation of repetition rate multiplication in cold, thermal and hot neutron spectroscopy. *J Phys Conf Ser* 251:012079/012071-012074.

[13] M. Russina, F. Mezei and G. Káli (2010) First implementation of novel multiplexing techniques for advanced instruments at pulsed neutron sources. *J Phys Conf Ser* 340:012018/012011-012019.

Nuclear Instruments and Methods in Physics Research A 696 (2012) 75–84

Contents lists available at SciVerse ScienceDirect

Nuclear Instruments and Methods in Physics Research A

journal homepage: www.elsevier.com/locate/nima

Systematic performance study of common neutron guide geometries

Kaspar Hewitt Klenø [a,b,*], Klaus Lieutenant [c,d], Ken H. Andersen [e], Kim Lefmann [a,b]

[a] Nanoscience and E-Science Centers, Niels Bohr Institute, University of Copenhagen, Universitetsparken 5, DK 2100 Copenhagen, Denmark
[b] ESS Design Update Programme, Denmark
[c] Helmholtz-Zentrum, Hahn-Meitner Platz 1, 14109 Berlin, Germany
[d] ESS Design Update Programme, Germany
[e] European Spallation Source ESS AB, Box 176, 22100 Lund, Sweden

ARTICLE INFO

Article history:
Received 27 March 2012
Received in revised form
8 August 2012
Accepted 8 August 2012
Available online 1 September 2012

Keywords:
Neutron guides
Ray tracing
Monte Carlo
Neutron scattering
European Spallation Source
Elliptic guides

ABSTRACT

In this report, we present the results from a systematic benchmarking of four different long neutron guide geometries: elliptic, parabolic, ballistic (piecewise linearly focusing/defocusing), and straight, for various wavelength, divergence restriction, and guide length settings. In this work, we mapped relevant parts of the neutron phase space to show where advanced guide geometries have significant transport advantages over simple guide geometries. The primary findings are that the elliptic and parabolic geometries perform almost equally well, and they are considerably superior to the other geometries, except for low-divergence, cold neutrons. In addition, it was observed that transporting thermal neutrons more than 100 m using elliptic guides was possible with only a 10% loss in the phase space density for divergences up to $\pm 0.5^{\circ}$, which enables the construction of very long thermal neutron instruments. Our work will allow instrument designers to use tabulated, standard geometries as a starting point for optimising the guide required for the particular instrument.

1. Introduction

Currently a considerable amount of research is focused on determining the guide geometries that should be selected for instruments at the European Spallation Source (ESS). Because the ESS will be a long-pulse source, long instruments will often be required to achieve the necessary wavelength resolution, even when pulse-shaping choppers are used [1]. Therefore, efficient neutron transport is crucial.

Neutron guides date back to the 1960s, and are used to transport parts of the 5-dimensional neutron phase space, which is composed the of transverse position (x,y), divergence (ϕ_x,ϕ_y), and wavelength (λ), with a loss considerably less than $1/r^2$, where r is the source–sample distance. The use of neutron guides allowed experiments to be moved to low background areas and increased the available space around the neutron source [2]. Initially, beam focusing was only possible using focusing monochromators [3,4], but with the advent of supermirror guide coatings, which can reflect neutrons up to m times the critical scattering angle of Ni [5–7], combined with the use of focusing optics [8], polychromatic beam focusing using progressively more advanced neutron guide shapes began to become practical. Ballistic guides, where the guide cross-section first increases and then remains constant before decreasing immediately before the sample, were first suggested in 2000. These guides offered significant phase space transport advantages over conventional, straight guides [9]. The use of ballistic guides quickly led to the development of focusing guides that use an elliptic or parabolic geometry, rather than linearly tapering focus, which led to even further gains in terms of phase space transport and homogeneity [10]. Although a geometrically perfect ellipse would transport a beam from a point source with only a single reflection in each plane, a finite source size will naturally result in multiple scattering, and the ellipse then works more as a guide system than as an optical element.

In this study, we systematically quantified the performance of these various guide geometries, and we tabulated the performance parameters for different areas of the neutron phase space and guide lengths. Our aim with this study is twofold:

(i) to provide quantitative information on the feasibility of constructing very long instruments in terms of neutron transport performance,
(ii) to provide a tool for determining the guide geometry that would be appropriate for a given instrument based on its neutron phase space requirements.

However, we do not intend for this study to be used as a repository of ready-made guide geometries for new instruments, because

* Corresponding author at: Nanoscience and E-Science Centers, Niels Bohr Institute, University of Copenhagen, Universitetsparken 5, DK 2100 Copenhagen, Denmark.
E-mail address: kaspar@fys.ku.dk (K.H. Klenø).

0168-9002/$ - see front matter © 2012 Elsevier B.V. All rights reserved.
http://dx.doi.org/10.1016/j.nima.2012.08.027

guide design requires further customisation and optimisation for individual instruments.

2. Guide design and simulations

We selected four different geometries for comparison, each with a square cross-section, as the target of our neutron guide study. These geometries are illustrated in Fig. 1.

1. A guide that has a constant cross-section (usually called a straight guide in this paper), which is commonly used for traditional neutron instruments. This guide has an $m=3$ coating.
2. A 3-section ballistic guide that uses a linearly diverging section, a straight section, and a linearly tapering, focusing section. The expanding and converging sections use $m=6$ coatings, whereas the straight section uses $m=3$ coatings.
3. An elliptic guide that is approximated by 50 linearly diverging or converging guide segments of different lengths, which uses $m=6$ coatings in the first and last 15 sections that each extend over approximately 10% of the total length, and $m=3$ coatings in the middle 80%. The figure 10% was arrived at in preliminary studies and will be detailed in Ref. [11].
4. A parabolic–straight–parabolic guide assembly, where the parabolically expanding section at the moderator and the focusing section at the sample are each approximated by 25 linearly diverging or converging segments of guide, using $m=6$ in the first and last 15 sections which each extend over approximately 10% of the total parabolic length, with $m=3$ in the rest. In between these sections is a long, straight segment of guide, which uses an $m=3$ coating.

Each of these four geometries was numerically optimised for four different instrument lengths (50, 100, 150 and 300 m) and for four different combinations of settings for each length: low divergence ($\leq 0.5^\circ$), high divergence ($\leq 2.0^\circ$), a cold neutron bandwidth centred on 5 Å, and a thermal neutron bandwidth centred on 1.5 Å. This combination provides a total of 64 combinations that were individually optimised. The figure of merit (FoM) for the optimisations was selected to be the divergence restricted flux on a $1\times 1\,\mathrm{cm}^2$ sample. Therefore, we register neutrons only if they hit the sample with a divergence within a specific range. We simulate neutrons with the wavelength band given by the instrument length and the presumed ESS source frequency of $16\frac{2}{3}$ Hz. The neutron wavelength, λ, for a particular neutron is constant throughout the simulation. Optimisation was performed using either the program McStas (elliptic, parabolic, and straight guides) [12,13] or VITESS (ballistic guide) [14]. The final simulations were then performed using both packages to simulate identical geometries to compare the results.

The moderator has a size of $12\times 12\,\mathrm{cm}^2$ and a wavelength spectrum as described in Ref. [15]. All guides begin 1.5 m from the moderator surface. Gravity was simulated throughout the guides, and a realistic guide waviness of 0.01° HWHM Gaussian distribution was used [16]. We did not observe a substantial impact of the waviness on the results presented in this paper, but the detailed effects of waviness will be covered in a forthcoming publication [17].

The free parameters vary between the shapes; in all cases, the maximum width, w, (which is the width of the straight section in most cases) is a free parameter; it is restricted to 40 cm because we estimated this width to be close to the current limit for a frame overlap disk chopper but still within the present production limit of 50 cm [7]. The distance of the guide to the sample position (L_3) is another free parameter; the minimal value of this free parameter was set to 0.5 m to allow space for the sample environment. In most cases, the entrance and exit widths (w_e, w_f) (or the distance to the focal points (F_0, F_3)) were also free parameters. For the ballistic and parabolic guides, the lengths of

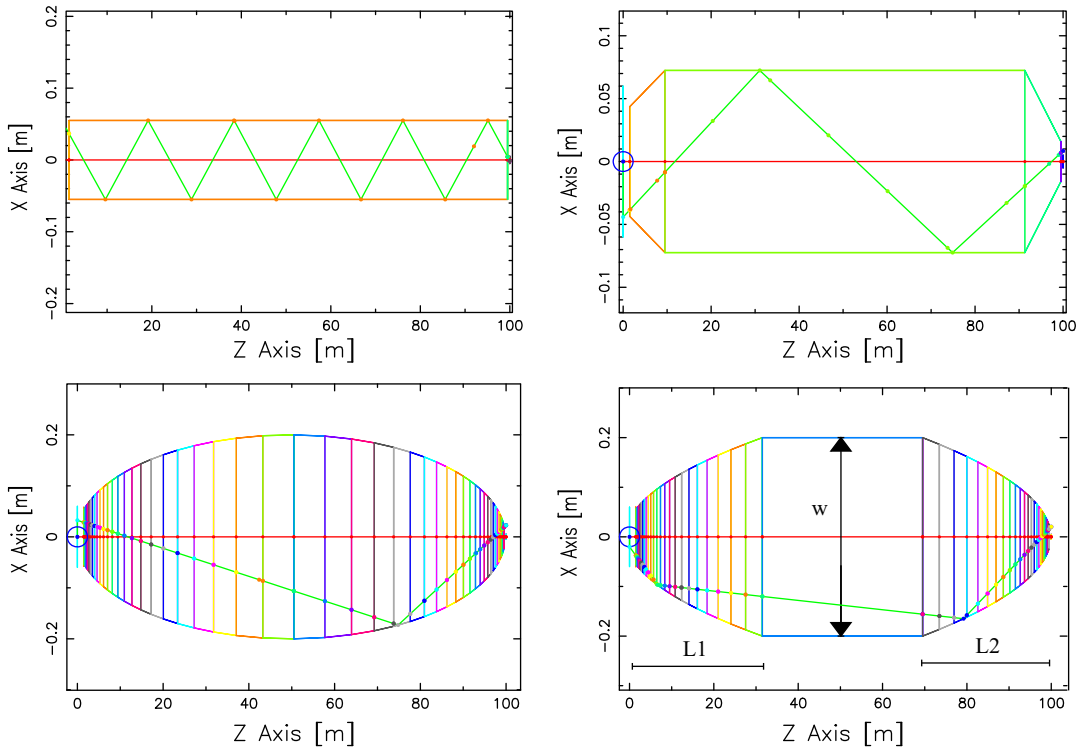

Fig. 1. Top-down view of the four different guide geometries a for 100 m source–sample distance. The green line in the guides show a neutron trajectory. Top left: Straight. Top right: Ballistic. Bottom left: Elliptic. Bottom right: Parabolic. (For interpretation of the references to color in this figure caption, the reader is referred to the web version of this paper.)

the diverging and converging sections (L_1, L_2) were additional parameters, which were each restricted to lie below 30% of the total length. We imposed symmetry constraints between the horizontal and vertical directions to reduce the number of free parameters for the optimisation process. The parameters are summarised in Table 1 and further explained in Section 3.

The optimisations in McStas were performed using a Simplex algorithm [18], whereas VITESS used a gradient method adapted for Monte Carlo simulations. The VITESS gradient method is a standard method that uses the matrix of the 2nd derivatives to determine the optimum of a linearised function. This method is based on a fit algorithm [19], which is simplified to not optimise on the edges of the parameter space, and it is then altered to allow for statistical effects caused by the Monte Carlo method.

2.1. Bandwidths

The wavelength ranges used for the optimisations and simulations are provided in Table 2. These values correspond to the maximum bandwidth that avoids frame overlap for a pulse period of $T=60$ ms, which was the 2011 baseline value for the ESS. These ranges are derived from the general ToF equation, which is

$$t = \alpha L \lambda, \tag{1}$$

where L is the instrument length, $\alpha = m_n/h$ is 252.7 μs/m/Å (where m_n is the neutron mass and h is Planck's constant), and t is the flight time. To avoid frame overlap, we required that the flight time difference between the fastest and slowest neutrons not be greater than the pulse period. This requirement results in the following:

$$T = \alpha \Delta\lambda L, \tag{2}$$

which provides us the following bandwidth:

$$\Delta\lambda = \frac{T}{\alpha L}, \tag{3}$$

which is 1.59 Å for an instrument length of 150 m. We chose to centre the bandwidth on 1.5 Å for thermal neutrons and 5 Å for cold neutrons and round the bandwidth to 1.5 Å. This selection then provides us the λ-ranges of 0.75–2.25 Å and 4.25–5.75 Å. Refer to Table 2 for all of the wavelength ranges used in the simulations.

Table 1
Guide parameters that were free in the computer optimisations. The value given in each cell is the boundary condition placed on the parameter. If blank, the parameter was not used for that geometry. w is the centre width, L_3 is the sample-guide distance, L_1 is the length of the expanding section, L_2 is the length of the focusing section, w_e is the entry width of the expanding section, w_f is the exit width of the focusing section, F_0 is the focus point of the expanding section, F_3 is the focus point of the focusing section.

	w (cm)	L_1	L_2	L_3 (m)	w_e	w_f	F_0	F_3
Straight	< 40			> 0.5				
Ballistic	< 40	< 15 m	< 15 m	> 0.5	< 20 cm	< 20 cm		
Elliptic	< 40			> 0.5			Free	Free
Parabolic	< 40	< 30%	< 30%	> 0.5			Free	Free

Table 2
Wavelength ranges used in the simulations.

Instrument length (m)	Thermal wavelength range (Å)	Cold wavelength range (Å)
50	0.2–4.7	2.75–7.25
100	0.35–2.65	3.85–6.15
150	0.75–2.25	4.25–5.75
300	1.12–1.88	4.62–5.38

2.2. Brilliance transfer

Liouville's Theorem states that the phase space density can never be increased under passive processes [20]. In terms of neutron optics, this theorem means that we can never do better than transport the number of neutrons/s/cm^2/Å/sr at the moderator surface to the sample without losses. We call this number the phase space density or the Brilliance of the beam.

To compare the guide performance for different instrument lengths, we simulated a 1×1 cm^2 divergence- and wavelength-restricted monitor at the moderator surface and an identical one at the sample position. Through the measurements of the phase space density at these two positions, we define the Brilliance transfer as the ratio of these two numbers: $B = \Psi_2/\Psi_1$, where Ψ_1 (Ψ_2) is the measured Brilliance at the source (sample). As a consequence of Liouville's Theorem, this number can never exceed unity. Therefore, B provides a quantitative measure of how well the guide performs the transport of the neutrons under consideration.

2.3. Guide coating values

One aspect of the guide design that we have not included in this study is the optimisation of supermirror coating of the individual guides. Including this aspect would have extended the already considerable simulation/optimisation task of this work into an unsolvable task.

Instead, we have chosen to fix the majority of the coating values to $m=3$. Based on our experience, the value $m=3$ is (more than) sufficient for many long, straight guides, and a higher m-value would only increase the price of the instrument because high-divergence neutrons would be too attenuated by the large number of reflections within the guide.

However, for the shorter expanding and converging sections, we selected a considerably higher supermirror reflectivity at higher angles, $m=6$, which was the highest available in larger quantities at the time of this study. For these sections, a high reflection angle is used for the first reflection of high-divergence neutrons, thereby reducing their divergence, or for the last reflection, which compresses the beam down to the sample.

The reflectivity curves used in this study are shown in Fig. 2. We will exemplify the validity of our choice of guide parameters in Section 3.

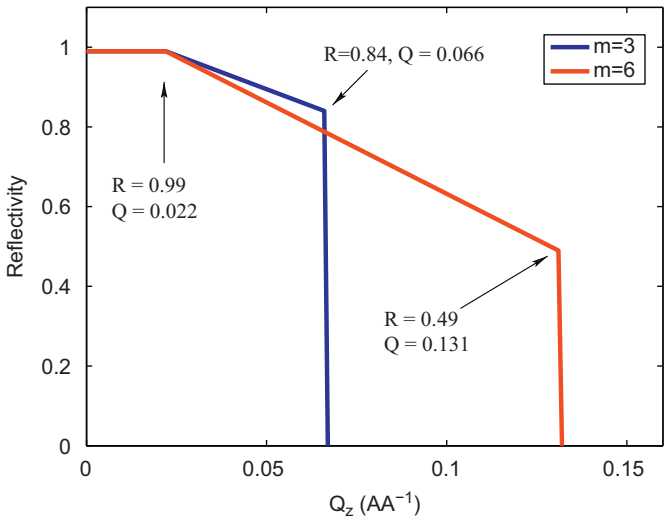

Fig. 2. Reflectivity curves used in the simulations. The curves are conservatively modelled using empirical data from SwissNeutronics. The scattering vector is $\boldsymbol{Q} = \boldsymbol{k_i} - \boldsymbol{k_f}$, where $\boldsymbol{k_i}$ ($\boldsymbol{k_f}$) is the initial (final) wave vector.

A more thorough approach to this problem would be to divide the guide into many sections, where each section has an optimal coating for the guide geometry in question. A study of this character, where the price of the guide system is also included in the simulations, is underway for one particular guide geometry [11].

3. Example of simulation and optimisation

Before presenting the general results, let us present one simulation in detail. We choose the 150 m long guide with parabolic ends, as shown in Fig. 1, lower right, optimised for high divergence $\pm 2^\circ$ in the cold neutron bandwidth. This parabolic guide was selected because it would be one of the guide types to be considered for the ESS.

We simulate the cold neutron moderator with a size given by the ESS baseline parameters, 12×12 cm^2, and with an isotropic flux. Each neutron 'ray' is generated at a random position on the moderator, and with a random wavelength within the specified bandwidth. However, as a routine procedure in McStas and VITESS, only neutrons emitted in directions that enable them to reach the guide entry are simulated. An appropriate 'weight factor' is adjusted for each simulated ray to compensate for this solid angle bias. Both the McStas and VITESS codes propagate neutrons in a deterministic fashion through the guide system, where the reflectivity losses are accounted for by the 'weight factor'. Neutrons are detected when they reach the 1×1 cm^2 sample area. Each simulation consists of the propagation of several million neutrons from the moderator.

Our initial guess for the guide parameters is that the guide starts $L_0 = 1.5$ m from the source, with an opening of 8.5×8.5 cm^2, which means that the first focal point is $F_0 = 0.5$ m behind the source. The parabolic beginning is $L_1 = 20$ m long and widens out to the size of the middle piece, $w \times w = 20 \times 20$ cm^2. The focusing section has a length of $L_2 = 20$ m and ends $L_3 = 0.5$ m from the sample with the focal point exactly at the sample, $F_3 = 0$. A simulation of this initial design provides a flux of neutrons within the divergence limitations of $\Psi_1 = 1.04 \times 10^{11}$ n/cm^2/s at the guide opening, while the number is $\Psi_2 = 4.13 \times 10^{10}$ n/cm^2/s at the sample position, within the cold neutron bandwidth defined above. These flux numbers gives an initial Brilliance transfer value of $B_{\text{init}} = \Psi_2/\Psi_1 = 0.40$.

The next step is to optimise B by varying the six free parameters: three lengths (L_1,L_2,L_3), 2 focal point positions (F_0,F_3), and one guide width (w). The optimised Brilliance transfer was determined to be B=0.89, which means the guide transport is only 11% lower than the theoretical maximum. The optimal parameters were: $L_1 = 42.16$ m, $L_2 = 35.61$ m, $L_3 = 0.5$ m, $F_0 = 1.02$ m, $F_3 = -0.05$ m, w=0.40 m. Note that this parameterisation was chosen to be easily understandable to the reader and that it differs slightly from the one provided in reference [21], because the latter is intended for other simulators who want parameters to input into the software.

The effect of the parabolic guide sections are illustrated in Fig. 3. This figure shows the divergence profile of the beam at various positions in the guide. At the beginning of the guide, the divergence is high, more than $\pm 2^\circ$ in each direction, due to the size of the moderator. After the initial parabolic, expanding section, the divergence is strongly reduced, $\pm 0.8^\circ$, although there are "stripes" in the divergence profile due to the non-ideal (de)focusing conditions. This picture is more or less unchanged after the long straight section. However, at the 1×1 cm^2 sample position, the high divergence is restored. A single 'dip' remains at $\pm 0.4^\circ$ in both directions. We will return to this effect later.

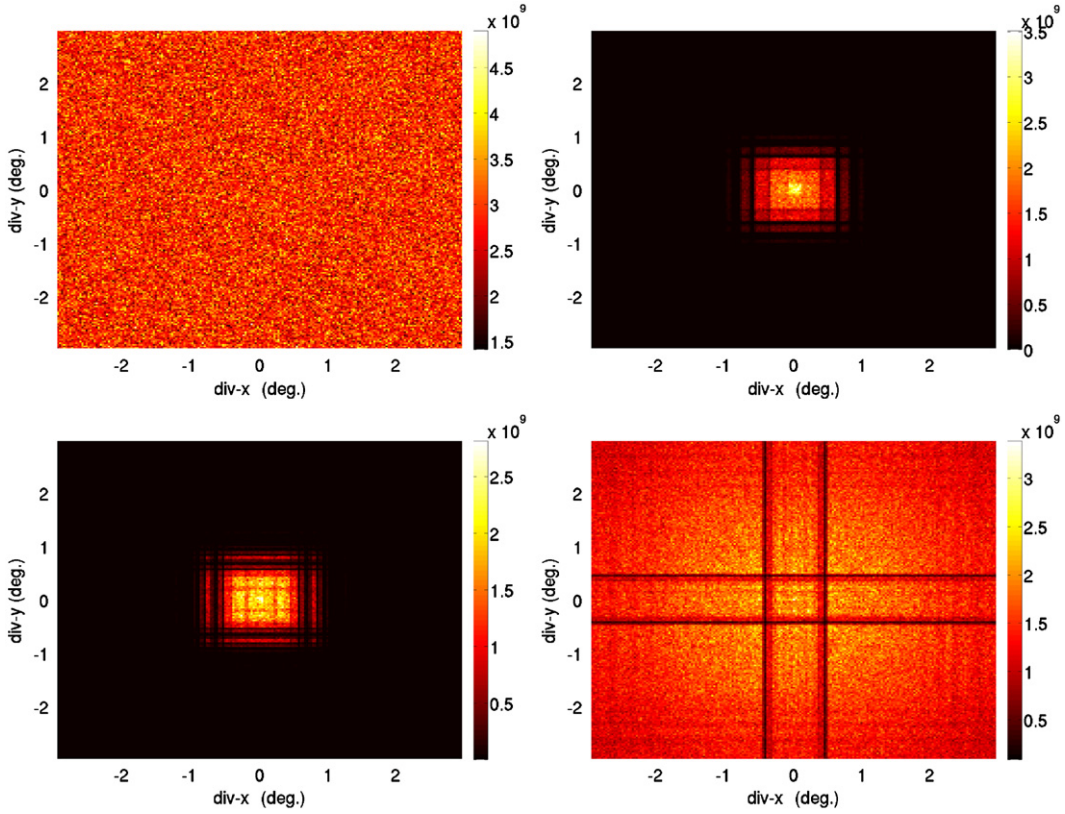

Fig. 3. Development of the divergence profile of the beam for a 150 m parabolic guide, which was optimised for cold, high divergence neutrons. From top left to bottom right, the figures show the profile at the central 1×1 cm^2 of the beam at the guide beginning, the end of the parabolic expanding section, the end of the straight section, and at the sample position, respectively.

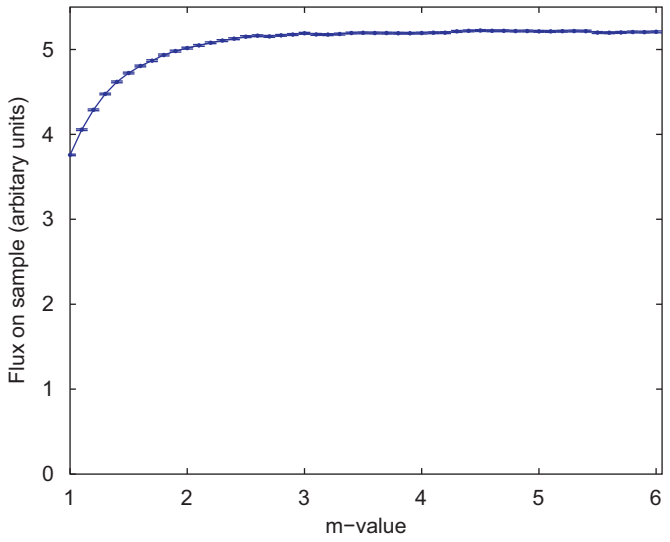

Fig. 4. Effect on flux at the sample position for varying m-values of the middle section of a 150 m parabolic guide. The guide geometry was optimised for high-divergence $\pm 2^\circ$ cold neutrons using $m=3$.

As mentioned earlier, we chose $m=3$ as our lower m-value and $m=6$ as our high m-value for the guide sections. To justify this choice, we present Fig. 4, which shows how the Brilliance transfer varies with the choice of the lower m-value. It is clearly observed that no gain in guide performance is observed by increasing beyond a value of $m=3$. $m=6$ was the highest m-value readily available at the time this study was planned, and it can clearly be observed that it is sufficient for the transport of cold neutrons from the high final B-values. However, highly divergent, thermal neutrons could likely benefit from a coating with better reflectivity than what is used here.

4. Results

Here, we present the result of our simulations of the 64 different configurations described earlier.

4.1. Optimised parameters

The optimisations produced a considerable amount of data, more than can be presented here. One general property is that the guide exits are larger for long wavelengths. Another finding is that the optimal guide—sample distance (L_3) is the minimal allowed value (50 cm) for high divergence, but for low divergence, it is often larger. Elliptic guides usually have the maximum guide width (w) allowed (40 cm), and their average maximum guide width is 34 cm. The straight sections of the parabolic guides are somewhat narrower, typically 30 cm. The straight sections of the ballistic guides have a width of only 13.5 cm on average. The optimised width of a straight guide is always close to 10.5 cm (for the given moderator width of 12 cm).

The complete list of optimised parameters is available on the ESS simulation group's homepage [21].

4.2. Comparison between packages

Table 3 shows the ratios of the figures of merit obtained in the simulations using the McStas and VITESS packages. Although the packages completely agree for the intensities at the guide entrance, the FoM at the sample position shows slight discrepancies. There are a few cases with differences greater than 3%. However, this difference be expected statistically, because the individual simulations were performed with an accuracy of approximately 1%, which provides approximately 1.5% error on each the values in Table 3.

The consistent overall agreement between independent packages provides a strong indication that the guide simulations by the packages are trustworthy and provides confidence in the results.

Table 3
Comparison between the main results from the simulations using the two packages for all 64 guide types studied. The numbers shown are the ratio of the FoM produced by McStas vs. the FoM produced by VITESS. L: Length, MD: Maximum divergence (°), λ: wavelength (Th: thermal or C: cold), Ell: elliptic, Par: parabolic, Bal: ballistic, Str: straight.

L (m)	MD	λ	Ell.	Par.	Bal.	Str.
50	0.5	Th	**1.00**	**0.98**	**1.00**	**1.04**
50	0.5	C	**1.00**	**0.99**	**1.01**	**0.99**
50	2	Th	**1.01**	**1.00**	**1.01**	**1.02**
50	2	C	**1.01**	**1.00**	**1.00**	**1.02**
100	0.5	Th	**0.99**	**0.98**	**1.00**	**1.02**
100	0.5	C	**1.02**	**1.00**	**0.96**	**0.98**
100	2	Th	**1.02**	**1.00**	**1.02**	**1.04**
100	2	C	**0.99**	**0.99**	**0.99**	**0.99**
150	0.5	Th	**1.03**	**0.98**	**0.97**	**1.05**
150	0.5	C	**1.00**	**0.99**	**0.95**	**1.01**
150	2	Th	**0.99**	**1.01**	**1.01**	**1.04**
150	2	C	**1.00**	**0.99**	**0.99**	**1.02**
300	0.5	Th	**1.02**	**0.93**	**0.99**	**1.02**
300	0.5	C	**1.00**	**0.97**	**0.91**	**0.99**
300	2	Th	**0.96**	**1.00**	**1.01**	**1.03**
300	2	C	**0.99**	**1.00**	**0.98**	**1.01**

Table 4
Gain factors of various guide geometries. We show the FoM of the elliptic, parabolic, and ballistic guides relative to that of a straight guide in the same row. L: Length, MD: Maximum divergence (°), λ: wavelength (Th: thermal or C: cold), Ell: elliptic, Par: parabolic, Bal: ballistic, Str: straight.

L (m)	MD	λ	Ell.	Par.	Bal.	Str.
50	0.5	Th	**1.84**	**1.87**	**1.79**	**1.00**
50	0.5	C	**0.97**	**1.03**	**1.05**	**1.00**
50	2	Th	**9.50**	**8.29**	**4.97**	**1.00**
50	2	C	**5.03**	**5.34**	**3.79**	**1.00**
100	0.5	Th	**2.39**	**2.45**	**2.21**	**1.00**
100	0.5	C	**1.09**	**1.08**	**1.07**	**1.00**
100	2	Th	**14.56**	**12.24**	**6.32**	**1.00**
100	2	C	**6.85**	**6.51**	**5.04**	**1.00**
150	0.5	Th	**2.95**	**3.05**	**2.59**	**1.00**
150	0.5	C	**1.11**	**1.10**	**1.09**	**1.00**
150	2	Th	**20.03**	**18.14**	**7.18**	**1.00**
150	2	C	**8.35**	**8.00**	**5.92**	**1.00**
300	0.5	Th	**3.76**	**3.96**	**3.43**	**1.00**
300	0.5	C	**1.25**	**1.25**	**1.18**	**1.00**
300	2	Th	**26.82**	**22.6**	**9.50**	**1.00**
300	2	C	**9.35**	**10.9**	**7.78**	**1.00**

4.3. Guide gain factors

For comparison, the FoMs of the elliptic, parabolic, and ballistic guides are compared with the FoMs for the guides with constant cross-sections. The gain factors obtained in this manner are summarised in Table 4. It is observed that large gains in excess of a factor 20 by advanced guide shapes can be reached for high divergence and short wavelengths. In contrast, for low divergence and long wavelengths, the gain compared to a straight guide varies between a factor of 1 and 1.25. For low divergence and short wavelengths, or high divergence and long wavelengths,

intermediate improvements with factors between 2 and 10 are observed for the advanced guide shapes. The observed gains are explained by several physical factors; the most important factors are the geometrical beam expansion and focusing, which significantly reduce the number of reflections by high-divergence neutrons and thereby lower the transmission losses. Additionally, the reflections are concentrated on the focusing and expanding sections, where high m-value coatings can be used. The gain factors increase with decreasing wavelength, which is explained by the decreased reflectivity at constant scattering angle for low wavelength reflections; this problem is exacerbated when using a straight guides which does not geometrically reduce the number of reflections.

The gain factors tend to increase with the instrument length. Generally, the elliptic shape yields the highest gains, and the parabolic–straight shape is almost as good, whereas the ballistic shape only reaches smaller gain factors. In another study [22] of guide performance it was shown that the ballistic guide reaches gain factors that are comparable to the elliptic and parabolic guide for a limited maximum guide width. However, in contrast to the these two, the ballistic shape does not profit from extending the maximum width beyond a certain limit, which is approximately 12–15 cm under these conditions [22].

Table 5
Overall Brilliance transfers obtained from the McStas simulations. The fraction of the relevant phase space density that is successfully transported from the guide entrance to the sample. L: Length, MD: Maximum divergence (°), λ: wavelength (Th: thermal or C: cold), Ell: elliptic, Par: parabolic, Bal: ballistic, Str: straight.

L (m)	MD	λ	Ell.	Par.	Bal.	Str.
50	0.5	Th	**0.85**	**0.87**	**0.84**	**0.53**
50	0.5	C	**0.88**	**0.96**	**0.97**	**0.94**
50	2	Th	**0.36**	**0.31**	**0.21**	**0.04**
50	2	C	**0.83**	**0.87**	**0.68**	**0.20**
100	0.5	Th	**0.89**	**0.90**	**0.82**	**0.44**
100	0.5	C	**0.97**	**0.97**	**0.95**	**0.92**
100	2	Th	**0.39**	**0.32**	**0.19**	**0.03**
100	2	C	**0.92**	**0.87**	**0.73**	**0.17**
150	0.5	Th	**0.89**	**0.91**	**0.78**	**0.36**
150	0.5	C	**0.96**	**0.96**	**0.94**	**0.89**
150	2	Th	**0.45**	**0.42**	**0.18**	**0.02**
150	2	C	**0.93**	**0.89**	**0.70**	**0.14**
300	0.5	Th	**0.89**	**0.94**	**0.82**	**0.29**
300	0.5	C	**0.96**	**0.95**	**0.89**	**0.89**
300	2	Th	**0.48**	**0.41**	**0.17**	**0.02**
300	2	C	**0.79**	**0.86**	**0.63**	**0.10**

4.4. Brilliance transfer factors

Table 5 presents the Brilliance transfer values obtained for the 64 difference guide systems studied. These values are highest for the elliptic and parabolic guides and lowest for the straight guides. A transport fraction of $B=1$ corresponds to a complete preservation of the phase space density, and it is the theoretical limit using passive beam transport. This value does not significantly decrease with increasing instrument length, except for the straight guide.

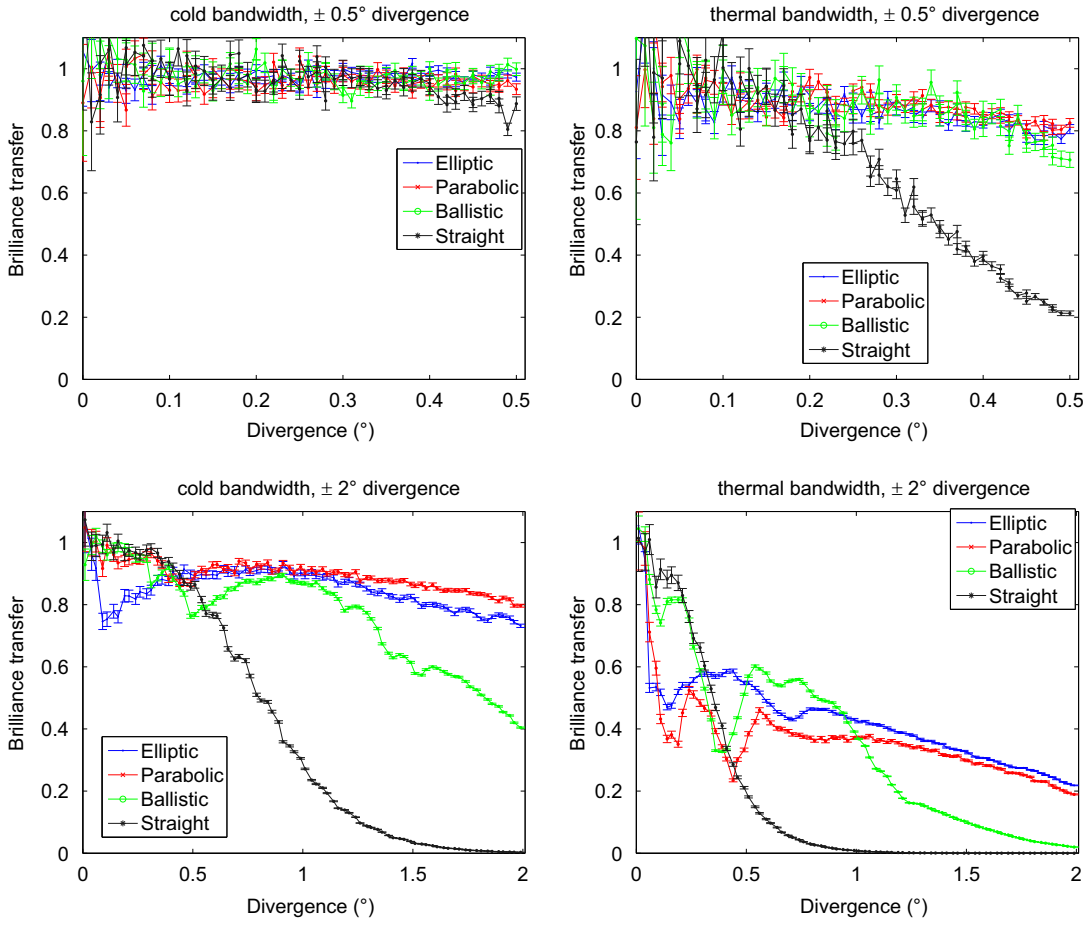

Fig. 5. Brilliance (phase space density) transfer for the four different neutron guide geometries over a 50 m distance, plotted as a function of radial divergence. Left: Optimised for cold neutrons. Right: Optimised for thermal neutrons. Top: Optimised for 0.5° divergence. Bottom: Optimised for 2.0° divergence.

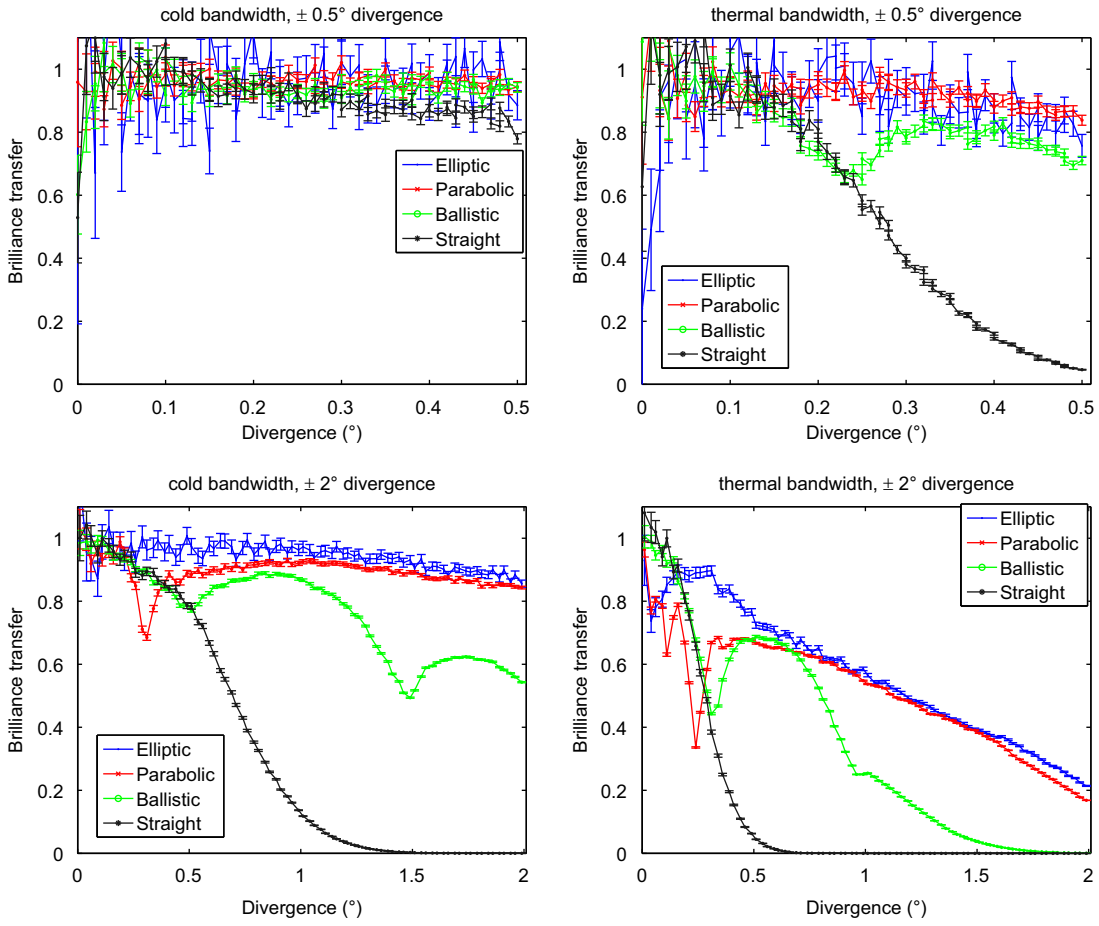

Fig. 6. Brilliance (phase space density) transfer for the four different neutron guide geometries over a 150 m distance, plotted as a function of radial divergence. Left: Optimised for cold neutrons. Right: Optimised for thermal neutrons. Top: Optimised for 0.5° divergence. Bottom: Optimised for 2.0° divergence.

For a more detailed analysis, we calculated the Brilliance transfer as a function of radial divergence at the sample position, i.e. $\phi_r = \sqrt{\phi_x^2 + \phi_y^2}$, where ϕ_r is the radial divergence. The results for the 50, 150, and 300 m lentos are shown in Figs. 5–7.

As shown in the top left figures, there is little difference in performance for the four geometries for low divergent, cold neutrons. This result is expected because low divergent, cold neutrons impart only a small momentum on impact with straight guide walls, and they are therefore easily reflected, as shown in Fig. 2. However, for thermal neutrons, the more advanced guide shapes (elliptic and parabolic) exhibit a significant gain over the simpler guide shapes. The bottom two graphs reveal that there is also a very significant gain when using the advanced guide shapes to transport highly divergent neutrons. Specifically note that we are very close to perfect transport for cold neutrons in an elliptic guide. Even high-divergence thermal neutrons are transported approximately 50%. In addition, the advanced guide shapes (specifically the elliptic one) have a remarkably smooth phase space transport in contrast to the low transmission divergence regions observed in the ballistic guides. These dips in the reflectivity curves for high divergence for the ballistic guides are explained by Fig. 8: The trajectories A and B correspond to rays bouncing only in the straight section of the guide, where the reflectivity curve of the ballistic guide closely follows that of the straight guide. Increasing divergence (case B) causes an increasing number of reflections in the straight section of the guide, thereby lowering the reflectivity—the first 'dip'. When the divergence (tracing back from the sample) becomes sufficiently high, a ray will be reflected on the focusing section, which will reduce the divergence, as shown in trajectory C, with a higher transmission as a result. When a second dip is observed, as in the lower left of Fig. 7 at 1.5°, the increased reflectivity to the right of the dip corresponds to a double reflection in the focusing section, which further lowers the divergence.

A close inspection of the bottom left corner of Figs. 5– 7 and Table 5 shows a rather surprising result; the transport for high-divergence, thermal neutrons increases with increasing guide length for the elliptic and parabolic guides. This result appears counterintuitive, but it is explained by the decreased wavelength band available for longer guides, as shown in Table 2. Fig. 9 shows that the transport efficiency for high-divergence neutrons begins to significantly decrease for wavelengths below 1.5 Å. Because the shorter guides have more bandwidth far below 1.5 Å, and the results shown in Figs. 5–7 and Table 5 are averaged over the wavelength band, this explains the seemingly better performance of the longer guides.

5. Discussion

Our results reveal that we can transport both cold and thermal neutrons over very long distances, which is in contrast to common beliefs. Even at a divergence of $\pm 2°$, the elliptic and parabolic guides have a transmission of the thermal neutron band of approximately 20% (Fig. 5 lower right corner), and for wavelengths as low as 0.8 Å, they have a 10% transmission in the high divergence range.

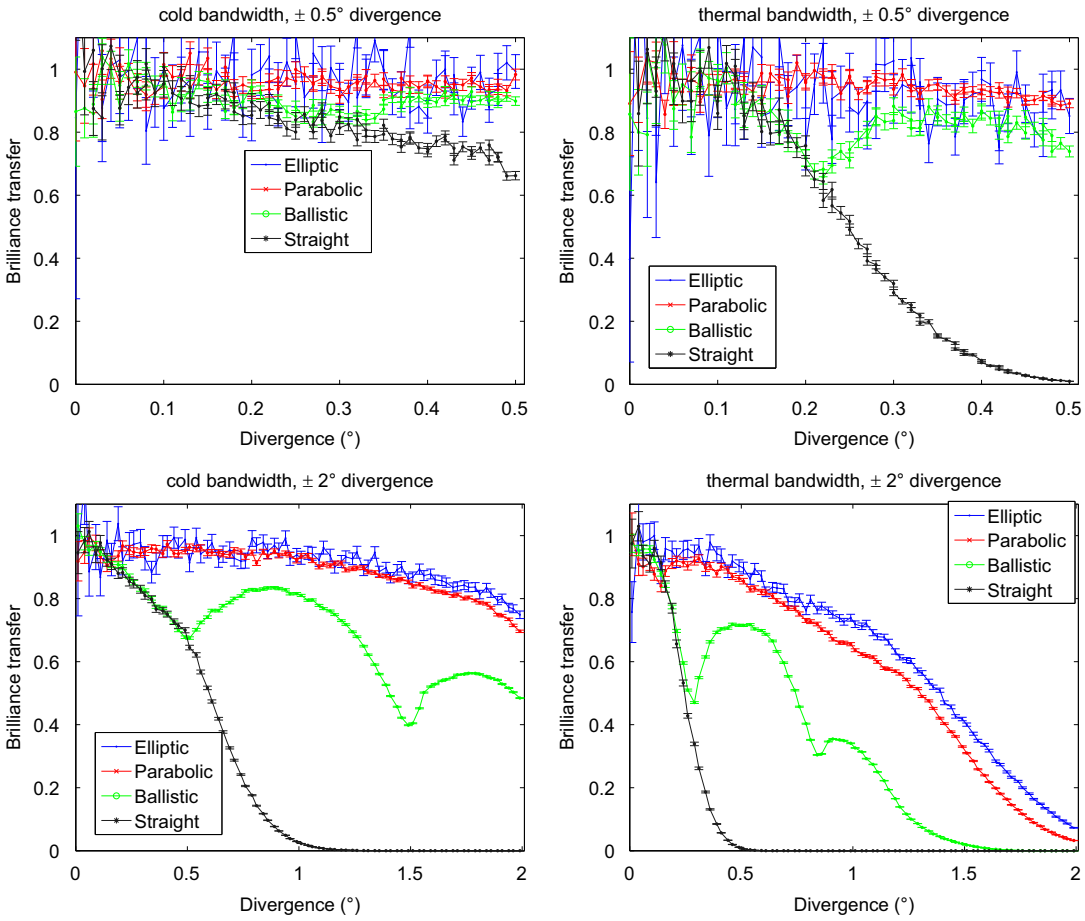

Fig. 7. Brilliance (phase space density) transfer for the four different neutron guide geometries over a 300 m distance, plotted as a function of radial divergence. Left: Optimised for cold neutrons. Right: Optimised for thermal neutrons. Top: Optimised for 0.5° divergence. Bottom: Optimised for 2.0° divergence.

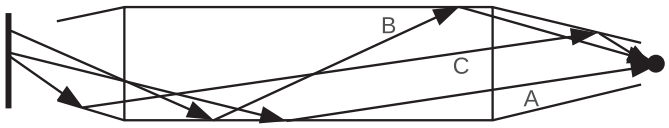

Fig. 8. Three sample trajectories (A–C) of increasing divergence in a ballistic guide, which explains the dips and humps observed in some of the reflectivity curves for the ballistic guide in Figs. 5–7. See Section 4.4 for further explanation.

Our highest divergence range of $\pm 2^\circ$ is more than can be used by most instruments, but we performed this optimisation to test an extreme case. The $\pm 0.5^\circ$ divergence criterion is appropriate for many single-crystal and powder diffraction instruments. Many instruments can in some cases use a fairly high divergence of more than $\pm 0.5^\circ$, such as direct geometry spectrometers, backscattering spectrometers, and some reflectometers (in one direction only). Instruments with very narrow divergence limits will not benefit from advanced guide shapes, but our results confirm the commonly accepted notion that simple guides shapes provide excellent transmission for neutrons with a divergence on the order of 0.1° to 0.3°.

The distributions of the coatings over the length of the guides used here are quite simple to reduce the number of variables. This simplification makes the guides presented in this work prohibitively expensive. However, careful optimisation can drastically reduce the *m*-value of the supermirror coating over large areas, and consequently the cost, without sacrificing the beam transport performance [11,23,24].

An example of the above is a concept for a 300 m long thermal chopper spectrometer for a long pulsed spallation source. Here, we have demonstrated that 1 Å neutrons with a divergence of $\leq 1.0^\circ$ can be transported over a distance of 300 m with a Brilliance transport of 60% to 80%. The guide designed for this case has an estimated cost of less than 5 M Euros [25].

An aspect we have not investigated in this work is the problem of direct line of sight (LoS) between the moderator and sample and the impact this has on the epithermal neutron background. This question is highly relevant because the common method of curving the guide out of the LoS may impact the focusing properties of an elliptic guide. This problem is something that we are investigating further in reference to these results in a current study [26]. Meanwhile, several other studies have already addressed this problem using various techniques, such as a massive beamstop in the centre of the guide that eliminates any neutrons flying directly through the guide [27], gravitational curving where the guide follows a parabolic curve calculated from a typical wavelength [28], and the traditional method of bending of a straight guide [29]. The method of bending can be applied for three of the guide shapes studied here, the parabolic, ballistic, and straight, which all have a long, straight section in the centre. Therefore, it is likely that the parabolic shape could be the geometry of choice in many cases.

6. Conclusions

We observed that we can deliver a very high fraction of the neutrons in the relevant phase space to a sample over distances of 50–300 m using elliptic and parabolic guides. This result even

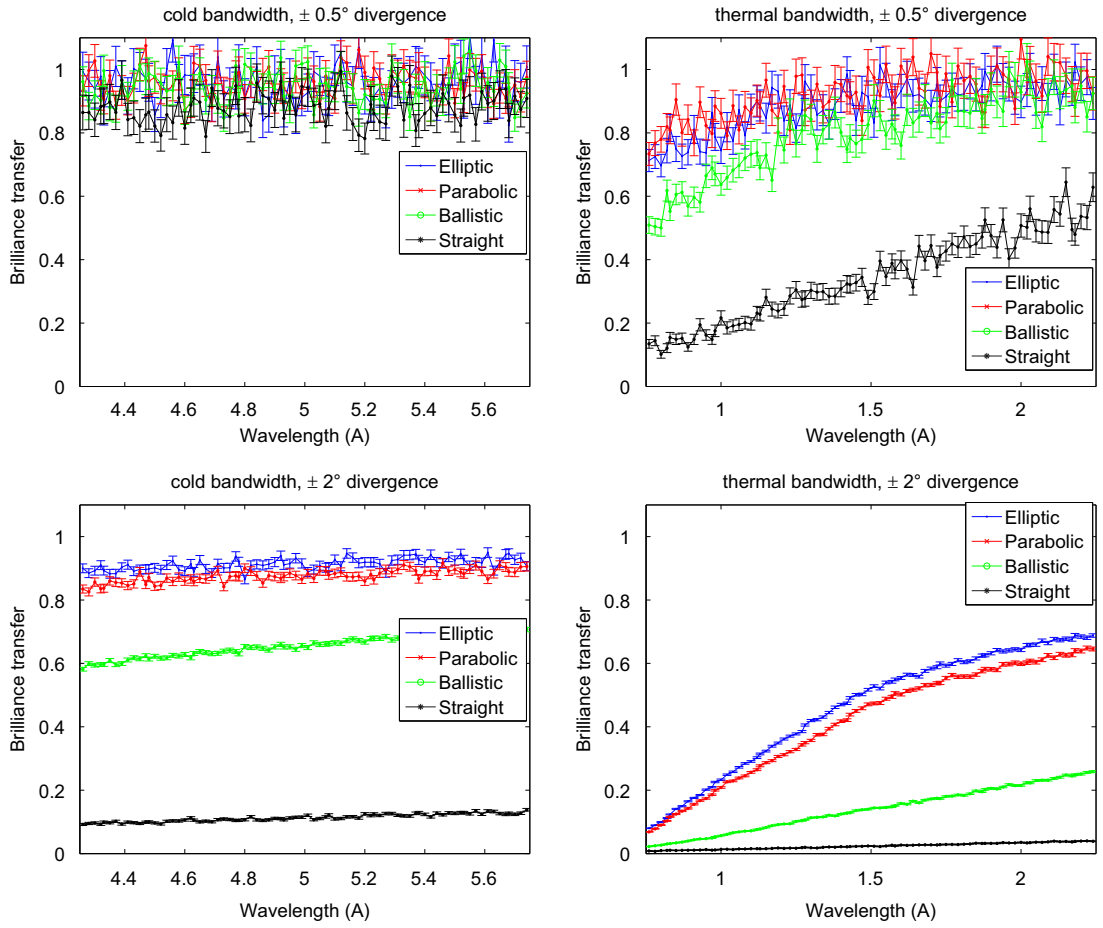

Fig. 9. Brilliance (phase space density) transfer for the four different neutron guide geometries over a 150 m distance plotted as a function of wavelength, integrated over divergence. Left: Optimised for cold neutrons. Right: Optimised for thermal neutrons. Top: Optimised for 0.5° divergence. Bottom: Optimised for 2.0° divergence.

holds for both highly divergent and thermal neutrons, although these would certainly benefit from supermirror coatings with a higher reflectivity at large q than is readily available today. For cold neutrons, the currently supermirrors are quite sufficient. It is also clear that the elliptic and parabolic guides are far superior to the simpler guide shapes. The exception is when the transport of only very low-divergent neutrons is desired, which makes focusing geometries redundant. More advanced guide shapes other than the ones covered here would not be able to bring significant improvements to the transport of cold neutrons because we are already very close to the Liouville limit.

For long guides, e.g., for the ESS, it is clear that advanced shapes, such as elliptic and parabolic shapes, would be advantageous in many cases. The detailed design of guides will be based on many more considerations than simply neutron flux, such as the line of sight, background, chopper placement, engineering and space constraints, and price.

Our results may specifically be used to conclude whether an advanced guide shape is relevant in the considerations for a particular guide length. For example, for a 150 m guide, it is relevant to consult Fig. 6. This figure shows that cold, low-divergence neutrons can be transported by a straight guide, whereas highly divergent and/or thermal neutrons would strongly favour the parabolic or elliptical shapes. The dips observed in the graphs at low divergence for the elliptic and parabolic guides have little impact on the integrated Brilliance transmission, which is the optimisation criterion. These dips may be smoothed when convoluting with other resolution functions, but for instruments where they would represent a problem, optimisation to lessen them would be required.

Similar conclusions can be drawn for a 50 m guide (Fig. 5) and a 300 m guide (Fig. 7).

References

[1] M. Sales, S.L. Holm, K. Lieutenant, K. Lefmann, Journal of the Physical Society of Japan 80SB (2011) SB018.
[2] H. Maier-Leibnitz, T. Springer, Journal of Nuclear Energy. Parts A/B. Reactor Science and Technology 17 (1963) 217.
[3] W. Bührer, Nuclear Instruments and Methods in Physics Research Section A: Accelerators, Spectrometers, Detectors and Associated Equipment 338 (1994) 44.
[4] L. Pintschovius, Nuclear Instruments and Methods in Physics Research Section A: Accelerators, Spectrometers, Detectors and Associated Equipment 338 (1994) 136.
[5] P. Böni, Physica B: Condensed Matter 234–236 (1997) 1038.
[6] F. Mezei, Communications on Physics 1 (1976) 81.
[7] Swissneutronics, personal communication, 2011.
[8] I. Goncharenko, I. Mirebeau, P. Molina, P. Böni, Physica B: Condensed Matter 234–236 (1997) 1047.
[9] F. Mezei, M. Russina, Physica B: Condensed Matter 283 (2000) 318.
[10] C. Schanzer, P. Böni, U. Filges, T. Hils, Nuclear Instruments and Methods in Physics Research Section A: Accelerators, Spectrometers, Detectors and Associated Equipment 529 (2004) 63.
[11] K.H. Klenø, K. Lefmann, Optimization of supermirror guide coating, in preparation.
[12] K. Lefmann, K. Nielsen, Neutron News 10/3 (1999) 20.
[13] P. Willendrup, E. Farhi, K. Lefmann, Physica B: Condensed Matter 350 (2004) E735.
[14] G. Zsigmond, K. Lieutenant, S. Manoshin, H. Bordallo, J. Champion, J. Peters, J. Carpenter, F. Mezei, Nuclear Instruments and Methods in Physics Research Section A: Accelerators, Spectrometers, Detectors and Associated Equipment 529 (2004) 218.
[15] F. Mezei, ESS Reference Moderator Characteristics for Generic Instrument Performance Evaluation, Technical Report, Hahn-Meitner-Institute, 2000.

[16] A. Perillo-Marcone, D11 waviness measurements, personal communication, 2011.
[17] K. Lieutenant, K.H. Klenø, Waviness of neutron guides, in preparation.
[18] W.H. Press, S.A. Teukolsky, W.T. Vetterling, Numerical Recipes in C, Cambridge University Press, 1992.
[19] D. Braess, Computing 1 (1966) 264.
[20] L.D. Landau, E.M. Lifshitz, Statistical Physics, 3rd ed., vol. 1, Elsevier, 1951.
[21] K.H. Klenø, Full optimization results, available at sim.esss.dk/index.php/reports, 2011.
[22] K. Lieutenant, in preparation.
[23] K. Lieutenant, J. Peters, F. Mezei, Journal of Neutron Research 14 (2006) 147.
[24] R.M. Ibberson, Nuclear Instruments and Methods in Physics Research Section A: Accelerators, Spectrometers, Detectors and Associated Equipment 600 (2009) 47.
[25] K.H. Klenø, K. Lefmann, Journal of the Physical Society of Japan 80SB (2011) SB004.
[26] P. Bentley, et al., in preparation.
[27] P. Böni, F. Grünauer, C. Schanzer, Nuclear Instruments and Methods in Physics Research Section A: Accelerators, Spectrometers, Detectors and Associated Equipment 624 (2010) 162.
[28] K.H. Klenø, P.K. Willendrup, E. Knudsen, K. Lefmann, Nuclear Instruments and Methods in Physics Research A: Accelerators, Spectrometers, Detectors and Associated Equipment 634 (2011) 100.
[29] J.C. Cook, Review of Scientific Instruments 80 (2009) 023101.

Proc. Int. Workshop Neutron Applications on Strongly Correlated Electron Systems 2011
J. Phys. Soc. Jpn. **80** (2011) SBarticle

Thermal Chopper Spectrometer for the European Spallation Source

Kaspar Hewitt Klenø[1,2], Kim Lefmann[1,2]

[1]*Nanoscience & E-science centers, Niels Bohr Institute, University of Copenhagen, Denmark*
[2]*ESS, Lund, Sweden*

One of the instruments being considered for the ESS is a thermal chopper spectrometer, intended for the study of lattice vibrations and magnetic excitations. However, as the ESS will be a long pulsed source, we propose a very long instrument (180 m - 300 m). We here present a guide system that can achieve a flux of 3.47×10^8 n/s/cm^2 and a resolution of $\frac{dE}{E}$ = 5.3 % for 1 Å neutrons on the sample with a transport efficiency of 80%. Furthermore, we demonstrate the efficiency of the instrument using a virtual experiment measuring an elastic line width.

KEYWORDS: Neutron scattering, instrumentation, ray-tracing, Monte Carlo simulation

1. Introduction

Thermal chopper spectrometers in direct geometry are used as workhorses to measure atomic motion, lattice vibrations, and magnetic excitations in liquids, powders, and single crystals. At existing short-pulsed spallation sources, such instruments are usually short, since the sharpness of the pulse ensures a sufficiently good energy resolution and since a shorter flightpath ensures a broader wavelength band of incoming neutrons, giving a higher flux on the sample.[18)]

One example of such instruments is MERLIN at ISIS with a moderator-sample distance of 11.8 m, giving an energy resolution of dE/E = 3-5% for energies of 10-300 meV.[1)] The beam divergence is 2% at 10 meV and 0.5% at the highest energies, due to a tapering $m = 3$ supermirror guide, giving a scattering vector resolution of dq/q = 1.5-3%. Its sister instrument MAPS has very similar specifications, but has no guide.[2)]

The spectrometer ARCS at SNS uses 13.6 m moderator-sample distance and has an energy resolution of dE/E = 2-5% for energies of 10-1500 meV.[3)] ARCS uses an $m = 3.6$ elliptical guide. The other SNS spectrometer SEQUOIA is in this respect similar to ARCS, only with a 20 m sample distance and a finer energy resolution down to 1%.[19)] Similar to this is the LANL spectrometer Pharos with 18 m sample distance, 2-4% energy resolution, and no guide.[5)]

At J-PARC, 4SEASONS has a moderator-sample distance of 18 m, giving an energy resolution of dE/E = 6% and a scattering vector resolution of dq/q = 1.5%,[6)] while the spectrometer HRC is slightly shorter with 15 m sample distance and $dE/E \approx 1\%$.[7)]

All these spectrometers are placed as close as possible to their respective moderators, since their short pulses essentially makes the energy resolution of the incoming beam "too good" compared to the resolution of the secondary spectrometer.

At the European Spallation Source (ESS), the pulse length will be long: 2-3 ms or 2 orders of magnitude larger than for equivalent instruments at ISIS, SNS, LANSCE, and J-PARC. This implies that either the instrument length will need to increase, the pulse will need to be shaped by choppers, or both. We have chosen to investigate the performance of a long thermal chopper instrument for ESS in direct geometry, where the instrument is an order of magnitude longer than for the instruments presented above, and where the moderator pulse is possibly shortened with respect to the full pulse width. The challenge posed by such long instruments is attaining a sufficiently good neutron transport, since thermal neutrons are usually not well transported by curved guides. We have therefore placed particular emphasis on the neutron transport of our proposed guide system. We shall demonstrate that a long thermal chopper spectrometer seems like a very powerful neutron instrument.

2. Instrument Design

The instrument was simulated using the McStas neutron ray-trace simulation package,[12)] and it is based on the design concept for a cold-neutron spectrometer from the Rencurel meeting in 2006.[8,9)] The source used is a model of the expected ESS thermal moderator, with a pulse width of 2 ms, a pulse period of 50 ms, and a size of 12×12 cm^2. Gravity was simulated throughout the guide system. A realistic waviness value of 0.01° was also simulated, and this was found to have no significant effect on the guide performance.[17)]

As the instrument concept calls for a energy resolution in the range of 3-5 %, the long ESS pulse requires us to either shorten the long pulse, or alternatively design a very long instrument. We will here investigate both options: an instrument with a 180 m source - sample distance, which has the 2 ms pulse chopped down into a 1.1 ms pulse; and an instrument with a 300 m source - sample distance, using the full pulse width.

Transporting thermal neutrons over such a long distance is a significant challenge. To handle this we chose an elliptical guide, in order to both focus the beam onto the sample and to reduce the number of bounces in the guide. Together with using a non-uniform supermirror coating distribution, this will provide near optimal flux on sample.[10,11,19)]

The elliptical guide begins 1.5 m from the moderator face and ends 50 cm from the sample position. It has the elliptical start and end focal points placed by numerical optimization at -7.11 m & 0.32 m (-6.75 m & 0.33 m) relative to the start and end of the guide, for the 180 m (300 m) spectrometer. The guide has a small axis of 28 (40) cm for the 180 (300) m long

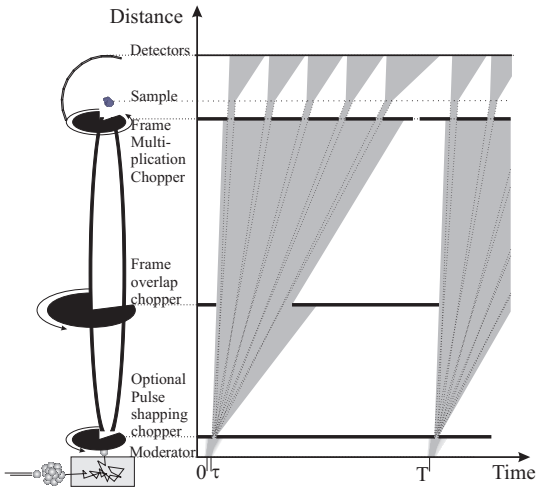

Fig. 1. Time of flight diagram of the instrument layout, showing the general layout of the instrument. The right part of the figure shows the passage of a neutron pulse through the chopper systems.

spectrometer.

The figure of merit (FoM) that the guide has been optimized after is flux on sample, counting only those neutrons with a divergence below 1 °. The beam is focused on a sample, which is cylindrical with a cross section in the beam of 1 × 1 cm^2.

The optimized instrument has a supermirror coating which gradually changes from $m = 6$ in the ends of the guide to $m = 1$ in the centre of the guide, as shown in fig. 3. This will give a high transmission without making the guide unrealistically expensive.[10)]

A pulse shaping disc chopper is placed 6 m from the moderator, and a pair of fast, counter-rotating resolution disc choppers are placed immediately after the end of the guide, as shown in fig. 1. The resolution choppers have an angular opening of 8 ° and run at 300 Hz. The effect of the choppers is both to monochromatize and to create wavelength frame multiplications,[16,20)] as can be seen in fig. 1 & 2.

A frame overlap chopper is also needed to restrict the bandwidth, so as to avoid any overlap with the next pulse from the moderator. For simplicity, this chopper is not actually simulated, rather the bandwidth is limited by the parameters of our virtual source.

The resolution of the instrument is calculated from the general ToF equation:

$$t = \alpha L \lambda, \tag{1}$$

where L is the source-sample distance, λ the neutron wavelength and $\alpha = 252\ \mu$s/Å/m. This leads to

$$\frac{d\lambda}{\lambda} = \frac{dt}{t} = \frac{\tau}{\alpha L \lambda} \tag{2}$$

where τ is the pulse width. Converting from wavelength to energy, we get:

$$\frac{dE}{E} = 2\frac{\tau}{\alpha L \lambda} \tag{3}$$

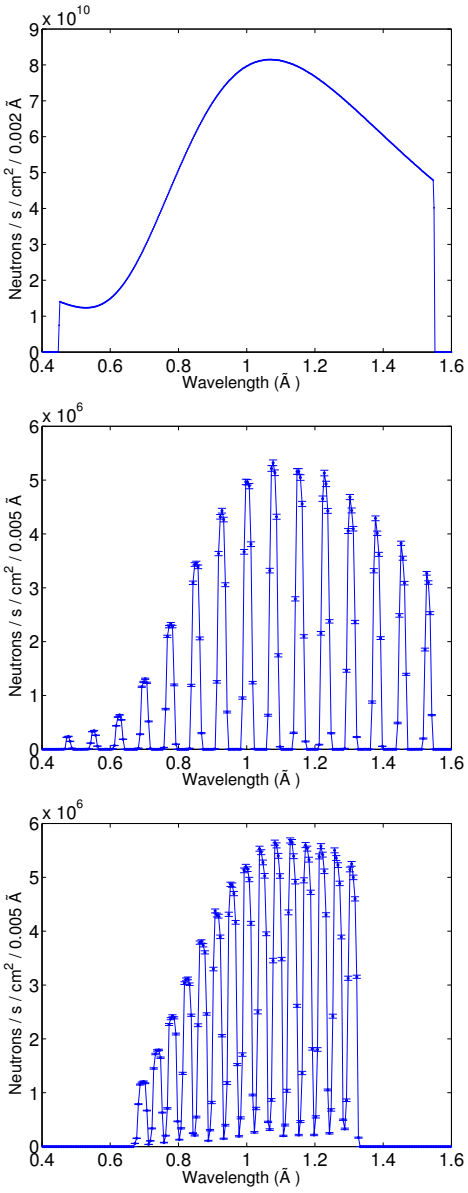

Fig. 2. Wavelength distribution of the beam, and the effect of the resolution choppers. Top: at the entrance to the guide. Middle: at the sample position, just after the resolution choppers, with the 180 m guide system. Bottom: at the sample position, just after the resolution choppers, with the 300 m guide system. The sharp cut-offs at the 0.45 and 1.55 Å positions are caused by the bandwidth restrictions discussed in the text.

$$L = \left(\frac{d\lambda}{\lambda}\right)^{-1} \frac{\tau}{\alpha\lambda} \tag{4}$$

So for an ESS pulse length of 2 ms and a sample distance of L = 300 m, this gives a resolution at the sample position of $\frac{dE}{E} = 5.3\%$ (full width, half max), for 1 Å neutrons.
In order to match this resolution for a 180 m sample distance, the pulse width need to be reduced to 1.2 ms using a pulse shaping chopper. However, when fine tuning the instrument to get identical resolution in the virtual experiments for the two different sample distances, we found that the pulse width had to be reduced from 1.2 to 1.1 ms. This difference can be explained by the finite opening/closing time of the choppers.

We now determine the maximum bandwidth that avoids

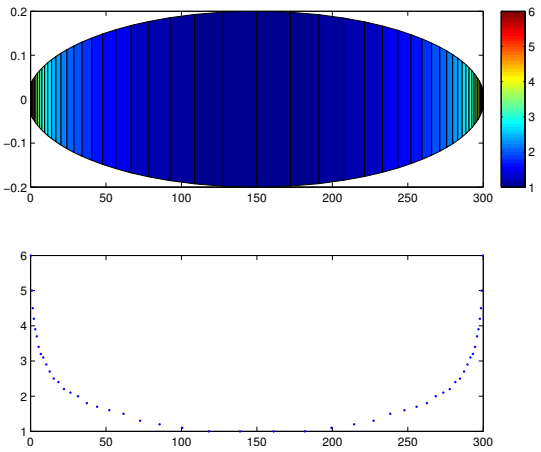

Fig. 3. Non-uniform supermirror coating distribution. Top: the guide shape, colour coded for coating quality (m-value). Bottom: m-value vs. distance (in meters) from guide start.

frame overlap, for a pulse period of T = 50 ms. Eq. 1 leads to:

$$T = \alpha\, \Delta\lambda\, L, \tag{5}$$

which gives us the bandwidths:

$$\frac{T}{\alpha L} = \Delta\lambda = 1.10\ (0.67)\ \text{Å} \tag{6}$$

for the 180 m (300 m) sample distance.

We chose to center the bandwidth on 1 Å, which then gives us the λ-ranges of 0.45-1.55 (0.67-1.33) Å.

3. Basic Simulation Results

When using the above settings for the instrument, we find that it is feasible to transport thermal neutrons over 300 m. When considering only neutrons with a divergence below 1° and within the above wavelength range, we get a flux on sample of 1.95×10^{10} n / s /cm^2. That figure is when the resolution choppers are disabled. When enabling the choppers, the above flux figure gets reduced to 3.47×10^{8} n / s /cm^2.

The increased bandwidth allowed by the 180 m sample distance, as well as the shorter guide transport distance, suggest that the 180 m version would outperform the 300 m version. Indeed this is the case when the beam choppers are disabled, as can be seen from table I. But when the beam choppers are turned on, the pulse shaping chopper has a significantly detrimental effect on the 180 m spectrometer, so that the 300 m version outperforms it by more than 50 %; and in addition has the neutron bands more closely spaced, as can be seen from fig. 2.

Another way to measure the performance of a guide system is to consider the brilliance transfer from the source to the sample, i.e. what fraction of the phase space density of the beam is successfully transported by the guide system in the above wavelength range. This is measured by placing a small divergence and wavelength sensitive monitor at the sample position, an identical one at the moderator, and taking the ratio of their outputs. This ratio must fullfill $\frac{B_{sample}}{B_{moderator}} < 1$ due to the Liouville theorem.[15)]

As can be seen from fig. 4, both guide systems have a very good brilliance transfer, up to 80 %, with the choppers turned

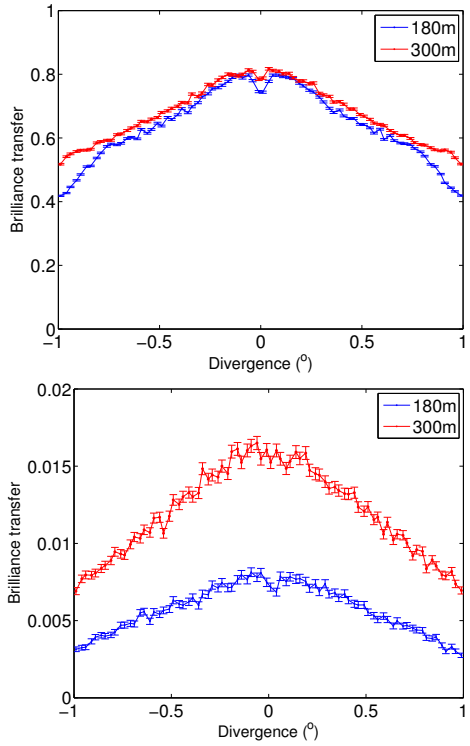

Fig. 4. Transport of phase space density of the full bandwidth beam from the source to the sample as a function of horizontal divergence, for the two difference guide systems. Top: with the choppers disabled. Bottom: with the choppers enabled.

off. When the choppers are activated, the 180 m guide system will naturally have a much lower transfer due to the pulse width of the chopper. The slight dip around 0 ° is caused by neutrons with so low a divergence that they do not impact the guide wall at all, and are thereby not focused onto the sample.

Surprisingly the 300 m guide system also has a higher transport when the choppers are disabled. This can be explained by the fact that in order to accommodate the pulse shaping chopper, a section of the guide had to be removed, which naturally retards the performance of the 180 m guide system, even with the choppers disabled.

4. Virtual Experiments

Virtual experiments[14)] were performed by placing a sample in the beam, with the scattered neutrons measured by a detector 4 m from the sample, orthogonal to the beam. The detector measures the arrival time of the neutron, and then calculates its perceived energy, from the time it took from the opening of the chopper to the neutron reached the detector. The detector has a size of 1×2.5 cm^2, corresponding to a single bin, and we assume for simplicity 100% detector efficiency.

Using an elastic sample to ascertain the energy resolution of the instrument, we get the results shown in fig. 5. The opening time of the pulse shaping chopper was tuned until we obtained the same resolution for both the 180 m and 300 m sample distances. The two peaks look quite similar, apart from the 20 % greater neutron count from the 300 m guide system for the 1 Å peak.

As seen from the Gaussian fit in fig. 5, the shape of the resolution peak is complex and needs modeling to obtain quan-

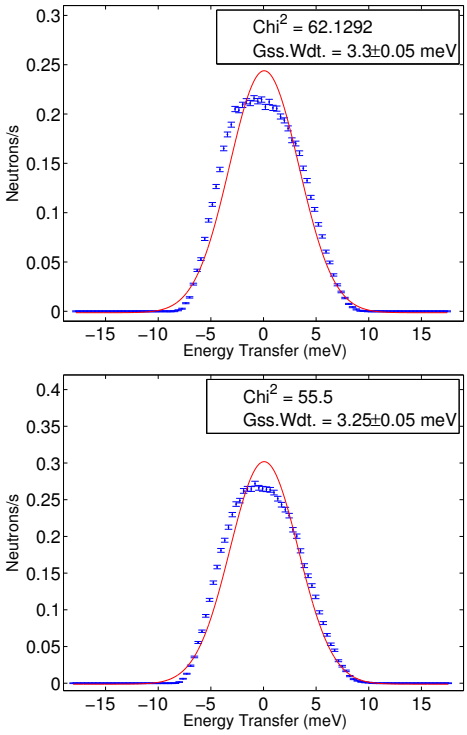

Fig. 5. A virtual experiment with an elastically scattering sample, fitted to a Gaussian. Top: 180 m sample distance. Bottom: 300 m sample distance. The bin size is 0.36 meV.

Table I. Results for simulations and virtual experiments. Refer to text for details.

Sample distance	180 m	300 m
FoM without choppers	2.63E+010 n / s / cm^2	1.95E+010 n / s / cm^2
FoM with choppers	2.25E+008 n / s / cm^2	3.47E+008 n / s / cm^2

titative results.

5. Conclusion

We have shown that it is indeed quite feasible to build a very long thermal spectrometer, where the resolution of the primary and secondary spectrometers are matched. The transport of thermal neutrons presents no problems for the elliptical guide: Even for a length of 300 m, we get an excellent brilliance transport though the guide with losses as low as 20 - 40 %, and at ESS we can deliver a monochromatic flux on sample of 3.47×10^8 n/s/cm^2.

As shown in fig. 5, the 180 m version of the instrument can attain the same resolution as the 300 m version, through the use of a pulse shaping chopper, but at the cost of 35 % reduced flux on sample, as seen from table I. This leads us to conclude that the 300 m version of the instrument might be preferable, as it can attain the same resolution as the 180 m instrument while delivering greater flux on sample, by using the full 2 ms ESS pulse width.

However, the cost of shielding, alignment difficulties, and other external factors, which we have not attempted to quantify in this article, may shift this preference.

Acknowledgment

We thank the Danish Ministry of Research for support during the ESS design update phase.

1) R.I. Bewley, T. Guidi, and S. Bennington, Notiziario Neutroni e Luce di Sincrotrone **14/1**, 22 (2009)
2) See the MAPS home page `http://www.isis.stfc.ac.uk/instruments/maps/`
3) D.L. Abernathy, Notiziario Neutroni e Luce di Sincrotrone **13/1**, 4 (2008)
4) G.E. Granroth, M. Chen, J.A. kohl, M.E. Hagen, and J.W. Cobb, J. Neutron Res. **15**, 91 (2007)
5) See the PHAROS home page `http://lansce.lanl.gov/lujan/instruments/Pha`
6) R. Kajimoto, T. Yokoo, K. Nakajima, M. Nakamura, K. Soyama, T. Ino, S. Shamato, M. Fujita, K. Ohoyama, H. Hiraka, K. Yamada, M. Arai, J. Neutr. Res. **15**, 5 (2007)
7) See the HRC home page `http://j-parc.jp/MatLife/en/instrumentation/bl1`
8) H. Schober et. al., Nuclear Instruments and Methods in Physics Research A 589 (2008)
9) K. Lefmann, H. Schober, and F. Mezei, Meas. Sci. Technol., 19, 034025 (2008)
10) K. H. Klenø et. al., in preparation (2011)
11) K. H. Klenø , K. Lieutenant et. al., in preparation (2011)
12) K. Lefmann and K. Nielsen, Neutron News 10/3, 20 (1999)
13) K. Lefmann et al., in preparation (2011)
14) K. Lefmann et. al., Journal of Neutron Research, 16 (2008), 97
15) L. D. Landau and E.M. Lifshitz, 'Statistical Physics: Volume 5', part 1 (1980)
16) F. Mezei, J. Neutron. Res. 6, 3 (1997)
17) K. Lieutenant and K. H. Klenø, in preparation (2011)
18) D.L. Abernathy, Applied Physics A (2002)
19) G.E. Granroth et al., Physica B (2006)
20) M. Nakamura, J. Phys. Soc. Jpn. 78 (2009)

Nuclear Instruments and Methods in Physics Research A 634 (2011) S100–S103

Contents lists available at ScienceDirect

Nuclear Instruments and Methods in Physics Research A

journal homepage: www.elsevier.com/locate/nima

Eliminating line of sight in elliptic guides using gravitational curving

Kaspar H. Klenø [a,b,*], Peter K. Willendrup [c], Erik Knudsen [c], Kim Lefmann [a,b]

[a] Nanoscience and E-Science Centers, Niels Bohr Institute, University of Copenhagen, DK-2100 Copenhagen, Denmark
[b] ESS, University of Lund, St. Algaten 4, Sweden
[c] Materials Research Division, Risø, Technical University of Denmark, DK-4000 Roskilde, Denmark

ARTICLE INFO

Available online 1 July 2010

Keywords:
Neutron guide
ESS
Backscattering spectrometer
Ray-tracing simulations

ABSTRACT

Eliminating fast neutrons ($\lambda < 0.5$ Å) by removing direct line of sight between the source and the target sample is a well established technique. This can be done with little loss of transmission for a straight neutron guide by horizontal curving. With an elliptic guide shape, however, curving the guide would result in a breakdown of the geometrical focusing mechanism inherent to the elliptical shape, resulting in unwanted reflections and loss of transmission.

We present a new and yet untried idea by curving a guide in such a way as to follow the ballistic curve of a neutron in the gravitational field, while still retaining the elliptic shape seen from the accelerated reference frame of the neutron. Analytical calculations and ray-tracing simulations show that this method is useful for cold neutrons at guide lengths in excess of 100 m.

We will present some of the latest results for guide optimization relevant for instrument design at the ESS, in particular an off-backscattering spectrometer which utilizes the gravitational curving, for 6.66 Å neutrons over a guide length of 300 m.

1. Introduction

Unless a neutron instrument blocks the direct line of sight between the moderator and the sample, fast neutrons and $\gamma-$rays will reach the sample and cause an unwanted background. Often these are removed by curving the neutron guide slightly, so that the fast neutrons and $\gamma-$rays penetrate into the guide walls and are absorbed in the shielding.

It has been shown that elliptical guide designs have superb transmission and focusing properties [3]. For an elliptical guide, however, curving would destroy the elliptical geometry; in a 100 m elliptical guide for example, this results in a flux loss on the order of 40% for 5 Å neutrons [2].

This article details a novel method for using gravity as an aid to eliminate direct line of sight between the moderator and the sample, for use with elliptical guides.

This article does not resolve the discussion of whether instruments at spallation sources can tolerate line of sight, e.g. by use of filters in the direct beam; rather we have looked for a way to eliminate line of sight while minimizing the impact on neutron delivery.

The method has been developed for use with a off-backscattering spectrometer, suggested for the European Spallation Source [8].

The instrument modelled is based on the OSIRIS instrument at ISIS, but modified to make use of the longer pulse of the ESS [8].

The basic principle of a backscattering instrument is that the scattering beam from the sample is reflected off analyser crystals onto a detector with scattering angles close to 180°. As the beam reaching the detector is thus highly monochromatic, the flight time from sample to detector is well determined, allowing the incident flight time, and thus the energy shift due to inelastic scattering, to be calculated to a high precision [11].

We will show by neutron simulations that it is possible to construct such a backscattering instrument with a gravitationally bent elliptical guide at a long-pulsed spallation source, where the bending will prevent fast neutrons, while still having the elliptical focusing properties.

2. Designing a very long neutron guide

Since the ESS will be a long pulsed source, it is unrealistic to design a backscattering spectrometer with the sub$-\mu$eV resolution as SPHERES at FRM2 or BASIS at SNS. This would require sacrificing the flux superiority of the ESS by chopping the beam into very short pulses. Instead we here aim for a coarser resolution as found at OSIRIS at ISIS, in combination with a high flux by using the full $\tau = 2$ ms pulse. The OSIRIS analyser system [4,5] has a resolution of $d\lambda_f/\lambda_f = 0.4\%$ with Si(1 1 1) analysers, corresponding to 6.66 Å. We want to match the time of flight (ToF) resolution with the analyser resolution, and this is found from the general ToF equation:

$$t = \alpha L \lambda \quad (1)$$

* Corresponding author at: Nanoscience and E-Science Centers, Niels Bohr Institute, University of Copenhagen, DK-2100 Copenhagen, Denmark.
E-mail address: kaspar@fys.ku.dk (K.H. Klenø).

0168-9002/$ - see front matter © 2010 Elsevier B.V. All rights reserved.
doi:10.1016/j.nima.2010.06.261

where τ is the pulse width, λ the neutron wavelength and $\alpha = 252\,\mu s/Å/m$. This leads to

$$\frac{d\lambda_i}{\lambda} = \frac{dt}{t} = \frac{\tau}{\alpha L \lambda_i}. \quad (2)$$

Matching $d\lambda_i$ with $d\lambda_f$, we reach the guide length:

$$L = \left(\frac{d\lambda_f}{\lambda_f}\right)^{-1} \frac{\tau}{\alpha \lambda_f}. \quad (3)$$

So for an ESS pulse length of 2 ms, we need a guide of length $L = 300$ m.

We now determine the maximum bandwidth that avoids frame overlap, for a pulse period of $T = 60$ ms. Eq. (1) leads to

$$T = \alpha \Delta\lambda L \quad (4)$$

which gives us the bandwidth:

$$\frac{T}{\alpha L} = \Delta\lambda = 0.8\,Å. \quad (5)$$

Hence the λ−range is 6.26–7.06 Å.

Such an immense guide length demands an advanced guide geometry to achieve a high flux to the sample position, and an elliptical guide solves this well [3,2]. In addition, a non-uniform coating distribution [6] allows us to keep the guide price down, and a systematic way of optimizing this will be presented in Ref. [2]. However, this still leaves the problem of how to eliminate the direct line of sight (LoS) from moderator to sample (Fig. 1).

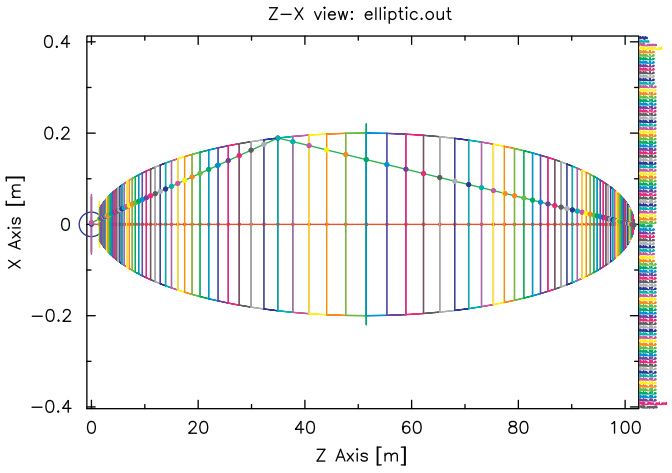

Fig. 1. A top down view of a 40 cm wide elliptic neutron guide. The line with coloured dots indicate one neutron trajectory. The colours denotes different straight sections of guide elements, which together form an ellipse. (For interpretation of the references to color in this figure legend, the reader is referred to the web version of this article.)

Table 1
Basic instrument geometry for the 300 m long guide.

Moderator size	$12 \times 12\,cm^2$
Guide length	300 m
Guide height (h_s) and width at entry	9.7 cm, 9.7 cm
Guide height (h_m) and width at midpoint	40 cm, 40 cm
Guide height (h_e) and width at exit	4.5 cm, 3.5 cm
Sample height and width	4 cm, 2 cm

3. Gravitational curvature

Our idea to solve the LoS problem is to exploit the deflection of the neutrons introduced by gravity, and curve the ellipse in the vertical plane, so that it follows the ballistic path of a particle in free fall. This gives an elliptical guide a banana-like shape when seen from the side, as shown in Fig. 3

The calculations for this are fairly simple: if a neutron takes the time

$$T = L/V$$

to pass through the guide, it will reach its maximum height at time $T/2$:

$$y_{max} = \frac{1}{2} g \left(\frac{L}{2V}\right)^2. \quad (6)$$

The maximum height required to block LoS is dependent on the guide width at the start, exit and middle. LoS is blocked if

$$y_{max} > \frac{h_s}{4} + \frac{h_e}{4} + \frac{h_m}{2}. \quad (7)$$

As the instrument is very long, we have, for now, chosen a rather substantial guide width of 40 cm (Table 1). Hence we require $y_{max} = 30$ cm to comfortably block LoS. Using this y_{max} in the above equation tells us that the guide should be bent for neutrons with a speed of 0.61 km/s, and thus a wavelength of 6.5 Å; a close match with the 6.66 Å required by the analyser system.

So, in order to block LoS, a 40 cm wide elliptical guide must be curved to follow gravitational flight path of a neutron with a

Table 2
Matching wavelengths for different guide lengths of 40 cm wide gravitationally curved guides.

Guide length (m)	Matching wavelength (Å)
50	38.0
100	19.5
160	12.5
300	6.5

For explanation, see text.

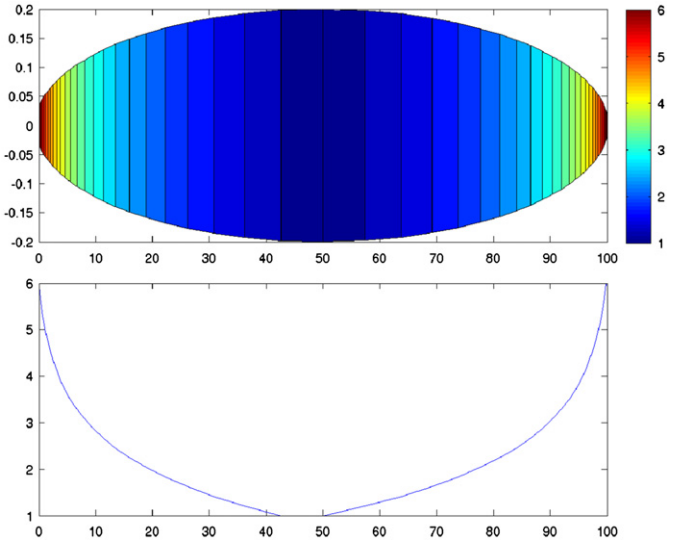

Fig. 2. Non-uniform supermirror coating distribution. Top: the guide shape, colour coded for coating quality (m-value). Bottom: coating quality vs. distance from guide start. (For interpretation of the references to color in this figure legend, the reader is referred to the web version of this article.)

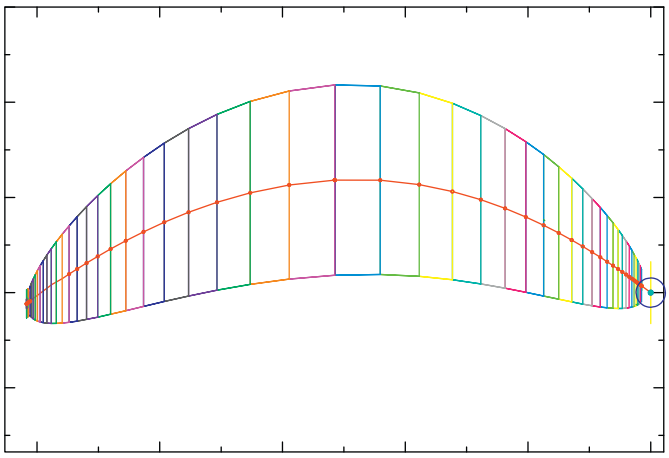

Fig. 3. Sideways view of a 40 cm wide gravitationally curved guide, composed of 50 straight sections. The red line denotes the transverse centre of the guide. Note that this figure is meant to give the reader a visual idea of the shape of a curved elliptical guide, and is not to scale. (For interpretation of the references to color in this figure legend, the reader is referred to the web version of this article.)

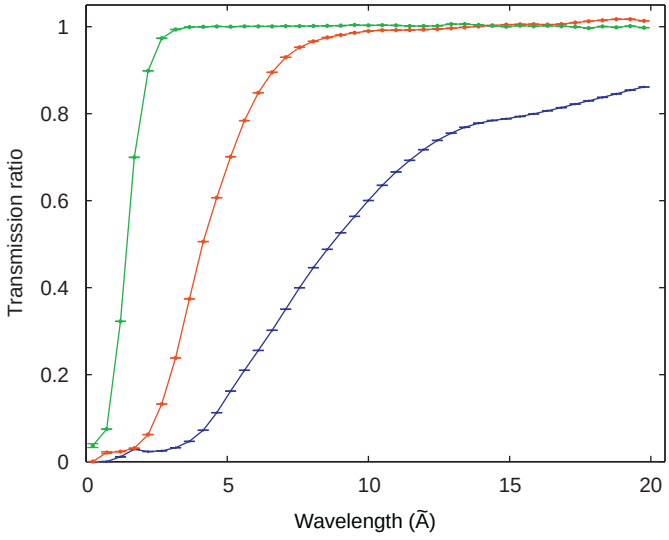

Fig. 4. The simulated transmission ratio of a 40 cm wide elliptical guide, gravitationally curved to eliminate LoS, vs. an identical, but uncurved guide, as a function of wavelength. The green line represents a 300 m long guide, red is 100 m, and blue is 50 m. (For interpretation of the references to color in this figure legend, the reader is referred to the web version of this article.)

certain matching wavelength. The shorter the guide system, the more pronounced is the curvature, leading to a longer matching wavelength. Table 2 presents the matching wavelengths for 40 cm wide gravitationally curved guides of different lengths.

For guide lengths below 300 m, the matching wavelengths are very long, but fortunately a gravitationally curved guide will have a high transmission of wavelengths in a significant interval around the curvature wavelength, as we will present below.

4. Simulations

To simulate the bent guide as explained above, we have performed simulations with the McStas neutron simulation package [9], using a custom built guide component.

We have chosen to model an identical analyser and detector system as that of OSIRIS at ISIS, which reflects 6.66 Å neutrons by $2\theta = 171^\circ$ off Si(1 1 1) analysers [5]. We use a gravitationally curved elliptical guide with a non-uniform supermirror coating distribution, as shown in Fig. 2.

Most simulations were performed with a 40 cm wide elliptical guide, but a guide width of 20 cm were tried as well. Results are given as simulated flux on a $4 \times 2\,\mathrm{cm}^2$ sample. The simulations show that the gravitational curvature as expected gives a slight boost in the transmission for the wavelength for which it is curved. This gain is very slight; for the transmission of 6.66 Å for the 300 m guide length, it is 0.06%, but this is of the order of the statistical uncertainty, which is 0.03%. Furthermore, it has only a small detrimental effect on transmission in a wide band around this wavelength, as seen in Fig. 4.

The above result holds for a 40 cm wide guide, which requires a more pronounced curvature than the slimmer guide of 20 cm. A 40 cm wide guide is usually preferable to a 20 cm one, as slimming the guide results in a loss of flux. E.g. a 20 cm wide 100 m long guide, loses 39% of 5 Å neutrons, compared to a 40 cm wide 100 m long guide. However, as Fig. 5 shows, the reduced curvature from a slimmer elliptical guide reduces the transmission loss for the shorter wavelengths significantly. Comparison of the red and blue curves reveals that for wavelengths at 8 Å or below for the 50 m guide, or 3 Å or below for the 100 m guide, the slim guide delivers a better absolute transmission to the sample position when gravitational curvature is needed. For instruments where a slimmer guide is required anyway, the green curve shows the effect gravitational curving would have on guide transmission.

The simulations verify that gravitational curvature does indeed block the low wavelength neutrons as intended. Fig. 6 shows the

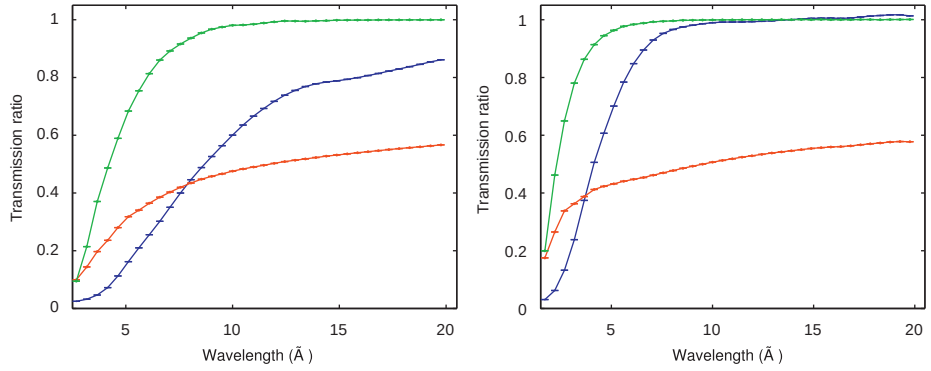

Fig. 5. The transmission ratio as a function of wavelength for long elliptical guides with 20 and 40 cm maximum width. Left: results for a 50 m long guide. Right: results for a 100 m long guide. Blue: The transmission ratio of a 40 cm curved vs. uncurved. Red: the transmission of a curved guide with a maximum width of 20 cm vs. an uncurved guide with a maximum width of 40 cm. Green: the transmission a curved guide with a maximum width of 20 m vs. an identical, but uncurved guide. Gravitationally curved guides are bent so as to eliminate LoS, as discussed in the text. (For interpretation of the references to color in this figure legend, the reader is referred to the web version of this article.)

transmission ratio for the 300 m guide. It is seen that the lowest wavelength transmission (0.2 Å) is reduced by several orders of magnitude, compared to an uncurved guide. This effect can be expected to be even more pronounced on shorter guides.

In order to test that neither the elliptical guide nor the gravitational curvature affects the final resolution of the instrument, a full virtual experiment was conducted, simulating a realistic source, the guide system, a diffusely elastic scattering sample, a model of the OSIRIS analyser system and the detector [10,7]. A comparative simulation was performed on the same backscattering instrument, but with a conventional straight guide,

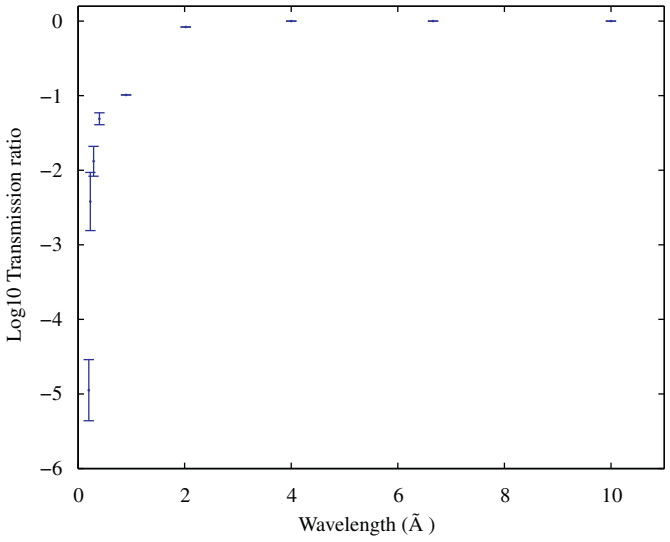

Fig. 6. The transmission ratio as a function of wavelength of a 40 cm wide, 300 m long gravitationally curved elliptical guide, vs. an identical, but uncurved guide. The transmission of undesired fast neutrons is reduced by several orders of magnitude. Note that the error indicated for the 0.2 Å transmission may be underestimated, as the simulations cannot give a good estimate for very low transmissions.

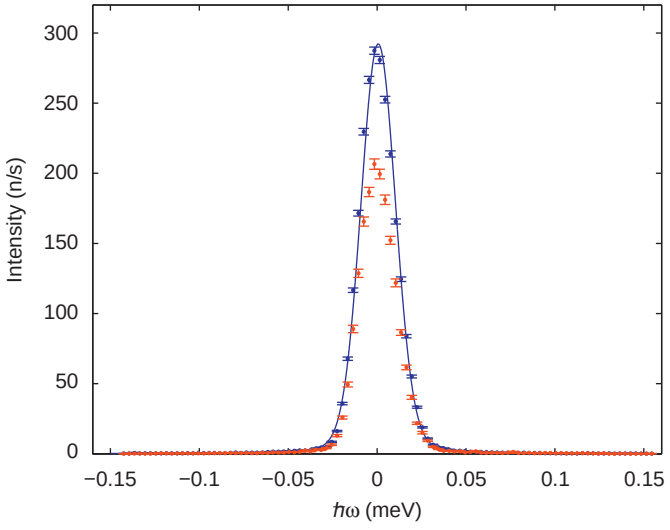

Fig. 7. A virtual experiment: The energy transfer perceived by analysis of detector data, after scattering off an incoherently scattering sample with 90% intensity in the elastic line and 10% in a quasi-elastic line with a Lorentz width of 20 μeV. The blue data is for an instrument with a gravitationally curved, elliptical guide, fitted to a Voigt line shape; the red data is for an identical instrument, but with a conventional straight guide. Note that the red intensity data has been multiplied by 20 to enable so it is visible on the graph. The width of the Gaussian fit for both datasets are 21.8 μeV ± 0.3 μeV. (For interpretation of the references to color in this figure legend, the reader is referred to the web version of this article.)

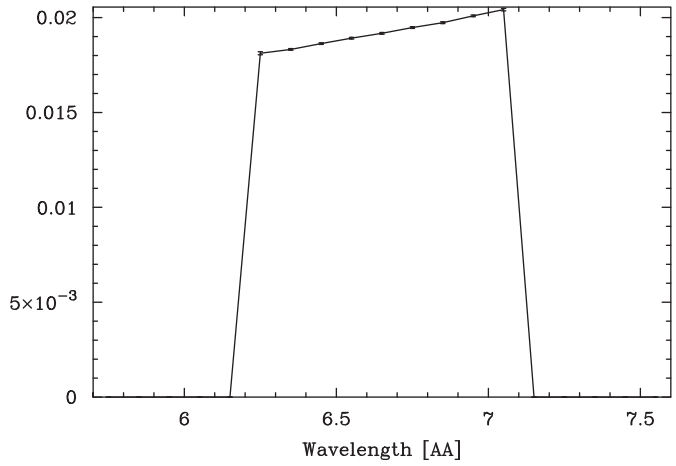

Fig. 8. The transmission from guide opening to sample as a function of wavelength, using a $12 \times 12\,cm^2$ moderator size. Note the sharp cutoffs at the sides, which are due to the frame overlap restrictions placed on the bandwidth, as defined by Eq. (5).

with a constant 12×3 cm^2 cross-section. Fig. 7 shows that although the intensity delivered to the sample is a factor 30 higher for the elliptical gravitationally curved guide, the resolution is not degraded.

Fig. 8 shows the simulated transmission of neutrons trough the gravitationally curved guide system, given as the ratio between the integrated neutron intensity over the sample, and the integrated neutron intensity over the guide start. The transmission was found to be just below 2% for the 0.8 Å wavelength band around 6.66 Å. The absolute average flux on the sample position, integrated over the 0.8 Å wavelength band and the current model for the ESS cold moderator [12] is 3.3×10^9 n/s/cm^2. The comparable figure for OSIRIS is 2.7×10^7 n/s/cm^2.

5. Conclusion

The elliptical guide with non-uniform coating allows excellent transmission even for a 300 m long guide [1,2]; furthermore, gravitational curvature allows us to block line of sight with no loss of transmission and no degradation of the energy resolution, as shown by our virtual experiments.

Gravitational curvature may also be a solution for a variety of other instruments, as this method performs well for a wide range of wavelengths and guide lengths.

While not all instruments utilizing elliptical guides have the right combination of guide length, width and desired wavelengths to allow for near loss-less gravitational curvature, a gravitational curvature will always performs at least as well as a conventional, horizontal bending of the guide.

References

[1] K.H. Klenø, Simulating Neutron Guides for the European Spallation Source, Chapters 5 and 7, M.Sc. Thesis 〈www.fys.ku.dk/∼kaspar〉.
[2] K.H. Klenø, et al., in preparation.
[3] C. Schanzer, P. Böni, U. Filges, T. Hils, Nucl. Instr. and Meth. A 529 (2004) 63.
[4] C.J. Carlile, M.A. Adams, Physica B 182 (1992) 431.
[5] K.H. Andersen, Internal ISIS Report, 15/6/99.
[6] R.M. Ibberson, Nucl. Instr. and Meth. A 600 (2009) 47.
[7] P.L.W. Tregenna-Piggott, et al., J. Neutron Res. 16 (2008) 1322.
[8] H. Schober, et al., Nucl. Instr. and Meth. A 589 (2008) 3446.
[9] K. Lefmann, K. Nielsen, Neutron News 10/3 (1999) 20 〈www.mcstas.org〉.
[10] K. Lefmann, et al., J. Neutron Res. 16 (2008) 97.
[11] A. Meyer, Rev. Sci. Instr. 74 (2003) 2759.
[12] F. Mezei, The ESS moderator, Note, 2000.

Simulation of a suite of generic long-pulse neutron instruments to optimize the time structure of the European Spallation Source

Kim Lefmann,[1,2] Kaspar H. Klenø,[1,2] Jonas Okkels Birk,[1,2,3] Britt R. Hansen,[4,5] Sonja L. Holm,[1,2] Erik Knudsen,[4,5] Klaus Lieutenant,[6,7,8] Lars von Moos,[9,5,10] Morten Sales,[1,2] Peter K. Willendrup,[4,5] and Ken H. Andersen[11]

[1]*Nanoscience and eScience Centers, Niels Bohr Institute, University of Copenhagen, Universitetsparken 5, 2100 Copenhagen Ø, Denmark*
[2]*Danish Workpackage for the ESS Design Update Phase, Universitetsparken 5, 2100 Copenhagen Ø, Denmark*
[3]*Laboratory for Quantum Magnetism, École Polytecnique Fédérale de Lausanne (EPFL), 1015 Lausanne, Switzerland*
[4]*Institute of Physics, Technical University of Denmark, 2800 Lyngby, Denmark*
[5]*Danish Workpackage for the ESS Design Update Phase, 2800 Lyngby, Denmark*
[6]*Institute for Energy Technology, Instituttveien 18, 2007 Kjeller, Norway*
[7]*Helmholtz Center for Energy and Materials, Hahn-Meitner Platz, 14109 Berlin, Germany*
[8]*German Work Package for the ESS Design Update, Hahn-Meitner Platz, 14109 Berlin, Germany*
[9]*Department of Energy Conversion and Storage, Technical University of Denmark, 4000 Roskilde, Denmark*
[10]*Institute for Energy Conversion, Technical University of Denmark, 4000 Roskilde, Denmark*
[11]*European Spallation Source ESS AB, 22100 Lund, Sweden*

(Received 18 January 2013; accepted 16 April 2013; published online 7 May 2013)

We here describe the result of simulations of 15 generic neutron instruments for the long-pulsed European Spallation Source. All instruments have been simulated for 20 different settings of the source time structure, corresponding to pulse lengths between 1 ms and 2 ms; and repetition frequencies between 10 Hz and 25 Hz. The relative change in performance with time structure is given for each instrument, and an unweighted average is calculated. The performance of the instrument suite is proportional to (a) the peak flux and (b) the duty cycle to a power of approximately 0.3. This information is an important input to determining the best accelerator parameters. In addition, we find that in our simple guide systems, most neutrons reaching the sample originate from the central 3–5 cm of the moderator. This result can be used as an input in later optimization of the moderator design. We discuss the relevance and validity of defining a single figure-of-merit for a full facility and compare with evaluations of the individual instrument classes. © *2013 AIP Publishing LLC*. [http://dx.doi.org/10.1063/1.4803167]

I. INTRODUCTION

The European Spallation Source (ESS) is designed to be a long-pulsed spallation neutron source – the first of its kind.[1,2] This opens new territory, including the challenges to design instruments that perform well for a long-pulsed source, to design the optimal moderator for these instruments, and to choose the pulsing time structure that matches these choices. Obviously, these optimizations are coupled, since, e.g., the instrument design depends upon the pulse length and the optimal moderator design depends on both desired pulse length and on the instrument geometries.

In this article, we are concerned with only one part of this optimization problem: the selection of the source time structure, i.e., its pulse length (τ) and repetition time (T). The original 2002 design was fixed at $\tau = 2$ ms, and $T = 60$ ms ($f = 16\frac{2}{3}$ Hz),[3] and we have therefore investigated time structures in the neighbourhood of these initial parameters.

In order to perform the time-structure optimization, we have selected a suite of generic instruments, covering a broad range of scientific utilizations. These instruments have then undergone a rough design and optimization for each setting of (T, τ), and the relative merits of the instruments at the different time structures have been compiled and compared.

The simulated instrument suite should not be seen as a draft day-one suite, neither should the individual instruments be seen as being close to their final design. Much design work and careful selection of an initial instrument suite is presently in progress. The present work is merely the first step in a long process.

Below, we present our generic neutron long-pulse instrument suite, the optimization procedure, and the obtained overall results. The simulation results of the 15 individual instruments are available online[4] and are or will be published individually in more detailed articles.[5–12]

As a result of this and other studies of the ESS time structure, covering its impact on the performance, reliability, construction cost, and operation of the facility, the time structure has now been fixed at $\tau = 2.86$ ms and $T = 71$ ms ($f = 14$ Hz). The results presented in this paper were an important input to this decision.

II. THE GENERIC INSTRUMENT SUITE

The instrument suite we discuss here was initiated by the Scientific Advisory Group (SAG) for ESS-Scandinavia, in September 2009. This list was expanded by the slightly different "straw-man-list" of instruments, decided upon by the

TABLE I. Properties of 15 generic ESS instruments, suggested by the ESS-S SAG and the ESS SAC. L_1 denotes the length of the instrument for a pulse length of $\tau = 1$ ms, while L_2 is the instrument length for $\tau = 2$ ms, and β is the "Frascati exponent," defined by (1).

Instrument	L_1 (m)	L_2 (m)	β
Cold chopper spect.	60	100	0
Therm. chopper spect.	100	100	0
Cold triple axis	40	40	0
Thermal triple axis	40	40	0
TOF triple axis	60	100	0
Backscatter spectrometer	151	302	0
Spin echo spectrometer	30	30	2.5
Short SANS (bio-)	12 + 1–4		2.5
Medium SANS	18 + 1–10		2.5
Long SANS (materials-)	28 + 2–20		2.5
Horizontal reflectometer	52	52	4
Vertical reflectometer	52	52	4
Cold powder diffract.	88	176	0
Thermal powder diffract.	102	102	0
Single crystal diffract.	31	42	0

Scientific Advisory Council for the ESS (SAC) in June 2010. Our starting list was found as a join of these two instrument suites, and is shown in Table I. It should be noted that due to time constraints, neither a tomography instrument, a protein diffractometer, nor a wide-angle spin-echo instrument have been included in these simulations, even though these classes of instruments were present in the straw-man suite. For an artists view on the present version of the straw-man suite, see Fig. 1.

In the optimizations, we have taken into account that neutrons of different wavelengths may not be equally useful for the individual instruments. In particular, spin-echo spectrometers, reflectometers, and small-angle diffractometers strongly prefer long wavelength neutrons. To account for this fact in a simplified way, we parametrize the relative "value," V, of each neutron by a simple expression

$$V(\lambda) = \lambda^{\beta}. \tag{1}$$

The values of β for different instrument types were selected by an expert meeting in Frascati, August 2009,[13] and Table I contains the chosen values of β. Here, a value of zero indicates that all neutrons are considered equally valuable, while a positive value of β gives preference to long-wavelength neutrons.

III. DESIGN AND OPTIMIZATION OF INSTRUMENTS

Over the last decade or more, a number of authors have addressed the issue of long-pulse instrumentation.[14–17] The instrument concepts and designs simulated here are in general adapted from the earlier work, except that we have adjusted the instrument lengths as described below and listed in Table I. Most instruments on this list are typical time-of-flight instruments, except the reactor-type triple-axis instruments. One untraditional instrument type, labeled "TOF Triple Axis" has been included in the list. This is a hybrid (or inverted-geometry) spectrometer[11] with a time-of-flight front-end and a triple-axis-like crystal analyzer back-end.

A. Instrument length and resolution

To qualify the discussion, let us first recall the equation for the neutron time-of-flight, t,

$$t = \alpha \lambda L, \tag{2}$$

where L is the flight length and $\alpha = m_n/h \approx 252.7\ \mu$s/(m Å). The relative uncertainty of the neutron wavelength can then be expressed by the uncertainty in flight time by

$$\frac{\delta\lambda}{\lambda} = \frac{\delta t}{t} = \frac{\delta t}{\alpha \lambda L}. \tag{3}$$

For long-pulse instruments, δt is either given approximately by the pulse length, τ, (at a long pulsed source, the exponentially decaying tail of the pulse can to first order be neglected compared to τ), or by the opening time of a pulse-defining chopper, as described below. In the latter case, L will be the flight length from the pulse-defining chopper to the detector, in the former it will denote the full instrument length to the detector (for chopper spectrometers, see later).

In analogy, the useful wavelength band, $\Delta\lambda$, of neutrons which can reach the detector without creating frame overlap

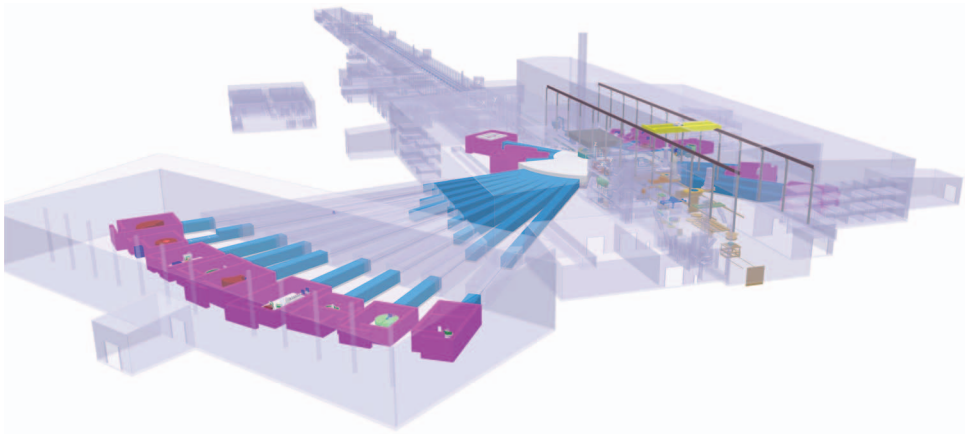

FIG. 1. Artists view of the ESS target/instrument buildings seen obliquely from above. Note that the long instruments are placed in a hall (foreground left) which is separated from the main target building (right). The accelerator is seen stretching into the background.

is given by

$$\Delta\lambda = \frac{\Delta t}{\alpha L}, \tag{4}$$

where for instruments using the full pulse, $\Delta t = T - \delta t \approx T$.

A number of the simulated instruments cannot directly utilize the full pulse length, τ, since this would result in a too bad resolution (too large $\delta\lambda/\lambda$). Therefore, pulse shaping must be performed at a fast pulse-defining chopper, close to the source. In this work, the distance between source and chopper is set to the smallest realistic value given by the biological shielding of the moderator: $L_{pc} = 6$ m.) A pulse-defining chopper at the distance L_{pc} effectively selects a wavelength band, given by $\Delta\lambda = \tau/(\alpha L_{pc})$. To let this wavelength band fill the whole time frame, T, at the detector, the instrument must be very long: $L = L_{pc}(1 + T/\tau)$, which for the parameters investigated in this work lies between 126 m and 606 m, since the inverse duty cycle, T/τ, lies in the range 20–100.

B. Wavelength frame multiplication and repetition rate multiplication

At some instruments with pulse-defining choppers, we have used an alternative scheme to having very long instruments: A number of closely spaced shorter pulses is produced at the pulse-defining chopper, which are then kept separated by a number of sub-frame-overlap choppers. This has been denoted "Wavelength Frame Multiplication" (WFM), as first presented by the group of Mezei.[18,19] In the present simulations, the WFM method is used at the thermal powder diffractometer and the thermal chopper spectrometer.

The cold chopper spectrometer uses a similar technique, which bears the name "Repetition Rate Multiplication" (RRM). Here, the full pulse length is used, but a monochromating chopper close to the sample produces up to 15 different monochromatic pulses for each moderator pulse,[14,20] as simulated in Ref. 5. Recently, this technique has been experimentally proven feasible at NEAT, HZB[21] and 4SEASONS, J-PARC.[22] In the present simulations, also the thermal chopper spectrometer employs RRM (in addition to using WFM).

C. The source

Lacking precise information about the source power and moderator performance for the different time structures, we have initially considered the two following scenarios.

1. The source has a constant time-average neutron flux.
2. The accelerator is limited by a maximum beam current; i.e., the source peak flux is constant.

These two scenarios differ only by a τ/T scaling of the source flux, whence we were able to use the same set of simulations/optimizations. As a reference point at the baseline settings, we use the characteristics of a 12×12 cm^2 moderator with uniform flux distribution, as given in Ref. 23.

D. The guide systems

For the short guide systems (below 60 m), we have everywhere used guides with constant cross section, where fast-neutron background from direct line-of-sight to the moderators is avoided by inserting a kink or curved section. At the reflectometers, we have used elliptical focusing in the direction perpendicular to the sample surface, combined with a kink in the other direction.

For instruments of 60 m and longer, and for the 40 m triple-axis instruments, we have employed elliptical guides for beam transport, since recent experiments and simulations have shown this design to be strongly superior over traditional curved guides.[6,24]

For the values of guide reflectivities, we have everywhere used recent information from one supplier.[25] In general, we use $m = 3$ along the main length of all guides, and $m = 6$ in the beginning and end of elliptical guides.

Guides have everywhere been assumed to consist of straight sections, with perfect alignment and zero waviness. The effect of waviness and misalignment of (in particular) long elliptical guides is a topic of future simulations.[26] A similar work was carried out earlier for straight guide geometries.[27]

In the optimizations, we have assumed 40 cm as the maximal guide width for the longest guides, relying on information that guides of this width and matching slow frame-overlap choppers can be produced.[25,28] Should it be necessary to place stricter limits on the guide width this will affect the absolute flux values at some instruments,[26] but not the relative comparisons relevant for the present work. This statement is valid for most other design parameters.

For the long guides, no attempt has been made to avoid line-of-sight. The key issue is that bending of the guides, as known from traditional guide systems, would disturb the elliptical focusing properties,[26] whence a solution to this issue is more involved and was postponed to later studies.[29,34]

An additional possibility to reduce the fast-neutron background would be to insert either a crystal filter or a heavy "straight-beam-block" in the middle of the guide, probably early in the guide.[30] Another possibility for guide design is the combination parabolic-straight-parabolic, where the straight section can be curved. This combination transmits almost as well as an elliptical guide.[24]

E. Optimization of instruments by simulation

All present simulations were performed using the Monte Carlo ray-tracing package McStas v. 1.12,[31] where the instrument designs were typically performed on individual computers, while the final optimization and data taking was performed on the computer cluster of the ESS Data-Management Center in Copenhagen. Typical runs used between 10^8 and 10^{11} neutron rays, depending on the type of instrument.

Instruments were first simulated at the baseline time structure settings of $\tau = 2$ ms and $T = 60$ ms. The instrument length and chopper settings were adjusted as to obtain a predetermined instrumental resolution, while remaining above a certain length limit, relevant for the SANS and spin-echo

instruments. Subsequently, the guide system of each instrument was optimized using a Figure-of-Merit (FoM) found from the time average flux, $\Psi(\lambda)$, on the sample position in the useful wavelength band, $[\lambda_{\min}, \lambda_{\max}]$ weighted by $V(\lambda)$,

$$\text{FoM} = \int_{\lambda_{\min}}^{\lambda_{\max}} \Psi(\lambda) V(\lambda) d\lambda. \quad (5)$$

Subsequently, the design of each of the 15 instruments was modified and optimized for each of 20 different time structure settings, in principle 300 optimizations and subsequent simulated data. In order to produce comparable simulations, all optimizations for a given instrument were restricted to have certain resolution characteristics. For spectrometers, this was given as $\delta\lambda/\lambda$ at the sample position for a certain value of λ. For diffractometers, this was given as a fixed $\delta\lambda/\lambda$ at the detector for a limited divergence matching this value, to obtain a certain low linewidth in the measured lattice spacing, $\delta d/d$, at a given scattering angle. For a few instrument types (spin-echo spectrometer and SANS), the worst resolution was in all cases deemed "sufficient," so these instruments were not restricted by resolution requirements and were thus simulated at their constant (minimum) lengths.

Since it has been proposed to place triple-axis spectrometers at the long-pulsed ESS, we have included a cold and a thermal instrument in these comparisons. For a triple-axis spectrometer at a pulsed source, the time structure is useful only for filtering of background and higher order harmonics. Hence, the instrument has identical FoM for all time structure settings, and we needed to simulate only one time structure for each of the two triple-axis spectrometers.

IV. RESULTS OF INSTRUMENT OPTIMIZATIONS

We now present the results of our optimizations over the time structure range, as described above. To exemplify, we begin with the results for two individual instruments, before describing the combined results of the full instrument suite. Finally, we discuss the validity of our FoM approach.

A. Simulation example 1: Cold chopper spectrometer

Let us first consider the simulation of the cold-neutron chopper spectrometer, with a design similar to IN5 at ILL. In this present (simple) version of this instrument, the monochromatization is performed by the (full) length of the pulse, in combination with the opening time of fast choppers just before the sample, as illustrated in Fig. 2. The instrument length is determined by the pulse length, to fulfill a constant $\delta\lambda/\lambda = 1.6\%$ at 5 Å wavelength. At the baseline time structure settings, the distance between the source and the fast chopper is $L = 100$ m, and the useful band is 2.2 Å wide (here chosen to be 3.9–6.1 Å). This is described in detail in Ref. 5, where, however, a more simple guide system was used. Our results can thus be seen as an update of the previous publication.

The present cold chopper spectrometer uses an elliptical guide with quadratic cross section, which is 27.3 cm at its widest place. The guide focuses to the sample, which is defined to be 2×2 cm^2. The instrument uses the RRM scheme,

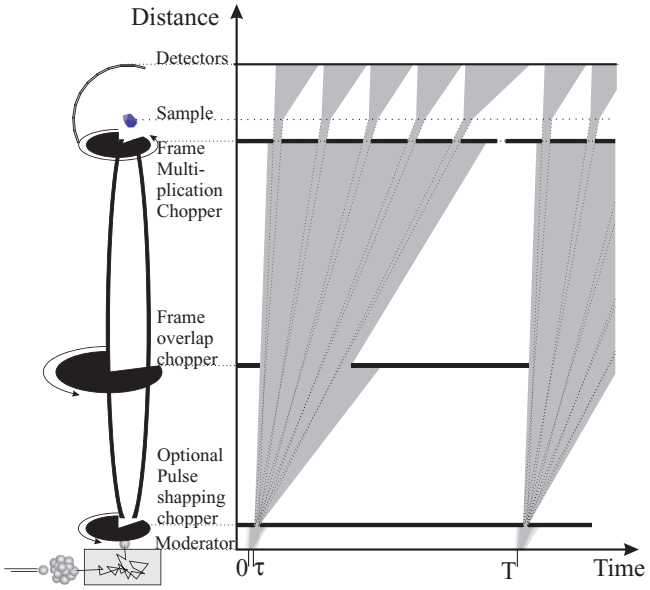

FIG. 2. (left) Sketch of the main elements of the cold chopper spectrometer. Picture is not to scale. (right) Time-of-flight diagram illustrating the selection of neutron pulses by choppers, with the spectrometer running in RRM mode with $N = 5$.

as presented earlier. This mode allows for each source pulse 9 monochromatic pulses on the sample, with a wavelength difference between neighbouring pulses of 0.25 Å, and 6 ms between pulses. In this way, the instrument reaches a combined monochromatic flux of 1.6×10^8 n/s/cm^2 for the wavelength band mentioned above, centered at 5 Å.

A shorter source pulse will allow for a shorter instrument; for pulses of 1.5 ms, 1.25 ms, and 1.0 ms, the instrument length becomes 80 m, 70 m, and 60 m, respectively. (The finite opening time of the monochromating choppers has the consequence that the 1.0 ms instrument is less than a factor two shorter than the 2.0 ms instrument.) A shorter instrument gives rise to a larger bandwidth and thus more neutrons on the sample (for constant time-average flux). For example, when going from 2 ms to 1 ms pulse length, the increase in FoM is more than 50%, as seen in Table II. A rather similar gain is found from lowering the source frequency from $16\frac{2}{3}$ Hz to 10 Hz, also due to the larger useful bandwidth.

Due to the point-to-point-like focusing of an elliptical guide, most neutrons at the sample originate from the

TABLE II. Relative Figure-of-Merit (FoM) values for the simulations of the IN5-like cold chopper spectrometer at ESS, under the assumption of constant time-average flux. Simulations are performed for 20 different settings of the time structure, (T, τ). The RRM scheme is parametrized by N, which indicates the number of possible monochromatic pulses at the sample per source pulse.

T (ms)	τ (ms)	1.0	1.25	1.5	2.0	N
100 (10 Hz)		2.39	2.24	2.05	1.67	15
80 (12.5 Hz)		2.08	1.83	1.59	1.26	11
60 (16.67 Hz)		1.72	1.48	1.29	1.00	9
50 (20 Hz)		1.35	1.17	0.98	0.76	7
40 (25 Hz)		0.91	0.81	0.68	0.56	5

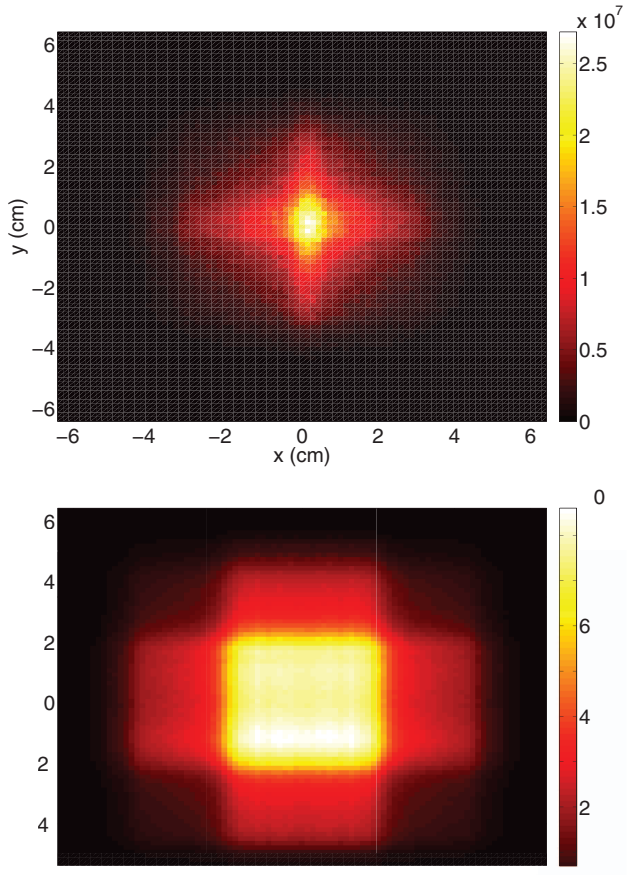

FIG. 3. Simulated plots of the moderator surface showing the number of neutrons which reach the sample at the IN5-like chopper spectrometer. Top panel shows the situation with a 60 m guide ($\tau = 1$ ms), while bottom panel shows the results for a 100 m guide ($\tau = 2$ ms).

innermost 4×4 cm^2 of the moderator surface, as shown in Fig. 3. Therefore, it would be beneficial if neutrons were emitted preferentially from the center of the moderator. A simulated hot spot with a factor 2.0 intensity gain over a circle of diameter $d = 3$ cm produces a gain in neutron flux at the sample of 30%.

Taken at face value, the flux number obtained at the base time structure settings represents an impressive factor 200 gain over IN5. However, care should be taken when comparing these numbers. First, the full gain is possible only if neutrons from all monochromatic pulses are equally useful to the actual experiment. Second, much of the flux increase comes from an increased divergence of neutrons in the elliptical guide system (compared to the straight/curved guide at IN5), and this part of the gain would be of value only to particular experiment types. Hence, the mentioned gain is for this instrument a best case scenario, where a worst case scenario (collimating down to IN5 divergence and using only one RRM frame) would lead to a gain factor of "just" 5.

B. Simulation example 2: Long SANS instrument

We now consider the longest of the three simulated cold-neutron small-angle scattering instruments. In analogy with the cold chopper spectrometer described above, the wave-

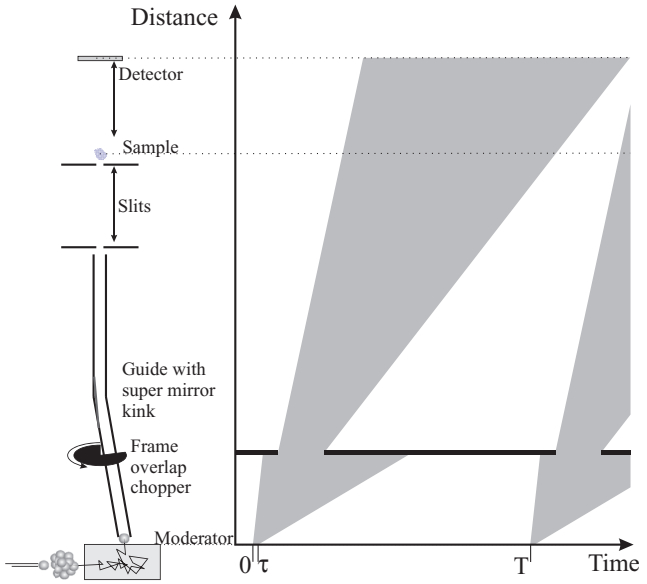

FIG. 4. (left) Sketch of the main elements of the long SANS instrument. Details are not to scale. (right) Time-of-flight diagram illustrating the selection of wavelength band by choppers, with the spectrometer running in the (20 + 20) m setting.

length uncertainty is determined by the full pulse length, since the incoming wavelength is determined by the measured time-of-flight in the detector (assuming elastic scattering at the sample).

The length of the instrument is in practice determined by the 20 m long double-pinhole collimator section, combined with an initial 8 m of guide, which includes a kink to avoid direct line-of-sight. The source-sample distance is thus always 28 m, while the sample-detector distance can vary between 2 m and 20 m. The relevant time-of-flight length, L, thus varies between 30 m and 48 m. At these lengths, the wavelength uncertainty at the SANS instrument at $\lambda = 5$ Å and $\tau = 2$ ms is of the order $\delta\lambda/\lambda \approx 3\%$–$5\%$, which is almost always "too good," since the double-pinhole collimation of $d_1 = 10.5$ mm and $d_2 = 7.0$ mm has the dominating contribution to the q-resolution.

The bandwidth of the instrument is rather large, of the order 8 Å at the shortest detector setting. In combination with the large angular range covered at the detector, this allows a large q-range detected in the same setting. A sketch of the long SANS instrument and the corresponding wavelength band selection is found in Fig. 4.

In our optimizations, we have employed three settings of the collimation length and the sample-detector distance: (2 + 2) m, (10 + 10) m, and (20 + 20) m. The results presented are an average of the three results, each normalized by the result at the baseline setting. For the baseline setting, the instrument reaches neutron fluxes of 1.8×10^8 n/s/cm^2, 9.0×10^5 n/s/cm^2, and 9.7×10^3 n/s/cm^2 for the three choices of distance, respectively, and the wavelength band centered around 10 Å.

A shorter source pulse will give better wavelength resolution, but the instrument cannot be shortened due to the kink and the collimation section. Therefore, this gives no gain in

TABLE III. Relative Figure-of-Merit (FoM) values for the simulations of the long SANS instrument at ESS under the assumption of constant time-average flux. Simulations are performed for 20 different settings of the time structure, (T, τ).

T (ms)	τ (ms)	1.0	1.25	1.5	2.0
100 (10 Hz)		1.69	1.69	1.69	1.69
80 (12.5 Hz)		1.34	1.34	1.34	1.34
60 (16.67 Hz)		1.00	1.00	1.00	1.00
50 (20 Hz)		0.83	0.83	0.83	0.83
40 (25 Hz)		0.67	0.67	0.67	0.67

bandwidth (or integrated flux), but a small improvement in q-resolution. If, on the other hand, the source frequency is lowered, e.g., to 10 Hz, at constant time-average flux, the instrument will benefit from an increase in useful bandwidth and hence the FoM will increase. All FoM data are displayed in Table III.

At the longest collimation length, all neutrons at the sample originate from a circle of $d \approx 2.5$ cm at the center of the moderator surface. This effect is less pronounced at the shorter collimation lengths. This is illustrated in Fig. 5. On average, a simulated hot spot with a factor 2.0 intensity gain

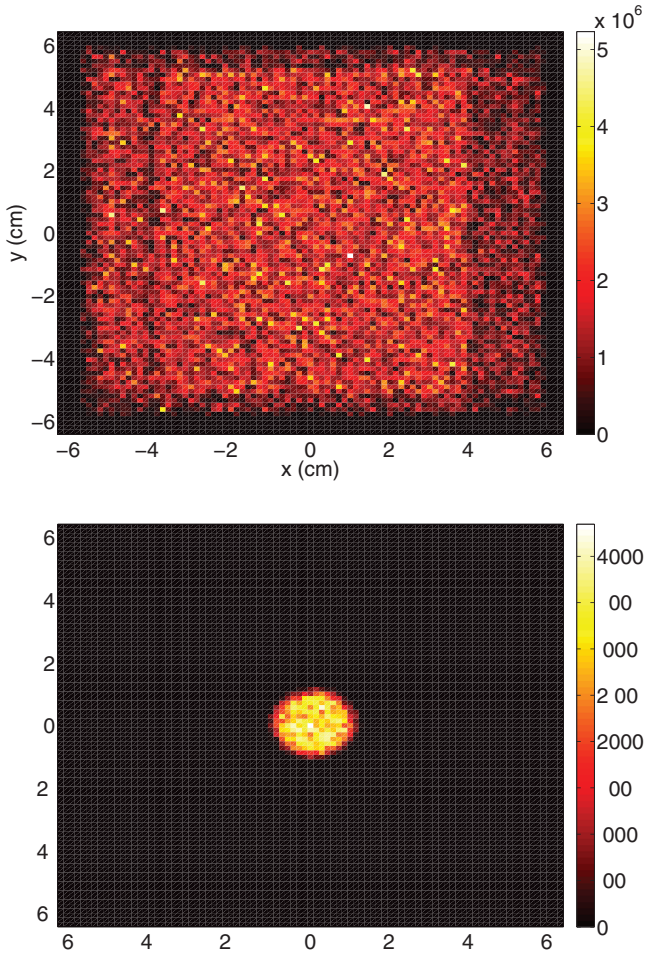

FIG. 5. Simulated plots of the moderator surface showing the number of neutrons which reach the sample for the 20 m SANS instrument. The results are valid for any time structure. (top) data for 2 m collimator-detector setting; (bottom) data for 20 m collimator-detector setting.

TABLE IV. Average relative Figure-of-Merit for the generic ESS instrument suite at different time structures, under the assumption of constant time-average flux.

T (ms)	τ (ms)	1.0	1.25	1.5	2.0
100 (10 Hz)		2.07	1.81	1.67	1.37
80 (12.5 Hz)		1.89	1.66	1.55	1.19
60 (16.67 Hz)		1.62	1.42	1.24	1.00
50 (20 Hz)		1.53	1.27	1.09	0.88
40 (25 Hz)		1.20	1.05	0.90	0.73

over a circle of diameter $d = 3$ cm produces a gain in neutron flux at the sample of 73%.

C. Optimization of the full instrument suite

After the optimization procedures, we record the resulting values of wavelength, bandwidth, flux at sample position, and FoM for each instrument and time structure setting. The results of the individual simulations are in general similar to the simulation results of the chopper spectrometer and the small-angle instrument shown above. (Results can be found from Ref. 4.) The obtained values of FoM have been normalized to the baseline setting of $T = 60$ ms and $\tau = 2$ ms.

For constant time-average flux, almost all instruments perform better towards the upper left-hand corner of the performance matrix. This is as expected, since (i) a longer T will allow for a larger useful wavelength band, $\Delta\lambda$, and (ii) a smaller τ will either (iia) allow L to be smaller, giving an increased $\Delta\lambda$, or (iib) allow a higher fraction of the total flux through the pulse-defining choppers.

In contrast, for the constant-peak-flux scenario, most instruments perform better towards the lower right corner of the performance matrix. This is most simply explained by the fact that here, more neutrons are produced in total, overcompensating the advantages of short pulses and low frequencies mentioned above.

To perform a global comparison of the different time structure settings, we use the relative instrument performances for each instrument. A simple arithmetic mean value has been used, since no decision on the relative importance of instruments has been taken. The results for the average performances are listed in Tables IV and V for the constant-time-average-flux and constant-peak-flux scenarios, respectively.

We see that the effect of shortening the pulse from 2.0 ms to 1.0 ms is typically around 60% increase at constant time-average flux – or around 20% decrease at constant peak flux. Likewise, the effect of going from 20 Hz to 10 Hz is

TABLE V. Average relative Figure-of-Merit for the generic ESS instrument suite at different time structures, under the assumption of constant peak flux.

T (ms)	τ (ms)	1.0	1.25	1.5	2.0
100 (10 Hz)		0.62	0.68	0.75	0.82
80 (12.5 Hz)		0.71	0.78	0.87	0.89
60 (16.67 Hz)		0.81	0.89	0.93	1.00
50 (20 Hz)		0.92	0.95	0.98	1.05
40 (25 Hz)		0.90	0.98	1.01	1.09

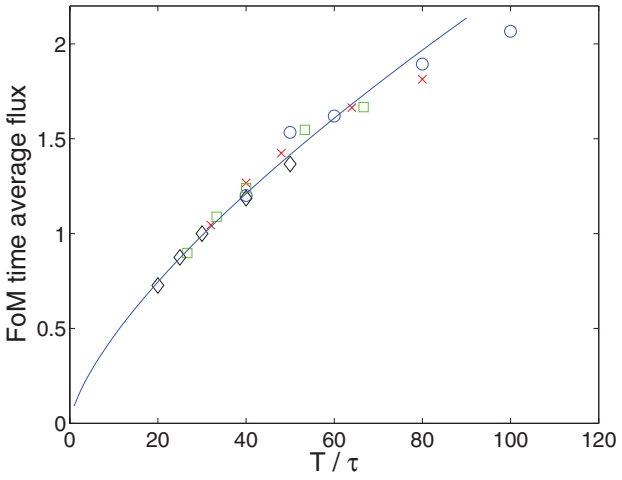

FIG. 6. Average Figure-of-Merit for the generic ESS instrument suite at different time structures, plotted as a function of the inverse source duty cycle, under the assumption of constant time-average flux. Diamonds, squares, crosses, and circles represent pulse lengths of 2.0, 1.5, 1.25, and 1.0 ms, respectively. The solid line is a fit to the power law (6), as explained in the text.

around a 50% increase at constant time-average flux – or around 30% decrease at constant peak flux.

The data for constant time-average flux is shown as a function of the inverse source duty cycle, T/τ, in Figure 6. It is seen that, except for the very smallest duty cycles, the data fall almost on a common curve, which can be approximately described by

$$\mathrm{FoM} \approx \Psi_{\mathrm{peak}} \left(\frac{\tau}{T}\right)^{\alpha} = \Psi_{\mathrm{peak}}^{1-\alpha} \Psi_{\mathrm{time\,av}}^{\alpha} = \Psi_{\mathrm{time\,av}} \left(\frac{T}{\tau}\right)^{1-\alpha}, \tag{6}$$

with $\alpha = 0.30$. This value confirms the trivial result that the long-pulse source of the ESS is intermediate in nature between a short-pulse source and a continuous source. Instruments at short-pulse sources aim to be optimized to benefit from the peak flux, while instruments at steady-state sources are optimized to benefit from the time-average flux. The exact value of the exponent will clearly depend on the chosen instrument suite, but it is interesting to note first that the instrument performance scales more closely with the peak flux than with the time-average flux. Second, Eq. (6) predicts that the global instrument performance depends only on the time-average flux and duty cycle. If both are kept constant, e.g., by changing T and τ simultaneously, the instrument performance should be independent of the time structure.

Our results can be seen as a natural continuation of the discussion on the merits of long-pulse sources, initiated in Ref. 14. While the previous work has used an analytical approach to address the usefulness of long neutron pulses, our results serve to quantify this usefulness, including important features like moderator spectrum and instrument-specific details across the instrument suite.

D. Considerations beyond a simple figure-of-merit

The analysis above is based on the assumption that it is possible to reduce the full scientific usefulness of a facility into one single number, the FoM, and to express its variation by essentially one parameter, the duty ratio τ/T, as illustrated in Figure 6. This assumption shares one problem with most numerical optimization work: Details that cannot be compressed into the FoM are easily overlooked. For this reason, we will look more into some of these details. To simplify the argument, we will consider the effect on the instrument performance under the condition that the duty cycle τ/T is unchanged. The effect of varying the time structure under this boundary condition depends rather sensitively on the type of instrument.

- SANS, reflectometry and spin-echo instruments will benefit from the increased wavelength range which a longer repetition period will give them. Their performance will not suffer significantly from the degraded wavelength resolution, which an associated increase in pulse length would give. Any increase in bandwidth translates directly into improved performance.
- Crystal-monochromator instruments, such as triple-axis spectrometers, do not make much use of the source time structure at all. In these cases, only the time-average flux counts. The time structure has little or no effect.
- Chopper spectrometers, or other instruments that may employ RRM, have a weak preference for shorter repetition periods. These instruments use the RRM to compensate for the fact that their preferred repetition frequency is higher than the source frequency. Increasing the source frequency reduces the need for RRM and makes their data-collection strategy more similar to existing instruments and simplifies the data analysis.
- Very high-resolution instruments, such as backscattering spectrometers and high-resolution diffraction also have a preference for shorter repetition periods. These instruments cut out only a small fraction of the pulse length to achieve the desired resolution and do not benefit significantly from the increased wavelength range offered by an increase in repetition period.

Overall, it seems clear that an increase in pulse length will translate into an increase in the average length of the instruments, which will, in turn, result in increased costs for guides and shielding along the guides. On the other hand, with modern ballistic-type guides, the transport of neutrons represents no essential problem,[24] while the instrument space becomes less restricted at the same time as the general background level decreases. In addition, certain combinations of T and τ may result in instruments with lengths which allow them to be grouped together in common instrument halls, rather than requiring separate buildings. In such a scenario, the cost savings associated with the reduction in the number of instrument buildings could cancel out the cost increase of the longer guides, as well as providing other benefits in terms of upgradeability and flexibility.

E. Optimizing the moderator parameters

The design and simulation of the target/moderator is much more computationally demanding than that of the

instruments. Hence, one aim of the instrument simulations has been to assist the moderator optimizations towards an improved functionality of the full ESS. We here describe the results obtained in this direction.

Often, the figure-of-merit in moderator optimizations is the number of neutrons produced, possibly in a given wavelength interval and for a given moderator size. However, the moderator simulations produce more detailed information than this. The result of each simulation is given as a history of neutron events, each event having 6 parameters: position at moderator surface ($\mathbf{r}$), time of emittance (t), wavelength (λ), and moderator emission angle ($\boldsymbol{\eta}$). By means of instrument simulations it was found possible to represent the transmission probability of a neutron from moderator surface to sample as

$$T(\mathbf{r}, \lambda) \approx T_r(\mathbf{r}) T_\lambda(\lambda). \tag{7}$$

Here, the dependence on divergence has been integrated out, since the moderator flux (even with complex geometries) is expected to vary insignificantly over the rather small solid angle of the guide entry, Furthermore, we have neglected the emission time, which corresponds to ignoring the tails from the moderators. For a total target/moderator optimization, the figure-of-merit to optimize is thus for each of the moderators (e.g., a cold and a thermal),

$$\mathrm{FoM}_{\mathrm{mod}} = \sum_j W_j \int N(\mathbf{r}, \lambda, t, \boldsymbol{\eta}) V_j(\lambda) \times T_{j,r}(\mathbf{r}) T_{j,\lambda}(\lambda) d^2\mathbf{r} d\lambda d^2\boldsymbol{\eta} dt, \tag{8}$$

where the summation label, j, represents the instruments at the moderator, W_j is a normalization and weighting constant for each instrument, N is the simulated density of neutrons from the moderator, and $V_j(\lambda)$ is given in (1).

We have for each instrument calculated the spatial transmission function, $T_r(\mathbf{r})$, as shown in the examples above, and listed in Ref. 4. The results show that for most instruments, the transmission peaks strongly in a 3–5 cm diameter circle (or square) in the center of the moderator. This effect results for some instruments from the use of elliptical guides, for others from using tight collimation and straight guides. Thus, it can for these simple guide systems be advantageous to concentrate the flux in a hot spot, while the size of the emitting part of the moderator can be limited, e.g., by reflectors. In this way, it should be possible to simultaneously increase the useful neutron flux and decrease the emission of fast neutrons. For each instrument, we have calculated the effect of producing a circular, 3 cm diameter, hot spot with 100% higher emittance – while maintaining the total emittance of the moderator. This set-up is close to what was presented in Ref. 32. For most instruments, the gain factor of such a hot spot is around 30%, while few instruments show a full 100% gain.

It should be added that more elaborate guide systems, in particular, an optimized guide extraction system for instruments with a pulse shaping chopper close to the moderator, will modify this picture. This problem will be addressed by further simulation work.[29]

V. CONCLUSION

We have performed a series of systematic ray-tracing simulations of the performance of a generic instrument suite for the ESS. These simulations were carried out for a large number of time structure settings, for constant, typical instrument resolutions. The performance parameters were found to increase with increasing peak flux, as well as with increasing time-average flux, while varying only weakly with the details of the time structure.

The variation with time-average and peak flux can be expressed as $\mathrm{FoM} \propto \Psi_{\mathrm{peak}}(\tau/T)^\alpha$, with $\alpha = 0.30$. If both the peak flux and the duty cycle are kept constant, the average instrument performance is largely independent of pulse-length or frequency, within the frequency range of the current study.

Since most instruments use tight collimations or (elliptical) focusing guides, most neutrons hitting the sample stem from a central part of the moderator of a diameter 3–5 cm. We suggest to use this knowledge for the optimization of the moderator design, in particular by considering "hot spots" at the moderator. However, this can be finalized only when the guide systems of the instruments are designed.

A. Implications for design of long-pulsed sources, e.g., ESS

As part of the study which resulted in the decision to fix the time structure of the ESS to $\tau = 2.86$ ms and $T = 71$ ms ($f = 14$ Hz), two boundary conditions were considered: (1) the time-average power is planned to be 5 MW. (2) the peak accelerator current cannot exceed 50 mA. The 5 MW number is judged to be important, so as to at least match the best existing instruments over the largest possible range. The limitation on the peak current results from a judgement, based on the experience of the SNS linear accelerator, as to the optimal compromise between performance, reliability and cost. In the interest of maximizing the instrument performance, it is clearly advantageous to push for the highest peak flux which the accelerator and target assembly can provide. We can therefore consider the 50 mA peak current as our specification, rather than an upper limit. These boundary conditions reduce the number of degrees of freedom when choosing τ and T from 2 to 1, as follows. The peak power on target is given by the product of the peak current and proton energy of 2.5 GeV. At 50 mA peak current, the instantaneous power is 125 MW. In order to achieve a time-average power of 5 MW, the source therefore needs to operate at a duty cycle τ/T of 5 MW/125 MW = 1/25, as a direct consequence of our two boundary conditions. If we set the repetition period to 100 ms (10 Hz), the pulse length will be 4 ms. At $T = 50$ ms repetition period ($f = 20$ Hz), the pulse length is 2 ms. The range of τ and T covered in the present study only overlaps partially with the duty cycle $\tau/T = 1/25$. In order to study the instrument performance over the 10–25 Hz frequency range, while maintaining a duty cycle of 1/25, we extrapolate based on the data in Tables IV and V and Eq. (6) that the performance of the instrument suite does not depend upon the value of the source frequency.

In general, our results imply that factors other than the flux-related FoM used here should be decisive when determining the time structure for a long-pulse spallation source. For the case of ESS, the time structure has now been locked to $\tau = 2.86$ ms and $f = 14$ Hz, as the best compromise between performance, reliability, and cost. The detailed considerations are outside the scope of this article.

B. Further design and optimization of ESS instruments

The instrument design work for ESS is currently taking place in a setting which is very different from when the design work described in the present paper was taking place. A large number of the neutron laboratories and university groups working in neutron scattering in Europe are now engaged in the process of designing instruments for the ESS and the number is still increasing. About 40 different concepts for instruments are currently being optimized, some pursued by researchers in partner countries and some by ESS instrument scientists. A subset of these concepts has been assembled into a reference suite of instruments which is described in the ESS Technical Design Report.[33] The reference suite has been chosen to maximize the scientific impact of the ESS by addressing a broad science case, while in each case being fully optimized to benefit from the natural strengths of the long-pulse concept. The choice of instruments to be built at the ESS will take place as a staged process in consultation with the European scientific community and will result in the reference suite gradually evolving into the actual instrument which will be available at the ESS.

ACKNOWLEDGMENTS

First of all we are strongly indebted to Ch. Vettier for initiating this project and to D. Argyriou for keeping up the urgency of the simulations. We would further like to thank the ESSS SAG, the ESS SAC, and H. M. Rønnow for illuminating discussions.

This project was supported by the Danish, Norwegian, and German contributions to the Design Update phase of the ESS. J. O. Birk was supported by PSI and the Danish Research Council through the graduate school C:O:N:T.

[1] See www.ess-scandinavia.eu for the home page of the ESS project.
[2] *The ESS Project*, edited by D. Richter (Jülich Research Center, 2002), Vol. I.
[3] *The ESS Project*, edited by D. Richter (Jülich Research Center, 2002), Vol. IV.
[4] See sim.esss.dk for the home page.
[5] K. Lefmann, H. Schober, and F. Mezei, Meas. Sci. Technol. **19**, 034025 (2008).
[6] K. Lefmann, U. Filges, F. Treue, J. J. K. Kirkensgård, B. Plesner, K. S. Hansen, and K. H. Klenø, Nucl. Instrum. Methods A **634**, S1 (2011).
[7] M. Sales, S. L. Holm, K. Lieutenant, and K. Lefmann, J. Phys. Soc. Jpn. **80**, SB018 (2011).
[8] K. H. Klenø and K. Lefmann, J. Phys. Soc. Jpn. **80**, SB004 (2011).
[9] K. H. Klenø, P. K. Willendrup, E. Knudsen, and K. Lefmann, Nucl. Instrum. Methods A **634**, S100 (2011).
[10] K. H. Klenø, S. Kynde, G. Nagy, K. Mortensen, K. Lefmann, J. Kohlbrecher, and L. Arleth, "A compact time-of-flight SANS instrument optimised for measurements of small sample volumes at the European Spallation Source," J. Appl. Crystallogr. (submitted).
[11] J. O. Birk *et al*., "Simulations of the inverse-geometry time-of-flight spectrometer CAMEA for the European Spallation Source" (unpublished).
[12] A. Vickery *et al*., "Comparing thermal spectrometers for a long-pulse spallation source" (unpublished).
[13] R. K. Crawford *et al*., Report of the Long-pulse Neutron Instrumentation Workshop, Frascati, August 2009, 2010.
[14] F. Mezei, J. Neutron Res. **6**, 3 (1997).
[15] G. Zsigmond *et al*., Appl. Phys. A **74**, S224 (2002).
[16] H. Schober *et al*., Nucl. Instrum. Methods A **589**, 34 (2008).
[17] K. Lefmann *et al*., Report from the Ven 2008 meeting (unpublished).
[18] K. Lieutenant and F. Mezei, J. Neutron Res. **14**, 177 (2006).
[19] M. Russina and F. Mezei, Proc. SPIE **4785**, 24 (2002).
[20] F. Mezei, M. Russina, and S. Schorr, Physica B **276**, 128 (2000).
[21] M. Russina and F. Mezei, Nucl. Instrum. Methods A **604**, 624 (2009).
[22] M. Nokamura *et al*., J. Phys. Soc. Jpn. **78**, 093002 (2009).
[23] F. Mezei, *ESS Reference Moderator Characteristics for Generic Instrument Performance Evaluation* (ESS Project, Jülich, 2000), see also http://rencurel.essworkshop.org/documents/ess_itg/ESS-moderators.pdf.
[24] K. H. Klenø, K. Lieutenant, K. H. Andersen, and K. Lefmann, Nucl. Instrum. Methods A **696**, 75 (2012).
[25] SwissNeutronics AG, personal communication (2012), see also www.swissneutronics.ch.
[26] K. H. Klenø *et al*., "Effects of non-idealities in long neutron guides" (unpublished).
[27] P. Allenspach, P. Böni, and K. Lefmann, Proc. SPIE **4509**, 157 (2001).
[28] Mirrotron Ltd., personal communication (2012), see also www.mirrotron.kfkipark.hu.
[29] M. Bertelsen *et al*., "Exploring performance of neutron guide systems using pinhole beam extraction," Nucl. Instrum. Methods. A (submitted).
[30] U. Filges, personal communication (2012).
[31] K. Lefmann and K. Nielsen, Neutron News **10/3**, 20 (1999), see also www.mcstas.org.
[32] Y. Kiyanagi *et al*., in Proceedings of the ICANS conference, PSI report, 2010.
[33] *ESS Technical Design Report*, edited by S. Peggs (European Spallation Source ESS AB, 2013).
[34] L. D. Cussen *et al*., Nucl. Instrum. Methods A **705**, 121 (2013).

Simulation of a suite of generic long-pulse neutron instruments to optimize the time structure of the ESS accelerator

Kim Lefmann[1,2], Uwe Filges[3], Sonja L. Holm[1,2], Kaspar H. Klenø[1,2] , Erik Knudsen[4], Klaus Lieutenant[5,6], Lars von Moos[1,2,4], Morten Sales[1,2], and Peter K. Willendrup[1,4]

[1] European Spallation Source (ESS), St. Algatan 4, Lund, Sweden

[2] Nanoscience and eScience Centers, Niels Bohr Institute, University of Copenhagen, Denmark

[3] Laboratory for Development and Methods, Paul Scherrer Institut, Villigen, Switzerland

[4] Materials Research Division, Risø, Technical University of Denmark

[5] Institute for Energy Technology, Kjeller, Norway

[6] Helmholz Center Berlin, Germany

October 26, 2010

Abstract

We here describe the result of simulations of 16 generic neutron instruments for the long-pulsed European Spallation Source. All instruments have been simulated for 17 different settings of the accelerator time structure, corresponding to pulse lenghts between 1 ms and 2 ms; and repetition frequencies between 10 Hz and 25 Hz. The relative change in performance with accelerator settings is given for each instrument, and an unweighted average is calculated. In combination with estimations of flux numbers for the different accelerator settings, this can be used to obtain the best accelerator parameters. In addition, the effect of a hot spot on the moderator is calculated, which will be used to optimize the moderator design.

1 Introduction

The European Spallation Source (ESS)(1) is designed to be a long-pulsed spallation neutron source - the first of its kind (2). This opens new territory, including how to design instruments to a long-pulsed source, how to design the optimal moderator for these instruments, and how best to choose the accelerator parameters that matches these choices. Obviously, these optimizations are coupled, since *e.g.* the instrument design depends upon the accelerator pulse width and *vice versa*.

In this report, we are concerned with one part of this optimization problem: the selection of the accelerator time structure, *i.e.* its pulse length (τ) and repetition time (T). The original 2002 design was fixed at $\tau = 2$ ms, and $T = 60$ ms ($f = 16\ 2/3$ Hz) (3), but we have allowed ourselves to investigate time structures in the neighbourhood of these parameters.

In order to perform the time-structure optimization, we have selected a suite of generic instruments, covering a broad range of scientific utilizations. These instruments have then undergone a rough design and optimization for each setting of (T, τ), and the relative merits of the different time structures have been compiled and compared. A disclaimer is, however, necessary here: The simulated instrument suite should not be seen as a draft day-one suite, neither should the individual instruments be seen as being close to their final design. Much design work and careful selection of an initial instrument suite still lie ahead of us. The present work could be seen as one step in this process.

Below, we present our generic neutron long-pulse instrument suite, the optimization procedure, and the obtained overall results. As an appendix, we include 14 one-page fact sheets, one for each individual instrument simulation (in two cases, pairs of instruments were simulated together).

2 The generic instrument suite

The instrument suite we discuss here was initiated by the Scientific Advisory Group (SAG) for ESS-Scandinavia, in September 2009. This was expanded by the slightly different "straw-man-list", decided upon by the Scientific Advisory Council for the ESS (SAC) in June 2010. An overview of these two instrument suites is given in Table 1.

Table 1 also contains the present status of the simulations of the individual instruments. Simulations marked by "done" are each described on a separate page in the appendix.

Finally, Table 1 contains the exponent β, which is the exponent determining the relative "value", Q of neutrons of different wavelengths:

$$Q(\lambda) = \lambda^{\beta}. \quad (1)$$

The values of β for different instrument types were selected by an expert meeting in Frascati, August 2009 (4)[p34].

Instrument	SAG	SAC	Sim.	β
Cold Chop. Spect.	X	X	done	0
Th. Chop. Spect.	X	X	done	0
Cold Triple Axis	X	X	done	0
Th. Triple Axis	X	X	done	0
TOF Triple Axis		X	done	0
Backscatter Spect.	X		done	0
Spin Echo Spect.	X	X	done	2-3
Wide-angle SE		X	done	2-3
Short SANS (bio-)		X	done	2-3
Medium SANS	X		done	2-3
Long SANS		X	done	2-3
Horiz. Reflect.	X	X	done	4
Vertic. Reflect.		X	done	4
Cold Powder	X		done	0
Thermal Powder	X	X	done	0
Single Xstal	X	X	done	0
Protein Xstal	X		i.p.	0
Tomography		X	-	?

Table 1. List of 18 generic ESS instruments, suggested by the ESS-S SAG and the ESS SAC. 4th column represent the status of the corresponding simulations; "i.p." meaning "in progress", and "-" meaning "not started". β is the "Frascati exponent", defined in the text.
The spectrometer labeled "TOF Triple Axis" is hybrid with a time-of-flight front end and a triple-axis back-end.

Due to time constraints, two instruments simulations are yet completed. This report will be updated according to progress.

3 Design and optimization of instruments

Over more than a decade, a number of authors have addressed the issue of long-pulse instrumentation (5; 6; 7; 8; 9). The instrument designs simulated here are in general adapted from the earlier work, except that we have adjusted the instrument lengths as described below.

3.1 Repetition rate multiplication

To qualify the discussion, let us first recall the equation for the neutron time-of-flight, t:

$$t = \alpha\lambda L, \quad (2)$$

where L is the flight length and $\alpha = 252.7\,\mu$s/(m Å). The relative uncertainty of the neutron wavelength can then be expressed by the uncertainty in flight time by

$$\frac{d\lambda}{\lambda} = \frac{dt}{t} = \frac{dt}{\alpha\lambda L}. \quad (3)$$

For long-pulse instruments, dt is either given approximately by the pulse length, τ, (ignoring the tail of the pulse), or by the opening time of a pulse-defining chopper. In the latter case, L will be the flight length from the pulse-defining chopper to the detector, otherwise it will denote the full instrument length.

In analogy, the useful wavelength band, $\Delta\lambda$ is given by

$$\Delta\lambda = \frac{\Delta t}{\alpha L}, \quad (4)$$

where for instruments using the full pulse, $\Delta t = T - \tau \approx T$.

A number of the simulated instruments cannot directly utilize the full pulse length, τ, since this would result in a too bad resolution, $d\lambda/\lambda$. Therefore, pulse shaping must be performed at a fast pulse-defining chopper, close to the source. In this case, to utilize the full wavelength band, $\Delta\lambda$, one must produce a number of shorter pulses with the pulse-defining chopper, which are then kept separated by a number of sub-frame-overlap choppers. This has been denoted "repetition rate multiplication" and was first presented in Refs. (5; 10).

In the present simulations, the technique of repetition rate multiplication is used with great advantage at the thermal powder diffractometer and the thermal chopper spectrometer; the latter also employs a fast monochromating chopper close to the sample. The cold chopper spectrometer uses a similar technique, which bears the same name. Here, the full pulse length is used, but a monochromating chopper close to the sample produces up to 15 different monochromatic pulses for each moderator pulse (5; 10), as simulated in Ref. (11). Recently, this technique has been experimentally proven at NEAT, HZB (12) and 4SEASONS, J-PARC (13).

In the appendix, use of reptitition rate multiplication is indicated by the parameter N, which represents the number of sub-pulses at the sample for each main accalerator pulse.

3.2 The source

Lacking precise information about the accelerator power and moderator performance for the different time structures, we have initially assumed one of two options

1. The source has a constant time-integrated neutron flux.
2. The source is limited by a maximum beam current; *i.e.* the peak flux is constant.

As a reference point at the baseline settings, we use the characteristics of the 12×12 cm^2 moderator as given in Ref. (14).

We are aware none of our assumptions on the source power are completely precise. Hence, the results we obtain should be corrected before use, as described in the following.

3.3 The guide systems

For the short guides (below 40 m), we have everywhere used straight guides, where fast-neutron background from direct line-of-sight to the moderators is avoided by inserting a kink or curved section. Two exceptions are the reflectometers, where we have used elliptical focusing in the direction perpendicular to the sample surface.

For instruments of 40 m and longer, we have everywhere employed elliptical guides for beam transport, since recent experiments and simulations has shown this design to be strongly superior over traditional curved guides.(15)

For the long guides, no attempt has been made to avoid line-of-sight, since bending would disturb the elliptical focusing properties (16), and since numerical work has shown that the fast-neutron background due to line-of-sight may be small at long distances (17). In addition, there would be the possibility to reduce fast-neutron background by inserting either a filter or a hydrogen-containing "straight-beam-block" in the middle of the guide within 6 m from the moderator (18). Another possibility for guide design is the combination parabolic-straight-parabolic, where the straight section can be curved. This combination is suggested to have a performance similar to an elliptical guide and is under investigation (15).

For the values of guide reflectivities, we have everywhere used recent information from Swiss-Neutronics (19).

Guides have everywhere been assumed to consist of straight sections, with perfect alignment. The effect of misalignment of (in particular) long elliptical guides is a topic of future simulation. A similar work was carried out earlier for straight guides (20).

In the optimization, we have assumed 40 cm as the maximal guide width for the longest guides, relying on information that frame-overlap "scissors" choppers can be produced for this guide width (21). However, should it be necessary to place stricter limits the the guide width or other design parameters, this will most probably not affect the relative comparisons presented here; only the absolute flux values (16).

3.4 Optimization of instruments by simulation

All present simulations were performed using the Monte-Carlo ray-tracing package McStas (22), where the instrument designs were typically performed on individual laptops, while the final optimization and data taking was performed on the 120-node computer cluster of the ESS Data-Management Center in Copenhagen. Typical runs used between 10^8 and 10^{11} neutron rays, depending on the type of instrument.

Instruments were first simulated thoroughly at the baseline accelerator settings of $\tau = 2$ ms and $T = 60$ ms. The instrument length and chopper settings were adjusted as to obtain a pre-determined instrumental resolution. Subsequently, the guide system was optimized using a Figure-Of-Merit (FOM) given as the flux on the

sample position in the useful wavelength band, weighted by $Q(\lambda)$:

$$\mathrm{FOM} = \int_{\lambda_{\min}}^{\lambda_{\max}} \Psi(\lambda) Q(\lambda) d\lambda. \qquad (5)$$

Subsequently, the design of each instrument was modified for each of the 17 settings for accelerator time structure. Simulations were used to maximize the FOM for each setting. In order to produce comparable simulations, all optimization for a given instrument was restricted to have certain resolution characteristics. For spectrometers, this was given as $d\lambda/\lambda$ at the sample position for a certain value of λ. For diffractometers, this was given as a fixed $\delta\lambda/\lambda$ at the detector for a limited divergence matching this value. For a few instrument types (spin echo and SANS), the worst resolution was in all cases deemed "sufficient", so these instruments were not restricted by resolution requirements and were thus simulated at constant lengths.

As a special case, the triple-axis spectrometers use only the time structure for background filtering, and thus perform virtually identical for all accelerator settings. For this reason, only one time structure was simulated for each of the two TAS.

3.5 Simulation example: Cold Chopper Spectrometer

As an example, let us consider the simulation of the IN5-like cold-neutron chopper spectrometer. In this instrument, the monochromatization is performed by the pulse length and fast choppers just before the sample. Thus, the instrument length is determined by the pulse length, to fulfill a constant $d\lambda/\lambda = 1.6\%$ at 5Å wavelength. At the baseline accelerator settings, the source-fast chopper distance is 100 m, and the useful bandwidth is 2.2 Å wide (3.9 Å to 6.1 Å). This is described in detail in Ref. (11).

The instrument uses an elliptical guide with quadratic cross section, which is 27.3 cm at its widest place. The guide focuses to a sample spot 2×2 cm^2. The instrument uses repetition rate multipliction, as mentioned above. This mode allows 9 monochromatic pulses on to the sample, with a wavelength difference of 0.25 Å. In this way, the instrument reaches a combined monochromatic flux of $1.6 \cdot 10^8$ n/s/cm^2 for the wavelength band mentioned above; an impressive factor 200 over IN5 at ILL.

A shorter acelerator pulse will allow for a shorter instrument, thus giving a larger bandwidth. Therefore the gain of going from the baseline setting to 1 ms is more than 50%. The same gains are found from lowering the accelerator frequency to 10 Hz, also due to the larger useful bandwidth.

Most neutrons at the sample originate from the innermost 4×4 cm^2 of the moderator surface. Therefore, at hot spot at the moderator will produce a clear intensity gain. A simulated hot spot with a factor two intensity gain over a circle of diameter $d = 3$ cm produces a gain in neutron flux at the sample of 30%.

Additional details about this (and the other) simulations are found in the appendix.

4 Results for instrument performance

After the optimization procedures, we record the resulting values of instrument length, wavelength bandwidth, flux at sample position, and FOM for each instrument and time structure setting. The results for the individual simulations are listed in the appendix. For easier comparison, the obtained values of FOM have been normalized to the baseline setting of $T = 60$ ms and $\tau = 2$ ms.

From the appendix it can be seen that apart from the triple axis spectrometers, all instruments perform much better towards the upper left-hand corner of the performance matrix. This is to be expected, since i) a longer T will allow for a much larger useful wavelength band, $\Delta\lambda$, and ii) a smaller τ will either iia) allow L to be smaller, giving an increased $\Delta\lambda$, or iib) allowing a higher fraction of the total flux through the pulse-defining choppers.

To perform a global comparison of the different accelerator settings, we have performed averages of the relative performances, which are listed in Table 2 and 3 for the constant-time-integrated-flux and constant-peak-flux scenarios, respectively. The average has been performed with equal weight given to each simulated instrument. However, a weighted average can easily be performed, when a suitable weight has been defined for each instrument.

T/τ (ms)	1.0	1.25	1.5	2.0
100 (10 Hz)	2.19	1.93	1.72	1.35
80 (12.5 Hz)	1.97	1.71	1.51	1.17
60 (16.67 Hz)	1.58	1.37	1.20	1.00
50 (20 Hz)	1.36	1.21	1.03	N/A
40 (25 Hz)	1.14	1.01	N/A	N/A

Table 2. Average Figure-of-Merit for the generic ESS instrument suite at different accelerator time structures, under the assumption of constant time-integrated flux. "N/A" represents time structures not initially simulated.

T/τ (ms)	1.0	1.25	1.5	2.0
100 (10 Hz)	0.66	0.72	0.77	0.81
80 (12.5 Hz)	0.74	0.80	0.85	0.88
60 (16.67 Hz)	0.79	0.86	0.90	1.00
50 (20 Hz)	0.82	0.91	0.93	N/A
40 (25 Hz)	0.86	0.95	N/A	N/A

Table 3. Average Figure-of-Merit for the generic ESS instrument suite at different accelerator time structures, under the assumption of constant peak flux. "N/A" represents time structures not initially simulated.

We see that the effect of shortening the pulse from 2.0 ms to 1.0 ms is typically around 70% increase at constant time-integrated flux - or 15% decrease at constant peak flux. Likewise, the effect of going from 20 Hz to 10 Hz is around a 60% increase at constant time-integrated flux - or 20% decrease at constant peak flux.

As soon more detailed information is available on the time-integrated (peak) proton current a function of (T, τ), it can be multiplied directly onto the performance matrix in Table 2 (3), to refine the results.

4.1 Accelerator power

When evaluating these results, it should be added that we assume the constant-integrated-flux scheme to give a time-integrated flux similar to the ILL at 5 MW power. For the constant-peak-flux scheme, we assume the recens values of 50 mA maximum current and 2.5 GeV accelerator energy, corresponding to $P_{\text{peak}} = 125$ MW peak power. The time-integrated effect is thus given by $P = P_{\text{peak}}\tau/T$. We have listed this value for the investigated settings in Table 4. As one example it can be noticed that going from (2 ms, 16 2/3 Hz) to (1.25 ms, 12 1/2 Hz), the accelerator power drops by 55%, while the average FoM falls only by 20%.

T/τ (ms)	1.0	1.25	1.5	2.0
100 (10 Hz)	1.25	1.56	1.88	2.50
80 (12.5 Hz)	1.56	1.95	2.34	3.13
60 (16.67 Hz)	2.08	2.60	3.13	4.17
50 (20 Hz)	2.50	3.13	3.75	5.00
40 (25 Hz)	3.13	3.91	4.69	6.25

Table 4. Average accelerator power (in MW) at different accelerator time structures, under the assumption of constant peak power of 125 MW.

4.2 Optimizing the moderator parameters

The simulation of the target/moderator design is much more involved than instrument simulation. In addition, this design is not as urgent for the ESS timeline as is the determination of the accelerator time structure. Hence, these simulations are still far from being completed. In order to assist the moderator optimizations towards an improved ESS functionality, we here sketch how the insight gained from instrument simulations can be used in the target/moderator optimizations.

Often, the figure-of-merit in moderator optimizations is the number of neutrons produced, possibly in a given wavelength interval and for a given moderator size. Now, the moderator simulations produce more detailed information than this. The result of each simulation is given as a history of neutron events, each event having 6 parameters: position at moderator surface (2), time of emittance (1), wavelength (1), and divergence (2). To simplify, we have ignored the emission time. It was then possible to represent the transmission probability from moderator to surface as

$$T(\mathbf{r}, \lambda) \approx T_r(\mathbf{r}) T_\lambda(\lambda). \tag{6}$$

Here, the dependence on divergence has been integrated out, since typical moderator fluxes vary slowly over the solid angle of the guide entry. For a total target/moderator optimization, the figure-of-merit to optimize is thus for each of the moderators (e.g. cold and thermal):

$$\text{FOM}_{\text{mod}} = \sum_j W_j \times \int N(\mathbf{r}, \lambda, t, \boldsymbol{\eta}) T_r(\mathbf{r}) T_\lambda(\lambda) Q(\lambda) d^2\mathbf{r} d\lambda d^2\boldsymbol{\eta} dt, \tag{7}$$

where W_j is an "importance weight factor" for each instrument, N is the simulated density of neutrons from the moderator, Q is given in (1),

and the sum runs over all instruments at the given moderator.

In the appendix, we present for each instrument the spatial transmission function, $T_r(\mathbf{r})$. We can see that for most instruments, the transmission peaks strongly in a "hot spot" of 3-5 cm diameter in the center of the moderator; a particular feature of using elliptical guides, or tight collimation for straight guides. Thus, it can be highly advantageous to concentrate the flux in a hot spot, while the size of the moderator can be limited; thus reducing the emission of fast neutrons. For each instrument, we have calculated the effect of producing a 3 cm diameter hot spot with a factor 2 higher emittance - while maintaining the total emittance of the moderator (close to what was presented by the J-PARC group at ICANS (23)). For most instruments, the gain factor of such a hot spot is around 30%.

4.3 Optimizing the ESS instruments

The optimization procedure for the ESS will end with a new round of instrument simulations, which will help deciding the choice of instrument and their final design. These simulations can be initiated only when the design of the accelerator and target/moderator is finalized.

5 Conclusion

We have performed a series of systematic raytracing simulations of the performance of (a large part of) a generic instrument suite for the ESS. These simulations have been performed for a large number of accelerator settings, for constant, typical instrument resolutions. The performance parameters were as expected found to increase with decreasing pulse length and decreasing pulse frequency for a constant time-integrated flux. for a constant peak flux, the performance decreased somewhat with decreasing pulse length and decreasing pulse frequency.

For the determination of the optimal parameters for the accelerator time structure, we still need details from the accelerator calculation. In particular, we should know the variation of average (or peak) proton current for the various accelerator settings. Possibly, non-linear effects from the behaviour of target/moderators should be included in these calculations.

Since most instruments use tight collimations or (elliptical) focusing guides, most neutrons hitting the sample stem from a "hot spot" in the central 3-5 cm of the moderator. We suggest to use this knowledge for the optimization of the moderator design.

References

[1] See the home page for the ESS project: `www.ess-scandinavia.eu`

[2] The ESS Project (2002), Vol I

[3] The ESS Project (2002), Vol IV

[4] R.K. Crawford *et al.*, Report of the Long-pulse Neutron Instrumentation Workshop, Frascati, August 2009 (2010)

[5] F. Mezei, Journal of Neutron Research **6**, 3 (1997)

[6] G. Zsigmond *et al.*, Appl. Phys. A **74**, S224 (2002)

[7] K. Lieutenant *et al.*, J. Phys.: Condens. Matter **17** S167 (2005)

[8] H. Schober *et al.*, Nuclear Instruments and Methods in Physics Research A **589**, 34 (2008)

[9] K. Lefmann *et al.*, Draft manuscript from the Ven 2008 meeting

[10] F. Mezei, M. Russina, and S. Schorr, Physica B, **276**, 128 (2000)

[11] K. Lefmann et al, Meas. Sci. Techn. (2008), 19, 034025

[12] M. Russina and F. Mezei, Nucl. Instr. Meth. A **604**, 624 (2009)

[13] M. Nokamura *et al.*, J. Phys. Soc. Jpn. **78**, 093002 (2009)

[14] F. Mezei, note on ESS moderator performance, December 2000

[15] K.H. Klenø and K. Lieutenant, in progress (2010)

[16] K.H. Klenø *et al.*, in progress (2010)

[17] P. Böni group, proceedings of the ICANS (2010)

[18] U. Filges, in preparation (2010)

[19] SwissNeutronics A.G., personal communication (2010); see also www.swissneutronics.ch

[20] P. Allenspach, P. Böni, and K. Lefmann, Proceedings of SPIE 4509 (2001)

[21] Mirrotron Ltd., personal communication (2010); see also www.mirrotron.kfkipark.hu

[22] K. Lefmann and K. Nielsen, Neutron News **10**/**3**, 20 (1999); see also www.mcstas.org

[23] J-PARC presentation at the ICANS conference (2010)

Cold Chopper Spectrometer

Simulated by Kim Lefmann and Kaspar Klenø

This high-flux medium-resolution spectrometer is a general workhorse for quasielastic and inelastic scattering in powders, liquids, and single crystals.

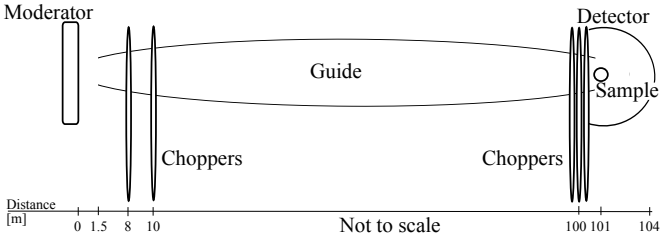

General design:
-*Resolution:* fixed at 5 Å: $d\lambda/\lambda = 1.6\%$.
-*Moderator:* Cold (possibly bispectral)
-*Guide:* Elliptical, max. 27.3 cm wide, begin at 1.5 m from moderator, end 0.2 m from sample.
-*Pulsing:* Use full pulse.
-*Choppers:* 2 frame-overlap; at 8 m and 16 m; 2 fast monochromating choppers 1.2 m from sample
-*Sample:* 4×2 cm^2
-*Detectors:* Cylinder, 4 m radius, 8 m high

Base-line design at 16.6 Hz, 2.0 ms:
-*Instrument length:* $L = 100$ m
-*Bandwith:* $\lambda_{min} = 3.9$ Å and $\lambda_{max} = 6.1$ Å
-*Flux:* (choppers at 150 Hz) 1.6×10^8 n/s/cm^2
-*Repetition rate:* Resolution choppers emits monochromatic pulses with different wavelengths

Effect of hot spot:
Factor 2 hot spot, $d = 3$ cm: 30% flux gain.

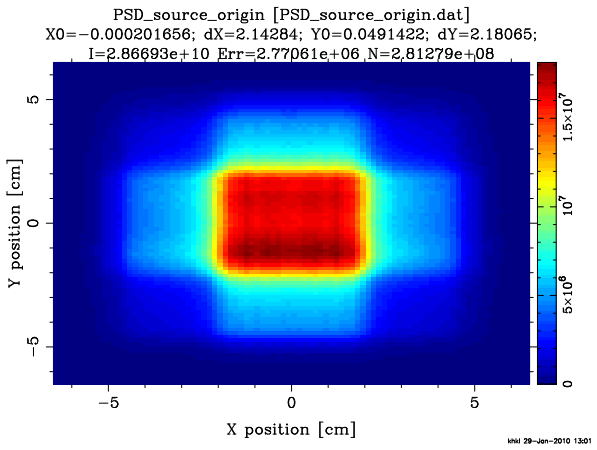

Design with other accelerator parameters:
-*Instrument length moderator-sample* , for constant resolution:

τ (ms)	0.8	1.0	1.25	1.5	2.0
L (m)	wait	60	70	80	100

-*Wavelength band (Å):*

T/τ (ms)	0.8	1.0	1.25	1.5	2.0
100 (10 Hz)	wait	6.33	5.43	4.75	3.80
80 (12.5 Hz)	wait	5.00	4.29	3.75	3.00
60 (16.67 Hz)	wait	3.67	3.14	2.75	2.20
50 (20 Hz)	wait	3.00	2.57	2.25	N/A
40 (25 Hz)	wait	2.33	2.00	N/A	N/A

-*Figure of merit:* (choppers at 150 Hz)

T/τ (ms)	0.8	1.0	1.25	1.5	2.0	N
100 (10 Hz)	wait	2.39	2.24	2.05	1.67	15
80 (12.5 Hz)	wait	2.08	1.83	1.59	1.26	11
60 (16.67 Hz)	wait	1.72	1.48	1.29	1.00	9
50 (20 Hz)	wait	1.32	1.15	0.99	N/A	7
40 (25 Hz)	wait	0.92	0.80	N/A	N/A	5

References:
-*The ESS Project (2002), Vol IV, p.2.34*
-*K. Lefmann et al, Meas. Sci. Techn. (2008), 19, 034025; and refs. therein*

Thermal Chopper Spectrometer

Simulated by Kim Lefmann and Morten Sales

This high-flux medium-resolution thermal spectrometer is a general workhorse for quasielastic and inelastic scattering in powders and liquids.

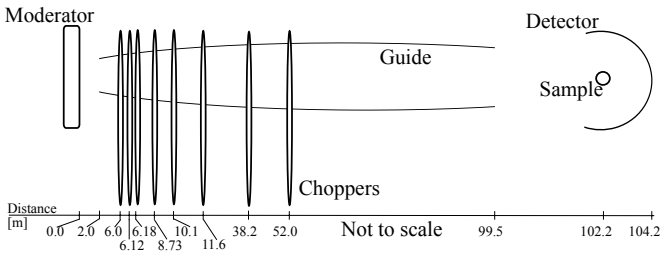

General design:
-*Resolution:* fixed at 1.27 Å: $d\lambda/\lambda = 2.2\%$.
-*Moderator:* Thermal
-*Guide:* Elliptical, max. 40 cm wide, begin at 2.0 m from moderator, end 0.5 m from sample.
-*Pulsing:* Use pulse shaping, repetition rate mode as Thermal Powder.
-*Choppers:* As Thermal Powder; plus 2 fast pulse-shaping at 100 m, 1 m from sample
-*Sample:* 4×2 cm^2
-*Detectors:* Cylinder, 5 m radius, 8 m high

Base-line design at 16.6 Hz, 2.0 ms:
-*Instrument length:* $L = 100$ m
-*Bandwith:* $\lambda_{\min} = 0.40$ Å and $\lambda_{\max} = 2.6$ Å
-*Flux:* (choppers at 200 Hz) 0.0×10^7 n/s/cm^2

Effect of hot spot:
Factor 2 hot spot, $d = 3$ cm: 48% flux gain.

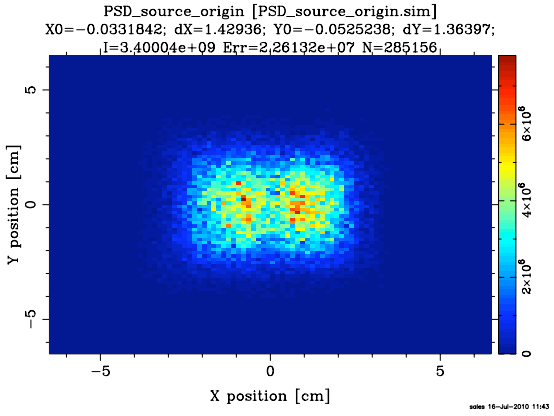

Design with other accelerator parameters:
-*Instrument length moderator-sample* , for constant resolution: Always 100 m

-*Wavelength band (Å):* ($\lambda_{\min} = 0.4$ Å in all settings)

T/τ (ms)	0.8	1.0	1.25	1.5	2.0
100 (10 Hz)	wait	3.80	3.80	3.80	3.80
80 (12.5 Hz)	wait	3.00	3.00	3.00	3.00
60 (16.67 Hz)	wait	2.30	2.30	2.30	2.30
50 (20 Hz)	wait	1.90	1.90	1.90	N/A
40 (25 Hz)	wait	1.50	1.50	N/A	N/A

-*Figure of merit:* (choppers at 400 Hz)

T/τ (ms)	0.8	1.0	1.25	1.5	2.0	N
100 (10 Hz)	wait	2.36	2.19	1.75	1.18	18
80 (12.5 Hz)	wait	2.36	1.88	1.45	0.92	14
60 (16.67 Hz)	wait	1.97	1.52	1.16	1.00	11
50 (20 Hz)	wait	1.41	1.26	0.94	N/A	9
40 (25 Hz)	wait	1.23	1.09	N/A	N/A	7

References:
-*The ESS Project (2002), Vol IV, p.2.34*
-*K. Lefmann et al, Meas. Sci. Techn. (2008), 19, 034025; and refs. therein*

Cold Triple Axis Spectrometer

Simulated by Kim Lefmann and Kaspar Hewitt Klenø

This high-flux medium-to-high resolution spectrometer is the classical workhorse for inelastic scattering of single crystals on reactor sources. At the ESS, this instrument will utilize the large time-integrated flux, while the pulse structure is used for background suppression only.

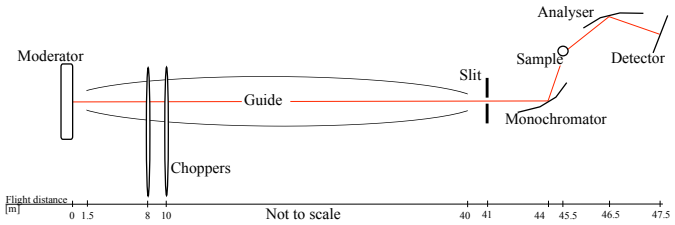

General design:
-*Resolution:* at 4 Å: $dE/E = 2.0\%$ (at sample).
-*Moderator:* Cold (possibly bispectral)
-*Guide:* Elliptical, max. 20 cm wide, begins 1.5 m from moderator, ends 4.1 m from sample; .
-*Guide price:* No estimate
-*Pulsing:* Use full pulse.
-*Choppers:* 1 frame-overlap; 1 background
-*Sample:* 1×1 cm^2
-*Detectors:* PSD, 0.5-2 m^2

Base-line design at 16.6 Hz, 2.0 ms:
-*Instrument length:* $L = 40$ m
-*Bandwith:* (monochromatic beam)
-*Flux:* 9.1×10^8 n/s/cm^2
-*Repetition rate:* Possible to use second order neutrons by time-of-flight seperation (not done)

Effect of hot spot:
Factor 2 hot spot, $d = 3$ cm: 13% flux gain.

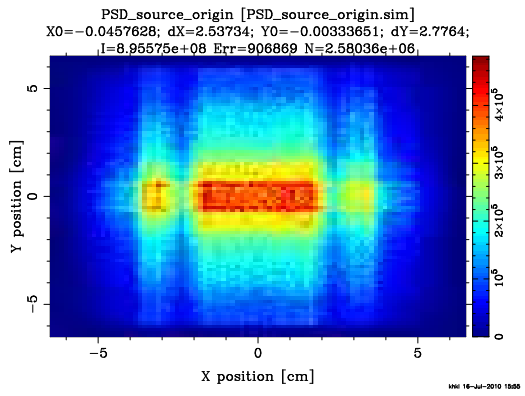

Design with other accelerator parameters:
-*Instrument length moderator-sample* , for constant resolution:

τ (ms)	0.8	1.0	1.25	1.5	2.0
L (m)	40	40	40	40	40

-*Wavelength band (Å):*

T/τ (ms)	0.8	1.0	1.25	1.5	2.0
100 (10 Hz)	-	-	-	-	-
80 (12.5 Hz)	-	-	-	-	-
60 (16.67 Hz)	-	-	-	-	-
50 (20 Hz)	-	-	-	-	N/A
40 (25 Hz)	-	-	-	N/A	N/A

-*Figure of merit:*

T/τ (ms)	0.8	1.0	1.25	1.5	2.0	N
100 (10 Hz)	1.00	1.00	1.00	1.00	1.00	1
80 (12.5 Hz)	1.00	1.00	1.00	1.00	1.00	1
60 (16.67 Hz)	1.00	1.00	1.00	1.00	1.00	1
50 (20 Hz)	1.00	1.00	1.00	1.00	N/A	1
40 (25 Hz)	1.00	1.00	1.00	N/A	N/A	1

References:
-*K. Lefmann et al, Nucl. Inst. Meth. A (2010), accepted*

July 14, 2010

Thermal Triple Axis Spectrometer

Simulated by Kim Lefmann and Kaspar Hewitt Klenø

This high-flux medium resolution thermal spectrometer is the classical workhorse for inelastic scattering of single crystals on reactor sources. At the ESS, this instrument will utilize the large time-integrated flux, while the pulse structure is used for background suppression only.

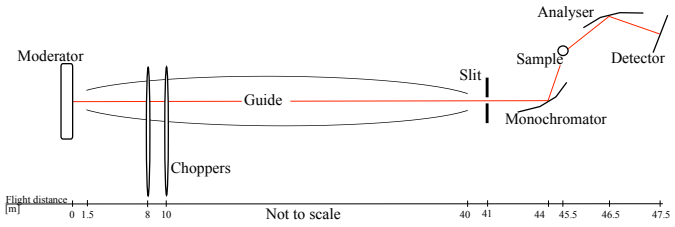

General design:

-Resolution: at 1.53 Å ($k_\mathrm{i} = 4.1$ Å^{-1}) : $dE/E =$ 5.0% (at sample).
-Moderator: Thermal
-Guide: Elliptical, max. 20 cm wide, begins 1.5 m from moderator, ends 4.0 m from analyzer; .
-Pulsing: Use full pulse.
-Choppers: frame definition; frame overlap
-Sample: 1×1 cm^2
-Detectors: PSD, 0.5-2 m^2

Base-line design at 16.6 Hz, 2.0 ms:

-Instrument length: $L = 40$ m
-Bandwith: (monochromatic beam)
-Flux: 1.75×10^9 n/s/cm^2 (1.53 Å; PG mono 60%)
-Repetition rate: Possible to use second order neutrons by time-of-flight seperation (not done)

Effect of hot spot:

Factor 2 hot spot, $d = 3$ cm: 12% flux gain.

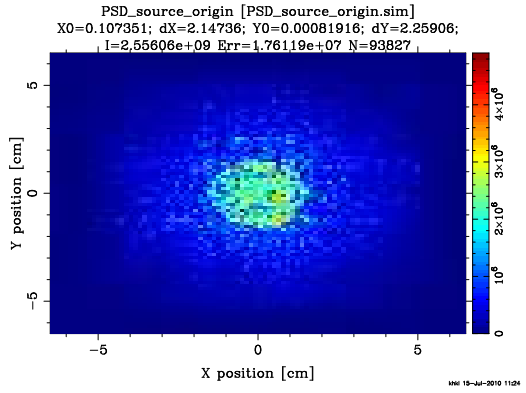

Design with other accelerator parameters:

-Instrument length moderator-sample , for constant resolution:

τ (ms)	0.8	1.0	1.25	1.5	2.0
L (m)	40	40	40	40	40

-Wavelength band (Å):

T/τ (ms)	0.8	1.0	1.25	1.5	2.0
100 (10 Hz)	-	-	-	-	-
80 (12.5 Hz)	-	-	-	-	-
60 (16.67 Hz)	-	-	-	-	-
50 (20 Hz)	-	-	-	-	N/A
40 (25 Hz)	-	-	-	N/A	N/A

-Figure of merit:

T/τ (ms)	0.8	1.0	1.25	1.5	2.0	N
100 (10 Hz)	1.00	1.00	1.00	1.00	1.00	1
80 (12.5 Hz)	1.00	1.00	1.00	1.00	1.00	1
60 (16.67 Hz)	1.00	1.00	1.00	1.00	1.00	1
50 (20 Hz)	1.00	1.00	1.00	1.00	N/A	1
40 (25 Hz)	1.00	1.00	1.00	N/A	N/A	1

References:

-K. Lefmann et al, Nucl. Inst. Meth. A (2010), accepted

TOF-TAS

Simulated by Kaspar Klenø; consultant Kim Lefmann.

This high-flux medium-resolution spectrometer uses the ToF principle to determine incoming energy, and the TAS method to determine outgoing.

Image not yet ready!

General design:
-*Resolution:* fixed at 4 Å: $d\lambda/\lambda = 2.0\%$.
-*Moderator:* Cold
-*Guide:* Elliptical, max. 40 cm wide, begin at 1.5 m from moderator, end 0.5 m from sample.
-*Pulsing:* Use full pulse.
-*Choppers:* Frame-overlap only.
-*Sample:* 1×1 cm^2
-*Detectors:* Depends on secondary spectrometer ????

Base-line design at 16.6 Hz, 2.0 ms:
-*Instrument length:* $L = 100$ m.
-*Wavelength band (Å):* $\lambda_{min} = 2.8$, $\lambda_{max} = 5.2$.
-*Flux:* 6.0×10^{10} n/s/cm^2.
-*Repetition rate:* None.

Effect of hot spot:
Factor 2 hot spot, $d = 3$ cm: 17.9% flux gain.

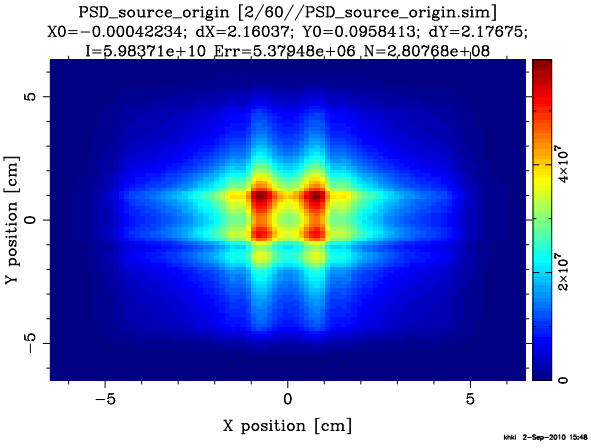

Design with other accelerator parameters: -*Instrument length moderator-sample*, for constant resolution:

τ (ms)	0.8	1.0	1.25	1.5	2.0
L (m)	wait	60	70	80	100

-*Bandwidth (Å):*

T/τ (ms)	0.8	1.0	1.25	1.5	2.0
100 (10 Hz)	wait	6.59	5.65	4.95	3.96
80 (12.5 Hz)	wait	5.27	4.52	3.96	3.16
60 (16.67 Hz)	wait	3.96	3.39	2.97	2.37
50 (20 Hz)	wait	3.30	2.83	2.47	N/A
40 (25 Hz)	wait	2.64	2.26	N/A	N/A

-*Figure of merit:*

T/τ (ms)	0.8	1.0	1.25	1.5	2.0
100 (10 Hz)	wait	1.80	1.75	1.69	1.42
80 (12.5 Hz)	wait	1.74	1.69	1.61	1.25
60 (16.67 Hz)	wait	1.64	1.53	1.36	1.00
50 (20 Hz)	wait	1.54	1.37	1.17	N/A
40 (25 Hz)	wait	1.34	1.14	N/A	N/A

References:
(New design)

Backscattering Spectrometer

Simulated by Kaspar Hewitt Klenø; consultant Kim Lefmann

This is a high-flux off-backscattering spectrometer for quasielastic studies, with a resolution similar to OSIRIS at ISIS.

Image not yet ready!

General design:
-*Resolution:* fixed at 6.66 Å: $d\lambda/\lambda = 0.39\%$ at sample ($dE/E = 1.2\%$ reconstructed at detector)
-*Moderator:* Cold
-*Guide:* Elliptical, max. 40 cm wide, begin at 1.5 m from moderator, end 0.2 m from sample.
-*Guide price:* 2.9 MEuro.
-*Pulsing:* Use full pulse.
-*Choppers:* Frame overlap + frame definition.
-*Sample:* 4×2 cm^2.
-*Detectors:* <1 m^2 below sample.

Base-line design at 16.6 Hz, 2.0 ms:
-*Instrument length:* $L = 301.7$ m
-*Wavelength band (Å):* $\lambda_{min} = 6.27$, $\lambda_{max} = 7.05$
-*Flux:* 3.16×10^9 n/s/cm^2.
-*Repetition rate:* None.

Effect of hot spot:
A factor 2 hot spot, 3×3 cm^2 will give 13 % gain.

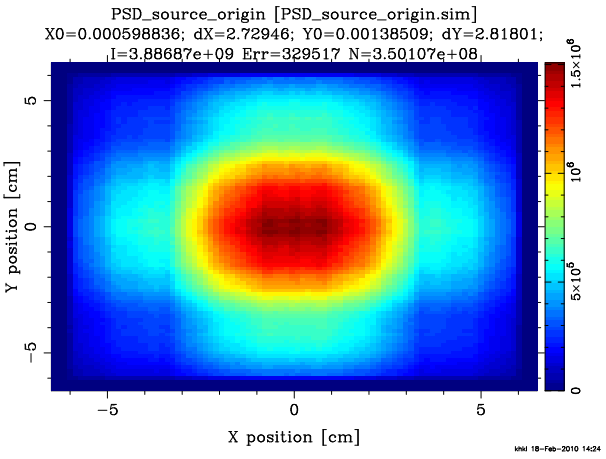

Design with other accelerator parameters:
-*Instrument length moderator-sample* , for constant resolution (m):

τ (ms)	0.8	1.0	1.25	1.5	2.0
L (m)	x	150.8	188.5	226.2	301.7

-*Bandwidth (Å):*

T/τ (ms)	0.8	1.0	1.25	1.5	2.0
100 (10 Hz)	wait	2.59	2.08	1.74	1.31
80 (12.5 Hz)	wait	2.08	1.66	1.39	1.05
60 (16.67 Hz)	wait	1.56	1.25	1.04	0.79
50 (20 Hz)	wait	1.30	1.04	0.87	N/A
40 (25 Hz)	wait	1.04	0.83	N/A	N/A

-*Figure of merit:*

T/τ (ms)	0.8	1.0	1.25	1.5	2.0
100 (10 Hz)	wait	5.24	3.48	2.70	1.71
80 (12.5 Hz)	wait	4.11	2.76	2.16	1.35
60 (16.67 Hz)	wait	3.03	2.04	1.58	1.00
50 (20 Hz)	wait	2.24	1.70	1.32	N/A
40 (25 Hz)	wait	1.96	1.36	N/A	N/A

References:
-*The ESS Project (2002), Vol IV, p.2.26*
-*K.H. Klenø et al., Nucl. Instr. and Meth. A (2010), doi:10.1016*
-*Tregenna-Piggott et. al. (2008),Journal of Neutron Research,16:1,13-22*
-*G. Zsigmond et al. / Nuclear Instruments and Methods in Physics Research A 457 (2001) 299-308*

Spin-Echo

Simulated by Erik Bergbäck Knudsen

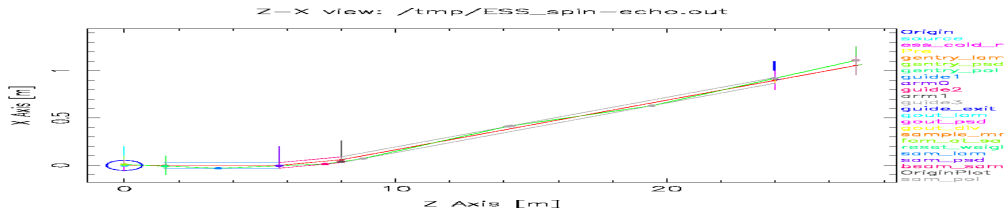

Design is based on the ESS-SANS and on general considerations from the Rencurel workshop (Schober). The design itself is based on a CW-NSE instrument: IN-11 @ ILL. A large bandwidth is desired for a large dynamic range of the instrument, i.e. a short instrument. This is offset by space requirements. Moderator to detector distance, $L_D = 30m$ is considered a conservative compromise. This should be reconsidered when more is known about instrument spacing.

General design:
-*Resolution:* At least $\frac{\Delta\lambda}{\lambda} < 10\%$ for $\lambda > 4$
-*Guide:* Straight with a double kink (3°) $8 \times 8cm^2, m = 4$. Guide starts $1.5m$ downstream from moderator, ends $3m$ prior to sample to leave rom for spin-echo coils.
-*Pulsing:* Use full pulse.

Base-line design at 16.6 Hz, 2.0 ms:
-*Instrument length:* $L_D = 30$ m
-*Bandwith:* $\lambda_{min} = 4$ and $\lambda_{max} = 11.91$

Effect of hot spot:
For the baseline design a factor 2 in intensity in a hotspot: $d = 3$, yields an unbiased gain of $\approx 6.5\%$. Biasing by $\lambda^{2.5}$ yields a gain of $\approx 6\%$
-*Origin plot:*

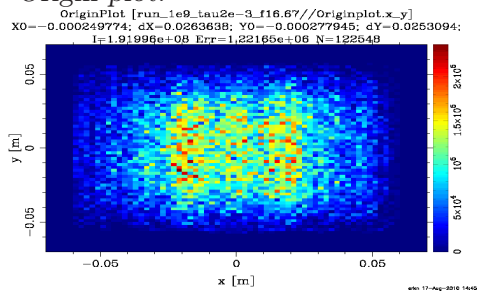

Design with other accelerator parameters:
Design is kept intact with instrument length at $L_D = 30m$ across all T/τ-parameters.
-*Table of gain factors:* Gain factor are computed according to the formula (Monkenbusch): $g = \ln\left(\frac{\lambda_{max}}{\lambda_{min}}\right)\left(\frac{\Delta\lambda}{\lambda}\right)$ Theoretical gain of pulsed vs. CW spin-echo with equal integrated flux. Assumes a fixed count time.

T	FW	Gain
100 (10 Hz)	13.2	6.33
80 (12.5 Hz)	10.5	5.61
60 (16.67 Hz)	7.91	4.74
50 (20 Hz)	6.59	4.23
40 (25 Hz)	5.27	3.65

Figure of merit used is as specified at the Frascati-workshop (2009)[1]: $FOM = \int_4^{4+BW} IF(\lambda)\,\lambda^{2.5}\mathrm{d}\lambda$
-*Table of figure of merit (rel. baseline design):*

T/τ (ms)	0.8	1.0	1.25	1.5	2.0
100 (10 Hz)	wait	1.192	1.194	1.203	1.203
80 (12.5 Hz)	wait	1.122	1.125	1.118	1.121
60 (16.67 Hz)	wait	1.013	1.005	1.003	1.000
50 (20 Hz)	wait	0.932	0.917	0.921	N/A
40 (25 Hz)	wait	0.817	0.814	N/A	N/A

References:
-*Schober et. al.*, Nuclear Instruments and Methods in Physics Research A, *v. 589, pp 34, 2008*
-*M. Monkenbusch et. al.*, Journal of Neutron Research, *v 13, pp 63, 2005*

[1]The workshop agreed on λ^{2-3} in the integrand. $\lambda^{2.5}$ is taken as a sensible compromise

4 m Bio-SANS

Simulated by Kaspar Hewitt Klenø; consultants Kim Lefmann and Lise Arleth

This is a short bio SANS instrument, that can cover a broad q-range with good resolution and intensity, with a 4 m max. collimation distance.

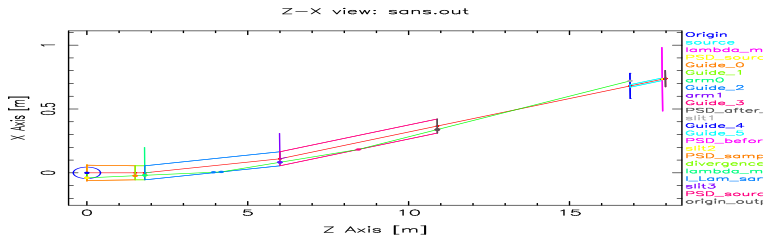

General design:
-*Resolution:* Not fixed with respect to pulse width.
-*Moderator:* Cold.
-*Guide:* Straight with a 3° double kink, const. 8 cm quadratic, begin at 1.5 m from mod., end at first coll. slit.
-*Guide price:* No data, but low.
-*Pulsing:* Use full pulse.
-*Choppers:*
-*Sample:* 0.5×0.5 cm^2
-*Detector:* 1×1 m^2

Base-line design at 16.6 Hz, 2.0 ms:
-*Instrument length:* $L = 12$ m + 1-4 m.
-*Wavelength band (Å):* $\lambda_{min} = 3.0$, $\lambda_{max} = 21.3$ (for 1 m collimation length).
-*Resolution:* $d\lambda/\lambda = 20.4\%$ at 3.0 Å (worst).
-*Flux:* $3.8{\times}10^8$ n/s/cm^2 (for 1 m coll. length).
-*Repetition rate:* None
-*q-range:* $0.93 - 0.00012$ Å^{-1}.

Effect of hot spot:
A factor 2 hotspot of a 3 cm diameter, increases the flux at the sample by 19.7 %, for the 4 m collimation length.

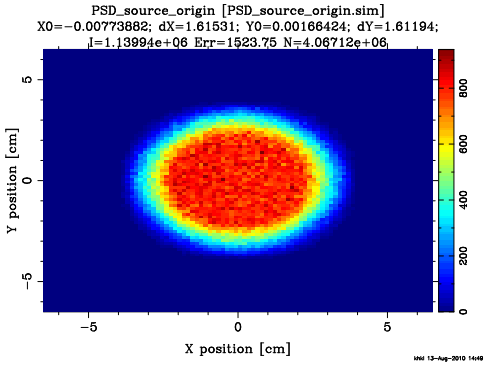

Design with other accelerator parameters:
-$d\lambda/\lambda$ *at 5 Å and 1 m coll.*

τ (ms)	0.8	1.0	1.25	1.5	2.0
$d\lambda/\lambda$ (Å)	4.9 %	6.1 %	7.6 %	9.2 %	12.2 %

-*Bandwidth (at 1 m coll. setting) (Å):*

T/τ (ms)	0.8	1.0	1.25	1.5	2.0
100 (10 Hz)	30.43	30.43	30.43	30.43	30.43
80 (12.5 Hz)	24.34	24.34	24.34	24.34	24.34
60 (16.67 Hz)	18.26	18.26	18.26	18.26	18.26
50 (20 Hz)	15.22	15.22	15.22	15.22	N/A
40 (25 Hz)	12.17	12.17	12.17	N/A	N/A

-*Figure of merit:*

T/τ (ms)	0.8	1.0	1.25	1.5	2.0
100 (10 Hz)	wait	1.01	1.01	1.01	1.01
80 (12.5 Hz)	wait	1.02	1.02	1.02	1.02
60 (16.67 Hz)	wait	1.00	1.00	1.00	1.00
50 (20 Hz)	wait	0.97	0.97	0.97	N/A
40 (25 Hz)	wait	0.92	0.92	N/A	N/A

References:
-*The ESS Project (2002), Vol IV, p.2.22*
-*Monte-Carlo simulations of small angle neutron scattering instruments at European spallation source, K. Lieutenant et. al., 2005*

Bio-SANS

Simulated by Kaspar Hewitt Klenø; consultants Kim Lefmann, Lise Arleth, and Klaus Lieutenant

This is a short 'workhorse' SANS instrument, that can cover a broad q-range with good resolution and intensity.

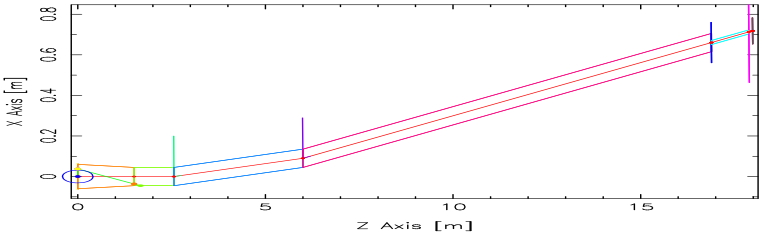

General design:
-*Resolution:* Not fixed with respect to pulse width.
-*Moderator:* Cold.
-*Guide:* Straight with a 3° double kink, const. 8 cm quadratic, begin at 1.5 m from mod., end at first coll. slit.
-*Guide price:* No data, but low.
-*Pulsing:* Use full pulse.
-*Choppers:*
-*Sample:* 0.5×0.5 cm^2
-*Detector:* 1×1 m^2

Base-line design at 16.6 Hz, 2.0 ms:
-*Instrument length:* $L = 18$ m + 1-10 m.
-*Wavelength band (Å):* $\lambda_{min} = 3.5$, $\lambda_{max} = 16.0$ (for 1 m collimation length).
-*Resolution:* $d\lambda/\lambda = 11.9\%$ at 3.5 Å (worst).
-*Flux:* $2.9{\times}10^8$ n/s/cm^2 (for 1 m coll. length).
-*Repetition rate:* None
-*q-range:* $0.80 - 0.00063$ Å^{-1}.

Effect of hot spot:
A factor 2 hotspot of a 3 cm diameter, increases the flux at the sample by 99.6 %, for the 10 m collimation length.

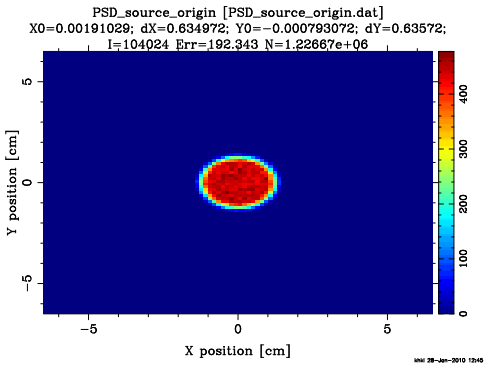

Design with other accelerator parameters:
-$d\lambda/\lambda$ *at 5 Å and 1 m coll.*

τ (ms)	0.8	1.0	1.25	1.5	2.0
$d\lambda/\lambda$ (Å)	3.3 %	4.2 %	5.2 %	6.3 %	8.4 %

-*Bandwidth (at 1 m coll. setting) (Å):*

T/τ (ms)	0.8	1.0	1.25	1.5	2.0
100 (10 Hz)	20.82	20.82	20.82	20.82	20.82
80 (12.5 Hz)	16.66	16.66	16.66	16.66	16.66
60 (16.67 Hz)	12.49	12.49	12.49	12.49	12.49
50 (20 Hz)	10.41	10.41	10.41	10.41	N/A
40 (25 Hz)	8.33	8.33	8.33	N/A	N/A

-*Figure of merit:*

T/τ (ms)	0.8	1.0	1.25	1.5	2.0
100 (10 Hz)	wait	1.54	1.54	1.54	1.54
80 (12.5 Hz)	wait	1.34	1.34	1.34	1.34
60 (16.67 Hz)	wait	1.00	1.00	1.00	1.00
50 (20 Hz)	wait	0.80	0.80	0.80	N/A
40 (25 Hz)	wait	0.65	0.65	N/A	N/A

References:
-*The ESS Project (2002), Vol IV, p.2.22*
-*Monte-Carlo simulations of small angle neutron scattering instruments at European spallation source, K. Lieutenant et. al., 2005*

20 m Materials-SANS

Simulated by Kaspar Hewitt Klenø; consultants Kim Lefmann and Lise Arleth

This is a long materials SANS instrument, that covers a wide q-range with high resolution and good intensity, with a 20 m max. collimation distance.

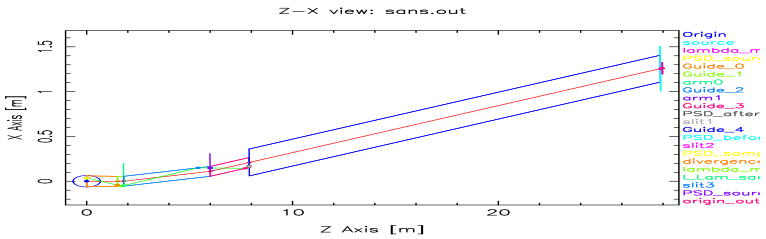

General design:

-*Resolution:* Not fixed with respect to pulse width.
-*Moderator:* Cold.
-*Guide:* Straight with a 3° double kink, const. 11 cm quadratic, begin at 1.5 m from mod., end at first coll. slit.
-*Pulsing:* Use full pulse.
-*Choppers:* Pulse definition & frame overlap.
-*Sample:* 1×1 cm^2
-*Detector:* 1×1 m^2

Base-line design at 16.6 Hz, 2.0 ms:

-*Instrument length:* $L = 28$ m + 2-20 m.
-*Wavelength band (Å):* $\lambda_{min} = 3.0$, $\lambda_{max} = 10.9$ (for 2 m collimation length).
-*Resolution:* $d\lambda/\lambda = 8.8\%$ at 3.0 Å (worst).
-*Flux:* $1.8{\times}10^8$ n/s/cm^2 (for 2 m coll. length).
-*Repetition rate:* None
-*q-range:* $0.51 - 0.00035$ Å^{-1}.

Effect of hot spot:

A factor 2 hotspot of a 3 cm diameter, increases the flux at the sample by 72.2 %.

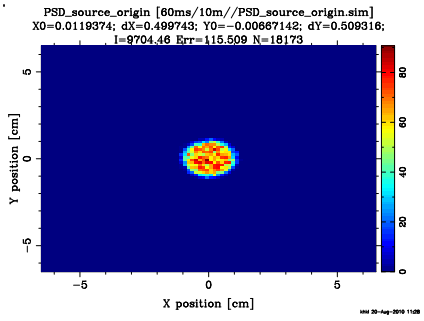

Design with other accelerator parameters:

-$d\lambda/\lambda$ *at 5 Å and 2 m coll.*

τ (ms)	0.8	1.0	1.25	1.5	2.0
$d\lambda/\lambda$ (Å)	2.1 %	2.7 %	3.3 %	4.0 %	5.3 %

-*Bandwidth (at 2 m coll. setting,* λ_{min} *fixed at 3 Å.) (Å):*

T/τ (ms)	0.8	1.0	1.25	1.5	2.0
100 (10 Hz)	13.2	13.2	13.2	13.2	13.2
80 (12.5 Hz)	10.6	10.6	10.6	10.6	10.6
60 (16.67 Hz)	7.9	7.9	7.9	7.9	7.9
50 (20 Hz)	6.6	6.6	6.6	6.6	N/A
40 (25 Hz)	5.3	5.3	5.3	N/A	N/A

-*Figure of merit:* (Average of 2, 10, & 20 collimation settings.)

T/τ (ms)	0.8	1.0	1.25	1.5	2.0
100 (10 Hz)	wait	1.69	1.69	1.69	1.69
80 (12.5 Hz)	wait	1.34	1.34	1.34	1.34
60 (16.67 Hz)	wait	1.00	1.00	1.00	1.00
50 (20 Hz)	wait	0.83	0.83	0.83	N/A
40 (25 Hz)	wait	0.67	0.67	N/A	N/A

References:

-*The ESS Project (2002), Vol IV, p.2.22*
-*Monte-Carlo simulations of small angle neutron scattering instruments at European spallation source, K. Lieutenant et. al., Nuclear Instruments and Methods in Physics Research A 553 (2005) 592-603*

July 16, 2010

Reflectometer

Simulated by Lars von Moos; consultants Klaus Lieutenant, Markus Strobl and Robert Cubitt

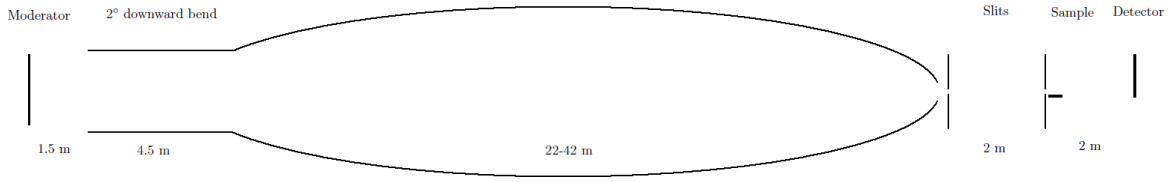

Horizontal reflectometer for study of solid and liquid surfaces.

General design:

- *Resolution:* Fixed worst resolution: $dq/q \leq 10\%$
- *q-range:* $0.005 - 0.3$ Å^{-1} covered by two sample angles ($\sim 0.45°$ and $3.42°$)
- *Moderator:* Cold
- *Guide:* Straight downward bend (2°), Elliptical, max. 20 cm wide and 30 cm high
- *Pulsing:* Uses full pulse of every 2. to 4. pulse
- *Choppers:* 3. Pulse shaping, frame overlap and bandwidth chopper
- *Sample:* 4×4 cm^2
- *Detectors:* Less than 1 m^2

Base-line design at 16.67 Hz, 2.0 ms:

- *Instrument length:* $L = 52$ m
- *Bandwidth:* $\lambda_{min} = 2.5$ Å and $\lambda_{max} = 20.4$ Å
- *Flux at sample:* Small angle $5.6 \cdot 10^5$ n/s/cm^2 Large angle $7.6 \cdot 10^6$ n/s/cm^2

Effect of hot spot:

A factor 2 hot spot, 3×3 cm^2 will give 31% gain

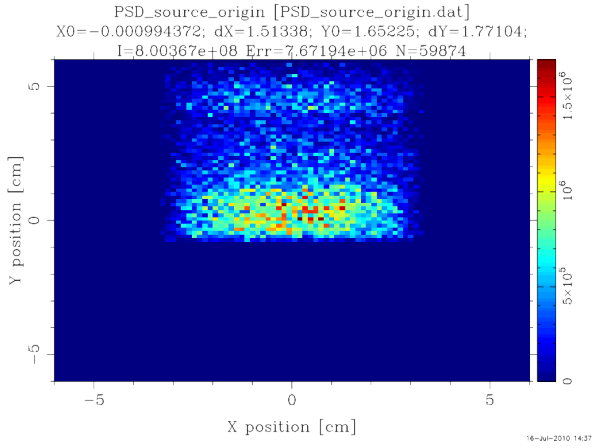

Design with other accelerator parameters:

- *Instrument length from moderator to detector(m) / Number of skipped pulses:*

T/τ (ms)	0.8	1.0	1.25	1.5	2.0
100 (10 Hz)	-	43/1	43/1	43/1	52/2
80 (12.5 Hz)	-	35/1	35/1	35/1	52/2
60 (16.67 Hz)	-	40/2	40/2	40/2	52/3
50 (20 Hz)	-	32/2	32/2	43/3	-
40 (25 Hz)	-	35/3	35/3	-	-

- *Wavelength band (Å):*

T/τ (ms)	0.8	1.0	1.25	1.5	2.0
100 (10 Hz)	-	18.1	18.1	18.0	22.5
80 (12.5 Hz)	-	17.7	17.7	17.6	18.0
60 (16.67 Hz)	-	17.5	17.4	17.4	17.9
50 (20 Hz)	-	18.1	18.1	18.0	-
40 (25 Hz)	-	17.7	17.7	-	-

- *Figure of merit (avg. for both angles):*

T/τ (ms)	0.8	1.0	1.25	1.5	2.0
100 (10 Hz)	-	3.09	2.92	2.66	1.36
80 (12.5 Hz)	-	3.16	2.98	2.74	1.35
60 (16.67 Hz)	-	1.99	1.90	1.61	1.00
50 (20 Hz)	-	2.13	1.84	1.25	-
40 (25 Hz)	-	1.60	1.47	-	-

References:

- *Reflectometry Group.* ESS meeting in Ven 2009. John Webster, Robert Cubitt, Jochen Stahn and Alan Menelle

Cold Powder Diffractometer

Simulated by Sonja Lindahl Holm; consultants Kim Lefmann and Klaus Lieutenant.

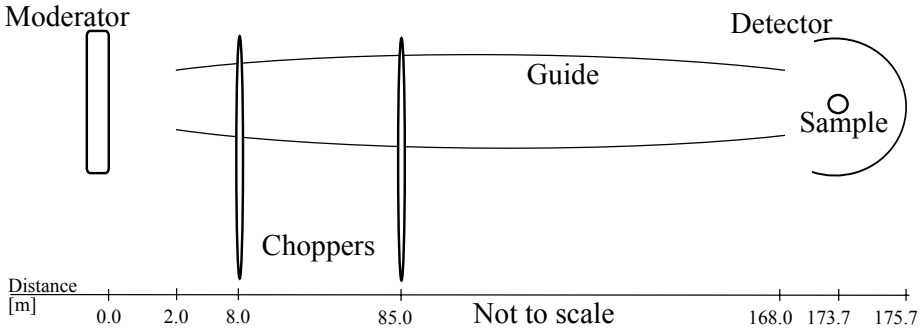

This high-flux low-resolution diffractometer is meant for magnetic structure determination, possibly under extreme environments.

General design:
-*Resolution:* fixed at 4.5 Å: $\frac{d\lambda}{\lambda} = 1.0\%$.
-*Moderator:* Cold (possibly bispectral).
-*Guide:* Elliptical, max. 20 cm wide.
-*Pulsing:* Use full pulse.
-*Choppers:* Two frame overlap choppers.
-*Sample:* 1×1 cm^2.
-*Detectors:* 2 m radius cylinder.

Base-line design at 16.6 Hz, 2.0 ms:
-*Instrument length:* $L = 175.7$ m
-*Bandwith:* $\lambda_{min} = 3.85$ Å and $\lambda_{max} = 5.15$ Å
-*Flux at sample:* $5.89{\cdot}10^8$ n/s/cm^2
-*Repetition rate:* None

Effect of hot spot:
A factor 2 hot spot, 3×3 cm^2 will give 28,7% gain.

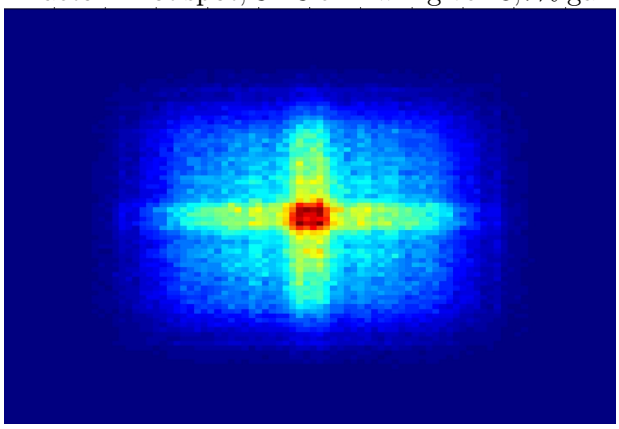

Design with other accelerator parameters:
-*Instrument length* from moderator to sample, for constant resolution:

τ (ms)	0.8	1.0	1.25	1.5	2.0
L (m)	70.3	87.8	109.8	131.8	175.7

-*Wavelength band (Å):*

T/τ (ms)	0.8	1.0	1.25	1.5	2.0
100 (10 Hz)	8.44	6.76	5.40	4.50	3.38
80 (12.5 Hz)	6.76	5.40	4.32	3.60	2.70
60 (16.67 Hz)	5.06	4.06	3.24	2.70	2.02
50 (20 Hz)	4.22	3.38	2.70	2.26	N/A
40 (25 Hz)	3.38	2.70	2.16	N/A	N/A

-*Figure of merit:*

T/τ (ms)	0.8	1.0	1.25	1.5	2.0
100 (10 Hz)	4.77	3.88	3.07	2.42	1.71
80 (12.5 Hz)	4.04	3.01	2.38	1.88	1.35
60 (16.67 Hz)	2.90	2.16	1.71	1.36	1.00
50 (20 Hz)	2.35	1.74	1.41	1.13	N/A
40 (25 Hz)	1.81	1.37	1.11	N/A	N/A

References:
-*The ESS Project (2002), Vol IV, p.2.22*

Thermal Powder Diffractometer

Simulated by Morten Sales; consultants Kim Lefmann and Klaus Lieutenant

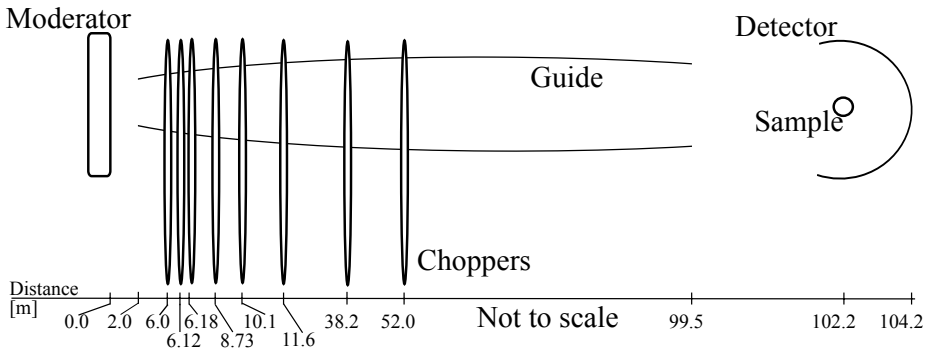

General design:
-Resolution: at 1.5 Å, fixed $d\lambda/\lambda = 5 \cdot 10^{-3}$.
-Guide: Elliptical with fixed shape and size: length 97.5 m, maximum width 0.11 m; beginning 2 m after moderator, ending 2.7 m before sample.
-Pulsing: The Instrument is using Wavelength Frame Multiplication, based on a design by K. Lieutenant and F. Mezei from [1].
-Choppers: Pulse shaping choppers are counter-rotating and generate new (sub)-pulses with a width of 0.2 ms thereby keeping a fixed resolution. The rest of the choppers prevent frame overlap and ensure that the full band is used. Phase delays of choppers are adjusted so that the chopper opening is centred in the guide when neutrons with the desired wavelength are passing.
-Detectors: Cylindrical with radius of 2 m and 2π coverage.

Base-line design at 16.6 Hz, 2.0 ms:
Two pulses from the pulse shaping choppers are selected; chopper frequencies and opening angles are adapted to this setting.
Flux at sample is $2.49 \cdot 10^8$ n/s/cm^2.

Effect of hot spot: with base-line settings and choppers selecting wavelengths around 2 Å.
A factor 2 hot spot with a diameter of 3 cm will give 48% gain.

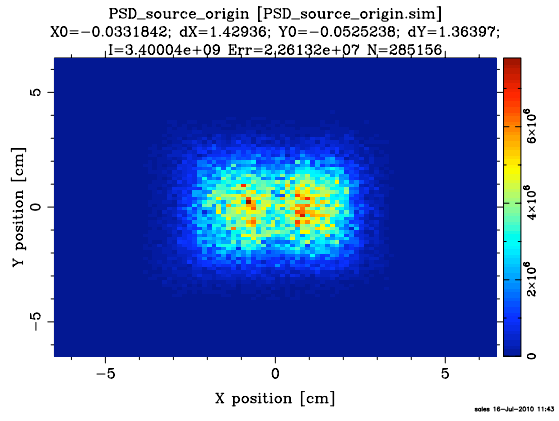

Design with other accelerator parameters: Between 2 and 7 pulses from the pulse generating choppers are used. Longer moderator period demands more generated pulses. Longer original pulse length yields fewer generated pulses.

-Wavelength band (Å):

T/τ (ms)	0.8	1.0	1.25	1.5	2.0
100 (10 Hz)	wait	3.8	3.8	3.8	3.8
80 (12.5 Hz)	wait	3.0	3.0	3.0	3.0
60 (16.67 Hz)	wait	2.3	2.3	2.3	2.3
50 (20 Hz)	wait	1.9	1.9	1.9	N/A
40 (25 Hz)	wait	1.5	1.5	N/A	N/A

-Number of sub-pulses used.

T/τ (ms)	0.8	1.0	1.25	1.5	2.0
100 (10 Hz)	wait	7	5	5	4
80 (12.5 Hz)	wait	5	4	4	3
60 (16.67 Hz)	wait	4	3	3	2
50 (20 Hz)	wait	4	3	3	N/A
40 (25 Hz)	wait	3	2	N/A	N/A

-Figures of merit:
Maximum divergence at sample is $\approx 0.5°$.

T/τ (ms)	0.8	1.0	1.25	1.5	2.0
100 (10 Hz)	wait	2.36	2.19	1.75	1.18
80 (12.5 Hz)	wait	2.36	1.88	1.45	0.922
60 (16.67 Hz)	wait	1.97	1.52	1.16	1.00
50 (20 Hz)	wait	1.41	1.26	0.938	N/A
40 (25 Hz)	wait	1.23	1.09	N/A	N/A

References:
[1] Journal of Neutron Research, Vol. 14, No. 2, June 2006, 177-191.
[2] The ESS Project (2002), Vol IV, Chap. 2, p. 21 - 25.

XESS - extreme environment single crystal diffractometer

Simulated by Peter Willendrup, Erik Knuden; consultants Kim Lefmann, Klaus Lieutenant, Arsen Goukassov.

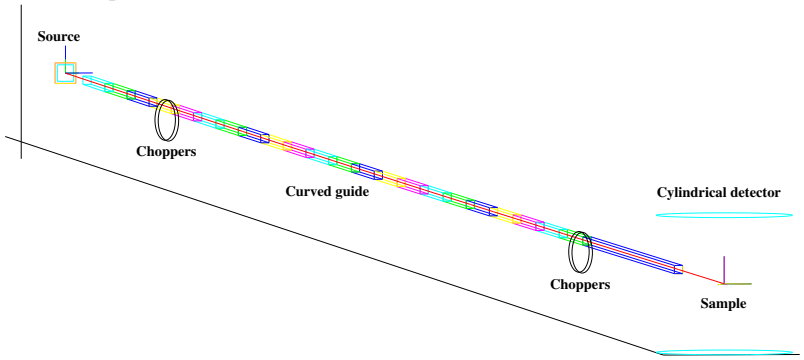

Medium resolution, high flux, single crystal ToF Laue diffractometer, for unit cell parameters in the range $(15)^3 - (25)^3$. Suitable for magnetic structures and phase transitions. Large detector coverage givs acces to large 3D volumes of reciprocal space in one measurement. Widely open sample area gives possibility of extreme environment.

General design:
-*Resolution:* Variable, see table.
-*Moderator:* Thermal (possibly bispectral)
-*Guide:* Curved with final straight section, 6x6 cm wide. Too short instrument for elliptic guide. Length never shorter than 31 m due to guide curvature.
-*Collimation:* 3 metres of distance collimation guide to samplepos.
-*Pulsing:* Use broad wavelength band.
-*Choppers:* 2 sets of bandwidth choppers, counterrotating
-*Sample:* 0.3×0.3 cm^2 , apx. $0.5° \times 0.5°$ div.
-*Detectors:* Cylindrical arrangement of anger cameras, each 25×25 cm^2, resolution 1×1 mm^2, radius $0.5m$, height $1m$
-*Other:* Pot. quasi-laue technique with chopper-slewing, narrowing wavelength band

Base-line design at 16.6 Hz, 2.0 ms:
-*Instrument length:* $L = 42$ m
-*Resolution:* $d\lambda/\lambda = 4.75$ at 4 Å%.
-*Bandwith:* $\lambda_{min} = 1.15$ Å and $\lambda_{max} = 6.85$ Å
-*Flux at sample:* 5.66×10^9 n/s/cm^2
-*Repetition rate:* None

Effect of hot spot:
Factor 2 hot spot, $d = 3$ cm: 15% flux gain.

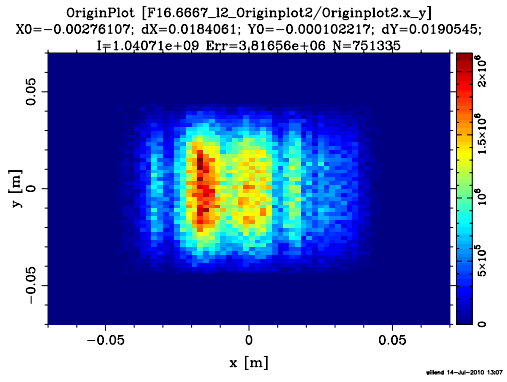

Design with other accelerator parameters: -*Instrument length* from moderator to sample, variable resolution:

τ (ms)	0.8	1.0	1.25	1.5	2.0
L (m)	wait	31	31	31	42
$\frac{\delta\lambda}{\lambda}$, 4Å, (%)	wait	3.17	3.96	4.75	4.75

-*Wavelength band (Å): (truncated towards $\lambda = 0$)*

T/τ (ms)	0.8	1.0	1.25	1.5	2.0
100 (10 Hz)	wait	10.3	10.3	10.3	8.74
80 (12.5 Hz)	wait	9.05	9.05	9.05	7.60
60 (16.67 Hz)	wait	7.60	7.60	7.60	5.70
50 (20 Hz)	wait	6.33	6.33	6.33	N/A
40 (25 Hz)	wait	5.1	5.1	N/A	N/A

-*Figure of merit:*

T/τ (ms)	0.8	1.0	1.25	1.5	2.0
100 (10 Hz)	wait	1.14	1.13	1.12	1.18
80 (12.5 Hz)	wait	1.13	1.10	1.15	1.17
60 (16.67 Hz)	wait	1.13	1.13	1.14	1.00
50 (20 Hz)	wait	1.13	1.12	1.10	N/A
40 (25 Hz)	wait	0.784	0.782	N/A	N/A

References:

-*Schober et. al. Nuclear Instruments and Methods in Physics Research A 589 (2008) 34-46*
-*Lefmann et. al. Tailored Instrumentation to Long Pulse Neutron Spallation Sources, II, to appear*
-*A. Goukassov, private communicaton*

Abstract

The effect of uncertainty in chopper phasing (jitter) has been investigated for the high-resolution time-of-flight spectrometer LET at the ISIS second target station. The investigation is carried out using virtual experiments, with the neutron simulation package McStas, where the chopper jitter is found to cause a Lorentzian tail in the resolution function. We find that jitter up to the unrealistic value of 2 μs can be tolerated without any noticeable degradation of resolution or incident intensity. The results are supported by simple analytical estimates and are believed to be general for chopper spectrometers.

Simulations of Chopper Jitter at the LET Neutron Spectrometer at the ISIS TS2

December 6, 2011

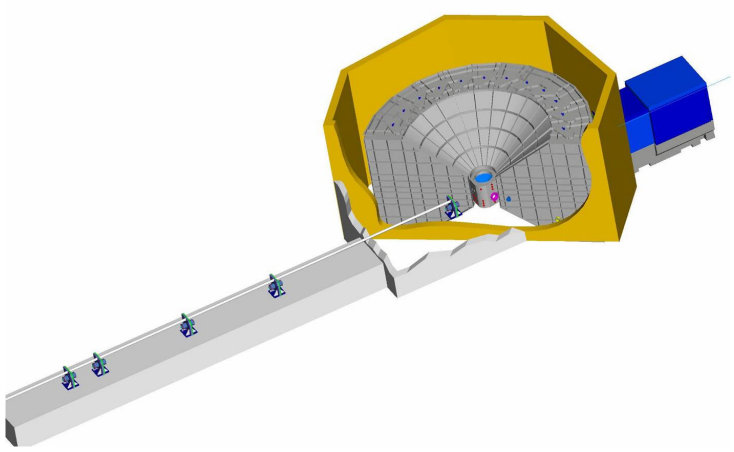

Figure 1: The LET spectrometer showing the large detector bank and multiple high speed disk choppers.

1 Introduction

More and more low energy, high resolution chopper spectrometers around the world are being commissioned, such as CNCS at the SNS [5], IN5 at the ILL [10], NEAT at the HZB [6], AMATERAS at J-PARC [7], and LET at ISIS [1].

The LET (Low Energy Transfer) instrument at TS2 is a cold neutron, multi-chopper, versatile direct geometry spectrometer, operating over a wide 0 - 80 meV energy range with an energy resolution ranging from 5 μeV at an incident energy of 1 meV, to 200 μeV at 20 meV. It will have a large solid angle detector populated with MAPS type position sensitive detectors (PSD) that will make it possible to map a vast swathe of (q, $\hbar\omega$) space in a single measurement [1].

This article explores the effects of imperfections in high speed disk choppers on the operation of high resolution chopper spectrometers, using the LET instrument as an example, and simulated using the McStas neutron simulation package [9]. The results are potentially relevant for many current high-speed chopper spectrometers, and the ones in preparation for the ESS [11].

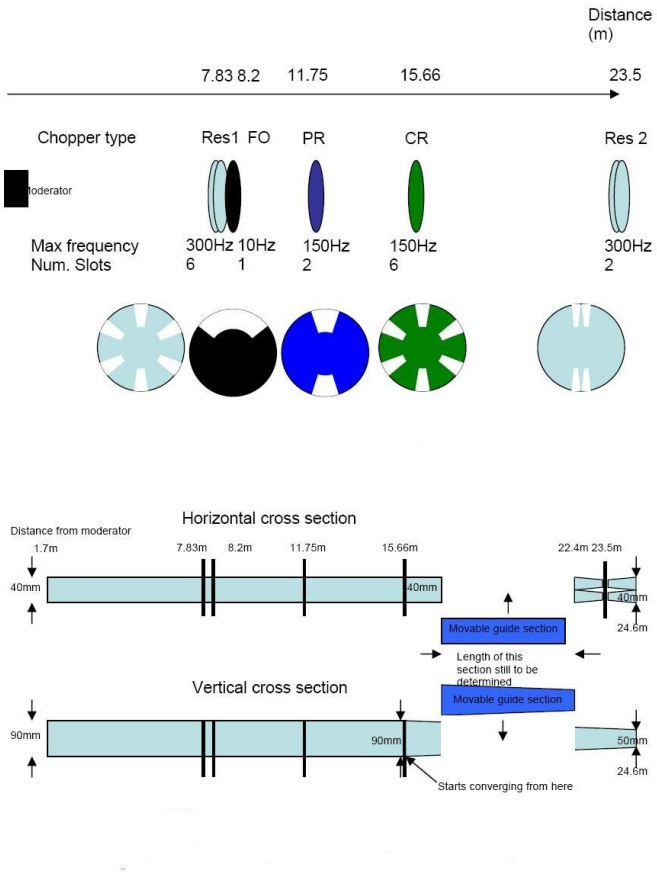

Figure 2: LET chopper and guide layout. Top panel shows the chopper distances and chopper geometry. Bottom panel shows the layout of the guide, with the chopper positions outlined. [4]

Figure 3: A picture of the actual Res 2 chopper, where the double slits are clearly visible.

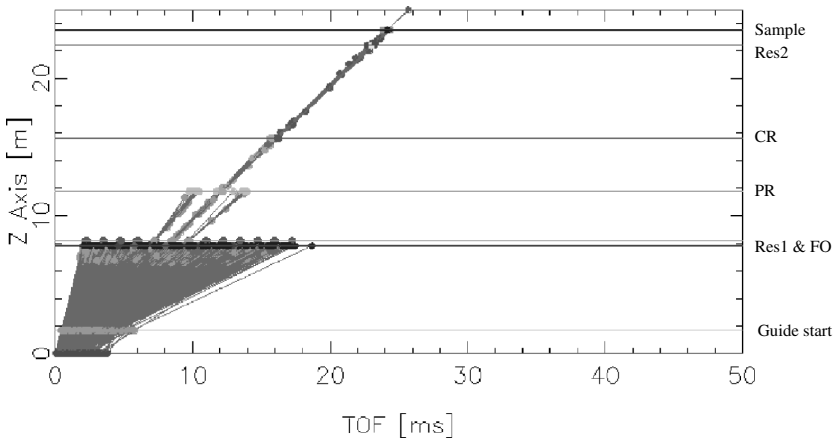

Figure 4: Flight distance vs time in ray tracing, showing the "white" beam from the moderator in the energy range 4.9-5.1 meV, being separated into a few distinct wavelengths by the first resolution choppers (Res1) at 7.83 m, with the desired wavelength singled out by the pulse removal (PR) chopper at 11.75 m

2 The LET Instrument

The primary part of the LET instrument, illustrated in fig. 2, selects neutrons of the desired energy using the Time of Flight (ToF) method.

The resolution choppers, Res1 and Res2, positioned at 7.83 m and 23.5 m, respectively, defines the energy profile. Because of the short opening times (5 μs at 300 Hz for Res2), they are the ones most susceptible to jitter, and are thus the choppers of interest for this article.
3 other beam choppers are present:

- The slow Frame Overlap (FO) chopper removes long wavelength neutrons from the previous moderator pulse.
- The Pulse Removal (PR) chopper selectively removes pulses, to increase pulse separation, by running at an integer factor slower than the resolution choppers. This is illustrated in fig. 4, where the PR is run at half the speed of the resolution choppers, to remove every second pulse.
- The contaminant removal chopper (CR) removes fast neutrons coming from the tail of the pulse. [2]

Illustrated by simulation results in figure 4, the white beam from the short pulsed (4 μs) moderator is separated into a few distinct wavelengths by the first set of fast resolution choppers (Res1). The desired wavelength is singled out by the slow pulse removal (PR) chopper, as can be seen in the energy distribution in fig. 5.

Note also the double funnel system at the Res2 choppers, seen in fig. 2, designed to further increase the resolution of the instrument, by allowing more narrow chopper windows without sacrificing neutron flux. [3]

3 Chopper Jitter

Physical beam choppers are never perfectly at the desired phase, but rather deviate by a random error at any given time. Whereas most neutron simulations are performed with mathematically perfect beam choppers, here a random phase error (jitter) is added to give more physically realistic choppers. For the purposes of this article we choose the jitter to be Gaussian.The

size of the jitter is then defined as the width of the Gaussian error, which is used as the jitter parameter.

For every event where a neutron ray reaches a chopper, the phase θ is calculated thus:

$$\theta = \theta_0 + j \cdot rand\_norm \cdot \omega \tag{1}$$

Where θ_0 is the chopper position without jitter, j is the jitter parameter for the chopper with units of time, $rand\_norm$ is a normalized Gaussian random number (with $\sigma^2 = 1$) and ω is the angular velocity of the chopper.

To illustrate the effect of chopper jitter, we consider the basic equation for flight time:

$$t = \alpha \cdot \lambda \cdot L \tag{2}$$

where λ is the neutron wavelength, L is the flight length, and the constant α is $\alpha = m_n/h \approx 252$ μs/m/Å.
Hence, if the jitter is the only source of uncertainty, the uncertainty in the wavelength is:

$$d\lambda = \frac{dt}{\alpha L} \tag{3}$$

So for a realistic jitter value, (dt), of 0.4 μs in the second resolution choppers, located at 15.7 m from Res1, this contributes to the uncertainty in the wavelength (dλ) of $1 \cdot 10^{-4}$Å, and thus a dE of 0.2 μeV for 5 meV neutrons. In comparison, the resolution is at about 20 μeV at 250 Hz. For a jitter value of 10 μs, this gives a dE of 6 mueV.

Since the energy of neutrons arriving in the physical detector bank is calculated by the ToF-method, a small discrepancy in the arrival time at the sample, can, over the 3.5 m from the sample to detector, translate into a much larger difference in the neutron energy perceived by the detector. Considering again the jitter $dt = 0.4$ μs in the 2nd resolution choppers, this corresponds to an uncertainty in the perceived wavelength (dλ) of $5 \cdot 10^{-4}$ Å, and thus a dE of 1 μeV for 5 meV neutrons. For a jitter value of 10 μs, this gives a dE of 25 mueV.

Some neutron instruments compensates for jitter with a 'veto' system, where an event is discarded if an unacceptable discrepancy of the chopper phase is detected. The veto scheme is not included in the present simulations.

4 Simulation results

The instrument was built in the McStas neutron simulation package [9], by adding the physical components (moderator, guide sections, beam choppers) sequentially, with monitors interspersed at suitable locations. Note that the monitors used in the simulations does not emulate physical detectors, in as much as they do not alter or absorb the detected neutron rays.
The simulations used to generate the figures in this paper were typically run with $5 \cdot 10^8$ rays, which corresponds to approximately 20 min. CPU-time on an ordinary dual-core laptop.
Fig. 5 shows the energy distribution of the beam at various positions in the instrument, with perfect beam choppers. Notice the multiple peaks after the first resolution choppers, reduced to the single 5 meV peak by the PR chopper, as would be expected in the physical instrument.

To illustrate the performance of the spectrometer, we have performed virtual experiments using an incoherent elastic scatterer [8]. Typical outcomes of these experiments are shown in fig. 6, while the deduced line width is shown in fig. 9.

With highly imperfect beam choppers (large jitter), the detected energy distribution can be seen to noticeably widen. This is illustrated in fig. 6, and clear effects are visible for jitter values of 10 μs. The line shape is almost perfectly Gaussian at zero jitter, then becomes increasingly Lorentzian with added jitter.

As expected from the ToF equation (2), the effect of the jitter depends significantly on the speed of the choppers, as can be seen in fig. 7, where the intensity drops off much more rapidly for increasing jitter, with the chopper set to the higher speed, as can be seen in fig. 7.

Simple analytical calculations of the time resolution at the detector position supports the simulated resolution increase with jitter, shown in figs. 6 and 9. We use the ToF equation to calculate the allowed arrival times of neutrons at the detector, for different values of jitter.

4.1 Side peaks in simulations

When building non-standard components, care and attention is needed to avoid simulation artifacts. As the chopper slits of the Res2 double choppers in the simulations are triangular, and the guide openings of the double funnel

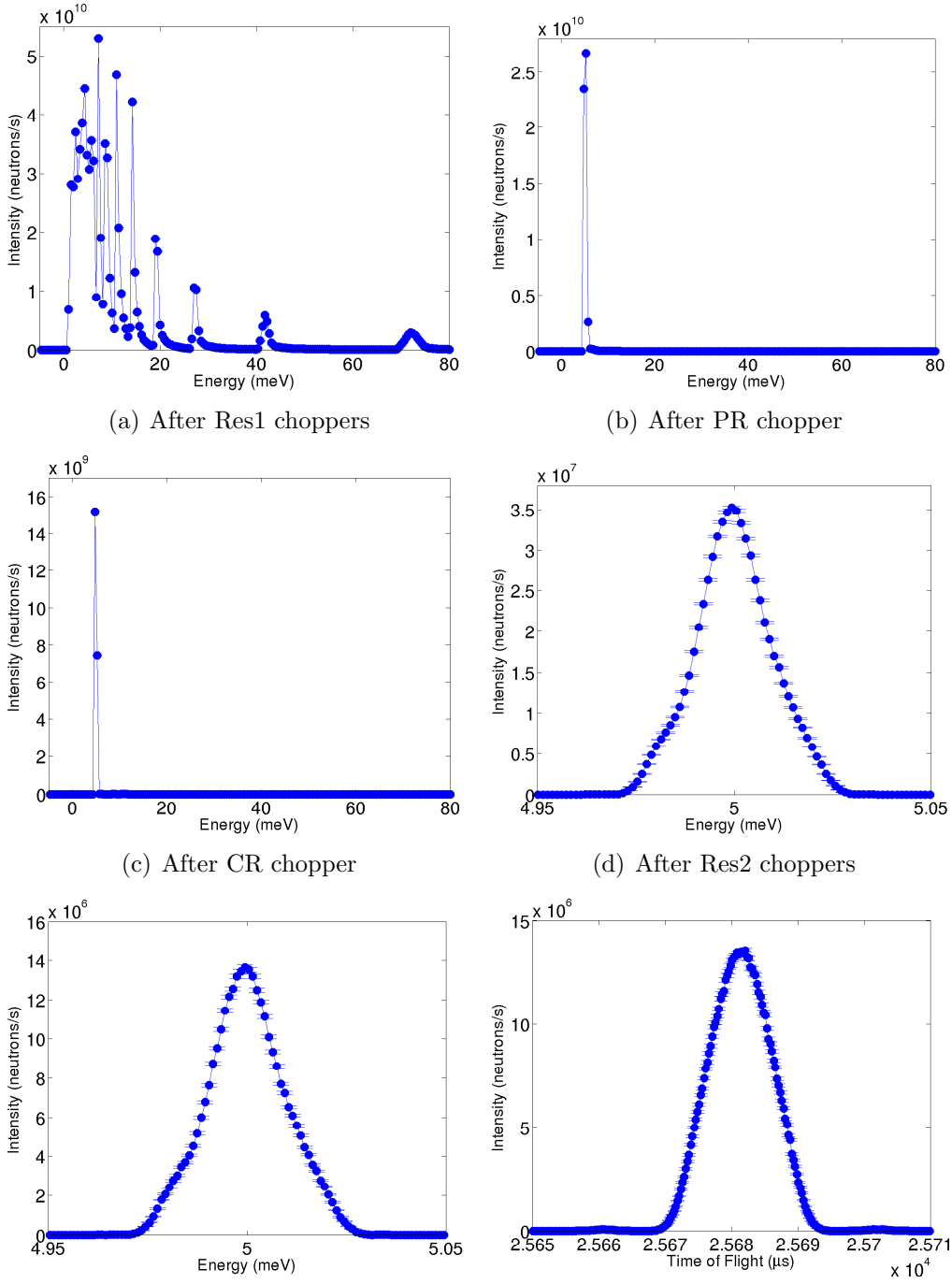

(a) After Res1 choppers

(b) After PR chopper

(c) After CR chopper

(d) After Res2 choppers

(e) Sample position

(f) TOF at sample position

Figure 5: a-e: Energy distribution of the beam at the chopper and sample positions, at nominal energy E = 5 meV. f: Time of flight (TOF) distribution at sample position. The slight tail seen on the left side of panels d,e can be traced back to the long time-tail of the source pulse. Note also the very small side peaks at 2.566 and 2.570 in panel f, explained in section

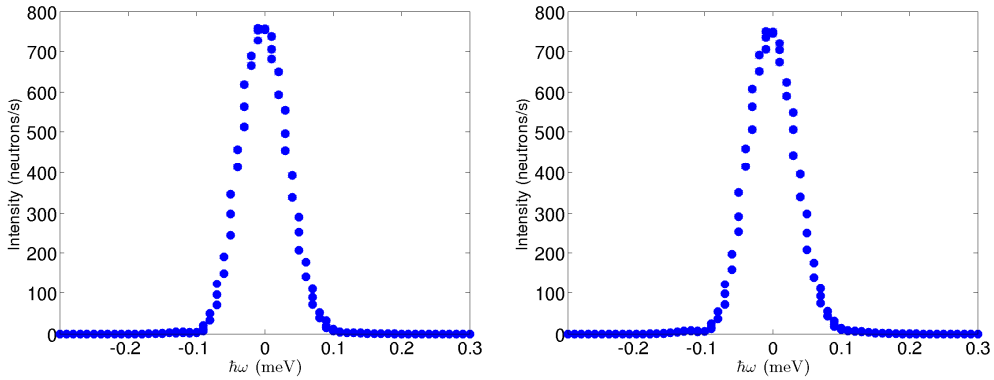

(a) Zero jitter

(b) 2 μs jitter

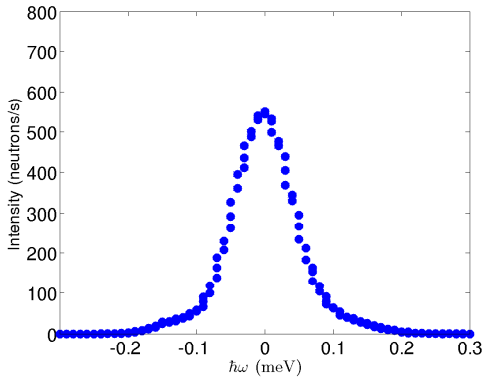

(c) 10 μs jitter

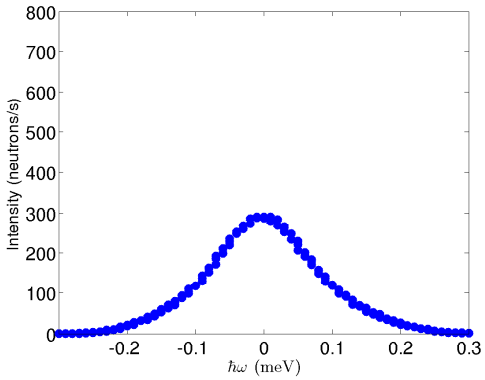

(d) 20 μs jitter

Figure 6: A virtual experiment: Detector output when scattering off a vanadium sample of radius 1 cm, with both beam choppers running at 140 Hz, and with 4 different jitter settings.

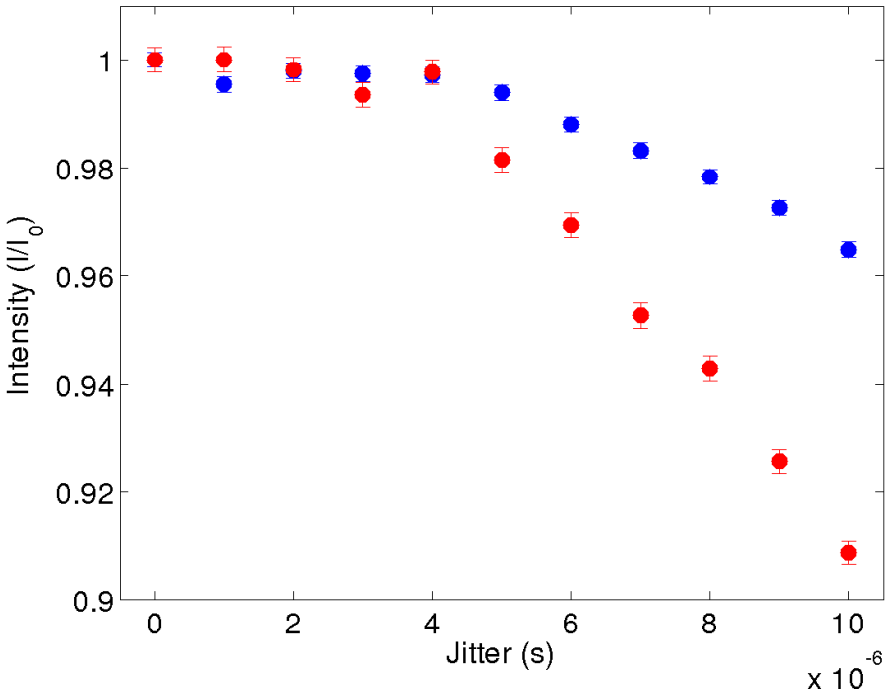

(a)

Figure 7: Intensity vs. jitter at the detector position, for two different chopper speed settings, from 0 to 10 μs jitter. At 140 Hz a drop of approximately 4 % can be seen, vs. 10 % at 250 Hz. Blue is 140 Hz, red is 250 Hz.

system are rectangular, trying to fit them onto the rectangular guide opening of the double funnel system, resulted in the side peaks shown in the (x, t) diagram in fig. 8. What happens is that a short time before and after the double chopper turns to the open alignment, small slices of the 10 mm wide guide openings are not covered by the absorbing section between the dual chopper slits (see fig. 2), which is 11 mm at its widest.
In the actual instrument, the chopper slits have been shaped so as to avoid this effect. See fig. 3

5 Discussion and Conclusion

We have conducted a detailed simulation of the LET spectrometer. We find that the instrument performs in general as expected.
As can be seen in fig. 9, jitter values at or below 2 μs have less than 1 % effect on the instrument resolution, judged from virtual experiments of elastic scattering, with the chopper speed set at 250 Hz. In comparison, the jitter when running the actual LET resolution choppers at the same speed, is at 0.4 μs. The simulated degradation of resolution at this jitter is well below the statistical uncertainty (0.04 %) of the simulation results.

The analytical calculations detailed in section 3 agree surprisingly well with the above simulation results, as they both indicate a resolution degradation of about 25 μeV when going from 0-10 μs jitter. This agreement is far from trivial, as the combined effect of jitter in all the choppers is quite complicated, whereas the analytical calculations use a rather naive model.

In conclusion, our simulations show that jitter will have negligible effect on the performance of the actual LET instrument. In cases where a Lorentzian tail in the resolution function is particularly detrimental, a more careful analysis is needed. Simulation of jitter effects on future designs of high resolution instruments could lead to a more detailed understanding of demands for chopper precision. In particular, it can be investigated whether precision can be sacrificed to reduce costs without degrading the resolution.

Acknowledgements

Thanks to Rod Steward for discussions and advice.

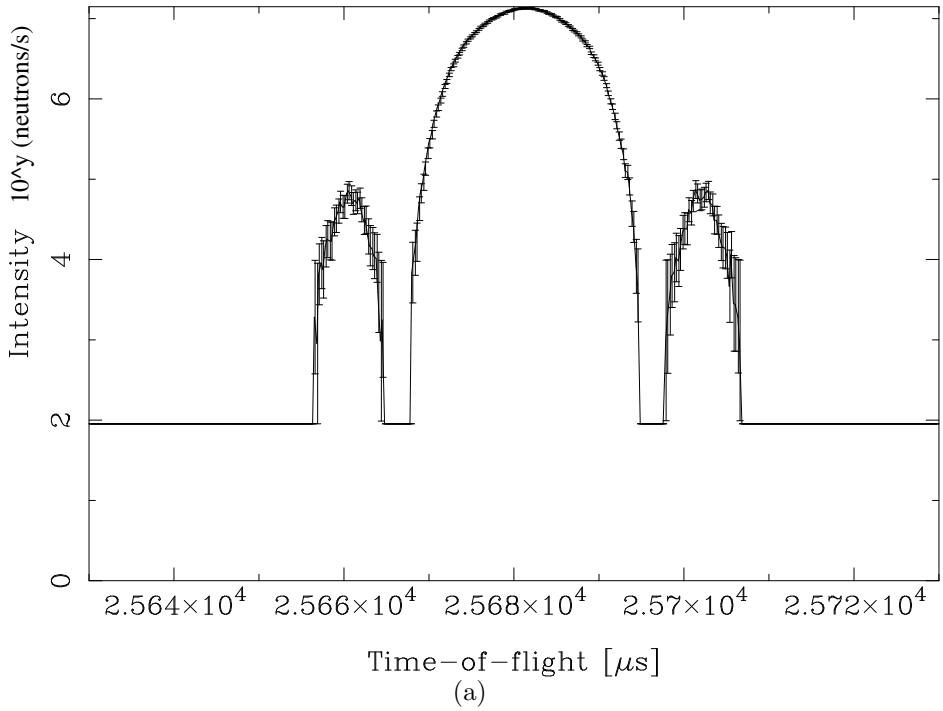

(a)

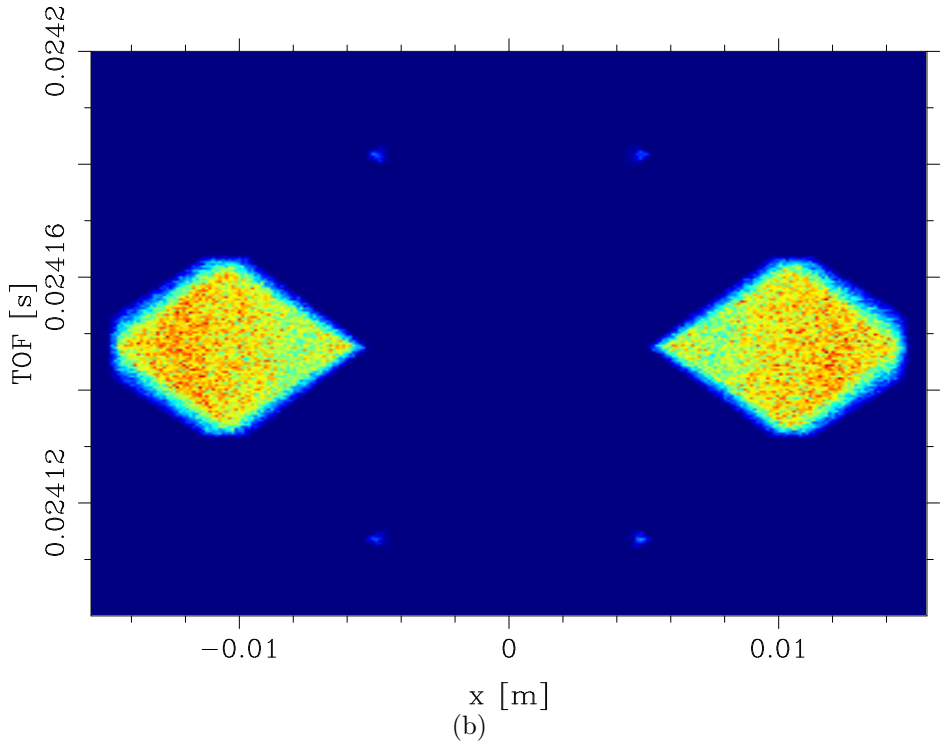

(b)

Figure 8: A simulation artifact: side peaks created by trying to fit the rectangular guide openings of the double funnel system, with the triangular chopper slits of the Res2 double choppers. Top panel: Logarithmic ToF at the sample position. Bottom panel: Horizontal position vs. time at the 2. resolution choppers, centered in time when the main peak in graph a hits.

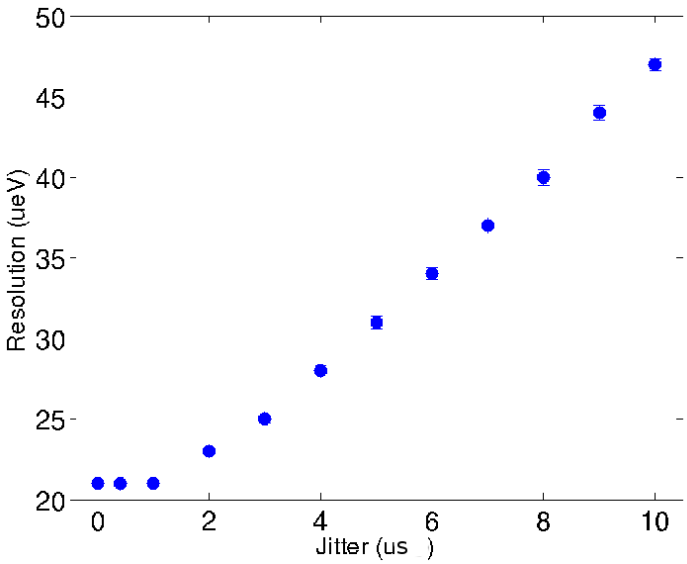

(a)

Figure 9: Resolution of the instrument detector, as a function of jitter, with resolution choppers running at 250 Hz. Line width is found by the standard deviation of the data, and not by actual curve fitting. Note that most errorbars are eclipsed by the dots.

References

[1] R.I. Bewley, J.W. Taylor, and S.M. Bennington. Let, a cold neutron multi-disk chopper spectrometer at isis. *Nuclear Instruments and Methods in Physics Research Section A: Accelerators, Spectrometers, Detectors and Associated Equipment*, 637(1):128 – 134, 2011.

[2] Robert Bewley. Multi-rep rate on let. Technical Report 3, ISIS, September 2005.

[3] Robert Bewley. Simulations of the double funnel construction for let. Technical report, ISIS, 2005.

[4] Robert Bewley. Let specification. Technical report, ISIS, January 2006.

[5] G. Ehlers, A. A. Podlesnyak, J. L. Niedziela, E. B. Iverson, and P. E. Sokol. The new cold neutron chopper spectrometer at the spallation neutron source: Design and performance. 82(8):085108, 2011.

[6] Zunbeltz Izaola and Margarita Russina. Virtual design of the neutron guide for the tof spectrometer neat. *Journal of Physics: Conference Series*, 251(1):012064, 2010.

[7] Takashi Kamiyama and Kentaro Suzuya. Neutron instruments at j-parc: Toward the state-of-the-art facility. *Neutron News*, 22(1):20–25, 2011.

[8] K. Lefmann, P. K. Willendrup, L. Udby, B. Lebech, K. Mortensen, J. O. Birk, K. Klenø, E. Knudsen, P. Christiansen, J. Saroun, J. Kulda, U. Filges, M. Konnecke, P. Tregenna-Piggott, J. Peters, K. Lieutenant, G. Zsigmond, P. Bentley, and E. Farhi. Virtual experiments: the ultimate aim of neutron ray-tracing simulations. *Journal of Neutron Research*, 16(3-4):97–111, 2008.

[9] Kim Lefmann and K Nielsen. Mcstas, a general software package for neutron ray-tracing simulations. *Neutron News*, 10/3:20–23, 1999.

[10] J Ollivier, M Plazanet, H Schober, and J.C Cook. First results with the upgraded in5 disk chopper cold time-of-flight spectrometer. *Physica B: Condensed Matter*, 350(1-3):173 – 177, 2004. ¡ce:title¿Proceedings of the Third European Conference on Neutron Scattering¡/ce:title¿.

[11] H. Schober, E. Farhi, F. Mezei, P. Allenspach, K. Andersen, P.M. Bentley, P. Christiansen, B. Cubitt, R.K. Heenan, J. Kulda, P. Langan, K. Lefmann, K. Lieutenant, M. Monkenbusch, P. Willendrup, J. aroun, P. Tindemans, and G. Zsigmond. Tailored instrumentation for long-pulse neutron spallation sources. *Nuclear Instruments and Methods in Physics Research Section A: Accelerators, Spectrometers, Detectors and Associated Equipment*, 589(1):34 – 46, 2008.

Nuclear Instruments and Methods in Physics Research A 634 (2011) S1–S6

Contents lists available at ScienceDirect

Nuclear Instruments and Methods in Physics Research A

journal homepage: www.elsevier.com/locate/nima

Optimal shape of a cold-neutron triple-axis spectrometer

K. Lefmann [a,b,*], U. Filges [c], F. Treue [a], J.J.K. Kirkensgård [d,e], B. Plesner [d], K.S. Hansen [d,f], K.H. Klenø [a,b]

[a] Nanoscience and eScience Centers, Niels Bohr Institute, University of Copenhagen, Universitetsparken 5, 2100 Copenhagen Ø, Denmark
[b] European Spallation Source, University of Lund, St. Algatan 4, Lund, Sweden
[c] Laboratory for Development and Methods, Paul Scherrer Institute, 5232 Villigen PSI, Switzerland
[d] Institute of Nature and Models, Roskilde University, Denmark
[e] Department of Basic Sciences and Environment, Faculty of Life Sciences, University of Copenhagen, Denmark
[f] Mid-Greenland High School, Nuuk, Greenland

ARTICLE INFO

Available online 1 July 2010

Keywords:
Neutron instrumentation
Triple-axis spectrometer
Ray-tracing simulation

ABSTRACT

We have performed a McStas optimization of the primary spectrometer for a generic 40 m long, cold-neutron triple-axis spectrometer with a doubly focusing monochromator. The optimal design contains an elliptically focusing guide, a virtual source point before a low-grade PG monochromator, and non-equidistant focusing at the monochromator. The flux at 5 meV shows a gain factor 12 over the "classical" design with a straight $12 \times 3\,\mathrm{cm}^2$, $m=2$ guide and a vertically focusing PG monochromator. In addition, the energy resolution was found to be improved. This unexpectedly large design improvement agrees with the Liouville theorem and can be understood as the product of many smaller gain factors, combined with a more optimal utilization of the beam divergence within the guide. Our results may be relevant for a possible upgrade of a number of cold-neutron triple-axis spectrometers—and for a possible triple-axis spectrometer at the European Spallation Source.

1. Introduction

The triple-axis spectrometer (TAS) is one of the oldest and most well-known types of neutron instrumentation; designed by the Nobel Laureate B.N. Brockhouse already in the 1950s [1]. Later ingenious instrument development has improved on the original design, most importantly the cold neutron moderator [2], and the neutron guide, which allows the transport of cold neutrons ($\lambda > 2$ Å) far away from the background-rich region around the neutron source [3]. An excellent recent textbook has been devoted to the description and use of the TAS [4]. However, there may still be some room for design improvements, which is the topic we investigate in this article.

Many cold-neutron TAS exist at continuous neutron sources around the world. Most of these instruments have adopted the 1990s design, where the neutrons are transported by a 30–50 m curved supermirror guide, and reflected down to the sample by a vertically focusing monochromator made by mosaic pyrolytic graphite (PG). Some examples of TAS of this design are IN-12 and IN-14 at ILL [5], TASP and RITA-2 at PSI [6], FLEX at HZB [7], and SPINS at NIST [8]. New developments in guide technology and the appearance of doubly focusing monochromators, implemented *e.g.* at PANDA (FRM-2) [9] and MACS (NIST) [10] have spawned ideas of upgrade of a number of cold-neutron TAS, *e.g.* at ILL, PSI, and HZB.

In this article, we will address the question of how to improve the configuration of the primary spectrometer of the cold-neutron TAS. We have simulated different instrument designs by use of the Monte Carlo ray-tracing package McStas [11]. We start by investigating the characteristics of the classical TAS design and then perform a number of controlled design changes. The optimal design is then found by a "free" computer optimization of all parameters, which is again restricted to find a realizable design. Finally, we explain the found results in terms of phase space densities and the Liouville theorem and discuss the optimal design of the complete cold neutron triple-axis spectrometer.

2. Design and simulation

The baseline design for these simulations is defined in terms of moderator, guide, and monochromator and can be seen as an idealization of the RITA-2 spectrometer at PSI. The moderator has a uniform neutron distribution over its $15 \times 10\,\mathrm{cm}^2$ area and follows a typical cold spectrum with an intensity corresponding to a medium flux source. We have chosen the parameters valid at 2002 for SINQ running at 1 mA current, as already used in Ref. [12]. The guide is 40 m long with $m=2$ supermirrors and a reflectivity of 90.5% at $q=mQ_c$ ($\alpha=4.38$ in McStas units) and has

* Corresponding author at: Nanoscience and eScience Centers, Niels Bohr Institute, University of Copenhagen, Universitetsparken 5, 2100 Copenhagen Ø, Denmark. Tel.: +45 35320476.
E-mail address: lefmann@fys.ku.dk (K. Lefmann).

0168-9002/$ - see front matter © 2010 Elsevier B.V. All rights reserved.
doi:10.1016/j.nima.2010.06.273

a cross-section of $30 \times 120\,\mathrm{mm}^2$. The guide starts 1.5 m from the moderator with a 5 m straight section, followed by a 20 m curved section with a curvature of $R=2$ km, and finally a 15 m straight section. The monochromator is placed 0.5 m after the guide opening and is made from PG with 30′ mosaicity and a reflectivity of 80%. The monochromator has five vertically focusing blades, each 30 mm tall and 200 mm wide, with a 1 mm gap between blades. The sample is positioned 1.5 m from the monochromator, the smallest distance achievable in practice due to shielding and sample environment requirements.

All simulations were performed with 5×10^7 neutron rays (2×10^7 when only flux numbers were required), corresponding to 5 min (2 min) processing time on a standard 2 GHz laptop for the straight guide. In most simulations, the monochromator was set to reflect neutrons of 5.0 meV ($\lambda = 4.045$ Å). We recorded neutrons reaching the sample area, which is $1 \times 1\,\mathrm{cm}^2$. The absolute flux value was for the baseline design found to $\Psi = 4.03(2) \times 10^6\,\mathrm{n/s/cm}^2$, with a spread (FWHM) of the incoming neutron energy of $\Delta E_\mathrm{i} = 127\,\mu\mathrm{eV}$. These baseline results were used as the starting point for the optimization procedure, see Table 1.

Simulation of a very similar primary spectrometer has been performed for the RITA-2 spectrometer at PSI, and the results for both flux and (in particular) energy resolution of vanadium scans were found to agree well with the performance of the real spectrometer over a wide wavelength range [12,13]. This serves as a validation of the results of the present simulations, both in terms of absolute flux value and (in particular) on relative flux improvements and energy resolution. The energy spread of the incoming neutrons should be viewed in relation to the acceptance of the secondary spectrometer. For example, at RITA-2 this value is 141 μeV without collimation. The energy resolution of the complete spectrometer is found (for incoherent scattering) by adding the two contributions in quadrature.

2.1. Controlled design upgrades

Our initial simulations contained a series of individual optimizations to the design. The optimizations were performed in the order given below, and were mostly performed by optimizing the sample flux while varying a single parameter at a time. The gains mentioned should be understood as *additional* gain compared to last design change. The corresponding results are listed in Table 1.

- Improving the supermirror coating. This resulted in a surprisingly small flux increase (5%), reached at $m=4$.
- Increasing the guide width. This gave a large flux gain of almost 60% for $w=5$ cm, but a broadening in energy of around 40%.
- Increasing the guide height and inserting additional blades in the monochromator. This gave a further flux increase of 25% for $h=16$ cm.
- Increasing the PG mosaicity. A flux gain of almost 50% was found for $\eta = 70'$, surprisingly without change in ΔE
- Doubly focusing monochromator, composed of $25 \times 25\,\mathrm{mm}^2$ tiles. This resulted in an additional flux gain of 10% and an improvement of energy spread to almost the baseline design.
- Increasing the guide-monochromator distance to 2.4 m and the PG mosaicity to 45′. This gain was small, around 15%, and there was a small increase of energy spread.

Increasing the monochromator-sample distance to 2.1 m to almost obtain equidistant (Rowland) focusing decreased the energy spread by 30%, but simultaneously lowered the flux by 40%. Hence, this idea was abandoned.

At the end of this simulation round, we received a flux gain of a factor 3.9 and an enlarged spread of the incoming energy of only 35%. This agrees rather well with earlier optimization studies for RITA-2 [14].

Table 1
Results of the optimizations: flux (Ψ) and energy spread (ΔE_i) at the sample position.

Change	Ψ (10^6 n/s/cm^2)	ΔE_i (μeV)
Baseline	4.03(2)	127
Guide coating $m=4$	4.26(3)	130
Guide width 5 cm	6.62(5)	195
Guide height 16 cm	8.38(7)	195
Mosaicity 70′	12.24(8)	183
Doubly focusing mono.	13.52(8)	153
Fine-tuning mono.	15.82(6)	172
Elliptical guide, focus on mono.	26.7(4)	165
Virtual source, fine-tuning	35.7(3)	237
Free optimization	79.6(4)	137
Restrained, free optimization	44.9(2)	85

The individual steps are described closer in the text.

2.2. Optimization with an elliptical guide

The simulations in the previous section were performed with a conventional guide system with a constant cross-section. Recent developments in guide technology has enabled the construction of fully elliptical guides with strongly improved focusing possibilities [15]. Thus, it was natural to include elliptical guides in our design.

For truly elliptical guides, there is the complication that line-of-sight between moderator and monochromator will increase the fast-neutron background. At present a number of suggestion to circumvent this problem exist, none of which will cause substantial flux loss, including a bending of the elliptical guide, placing a beam stop within the guide, and accepting the (limited) additional background from the fast neutrons [16–18]. It is, however, at present not clear which of these solutions will prove most efficient in practice. Therefore, we here continue the optimization using only neutron flux and energy spread as optimization parameters, ignoring the line-of-sight complication.

We have continued the optimization, replacing the curved guide with an elliptical guide of the same dimensions. As a reassurance, we first reproduced the results below for a guide of infinite focal length. Next, we used focal lengths of 2.0 m—meaning that both the focal points were placed 2.0 m outside the guide. This provided a significant flux gain (65%) over the straight guide. Then, we created a virtual source by using 1.4 m focal length and placing the monochromator at 2.9 m to obtain Rowland focusing. This was accompanied by fine tuning of the monochromator parameters, and additional height to the monochromator. This scheme gave a flux gain of additional 35%, but again an increase in the energy spread. In total, this design gives us a 9-fold increase in flux at the cost of a factor 2 increase in energy spread.

2.3. Total computer optimization

Having obtained the encouraging results by the manual single-parameter optimizations, we went to explore unknown territory by performing a total computer optimization of most parameters describing the guide-monochromator system. The total number of parameters was 14, small enough to be achievable by the Simplex algorithm already implemented in McStas.

To avoid the degradation of the energy spread, seen is the hand-optimizations above, we entered the energy spread into a Figure-of-Merit given by

$$\mathrm{FoM} = \Psi^2/\Delta E_{\mathrm{i}}. \quad (1)$$

This was implemented into McStas by writing a Figure-of-Merit monitor component, and using its output as the parameter to be maximized by the Simplex algorithm.

The results of the free computer optimization are presented in Table 1. It can be seen that these optimizations gave an additional flux gain of more than a factor 2, resulting in a total gain factor of 20; with almost the same energy spread as the baseline instrument. However, by inspecting the solution this was found to feature a very large guide ($180 \times 120\,\mathrm{mm}^2$ at both start and exit) and a 400 mm tall monochromator, 4.7 m from the guide exit. This was deemed unreasonable, since the fast-neutron background would be much too high and the vertical divergence would exceed 7°.

In the second attempt, we restricted the guide size indirectly by placing a slit, limiting the virtual source point to $80 \times 50\,\mathrm{cm}^2$, while limiting the monochromator height to 300 mm. From this arrangement, the optimal figuration was found to have a sample flux 25% better than the manually optimized solution, while the energy spread was surprisingly 35% lower than that of the baseline design.

Studying the optimal parameters, we can see that the final instrument has a number of interesting features. Foremost, the distance between guide opening and the 60′ PG monochromator is increased to 4.05 m, while the virtual source point is placed already after 0.60 m. The corresponding beam profiles are shown in Figs. 1 and 2. Since the monochromator-sample distance is still fixed to 1.5 m, the monochromator focusing does not fulfill the Rowland condition. Hence, to optimize the energy resolution, the monochromator support was turned 17° away from the half scattering angle, while keeping the blades in the correct scattering angle. This scheme is known *e.g.* from the non-equidistant monochromatic focusing analyzer mode at RITA-2 [19,20].

3. Phase space considerations

The large gain in both neutrons flux and energy resolution found by the computerized optimizations calls for a closer investigation of the final design. Our guideline to obtain insight

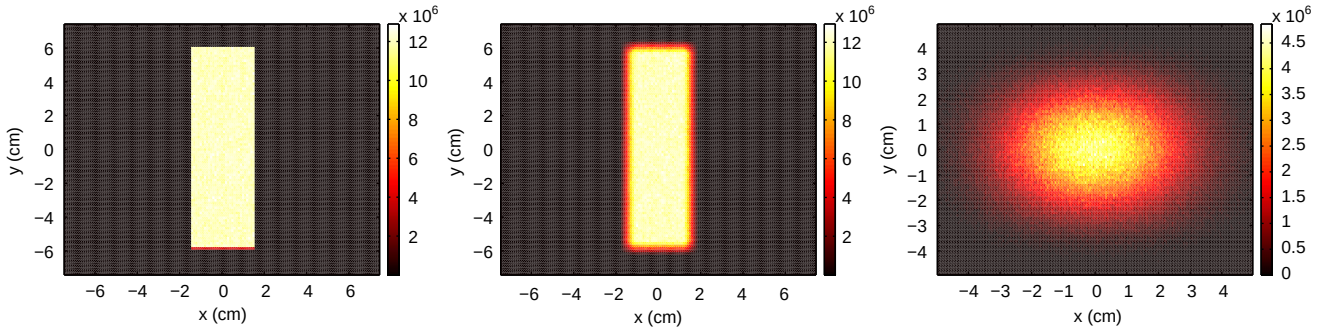

Fig. 1. Simulated beam cross-sections for 5 meV neutrons at different positions in the baseline instrument, given in flux units: n/(s cm^2). (a) At the exit of the straight/curved guide; (b) 0.20 m before the monochromator; (c) at the sample position.

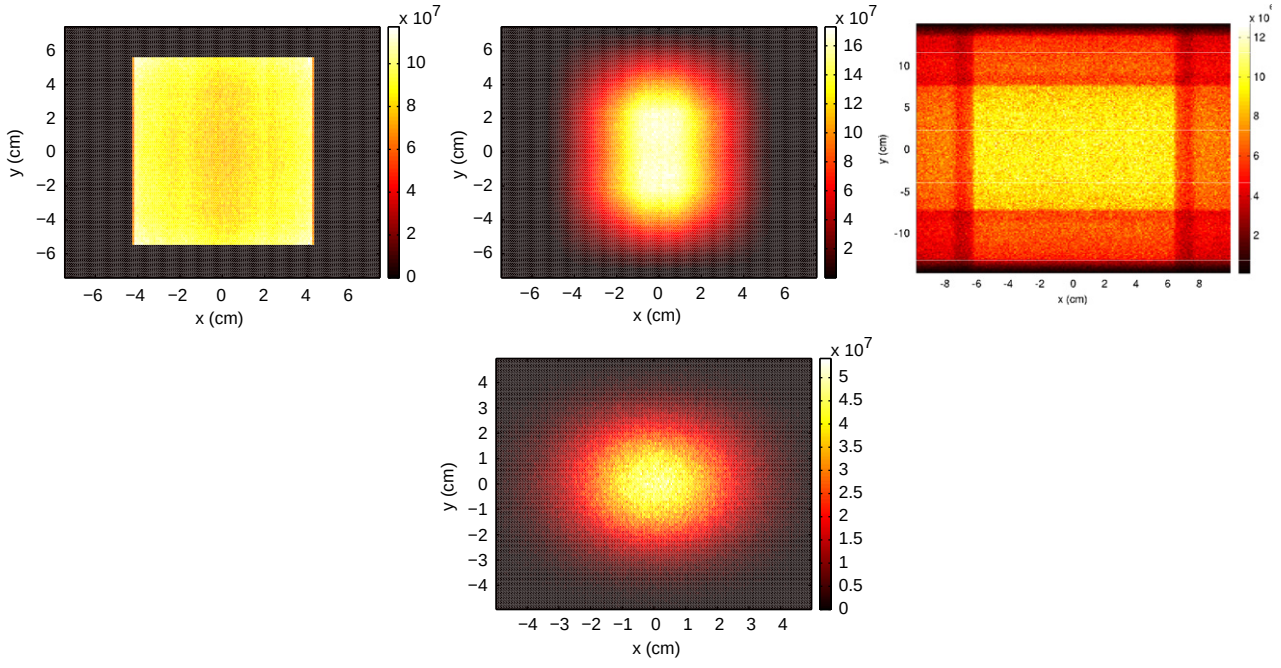

Fig. 2. Simulated beam cross-sections for 5 meV neutrons at different positions in the final instrument, given in flux units: n/(s cm^2). (a) At the exit of the elliptical guide; (b) at the virtual source point 0.60 m after the guide end; (c) 0.20 m before the monochromator; (d) at the sample position.

Table 2
Brilliance simulated at different positions along the spectrometer, given in 10^6 brilliance units, as found by integrating over flux in a 1% wavelength band within ± 30 arc minutes divergence angle.

Position	Baseline design	Elliptical, manual	Elliptical, optimized
Moderator	1.43(1)	1.50(1)	1.53(2)
Guide entry	1.50(1)	1.50(1)	1.54(2)
Guide exit	1.42(1)	1.34(1)	1.31(2)
Before mono.	1.41(1)	1.33(1)	1.23(2)
After mono.	0.54(1)	0.63(1)	0.79(1)
At sample	0.51(1)	0.69(1)	0.79(1)

Results are given for the baseline design TAS, for the manually optimized spectrometer with an elliptical guide, and finally for the fully (computer) optimized solution.

in the functioning of the guide-monochromator system is the Liouville theorem [21], stating that the phase space density of a particle ensemble cannot increase under elastic processes.

The true statistic-mechanical phase space contains six variables: the particle position, **r**, and velocity, **v**. Since all neutrons travel along the same direction, we essentially integrate out the position along the beam direction by counting the number of neutrons passing an area during a time much longer than the typical time between the arrival of two neutrons. We are thus left with five variables: two spatial, two concerning divergence, and the magnitude of the neutron velocity (or equivalently the wavelength). The phase space density is now given by the neutron flux per unit of divergence per wavelength interval. This strongly resembles the definition of brilliance used in X-ray instrumentation, where the unit is typically photons/(s mm^2 mrad^2 0.1% wavelength bandwidth) [22]. In our investigation below, we will use the brilliance unit neutrons/(s cm^2 deg^2 1% wavelength bandwidth).

To calculate the neutron brilliance in a ray-tracing simulation, we tracked the neutron flux through a small area (1 cm^2), for neutrons within a particular divergence interval (± 10 arc minutes or ± 30 arc minutes in both directions), when the moderator is limited to emit a narrow wavelength band ($\delta\lambda/\lambda = 1\%$). The simulated neutron flux for the wider divergence thus equals the brilliance units defined above. We sampled the brilliance at several places along the beam path:

- At the moderator surface.
- At the guide entry.
- At the guide exit.
- Just before the monochromator.
- Just after the monochromator.
- At the sample position.

The brilliance was calculated for both the original TAS (the baseline design), for the manually optimized spectrometer, and for the fully optimized TAS. The results are listed in Table 2. We see that the baseline design loses almost $\frac{2}{3}$ of its brilliance at the monochromator, while the hand optimized elliptical design loses a factor $\frac{1}{2}$, and the elliptical design only loses 45%. This is, however, not enough to account for the factor 12 in flux gain with a concurrent decrease in energy spread.

4. Discussion

Our results show that the classical design of a primary spectrometer for a cold-neutron TAS can be strongly improved. The new design includes an elliptical guide, focusing on a virtual source point. Placed 3.4 m after this virtual source, a doubly focusing monochromator performs non-equidistant focusing onto the sample position.

In our simulations, the sample flux is found to increase by a factor 12, while the energy spread decreases. The phase-space density analysis shows that the brilliance at the sample position is improved. The flux can be written as the brilliance multiplied with the energy spread and the divergence range, in the case where energy and divergence are uncorrelated (this will be shown below). This implies that the performance of the new design can be understood by a combination of a better transport (factor 1.6) of the brilliance onto the sample with lower energy spread (factor 0.65), and a higher divergence (factor 10) transported onto the sample position. This is verified by the divergence simulations, shown in Figs. 3–5.

In the final solution, the value of the brilliance at the sample is about 50% of that at the moderator. Taking Liouvilles theorem into account, there may thus be up to a factor 2 to gain for future design optimizations. However, when taking into account that the used reflectivity of PG (80%) is probably the highest diffraction reflectivity of any material, the maximal remaining gain factor is 1.5. One of the ways forward could be to employ anisotropic mosaicity of the PG material to minimize the increase in vertical divergence introduced by the mosaicity. It should also be considered to use non-elliptical guide shapes, which may produce an even better focusing at the virtual source point [23].

In cases where high divergence is unwanted, *e.g.* for single crystal diffraction, or when the design is used for a powder diffractometer, a simple Soller collimator can be employed. Additional simulations have showed that for tight collimations (20′), the new design is a factor 3 better than the baseline design, most of which (a factor 2) comes from the increase in vertical divergence. The energy resolution of the final solution is still about 20% better than the baseline design with collimation.

To understand the improvement in energy spread over the manually optimized solution, we consider the correlation between the horizontal divergence and wavelength, shown in Fig. 6. It can be seen that the shape of the divergence-wavelength "ellipsoid" has been rotated by the use of the non-equidistant focusing, so that the divergence and energy are essentially uncorrelated, since all divergences essentially represent the same energy. This insight allows for designing a controlled tuning of the resolution ellipsoid by rotating the analyzer mount to be somewhere between the Rowland position and the present optimal position. Much of the power of the TAS during the decades was based upon the fact that the resolution function can be shaped to fit the particular problem, *e.g.* by varying incident wavelength, collimations, and scattering angles [4]. Here we show that we can shape the correlations between energy and divergence.

The full four-dimensional (q,ω) resolution function can, however, only be investigated by studying a design of the complete spectrometer. It can be foreseen that the secondary spectrometer for a fully optimized TAS will be a multi-analyzer design, either of the RITA-type with closely spaced analyzers [24,25], a multi-analyzer system with broad coverage like MACS at NIST [10] or the ILL flat-cone type [26], or of the even more advanced multi-energy CAMEA type [27]. It is, however, too early to discuss the performance of these combinations of possible primary and secondary spectrometers. Additional simulations elucidating this problem are underways [28].

In the light of the current work towards realizing the European Spallation Source (ESS) [29], it is worth considering whether the spectrometer designed in this work would be suitable for a long-pulsed spallation source. Here, one could utilize the full time-integrated neutron flux produced at the moderator—the best estimate is that this will equal the ILL flux, giving an impressive sample flux of 9×10^8 neutrons/(s cm^2) at 5 meV. An important benefit of this design is that fast-neutron background can be

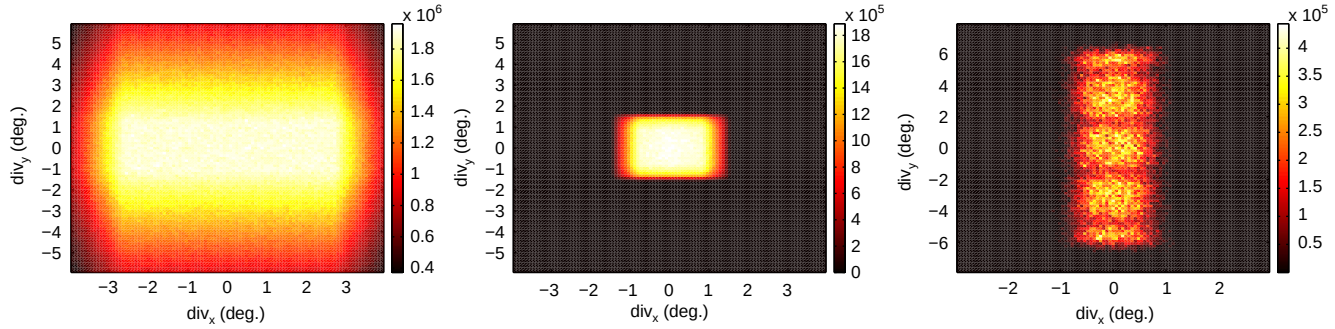

Fig. 3. Divergence plots sampled at a $10 \times 10\,\mathrm{mm}^2$ area at the baseline instrument using the full wavelength band of $\Delta\lambda = 2\,\mathrm{A}$. The data are presented in units of wavelength-integrated brilliance: $\mathrm{n}/(\mathrm{s\,cm}^2\,\mathrm{deg}^2)$. (a) The guide entry; (b) the guide exit; (c) the sample position.

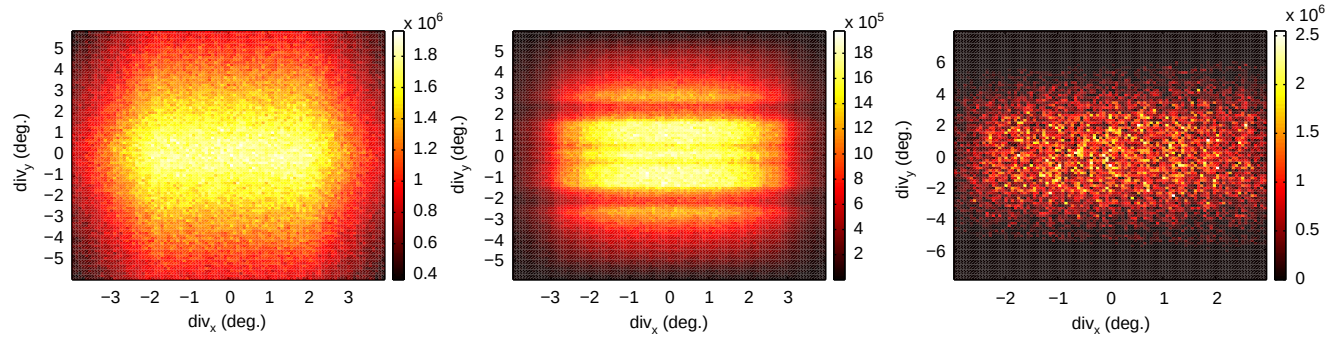

Fig. 4. Divergence plots sampled at a $10 \times 10\,\mathrm{mm}^2$ area at the hand optimized elliptical instrument using the full wavelength band of $\Delta\lambda = 2\,\mathrm{A}$. The data are presented in units of wavelength-integrated brilliance: $\mathrm{n}/(\mathrm{s\,cm}^2\,\mathrm{deg}^2)$. (a) The guide entry; (b) the guide exit; (c) the sample position.

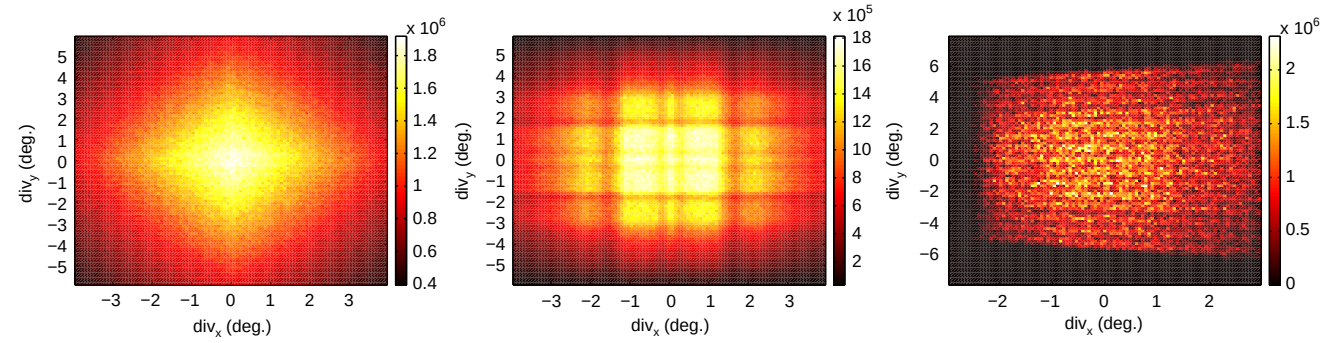

Fig. 5. Divergence plots sampled at a $10 \times 10\,\mathrm{mm}^2$ area at the final instrument using the full wavelength band of $\Delta\lambda = 2\,\mathrm{A}$. The data are presented in units of wavelength-integrated brilliance: $\mathrm{n}/(\mathrm{s\,cm}^2\,\mathrm{deg}^2)$. (a) The guide entry; (b) the guide exit; (c) the sample position.

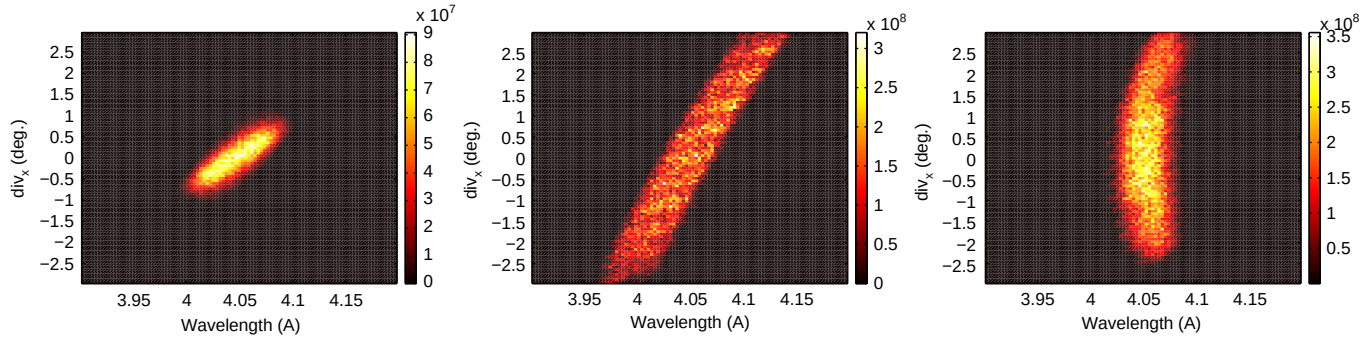

Fig. 6. Correlations between wavelength and horizontal divergence at the sample position, in arbitrary units. (a) The baseline design; (b) the manually optimized solution; (c) the final elliptical solution.

strongly suppressed by time-of-flight analysis, in particular when using incoming wavelengths which have frame overlap with fast neutrons from the previous pulse. For a 40 m instrument, this would imply that the incoming wavelengths should stay below 6 Å, which in practice is almost always the case for a cold-neutron TAS. As an additional advantage, thermal-neutron background and second-order scattering from the monochromator could here easily be suppressed by a slow chopper.

5. Conclusion

Based upon extensive simulations, we suggest a design of a primary spectrometer for a triple-axis spectrometer, consisting of an elliptical guide, a virtual source point, and a doubly focusing monochromator, which uses non-equidistant focusing. The performance of this primary spectrometer is strongly superior to the classical design, with a gain in incoming flux by a factor 12, with a slight improvement in energy resolution. Future detailed analysis, including background estimates, will show whether it will be worth building such an instrument on an existing or future neutron source. In particular, the issue of line-of-sight between moderator and monochromator should be considered. In addition, it will be interesting to study this type of design for a primary spectrometer for a thermal neutron instrument; and for use on a long-pulse spallation source like ESS.

The phase-space analyses shows that our suggested primary spectrometer for a TAS—or other similar instruments—does not yet have the optimal shape and that it theoretically should be possible to improve it by a factor 1.5.

As a final remark, we like to add that a very similar solution to the TAS optimization problem has recently been found by an independent work [30]. This work differs from ours in that they consider an addition of an elliptical guide to an existing conventional guide. However, the design of virtual source and doubly focusing monochromators are very similar. The agreement between the solutions is remarkable, not least due to the fact that our design improvement was found from a global computer optimization, while the design reported in Ref. [30] was found guided by a deliberate, experience-based effort.

Acknowledgements

We like to thank H.M. Rønnow, R. Pynn, and P. Böni for illuminating discussions. This project was supported by the Danish Research Council of Natural Sciences (FNU) through DANSCATT.

References

[1] B.N. Brockhouse, Phys. Rev. 98 (1955) 1171.
[2] I. Butterworth, P.A. Egelstaff, H. London, F.J. Webb, Philos. Mag. 2 (1957) 917.
[3] H. Maier-Leibnitz, T. Springer, J. Nucl. Energy A/B 17 (1963) 217.
[4] G. Shirane, S.M. Shapiro, J.M. Tranquada, Neutron Scattering with a Triple Axis Spectrometer, Cambridge University Press, 2002.
[5] See the ILL home page at ⟨www.ill.eu⟩.
[6] See the PSI home page at ⟨www.psi.ch⟩.
[7] See the HZB home page at ⟨www.heltmoltz-berlin.de⟩.
[8] See the NIST home page at ⟨www.nist.gov⟩.
[9] R. Schedler, M. Rotter, M. Löwenhaupt, N.M. Pyka, Appl. Phys. A 74 (2002) S1468.
[10] J.A. Rodriguez, et al., Meas. Sci. Technol. 19 (2008) 034023.
[11] K. Lefmann, K. Nielsen, Neutron News 10 (3) (1999) 42 see also ⟨www.mcstas.org⟩.
[12] S.N. Klausen, et al., Appl. Phys. A 74 (2002) S1508.
[13] L. Udby, et al., Nucl. Instr. and Meth A, this issue, doi:10.1016/j.nima.2010.06.235.
[14] J.K. Hansen, K.S. Hansen, B.P. Christensen, Student Report, University of Roskilde, 2004.
[15] C. Schanzer, P. Böni, U. Filges, T. Hils, Nucl. Instr. and Meth. A 529 (2004) 63.
[16] K.H. Klenø et al., Nucl. Instr. and Meth A, this issue, doi:10.1016/j.nima.2010.06.261.
[17] U. Filges, in preparation.
[18] P. Böni, et al., in: Proceedings of ICANS, 2010.
[19] K. Lefmann, et al., Physica B 283 (2000) 343.
[20] C.R.H. Bahl, P. Andersen, S.N. Klausen, K. Lefmann, Nucl. Instr. and Meth. B. 226 (2004) 667.
[21] See e.g. L.D Landau, E.M. Lifshitz, Course of Theoretical Physics, Statistical Physics, Part 1, vol. 5, Butterworth-Heinemann, 1980.
[22] J. Als-Nielsen, D.F. McMorrow, Elements of Modern X-ray Physics, John Wiley & Sons, 2001.
[23] P. Bentley, et al., these proceedings.
[24] K. Hradil, personal communication, 2010.
[25] C.R.H. Bahl, et al., Nucl. Instr. and Meth. B 246 (2006) 452.
[26] M. Kempa, B. Janusova, J. Saroun, P. Flores, M. Boehm, F. Demmel, J. Kulda, Physica B 385–386 (2006) 1080.
[27] H.R. Rønnow, personal communication, 2010.
[28] J.O. Birk, et al., in preparation.
[29] See the ESS project home page at ⟨www.ess-scandinavia.eu⟩.
[30] M. Janoschek, P. Böni, M. Braden, Nucl. Instr. and Meth. A 613 (2010) 119.

Journal of Neutron Research, Vol. 16, Nos. 3–4, September–December 2008, 97–111

Virtual experiments: the ultimate aim of neutron ray-tracing simulations

K. LEFMANN†‡||||*, P. K. WILLENDRUP†, L. UDBY†, B. LEBECH†‡, K. MORTENSEN§, J. O. BIRK†‡, K. KLENØ†‡||||, E. KNUDSEN†, P. CHRISTIANSEN†¶, J. SAROUN##, J. KULDA#, U. FILGES**, M. KONNECKE**, P. TREGENNA-PIGGOTT††, J. PETERS‡‡#§§***, K. LIEUTENANT¶¶, G. ZSIGMOND††, P. BENTLEY#‡‡ and E. FARHI#

†Risø National Laboratory, Materials Research Division, Technical University of Denmark, Lyngby, Denmark
‡Niels Bohr Institute, University of Copenhagen, Copenhagen, Denmark
§Faculty of Life Science, University of Copenhagen, Copenhagen, Denmark
¶Institute of Physics, University of Lund, Lund, Sweden
#ILL, Grenoble, France
**Laboratory for Development and Methods, PSI, Villigen, Switzerland
††Laboratory for Neutron Scattering, PSI, Villigen, Switzerland
‡‡Helmholz Zentrum für Materialien und Energie, Berlin, Germany
§§J. Fourier University, Grenoble, France
¶¶IFE, Kjeller, Norway
||||European Spallation Source Scandinavia, University of Lund, Sweden
##Nuclear Physics Institute, AS CR, Rez near Prague, Czech Republic
***Institute de Biologie Structure, Genoblie, France

(Received 20 April 2007 in final form 18 February 2008)

We define a virtual neutron experiment as a complete simulation of an experiment, from source over sample to detector. The virtual experiment (VE) will ideally interface with the instrument control software for the input and with standard data analysis packages for the virtual data output. Virtual experiments are beginning to make their way into neutron scattering science with applications as diverse as instrument design/upgrade, experiment planning, data analysis, test of analysis software, teaching, and outreach. In this paper, we summarize the recent developments in this field and make suggestions for future developments and use of VEs.

Keywords: Monte Carlo simulations; Neutron scattering; Neutron instrumentation; Data analysis

Introduction

The field of neutron ray-tracing simulations for scattering purposes has exploded during the last decade. This has primarily been caused by the increase in detailing level and user friendliness of the available software packages. The topic was pioneered by the legendary

*Corresponding author. Email: lefmann@fys.ku.dk

Journal of Neutron Research
ISSN 1023-8166 print/ISSN 1477-2655 online © 2008 Taylor & Francis
www.informaworld.com/journals
DOI: 10.1080/10238160902819684

neutron transport code MCNP (MCNP home page, mcnp-green.lanl.gov) and for scatteringpurposes by the NISP package (NISP home page, paseeger.com). In the late 90s, a new generation of freeware simulation packages were initialized, the most prominent being McStas [1], VITESS [2], RESTRAX [3], and IDEAS [4]. These packages have been developed concurrently since, in an atmosphere of friendly competition and have actively compared results and shared ideas for common benefit. At present, the packages have reached a level where actual 'virtual experiments' (VEs) can be performed. In this paper, we will make a proper definition of VEs and give recent examples of their broad usefulness.

Definition of VEs

The term VE is being widely used within the neutron simulation community, but has never been clearly defined. We will here establish the term VE by the definitions:

- The neutrons rays must have absolute intensity units and should be traced through the whole instrument, from source to detector [5]. (This can be done either by simulating each ray through the instrument or by breaking the simulation up into several bits.)
- The description of the instrument should be as close as possible to the reality. This is in particular the case for the sample.
- The virtual instrument is controlled like the real instrument, and the resulting data are analyzed like real data.

The input to a VE is the complete state and setting of the instrument: angles and collimation for a steady-state instrument, and chopper phases, etc. for a time-of-flight instrument. In addition, the state of the sample (*e.g.* orientation and temperature) must be specified. Preferably, the input to the VE should come from the instrument control software itself.

The outcome of VE are virtual data sets, which can be handled by standard analysis programs. The virtual data are used to obtain knowledge of the response of the neutron instrument to a particular sample.

One thing that cannot be deduced from the virtual data is, of course, the properties of the sample itself. In all simulation packages, this is specified by the user. However, it is very useful to simulate a sample with certain characteristic scattering features, in order to test whether a particular instrument is able to resolve these features. Examples of this are shown in the following.

Instrument upgrade and design

The most frequent application of VE – and of neutron ray-tracing simulations as such – is design of novel instruments. Initially, the most frequent use was for design of primary spectrometers (in particular guide systems), but with the advent of realistic sample components, also features of the secondary spectrometer have been simulated. This is in particular the case for the new and emerging sources FRM-II, OPAL, SNS, J-PARC, and ESS, but also for major existing source upgrades like the ILL millennium program and ISIS second target station.

The use of VE in instrument design is straightforward. By performing a VE on the instrument under design, one can obtain an idea of typical data, with respect to signal quality (*e.g.* peak shape), intensity, and possibly sample background. Simulation of room

background from *e.g.* fast neutrons is, however, usually out of reach for ray-tracing simulations, and more exact neutron transport codes must be employed, *e.g.* MCNP.

To estimate the value of the improvement by new instrument design – or instrument upgrade – it is usual to compare VE data from the new instrument and a baseline instrument. In principle, a comparison can be also performed between VE data and data measured on an existing instrument. One should, however, bear in mind that non-ideal properties of the instrument, not considered in the simulations, may lead to over- or underestimation of the simulated instrument performance, typically in the absolute intensities. Hence, a comparison between two simulations is usually the preferred procedure.

The IN20 flat-cone multianalyzer (ILL)

One of the first examples of VE in instrument design was the flat-cone upgrade of IN20, ILL. Here, the upgrade consists of replacing the standard triple-axis analyzer with a bank of 31 analyzers, 2.5° apart, which scatter out of the horizontal plane. All analyzers are fixed to accept the same energy [6]. This mode of running a triple-axis instrument compares with the monochromatic imaging mode of the 7 blade analyzer at RITA-2, PSI [7]. However, the flat-cone design has a much larger angular coverage.

The IN20 VE was performed using a sample with phonon dispersion in Si. In the VE, the sample rotation was scanned. This effectively produced a cut of constant energy transfer, obtaining a two-dimensional monochromatic cut in reciprocal space. Figure 1 shows the cut through the phonon dispersion ifself and the comparable outcome of the VE. All phonon features are clearly reproduced. This was a strong support for the decision of actually performing the flat-cone upgrade.

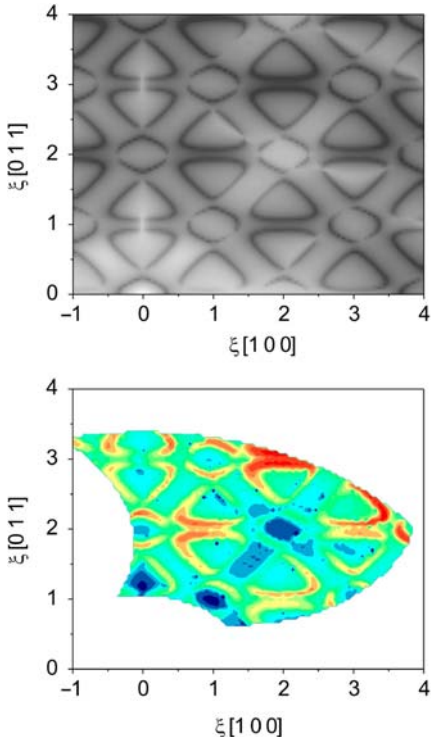

Figure 1. Inelastic (20 meV) 2-dimensional cut through the phonon dispersion of Si. Top panel shows the phonon dispersion model, bottom panel shows virtual data, obtained from a RESTRAX VE on IN20 (ILL).

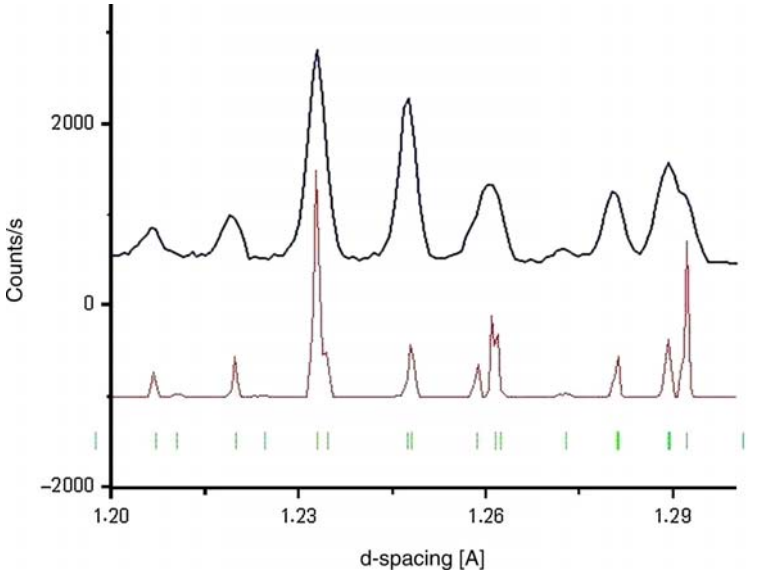

Figure 2. Powder diffraction pattern of $TbMnO_3$. Data from a VITESS VE at the planned HMI diffractometer EXED (middle, red), measured data at E9, HMI (top, blue), and the nominal peak positions for $TbMnO_3$ (bottom, green) (colour online).

Design of EXED (HMI)

VE has been used to evaluate the performance of the extreme environment diffractometer (EXED), under construction at the new guide hall at HMI. This instrument is special in the sense that is contains a set of unsplit solenoid coils for very high magnetic fields in the direction of the incident beam. Hence, scattering can be observed only in small angles and close to backscattering. Using the time-of-flight technique, the incoming wavelength can be scanned so that one has access to a large range of q-values. The backscattering condition gives a very high resolution in powder diffraction. This is illustrated in figure 2, where part of the virtual data are presented, together with the nominal peak positions. The data is compared with (scaled) real diffraction data from $TbMnO_3$, recorded at E9 (HMI). For this example, the resolution of EXED is clearly superior to E9. For more details about EXED, we refer to Ref. [8].

Instruments for ESS long-pulse target station (LPTS)

As the last examples of VE for design of new instruments, we show simulations of two instruments for the ESS long-pulse target station. A powder diffractometer on a long-pulsed source nominally suffers from lack of resolution. However, a clever use of pulse-shaping choppers close to the source makes the instrument strongly competitive to a diffractometer on a similar short-pulsed target [9]. Figure 3 shows a comparison between VE data on these two instruments. The LPTS instrument has both better intensity and a superior peak shape.

ESS LPTS instruments in general take advantage of the high integrated intensity of the 2 ms long pulse. The simulated cold-neutron chopper spectrometer further utilizes the low repetition rate (16 2/3 Hz), to select a number of pulses from each frame with different wavelengths. As an example, if the pulses are taken 5 ms apart (at the sample position), one can record up to 11 data sets for each pulse, with a wavelength difference of 2 Å between the first and the last pulse [10]. The data from the VE is shown in figure 4. As anticipated, the energy resolution and overall intensity vary significantly with wavelength. From the data, it is clear that the intensities of the different wavelengths are useful but cannot be directly added to obtain the overall performance

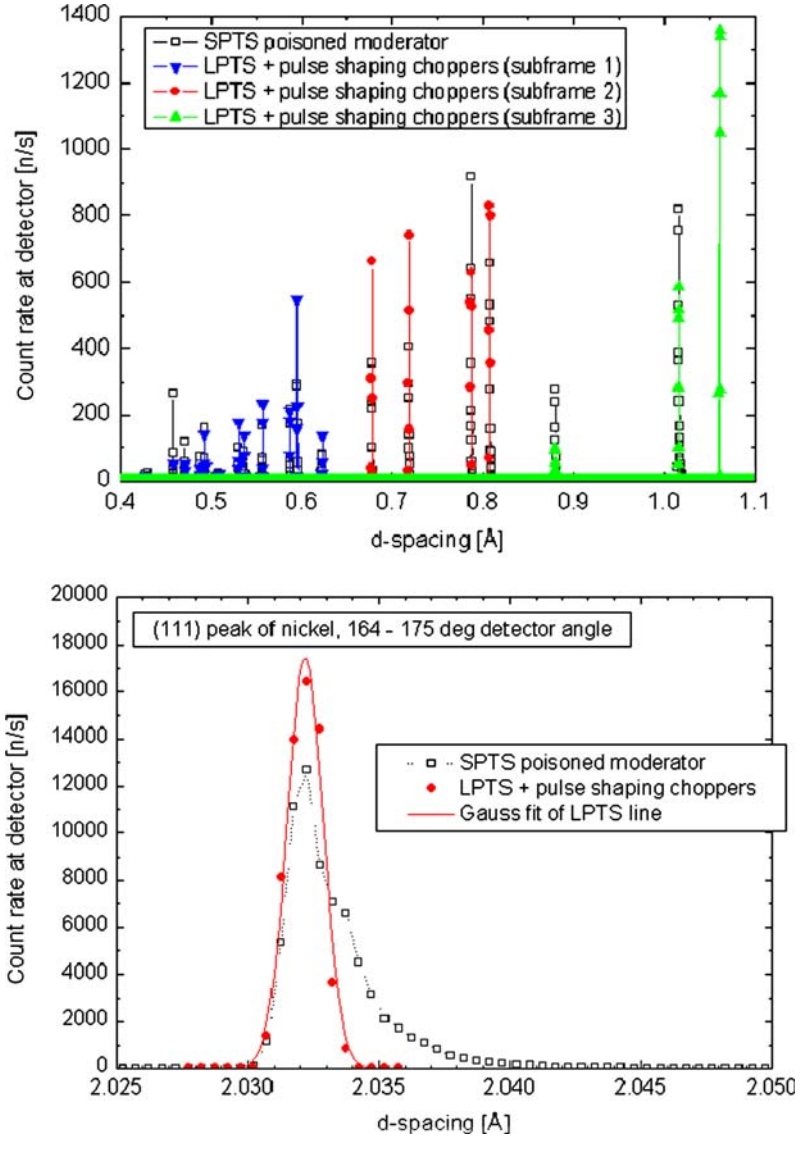

Figure 3. ESS long pulse powder lines, simulated by VITESS. Top panel shows a number of small-d diffraction peaks. Bottom panel shows a zoom on a single large d-peak. From [9].

of the spectrometer. This presents challenges for the optimization of the instrument and for the subsequent data analysis packages. This spectrometer and other instruments were simulated at a workshop in Rencurel (F), September 2006, later at the island of Ven (S), October 2008 (homepage of the Rencurel 2006 meeting, wwwold.ill.fr/Computing/links/meetings/ESS-LP/).

Experiment planning and optimization

In principle, a VE on a detailed model of an existing instrument can help users and instrument responsibles to estimate the feasibility of a planned project and help selecting the mode of running the instrument. This task is non-trivial, since it requires detailed models of the (expected behaviour of the) sample. Furthermore, a useful optimization tool for the

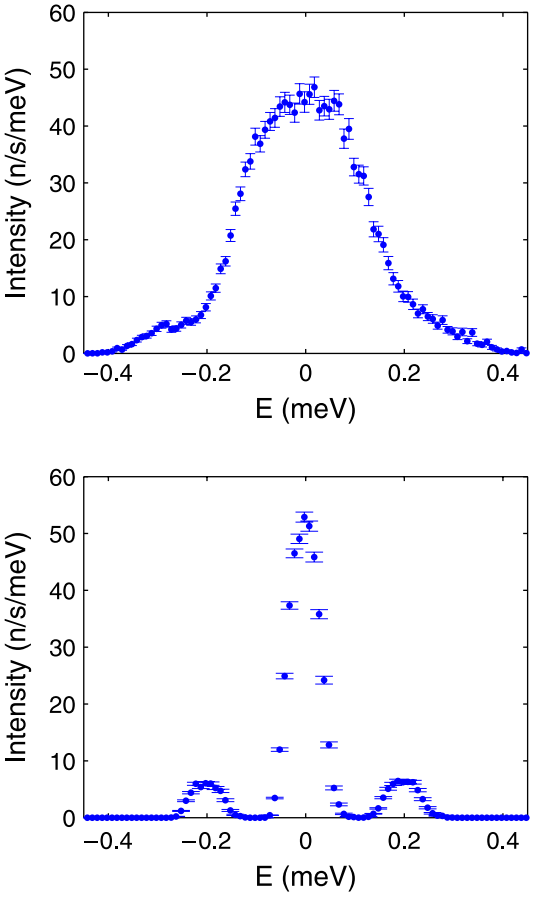

Figure 4. Inelastic scans on the cold-neutron chopper spectrometer for ESS long pulse target station. The data shows inelastic cuts through scattering data for a generic sample with an elastic line and 'tunnel peaks' at ± 0.2 meV. Top and bottom figure shows McStas virtual data for the same pulse with incoming wavelengths of 4 and 6 Å, respectively.

experimental mode must be easily available for non-specialist users. This is in sharp contrast to present-day optimization, which requires much expert knowledge and detailed analysis of simulated data, *e.g.* due to strong correlation between parameters.

Web simulation tools for neutron users

As the first prototype towards this goal, a simple user simulation tool has been constructed for the cold-neutron powder diffractometer DMC, PSI. The McStas simulation is controlled via the PSI instrument control program, SICS, which is in turn run from the instrument home page (DMC home page sinq.web.psi.ch/sinq/instr/dmc) [11]. Only the few most used settings of the instrument can be selected. The user will upload a standard crystallographic definition file, which is used together with geometrical information to define the sample. An illustration of this home page is shown in figure 5.

Scaling to absolute measurement times

One of the foreseen uses of VE is experiment planning. One aspect of this is the optimal configuration of the instrument, which will be considered below. Here, we will consider the determination of the total measurement time, relevant *e.g.* in connection with beamtime

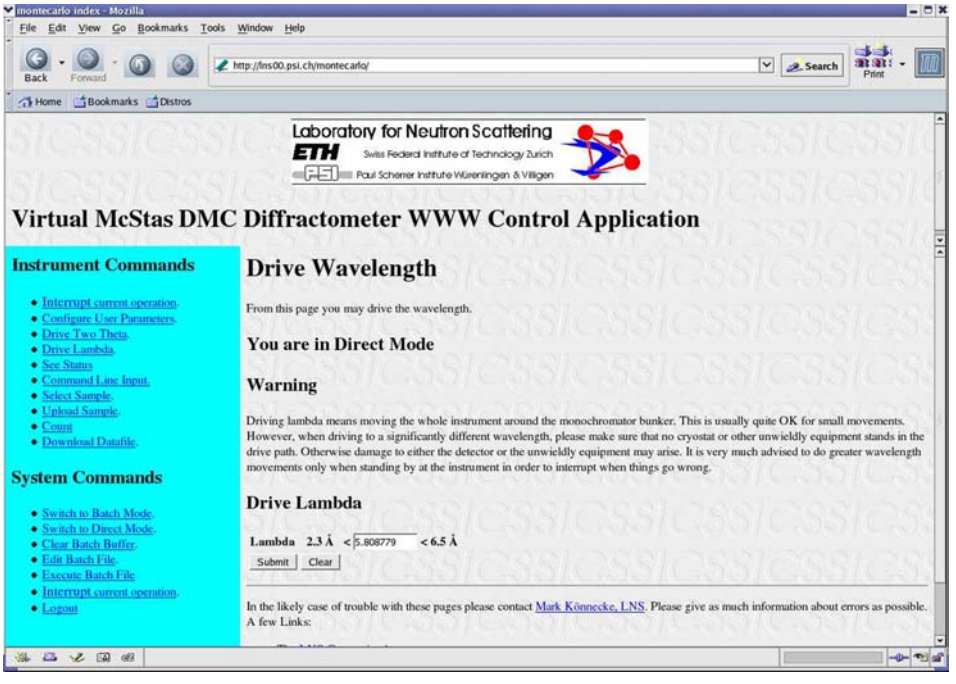

Figure 5. Front screen of the SICS–McStas web interface for the DMC powder diffractometer af PSI. The user can change the most standard settings of the VE through this portal.

proposals. It is thus essential for the simulations to give reliable estimates of the actual detector counts.

The ray-tracing simulation packages deal with intensities and error bars in very similar ways. The primary simulation unit is intensity (counts per second), so the assumed measurement time (the 'virtual time') is used to scale the virtual data to obtain integrated detector counts. In order to estimate total measurement time, realistic counting statistics must be imposed on the simulation counts, C, to reach the counts of the VE, C_{VE}. Since this has not been discussed in the litterature, let us describe it more thoroughly here.

Let n be the number of neutron rays reaching the detector, and let the rays have (different) weights, w_i. The simulated intensity is then given by

$$I = \sum_{i=1}^{n} w_i. \tag{1}$$

The estimate of the error on this number is calculated in the McStas manual [1], and the standard deviation is approximated by

$$\sigma^2(I) = \sum_{i=1}^{n} w_i^2. \tag{2}$$

In real experiments, $w_i = 1$, whence we reach $I = n$ and $\sigma(I) = \sqrt{I}$ as expected (for counts exceeding 10). Let the virtual time be denoted by t. The simulated counts during this time becomes

$$C = tI, \tag{3}$$

and its error bar estimate is

$$\sigma^2(C) = t^2\sigma^2(I). \tag{4}$$

However, to simulate a realistic counting statistics, we must fulfill

$$\sigma_{\mathrm{VE}}(C_{\mathrm{VE}}) = \sqrt{C_{\mathrm{VE}}}. \tag{5}$$

This is obtained by adding to (3) a Gaussian noise $E(\Sigma)$ of mean value zero and standard deviation Σ:

$$C_{\mathrm{VE}} = tI + E(\Sigma). \tag{6}$$

The standard deviation for the VE becomes

$$\sigma^2_{\mathrm{VE}}(C) = t^2\sigma^2(I) + \Sigma^2. \tag{7}$$

Now, the requirement (5) allows us to determine Σ:

$$\Sigma^2 = tI - t^2\sigma^2(I). \tag{8}$$

Since Σ^2 must remain positive, we reach an upper limit on t

$$t_{\max} = \frac{I}{\sigma^2(I)}. \tag{9}$$

Above this virtual time, it is not possible to obtain realistic error bars in the VE. This rule applies to each bin in a detector array, so the effective value of $t_{\max}$ is the smallest of the values in the individual bins.

One sentence of caution should be added: to avoid bins with zero (or very low) count rates, it may be necessary to apply a suitable rebinning and/or including an overall background (representing fast neutrons and/or electronic noise) before adding counting statistics.

Generic optimization

As a step towards easing optimization of instruments and experimental set-ups, we have been developing the use of evolutionary algorithms, widely used in machine-learning, engineering, and finance applications [12]. Through series of VE, these methods are able to evolve the design of instruments to arrive at the best possible configuration, *e.g.* for a given experiment.

In the first instance, it was demonstrated that genetic algorithms are able to adapt an existing spectrometer to accommodate new hardware at the maximum possible resolution, and find an operating configuration at the physical tolerance limits of components [13]. Figure 6 shows the convergence of a genetic algorithm upon a set of operating currents of a neutron spin-echo spectrometer, which are strongly dependent on the position of the 1 m diameter coils (also adjusted by the algorithm but not shown in the figure). In this figure, the vertical bars indicate the standard deviation of the parameters across the whole population of solutions, (but the deviations are not normally distributed around the mean value). Clearly seen are frequent fluctuations in parameter values, leading to a large change in the standard deviations, caused by the pseudo-random nature of the evolution process. The use of such algorithms allows scientific instruments to be quickly adapted for new experiments that were not considered in the original design.

Another application of these ideas was to evolve the design of an entire neutron spin-echo spectrometer. It was shown that a genetic algorithm was capable of arriving at a superior design to that obtained by traditional, manual means [14]. Furthermore, whereas the human

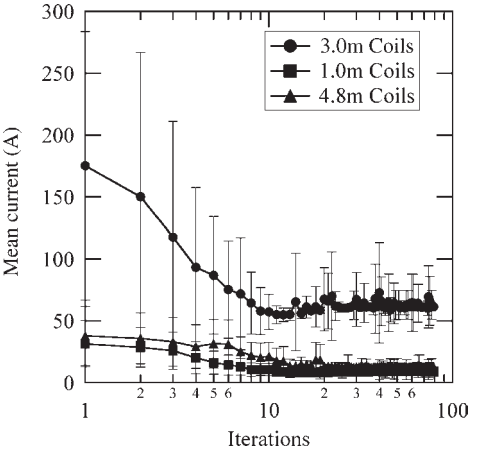

Figure 6. Evolving adjustment of the precession coils' and correction coils' currents on the spin-echo spectrometer SPAN, taken from [13], as described in the text.

design typically takes several weeks, the total calculation time for a genetic algorithm was less than 24 h. It is this ability, to change the criteria of the instrument design and find a new optimum at such short notice, which makes such artificial-intelligence based solutions such an attractive and powerful tool. The total programming time required is approximately equal to the manual design of an instrument, but thereafter the design can be modified at will, based upon new engineering constraints, adjacent experiments, and so forth. Clearly, this method is attractive for the optimization of any type of scientific instruments, with the figure-of-merit being the quality of the virtual data, evaluated by automated data analysis.

VEs play a crucial role in assessing the quality of the instrument for any given set of configuration parameters, since a figure of merit is used as a quantitative comparison of the quality of competing designs. The more accurate the results of the simulation, the better optimized the design will be for a given experiment. This makes such evolutionary algorithms very attractive for optimizing experiment with a given instrument and sample, and for a given region of interest of data. It has been demonstrated, albeit at an early stage [13,15], that genetic algorithms are also well suited for the tuning of resolution ellipsoids to a given dispersion curve in triple axis spectrometers. With further developments, we are confident that this will become a routine method of optimizing neutron instruments to a given experimental configuration. For example, the user can enter the desired resolution and the position in reciprocal space, and the artificial intelligence algorithm is able to select the optimum configuration to make the best use of experimental time, taking into consideration external factors such as background, multiple scattering, etc., and an accurate simulation of the behaviour at the sample. Such a tool would be invaluable for making the best use of experimental time for many scientific instruments.

Data analysis

To analyze data from VE, it is strongly preferable to use existing data analysis programs. This avoids discrepancies in analysis schemes and saves the simulator from developing new tools, at the expense of developing interfaces to suitable data format One emerging, site-independent format, sufficiently general to contain all types of neutron data, is NeXus (NeXus home page www.nexus.anl.gov). The packages VITESS, RESTRAX, and McStas all support NeXus.

An important use of VE is to obtain additional knowledge of the interplay between instrument and sample, allowing for high accuracy in the data treatment. This is detailed below.

Resolution effects

An obvious example of VE taking non-idealities into account is that the instrument resolution is automatically included in simulations. Furthermore, VE have the capabilities of determining the resolution to a higher precision than analytical calculations (for most instruments).

This effect was recently used to analyze data from an experiment at RITA-2, PSI. Here it was of high importance to conclude whether finite-size broadenings could be detected in certain diffraction signals [16]. To obtain maximal accuracy in determining the intrinsic instrument resolution, an 'alignment' was performed on parameters of the simulated instrument. This lead to a very good (within 1%) agreement in widths between a series of experimental and simulated scans (standard powder, vanadium, and sample rocking curve) [17]. Figure 7 compares the simulated resolution to the experimental results. It is seen that while the left and right peaks are broadened, the central signal appears to be resolution limited.

Multiple scattering

One feature that is inherently present in neutron scattering data is the unwanted scattering from the sample environment, multiple scattering in the sample, or multiples between sample and sample environment. Analysis of these effects is very well suited for ray-tracing simulations, and the first analyses of multiple scattering was performed long ago by the sample-scattering package MSCAT [18].

Recent advances in full-fletched VE have incorporated this functionality, and it is now possible not only to simulate sample environment background but also to distinguish different contributions. This very powerful capability is illustrated by a virtual inelastic time-of-flight experiment as shown in figure 8. This is a part of a larger effort, to be presented elsewhere [19].

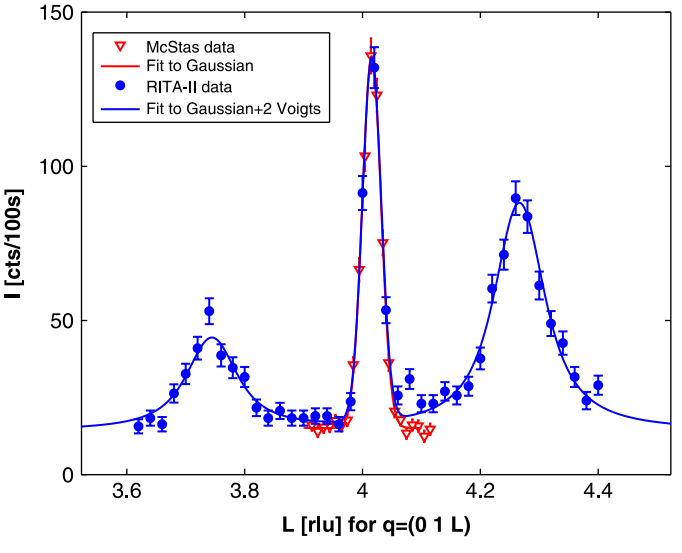

Figure 7. Real (circles) and VE (triangles) diffraction data on a single crystal, performed at RITA-2, PSI. The McStas model has been adjusted with respect to mosaics of the monochromator, analyzer, and sample to obtain agreement between virtual and real line-up scans. The central peak is clearly seen to be resolution limited [16].

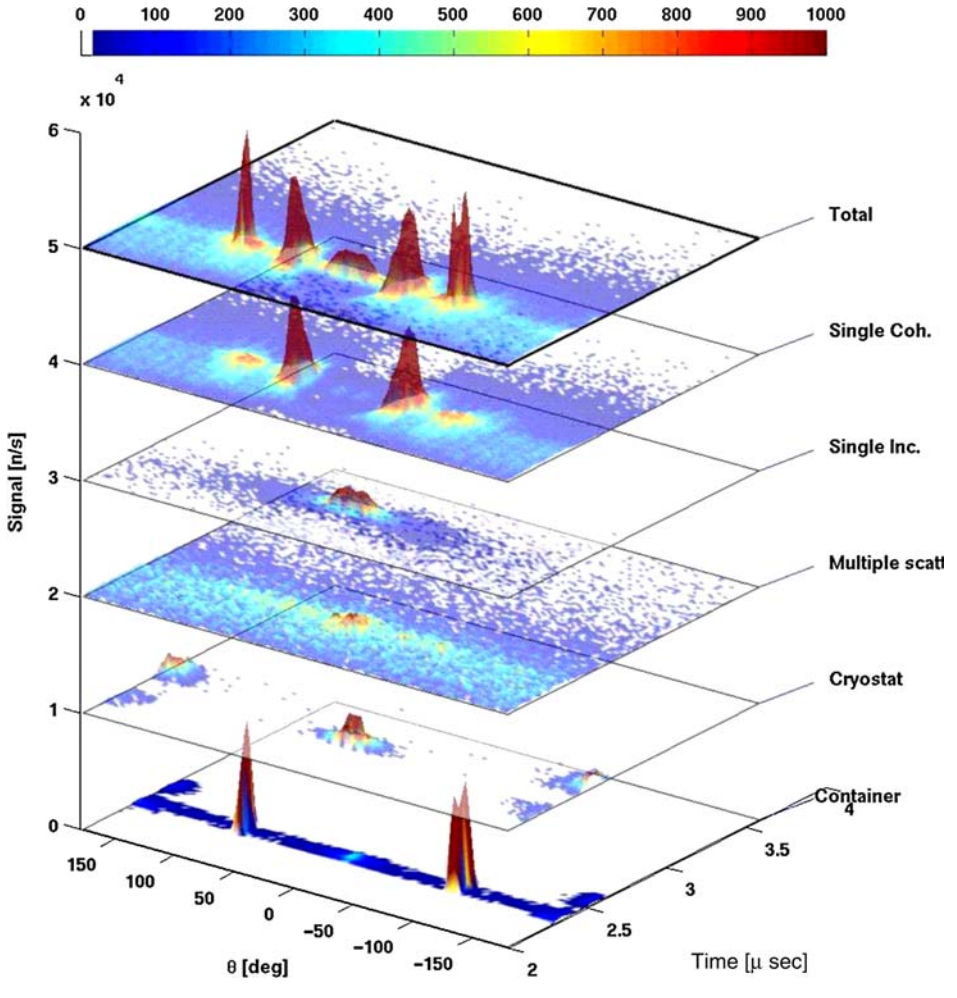

Figure 8. Data from a virtual inelastic time-of-flight experiment on a liquid metal sample, performed by McStas at a model of IN6, ILL. The scattering is presented horizontally and color coded, as a function of time-of-flight (depth) and scattering angle (vertical). The different layers in the figure represent different, clearly recognizable contributions to the total observed scattering (top layer). From [19] (colour online).

Testing analysis programs

By combining analysis programs and VE, the possibility opens to perform detailed, quantitative tests of the analysis programs themselves. The essential advantage of this test procedure is that the scattering cross section producing the virtual data is known.

Detailed VE data have been used to test the analysis program for the new time-of-flight backscattering instrument MARS, PSI. This was performed prior to the commissioning of the instrument [20]. A detailed analysis of a virtual quasielastic spectrum with the MARS analysis software, using a VE on a prototype instrument, resembling OSIRIS (ISIS) is shown in figure 9.

Analysis of non-standard experiments

The last example of data analysis deals with an individual experiment of non-trivial and non-standard character. Instead of writing a stand-alone analysis program for this single purpose, the VE scheme for data analysis may in fact be the most effective and fruitful way.

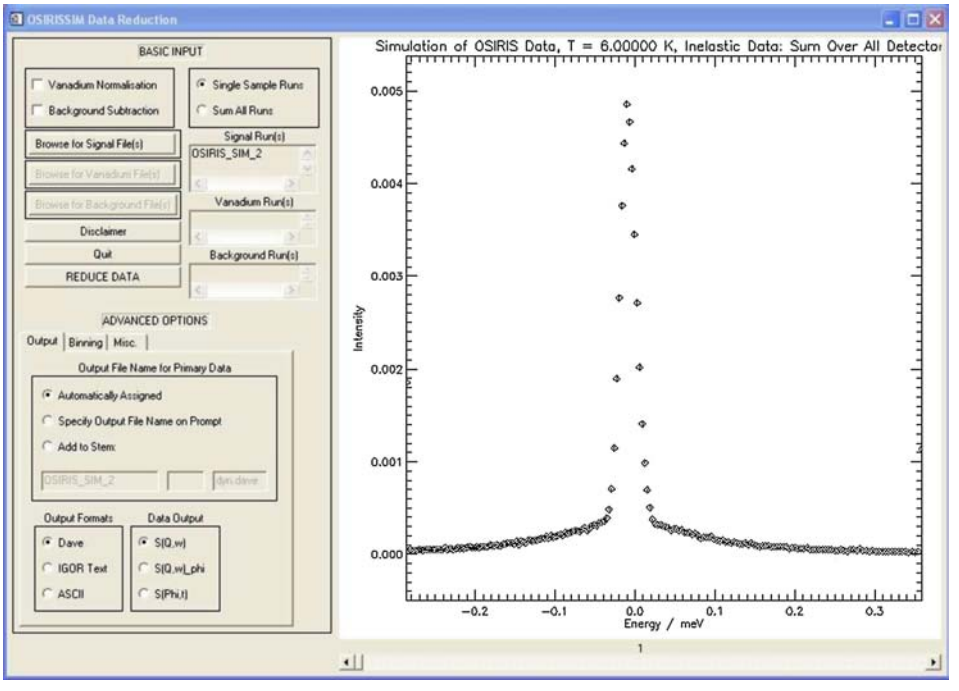

Figure 9. Data from a VE on a backscattering time-of-flight spectrometer, resembling OSIRIS (ISIS). The virtual sample has an incoherent elastic line and a quasielatic component. The data points show the data produced by a McStas VE, processed through the data analysis program [20].

One example in this direction is the determination of Fermi potential parameters of diamond-like carbon. This was determined through transmission measurements and concurrent VE of the experimental set-up [21,22]. The data are shown in figure 10.

Teaching and outreach

As an additional benefit to their intended scientific use, simulations have proved to be of very high value for illustration and teaching purposes, both at the university and the general public level. A few recent examples are shown below.

University teaching

Since 2005, simulations have been employed as a teaching tool for a course in neutron scattering for 4th year undergraduates and 1st year graduates at University of Copenhagen. The students are taught the simulations tools alongside the usual theory, and perform VE on guide construction, small-angle scattering, powder diffraction, and triple-axis spectroscopy. The data from VE are analyzed using standard packages, like MFIT (MFIT home page, www.ill.fr/tas/matlab/doc/mfit4/mfit.html) and FULLPROF (FULLPROF home page, www.ill.fr/dif/Soft/fp), see figure 11. The course ends by real experiments at RITA-2 and SANS-2, PSI.

The effect of including VE in the teaching has been surprisingly strong. The students learn the theoretical material faster than usual, maintaining a high level of motivation. In addition, the students obtain a genuine ‘hands on’ experience with neutron scattering, including data analysis and instrumention, before the arrival at the facility. This use of VE can be of great

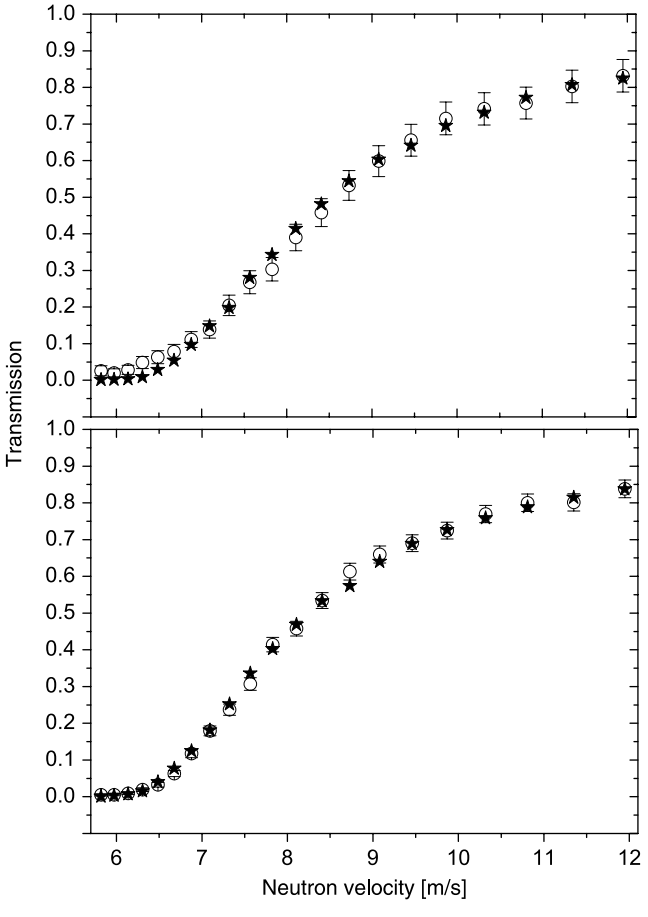

Figure 10. Measured reflectivity data (open circles) and data from the corresponding VE (stars) for the transmission of ultracold neutrons through material foils. Top: 150 nm diamond-like carbon (DLC) on 180 μm aluminium. Bottom: 200 nm beryllium on a 525 μm silicon wafer. The neutron Fermi pseudo-potential parameters for DLC and beryllium were extracted by fitting the measured data with the simulated ones via scanning the model parameters using VITESS. From Refs. [21,22].

importance for training of new users at the emerging powerful facilities, where real beam time may become too valuable (and too short) to use for training purposes.

Public outreach

Another use of VE is for the purpose of addressing the general public. Figure 12 shows a snapshot from a Danish home page, targeted at the educated public (high school level). Here, the basics of neutron scattering is presented, and much of the home page functionality is supported by ray-tracing simulations. The users can 'control' a selected set of easy VE and use them to rediscover important historical moments in neutron scattering, *e.g.* the discovery of antiferromagnetism and the first phonon dispersion curves.

Summary and outlook

As we have shown with a series of examples, VEs have large potential benefits for neutron scattering community as a whole, some of which unfold as we write. VE are already in use

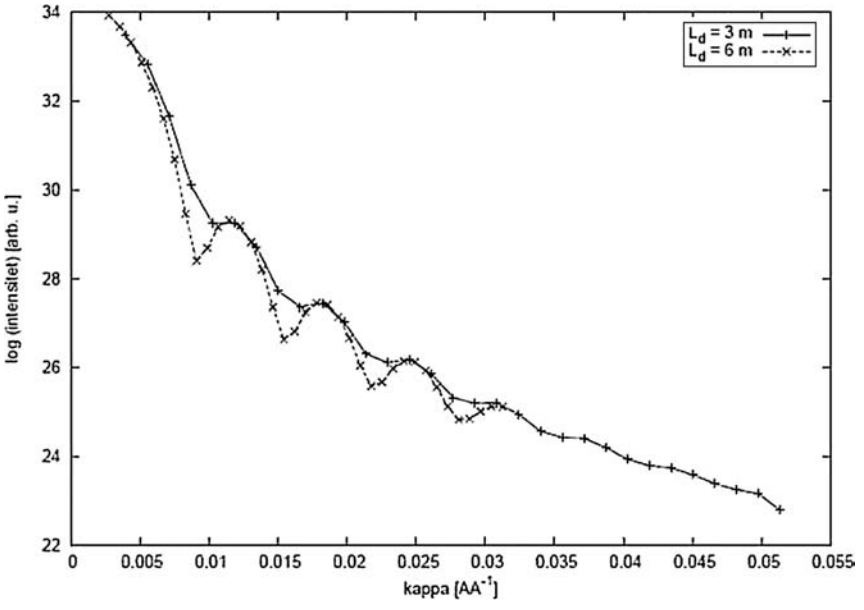

Figure 11. Virtual SANS data from a course in neutron scattering at University of Copenhagen, 2006. The McStas VE was performed on a model of SANS-2 (PSI), using a sample of dilute, hard spheres. The VE is performed for two settings of the instrument: collimator/detector lengths of 3 and 6 m.

for the design of new instruments and instrument upgrade at all major facilities. It is likely that VE will soon be a common tool for experiment preparation and in analysis of subtle effects of non-idealities in the obtained data.

VE is found to be very demonstrative for educational purposes at different levels. Furthermore, we can foresee that VE will be used as on-the-fly diagnostics tool for spotting problems during experiments.

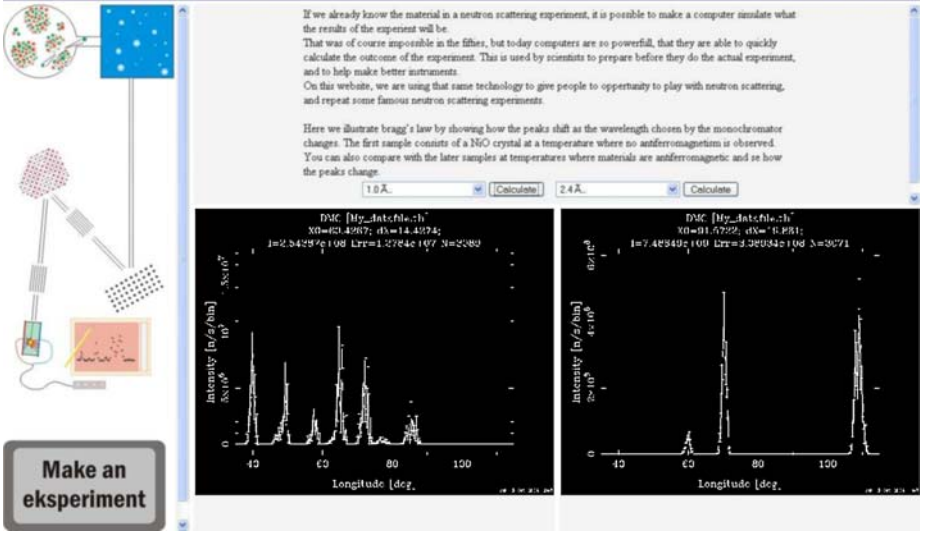

Figure 12. Simulations are used to illustrate the process of neutron scattering in an interactive home page for the broader public. The figure shows virtual diffraction patterns from NiO, at two different wavelengths, below the antiferromagnetic transition temperature.

It should be made clear, however, that each of the examples shown have required significant preparation time. Thus, development of VE on most neutron instruments worldwide will be a major, although potentially very rewarding task, involving users, instrument responsibles, and dedicated simulators alike.

Acknowledgements

The development of VEs has been a major task of the Joint Research Activity 'MCNSI' (MCNSI home page, www.mcnsi.risoe.dk), which was a part of the EU-supported integrated infrastructure initiative NMI3 (NMI3 home page, www.neutron-eu-net), EU contract number RII3-CT-2003-505925 under FP6. The co-authors of this paper have all contributed to the developments in MCNSI.

Part of this work has been supported by the EU grant to contruct ISIS second target station, and by the Danish Research Council through the neutron instrument centre DANSCATT.

References

[1] K. Lefmann and K. Nielsen, Neutron News **10**(3) 20 (1999), see also the McStas home page. Available at www.mcstas.org.
[2] G. Zsigmond, K. Lieutenant and F. Mezei, Neutron News **13**(4) 11 (2002), see also the VITESS home page. Available at http://www.hmi.de/projects/ess/vitess/.
[3] J. Saroun and J. Kulda, Physica B **234–236** 1102 (1997); J. Saroun and J. Kulda, SPIE Proc. **5536** 124 (2004); see also the RESTRAX home page. Available at http://omega.ujf.cas.cz/restrax.
[4] W.-T. Lee, X.-L. Wang, J.L. Robertson, F. Klose, and C. Rehm, Appl. Phys. A **74** S1502 (2002); see also the IDEAS home page. Available at www.sns.gov/ideas.
[5] K. Lefmann, E. Farhi and V. Hugovieux, Neutron News **16**(2) 34 (2006).
[6] M. Kempa, B. Janusova, J. Saroun, P. Flores, M. Boehm, F. Demmel and J. Kulda, Physica B **385–386** 1080 (2006).
[7] C.R.H. Bahl, K. Lefmann, A.B. Abrahamsen, H.M. Rønnow, F. Saxild, T.B.S. Jensen, L. Udby, N.H. Andersen, N.B. Christensen, H.S. Jacobsen, T. Larsen, P.S. Häfliger, S. Streule, and Ch. Niedermayer, Nucl. Instr. Meth. B **246** 452 (2006).
[8] J. Peters, K. Lieutenant, D. Clemens and F. Mezei (2004), Proceedings of the European Powder Diffraction Conference, Prague, September 2004; Z. Krist, Suppl. **23** 189 (2006); K. Lieutenant, J. Peters, F. Mezei, J. Neutron Res. **14** 147 (2006).
[9] K. Lieutenant and F. Mezei, J. Neutron Res. **14** 177 (2006).
[10] K. Lefmann, H. Schober, and F. Mezei, Meas. Sci. Technol. **19** 034025 (2008).
[11] P.K. Willendrup, K. Lefmann, E. Farhi, and L. Keller, Physica B **385–386** 1032 (2006).
[12] P.J. Bentley, *Evolutionary Design by Computers*, Morgan Kaufmann, San Fransisco, CA, 1999, pp. 1–73.
[13] P.M. Bentley, C. Pappas, K. Habicht and E. Lelièvre-Berna, Physica B **385–386** 1349 (2006).
[14] R. Hölzel, P.M. Bentley and P. Fouquet, Rev. Sci. Instrum. **77** 105107 (2006).
[15] K. Habicht, private communication (2006).
[16] L. Udby, N.H. Andersen, K. Lefmann, B.O. Wells, H.E Mohottala, Ch. Niedermayer, N.B. Christensen, J.W. Lynn, and F.C. Chou, in preparation 2008.
[17] L. Udby, P.K. Willendrup, E. Knudsen, K. Lefmann, in preparation 2009.
[18] J.R.D. Copley, Comput. Phys. Commun. **7** 289 (1974).
[19] E. Farhi et al., in preparation.
[20] P. Tregenna-Piggott, F. Juranyi, P. Christiansen, P.K. Willendrup, and K. Lefmann, J. Neut. Res. **16** 13 (2008).
[21] F. Atchison, B. Blau, M. Daum, P. Fierlinger, A. Foelske, P. Geltenbort, M. Gupta, R. Henneck, S. Heule, M. Kasprzak, M. Kuźniak, K. Kirch, M. Meier, A. Pichlmaier, Ch. Plonka, R. Reiser, B. Theiler, O. Zimmer, and G. Zsigmond, Phys. Lett. B **642** 24 (2006).
[22] F. Atchison, B. Blau, M. Daum, P. Fierlinger, P. Geltenbort, M. Gupta, R. Henneck, S. Heule, M. Kasprzak, A. Knecht, M. Kuźniak, K. Kirch, M. Meier, A. Pichlmaier, R. Reiser, B. Theiler, O. Zimmer, and G. Zsigmond, Nucl. Instr. Meth. B **260** 647 (2007).